Deliverable D13.1
Multiscale monitoring of civil assets system implementation & bridges and earthworks asset management system implementation report

Project acronym:	FP3 - IAM4RAIL
Starting date:	01/12/2022
Duration (in months):	48
Call (part) identifier:	HORIZON-ER-JU-2022-01
Grant agreement no:	101101966
Due date of deliverable:	Month 32
Actual submission date:	16-09-2025
Responsible/Author:	Margherita Lupi (FS)
Dissemination level:	PU
Status:	Issued

This project has received funding from the European Union's Horizon Europe research and innovation programme under Grant Agreement No 101101966.

Document history		
Revision	*Date*	*Description*
0.1	20.01.2025	Table of contents
0.2	05.05.2025	First version full UCs (paragraph and chapter)
0.3	30.05.2025	Final draft version
0.4	25.06.2025	Final version
1.0	16.09.2027	Final approved version submitted to ERJU

Report contributors		
Name	Beneficiary Short Name	Details of contribution
Margherita Lupi	RFI	Contribution on chapter 1, 2, 3, 4, 7 and 8, Coordination of contributes on other sections of document (chapter 5,6,9)
Nazzareno Lopez	RFI	Contribution on chapter 5.4
Giulia Polimanti	RFI	Contribution on chapter 5.4
Marco Fussotto	RFI	Contribution on chapter 5.4
Chiara Cesali	ITALFERR	Contribution on chapter 5.6
Jose Solís Hernández	CEMOSA	Table of contents and contributions on Spain Use Case
Pablo Jose Vallhonrat Blanco	CEMOSA	Impact of climate change (5.6) and Appendix I
Antonio Vallecillo Morcillo	CEMOSA	Contributions on Spain Use Case
Teodora Palmas	Mer Mec	Main contributor to 5.2, 5.3, 5.4
Ignazio Rana	Sitael	Main contributor to 5.5
Vito Amoruso	Mer Mec Engineering	Contribution on chapter 5.4, 5.7
Cosimo Cagnazzo	Mer Mec Engineering	Contribution on chapter 5.4, 5.7
Apollonia Netti	Mer Mec Engineering	Contribution on chapter 5.7
Nicola Ranieri	Mer Mec Engineering	Drone pilot & Contribution on chapter 5.4
Pedro Martin Perez Martinez	ADIF	Contribution on chapter 6.3, 6.4, 6.5, 7.3
Andrea G. Serrano Campo	ADIF	Contribution on chapter 6.3, 6.4, 6.5, 7.3
Alejandro Rodríguez	INECO	Contribution on chapter 6
Eduardo López	CEDEX	Contribution on chapter 6
Vincenzo Scarnera	MER MEC	Work Package Leader, final internal revision

Table Of Content

List Of Figures

List Of Tables

1. Executive Summary

Deliverable 12.1 of WP 12 addresses specific needs and challenges of civil engineering, specifies the monitoring systems for infrastructure assets (bridges, tunnels, earthworks or geotechnics), defines the technologies and comes with first monitoring and inspection data from the field. This current deliverable, Deliverable 13.1 of WP 13, extensively implements and technically demonstrates the monitoring technologies specified and designed in WP12.

The present document is divided in the following chapters:

Chapter 3 recaps the background related to the implementation of monitoring and asset management systems for railway civil structures and earthworks (this involves lifecycle management of the assets in presence of external risks). This section showcases the background information for the Italian and Spanish use cases. The two use cases have been developed by industrial partners and infrastructure managers, accordingly to the specifications described in WP12.

Chapter 4 briefly describes the aims of both the Italian use case UC1 and the Spanish use case UC2. The Italian use case involves vegetation encroachment, bridge inspection, landslides, flood risk and implement a Web GIS platform. The Spanish use case focuses on bridges and earthworks in monitoring performed with different techniques in different locations.

Chapter 5 describes in detail the technical solutions of UC1 for vegetation encroachment (Milano-Magenta), bridge inspection (various bridges across Italy), landslides (in Cerignola Campagna and Talud Briones) and flood risk (Milano -Novara). Previous results, extensive new data collection and subsequent algorithms are finely detailed for each individual solution implemented. The web platform, capable to host and showcase each technical solution is presented. Data gathering and processing (landslides and flood risk) in selected locations across the two countries join the Italian UC (chapter 5) and the Spanish UC (chapter 6).

Chapter 6: The objective of this chapter is the development and implementation of systems, both for integral monitoring of the structures and preventive maintenance systems at the sites of the Arroyo de las Huertas de Mateo Viaduct and the Briones hillside, Haro. Each of the projects will be monitored in a specific way, looking for the best system to establish preventive maintenance systems that fit both the objective of the chapter and the data obtained by the sensors. In order to be able to observe these analyses and the solutions that will be achieved, a web platform will be developed where it will be possible to see in real time the monitoring of the data and the results of the analyses used. In addition, in both projects a period of 12 months will be established in which data will continue to be obtained, and algorithms will be improved to give the most appropriate and accurate results possible for this chapter.

Chapter 7: This section provides a description of the assets on which the Key Performance Indicators (KPIs) will be calculated in the upcoming deliverable D13.3: Civil Engineering Asset Management Demonstration and Validation Report. The MAWP KPIs will be linked to the performance indicators of Use Case 12.1 (Italy) and Use Case 12.2 (Spain).

2. Abbreviations and acronyms

Abbreviation / Acronym	Description
ADIF	Administrador de Infraestructuras Ferroviarias
AOI	Area of interest
BIM	Building Information Modeling
BMS	Bridge Management Systems
CEMOSA	Centro de Estudios de Materiales y Control de Obra, S.A.
CHM	Canopy Height Model
CMOS	Complementary Metal-Oxide-Semiconductor
CORDEX	Coordinated Regional Downscaling Experiment
DOMUS	Diagnostics Artwork Unified Maintenance Standard
DT	Digital Twin
EOC	Environmental Conditions
EOCs	Environmental and Operating Conditions
FEM	Finite Element Model
GA	Grant Agreement
GCM	Global Circulation Models
GEE	Google Earth Engine
GIS	Geographic Information System
GPM	Global Precipitation Measurement
GPS	Global Positioning System
IM	Infrastructure Manager
IMERG	Integrated Multi-satellite Retrievals
InSAR	Interferometric Synthetic Aperture Radar
IOT	Internet Of Things
IoU	Intersection over Union
KPI	Key Performance Indicators
KS	Kolmogorov-Smirnov
LST	Land Surface Temperature

Abbreviation / Acronym	Description
LVDT	Linear Variable Differential Transformer
MAE	Mean Absolute Error
MAWP	Multi Annual Work Program
ML	Machine Learning
MODIS	Moderate-Resolution Imaging Spectroradiometer
NASA	National Aeronautics and Space Administration
NN	Neural Network
OMA	Operational Modal Analysis
PCA	Principal Component Analysis
PSD	Power Spectral Density
RCM	Regional Climate Models
RCP	Representative Concentration Pathways
RFI	Rete Ferroviaria Italiana
RTK	Real Time Kinematics
RU	Railway Undertaking
SAR	Synthetic Aperture Radar
SHM	Structural Health Monitoring
STD	Standard deviation
TCL	Track Centre Line
UAV	Unmanned Aerial Vehicle
UC	Use Case

3. Background

The present document constitutes the Deliverable D13.1 – “Multiscale monitoring of civil assets system implementation & bridges and earthworks asset management system implementation report” in the framework of the Flagship Project 3 – IAM4RAIL (GA 101101966) as described in the EU-RAIL MAWP.

The work focuses on the implementation of systems (Multiscale Monitoring of civil assets and Bridges and Earthworks Asset Management system) whose development is aimed at improving the life cycle management of civil assets, which include both civil railway structures such as bridges, as well as civil works such as earthworks and the surrounding environments. The implementations of these asset management systems aim to develop solutions that also consider external factors affecting railway infrastructures, including vegetation encroachment, landslide and flood risk and other factors from various sources.

This specifications for this work can be found in deliverable D12.1 - “Civil Engineering requirements, architecture, inspection and monitoring report”.

In relation to each use case covered (Italian and Spanish), this document illustrates the Implementation Reports of the systems developed by the industrial partners and the Infrastructure Managers (IMs) to solve problems in compliance with measurable innovation objectives described in D12.1.

4. Objective/Aim

The present Deliverable D13.1 is linked to both task T13.1 (Italian Use Case) and task T13.2 (Spanish Use Case), as described in the Grant Agreement.
Regarding T13.1, this document has been prepared to provide and detail the user needs, the approaches for collecting and processing satellite and UAV data, ground data collection strategies, the data analysis methodologies and tests (e.g. bridge and vulnerability assessment) and the user data navigation platform developed for multiscale monitoring of civil assets.
The work related to task T13.2 presents developments on satellite data collection and processing, ground data collection involving bridges and earthworks; developments on information integration and processing; algorithms for predictive maintenance and developments on asset management platforms.
The two UCs are composed by different technologies and respective implementations:

- **Multiscale Monitoring of Civil Assets** (Italian UC). This UC works with following different assets:
    - Vegetation encroachment
    - Classification and change detection
    - Bridge inspection and defects analysis
    - Subsidence & Landslides
    - Flood risk assessment
    - Web GIS Platform for multiscale monitoring
- **Bridges and Earthworks Asset Management aided by Geotechnics** (Spanish UC). This UC works with following different assets:
    - Bridges
    - Earthworks. Two different locations are used for the earthwork's demonstration:
        - Briones
        - Vilar de Silva

5. Multiscale monitoring of civil assets (Use Case 13.1, Italy)

5.1. Introduction

Traditionally, field inspections on the rail corridor are used to report breaches of regulations and standards such as the presence of illegally constructed buildings, excavations, vegetation and any other material within a safe distance, including trespassing on private property and free-roaming livestock in the vicinity of the railway line.

In recent years, FS Group has set a strategic objective: to design, develop, and implement a comprehensive system for the control and management of the entire life cycle of civil infrastructure assets (e.g., bridges), railway infrastructure, and the surrounding territory. This includes monitoring external factors such as vegetation encroachment, asset identification, subsidence, landslides, floods, and other environmental conditions that impact railway operations. Another key objective is to significantly reduce response times during emergency situations. The new envisioned system integrates data from multiple sources and technologies, enabling a unified and intelligent approach to maintenance support. Currently, data is managed in silos, limiting its effectiveness. By merging and integrating these diverse data streams, the system will enhance data usability and accessibility for maintenance personnel, ultimately improving decision-making and operational efficiency. These objectives are in line with the Holistic Asset Management principles of FP3-IAM4RAIL.

The following sections will provide a detailed overview of the data acquisition process for the monitored assets, including their geographic and territorial references. It will also describe the tools, technologies, and devices employed for data collection and the subsequent processing methods, which leverage neural networks and artificial intelligence algorithms. The threads of Vegetation Encroachment, Automatic Classification, Change Detection, Bridge inspection and Landslide will all be countable and on the web platform, purposely developed for the FP3-IAM4RAIL project (section 5.8).

5.2. Vegetation Encroachment

Hazards due to vegetation and other potential interference along the railway (e.g. proximity of buildings) are monitored by carrying out periodic field visits and by dedicated video surveillance, which often involves a laborious, time-consuming and expensive vegetation management process. Routine field inspections provide a wide range of checks on the general health of the infrastructure, (tracks, structures, roads, fences, level crossings, signalling equipment, overhead contact line) with particular attention to the effects of flooding. The inspection-related activities are then recorded in the maintenance management system. The frequency and means of inspections depend on the category of the railway line, traffic type as well as the maintenance needs. Based on the results of the investigations evaluated by the maintenance personnel, maintenance actions are then focused.

5.2.1. Summary of previous results and achievements

In the initial phase of the project, a NN pipeline was developed to extract the Canopy Height Model (CHM) from a multispectral satellite image with six bands and a spatial resolution of 30 cm per pixel. The ground truth was derived from a CHM generated using a classified point cloud (PC), obtained from airborne lidar data. From this point cloud, a classification map was also extracted, containing three classes: *terrains*, *vegetation*, and *buildings*. These three classes, along with the background, formed four additional input channels, resulting in a ten-band input dataset.
The data used for this work covered a geographical area located above the city of Potenza, in the Basilicata region. By intersecting the satellite data with the ground truth, a usable area of 1.26 km² was obtained, which was then divided into 128x128 pixel square tiles.
The NN model used for CHM prediction was a convolutional U-Net with a ResNet18 encoder and a linear activation function in the final layer, designed for a linear regression task.
The training process yielded promising results, particularly for the *terrains* class, but also for the more relevant *vegetation* class. Conversely, the predicted height of the *buildings* was unsatisfactory. This last outcome was not surprising, as very few *buildings* were present in the satellite image, limiting the model's ability to learn their representation effectively.
An analysis comparing the predicted CHM and the ground truth showed average differences of 0.5 meters for *terrains*, 3 meters for *vegetation* (with a tendency to overestimate), and 6 meters for *buildings*.

5.2.2. Acquisition and processing of additional EO data

To improve model performance and enhance its generalization capabilities, the dataset was expanded by acquiring additional multispectral satellite images, once again endowed with six bands and a resolution of 30 cm per pixel. Acquiring new data allowed us to perform analysis and AI trainings on an area 24 times bigger than that presented in WP12.

Figure 5-1: New areas selected for CHM estimation.

The initial intention was to train the NN to generalize across seasons by using image pairs representing the same area at different times of the year. Moreover, acquiring image pairs for the

same area was not feasible due to the unavailability of high-quality images from the Pleiades Neo satellite constellation that met the neural network's requirements. Therefore, instead, seven new satellite images were selected, covering a geographical region between Milan and Novara, in Lombardy. The images are shown in Figure 5-1.

These images spanned from April 2022 to February 2024 and were temporally as close as possible to the airborne ground truth data. On average, a 2–3-month difference was observed between satellite and airborne acquisitions, while the acquisition time was consistently around 10 a.m. The satellite viewing angle ranged from 6-7 degrees, with one image taken at 17 degrees. The satellite data used during the initial phase of the work (WP12) was acquired in August 2022, too around 10 a.m., with an inclination of 19 degrees.
The characteristics of the previous and the new datasets were relatively homogeneous, except for the inclination angle, which can significantly affect the visual appearance of objects, as it can easily be seen in Figure 5-2. On the left a snippet of the old data is shown, with an inclination angle of 19 degrees, while on the right a snippet of the new data, with an inclination of 6 degrees. On the left, building facades are visible, whereas on the right they are not.

Figure 5-2: Left: piece of old data, with 19 degrees of inclination. Right: piece of new data, with 6 degrees of inclination.

In conclusion, after intersecting the satellite data with the ground truth, a usable area of approximately 23 km² was obtained. By adding the area from the previous dataset, the total usable area reached approximately 24 km².
This surface was then divided into 256x256 pixels square tiles, with an overlap of 64 pixels, to reduce discontinuity effects at the tile borders during predictions.

5.2.3. “Expanded Run” experiment: same process, bigger dataset

The first experiment conducted followed a procedure similar to that of the initial phase of the work but applied to a larger dataset. The model pipeline shown in Figure 5-3 was employed.

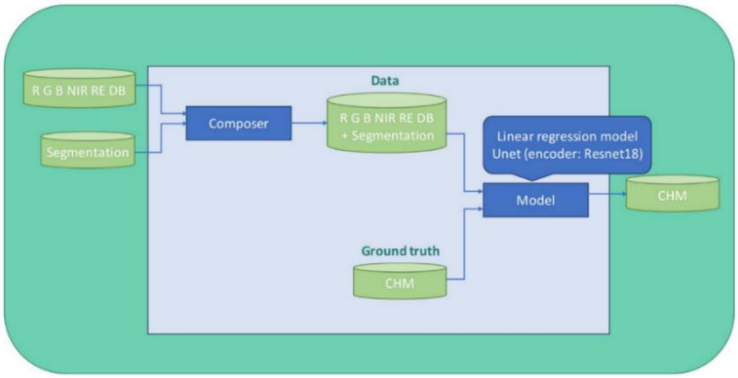

Figure 5-3: Pipeline created for the training of the neural network.

The neural network model designed to predict the CHM receives as input a dataset composed of its six original bands, along with four additional bands derived from the segmentation mask obtained from the classified point cloud.
The segmentation mask was generated by creating a grid in which each square represented a pixel with a side length of 30 cm. The input class assigned to a pixel depends on the number of instances, per point cloud’s class, falling within that pixel. In other words: the PC’s class with highest count within the pixel is assigned to that pixel. If a pixel remained empty (no point falling within it), the default class value assigned is *vegetation*.

As ground truth, the CHM generated from the PC was used.
Figure 5-4 shows an example of a piece of a satellite image along with the relative segmentation mask and CHM.

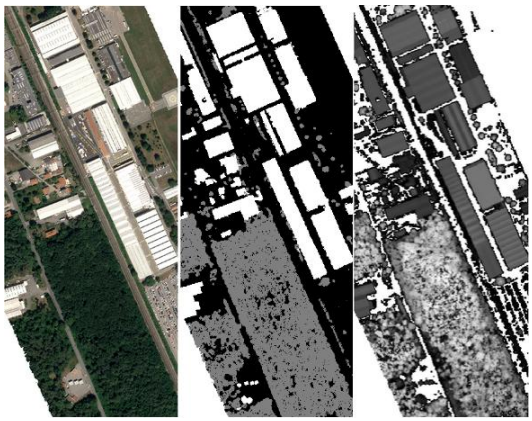

Figure 5-4: Left: snippet of multispectral image. Center: snippet of segmentation mask obtained from classified point cloud. Right: snippet of CHM, derived from the same point cloud.

5.2.3.1. Dataset creation for training and inference

The training dataset was created by excluding i) the portion of data used for inference in the initial phase of the work (WP12) and ii) a part of the new data, in order to apply both the previous model and the one resulting from the new training, and to compare the quality of the predictions. The inference area reserved for the original dataset covered approximately 0.27 km², while the area for the new dataset covered approximately 1 km².
For the training set, a total of 31569 tiles (90% of the total) were extracted, and for the validation set, 3507 tiles (10% of the total). The tiles' side was 256 pixels. These numbers were obtained after a data augmentation step, consisting of reflections along the x and y axes, aimed at increasing dataset variability.
For the inference dataset, it was necessary to generate two separate sets of tiles: one with tiles of 128 pixels per side and another with tiles of 256 pixels per side. This allowed for the application of both the old model (trained on 128-pixel tiles) and the new one. Tiles for inference were generated without data augmentation, as it is not beneficial in this phase.
In total, 149 tiles of 256 pixels per side were generated for the old dataset and 315 for the new dataset. Additionally, 988 tiles of 128 pixels per side were generated for the old dataset and 2587 for the new dataset.

5.2.3.2. Neural network training results

The selected neural network model is similar to the one used in the initial phase, specifically a U-Net with a linear activation function in the final layer. However, a ResNet34 encoder, characterized by a greater number of layers, was adopted to better accommodate the increased volume of data. The training run parameters are summarized in Table 5-1: Training parameters for "Expanded Run" experiment.

Input Data	Input Label	Training Batch Size	Validation Batch Size	Learning Rate Adam Optim.	Loss Function	Metric
Multispectral satellite orthoimages + Segmentation masks Shape: (256, 256, 10)	CHM Shape: (256, 256, 1)	64	32	0.01	MAE	MAE

Table 5-1: Training parameters for "Expanded Run" experiment.

The learning rate is adaptive and is reduced by a factor of 0.1 whenever the loss function does not improve for four consecutive epochs. The metric used as the loss function to be minimized was the Mean Absolute Error, whose trend during training is shown in Figure 5-5.

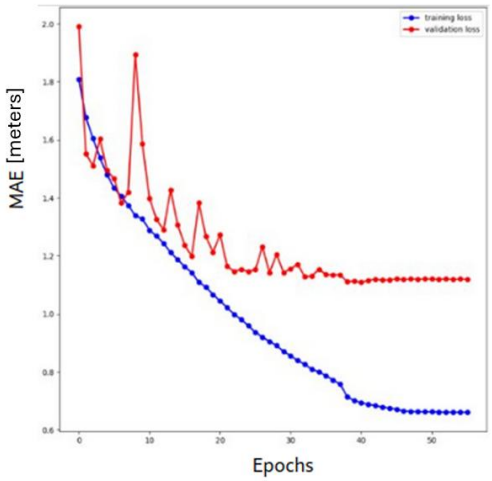

Figure 5-5:+ Mean Absolute Error (MAE) monitored during training as loss function for Expanded Run experiment. Red line: trend of validation loss function. Blue line: trend of training loss function.

It can be observed that the validation loss function curve closely follows the training loss function curve up to approximately the twentieth epoch, after which it begins to stabilize on a plateau. Variations become increasingly marginal, and after 16 consecutive epochs without improvement, the training process is halted. The best model was identified at epoch 41, when the MAE on the validation data set reached a value of 1.109 meters. This means that, on average, the difference between the best model predictions and the actual ground truth values is 1.109 meters.

5.2.3.3. Inference results on the old area

For each class, plots are presented showing the difference between the predicted values and the ground truth values for both the new and the old model, applied to the portion of the old data reserved for inference and therefore never seen by the neural network during training.

- ***Terrains***

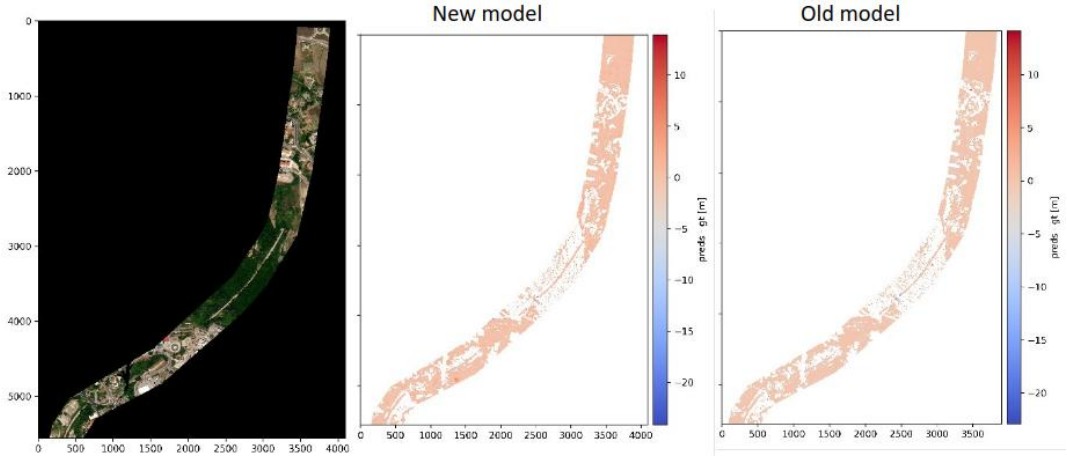

Figure 5-6: Comparison of predicted and ground truth CHM values for the terrains class. Left: old inference data. Center: error from the new model. Right: error from the old model.

In Figure 5-6 it can be observed that the plots are extremely similar, with negligible differences. The prediction is accurate in both cases: the new model achieved a MAE of 0.6 m, while the old model reached a MAE of 0.58 m on this data.

- ***Vegetation***

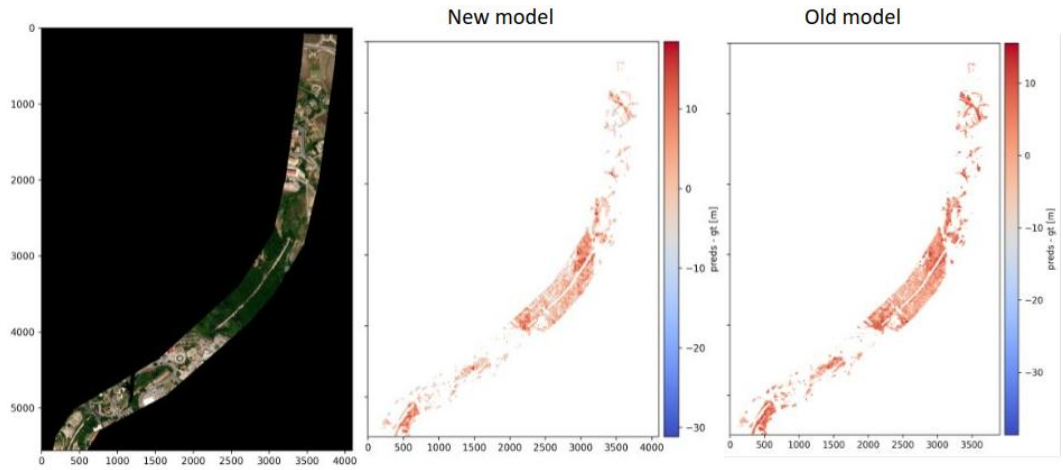

Figure 5-7: Comparison of predicted and ground truth CHM values for the vegetation class. Left: old inference data. Center: error from the new model. Right: error from the old model.

As shown in Figure 5-7, for the *vegetation* class a tendency to overestimation is observed in the results obtained with both models, although the values are generally less overestimated in the case of the new model. The MAE is 4 meters for the new model and 4.3 meters for the old model on this dataset, indicating an improvement.

- ***Buildings***

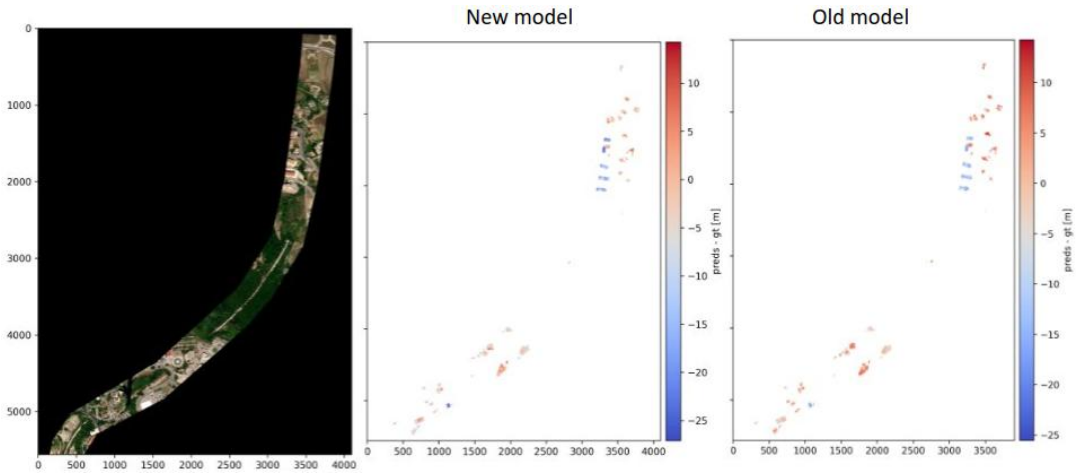

Figure 5-8: Comparison of predicted and ground truth CHM values for the buildings class. Left: old inference data. Center: error from the new model. Right: error from the old model.

For the *buildings* class, no significant change is observed, as noticeable in Figure 5-8 (MAE in both cases equal to 6 meters).

In conclusion, the two models demonstrated comparable performance on the old data, with a slight improvement on the vegetation class. The next step is to assess their inference performance on the new data (area).

5.2.3.4. Inference results on a new area

The results obtained by the new and the old model on the portion of new area are now presented for each class.

- ***Terrains***

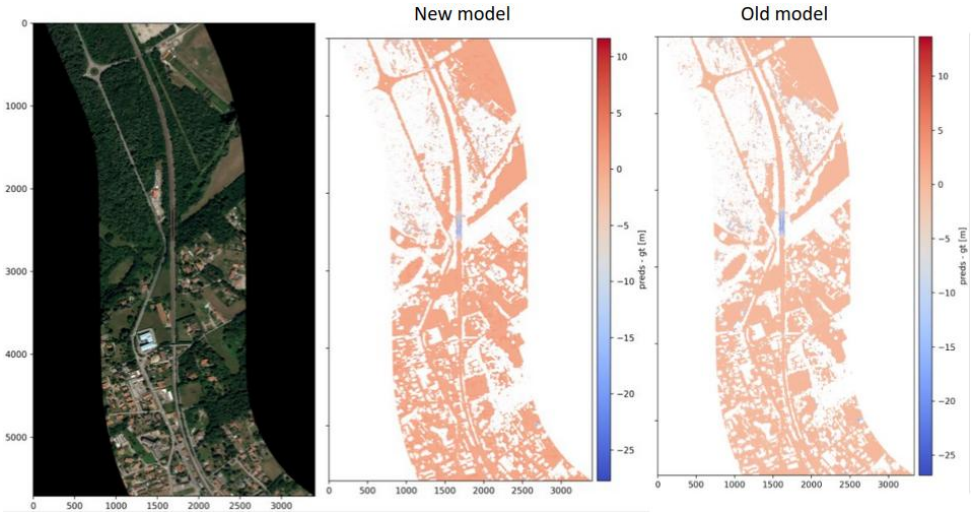

Figure 5-9: Comparison of predicted and ground truth CHM values for the terrains class. Left: new inference data. Center: error from the new model. Right: error from the old model.

In the case of the *terrain* class, Figure 5-9 shows that the prediction is accurate for both models. The new model exhibits a slight tendency to overestimate height values, but no substantial differences can be observed. In both plots, a small cluster of underestimated pixels is noticeable. This corresponds to an overpass, whose height was predicted as that of the road surface. MAE fpr both models is 1 meter.

- ***Vegetation***

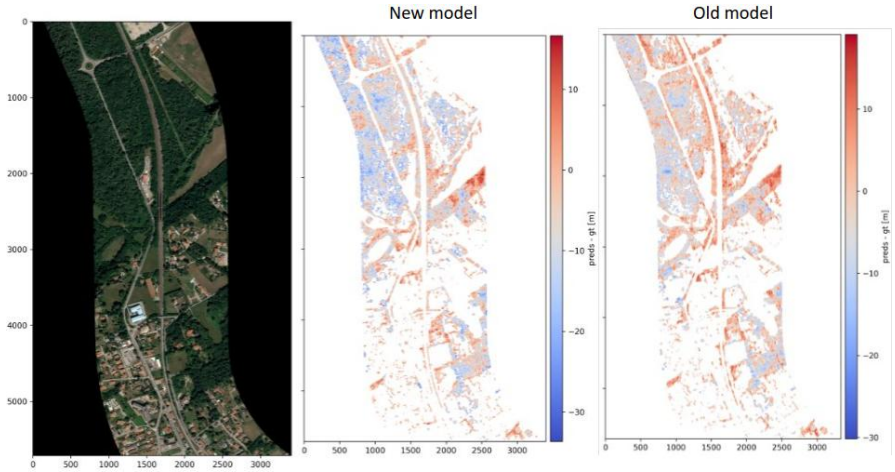

Figure 5-10: Comparison of predicted and ground truth CHM values for the vegetation class. Left: new inference data. Center: error from the new model. Right: error from the old model.

As shown in Figure 5-10, significant changes are observed for the *vegetation* class. In the results obtained with the new model, the values that were previously overestimated by the old model are now closer to the ground truth. However, a general tendency toward underestimation has emerged, particularly evident in dense tree clusters. It is also noted that near the railway tracks, the old model significantly overestimates tree height, while the new model predicts value close to the ground truth. The new model reached a MAE of 6.6 m, while the old model achieved 5.16 m. This data are average data on the whole area. So, although the average difference is considerable, the focus here is on the *vegetation* near the tracks, where the predictions from the new model are closer to the ground truth than those from the old model. Based on this observation, it is possible to develop strategies to compensate for these shortcomings, providing indicators that are still useful for identifying potentially hazardous situations near the railway tracks.

- ***Buildings***

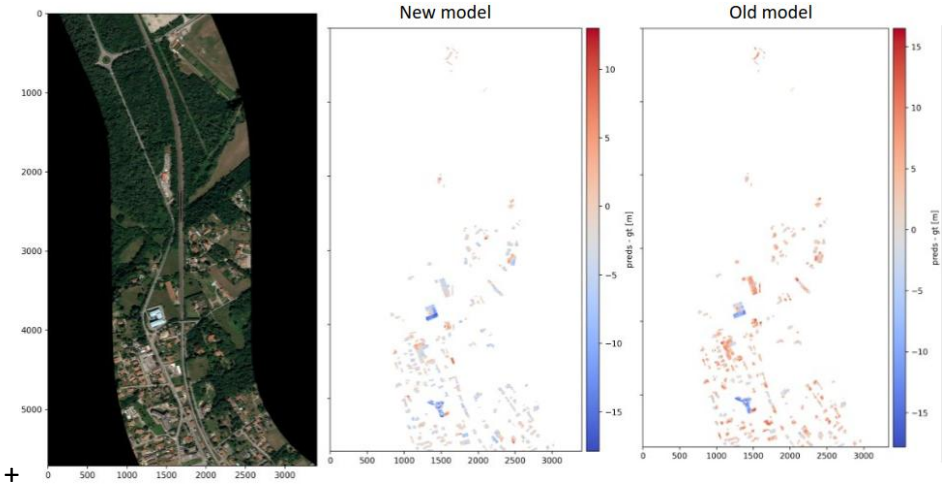

Figure 5-11: Comparison of predicted and ground truth CHM values for the buildings class. Left: new inference data. Center: error from the new model. Right: error from the old model.

Finally, for the *buildings* class (Figure 5-11) the new model predictions are closer to the ground truth than the older model. Specifically, the new model achieved a MAE of 3.2 m, while the old model reached 4.3 m.

5.2.3.5. Final considerations on "Expanded Run" experiment

In conclusion, the results of this experiment suggest that the model has ability to generalize (regardless of the selected area) and has benefited from the introduction of more diverse and varied training data. In some cases, such as in complex scenarios, a moderate decline in accuracy was recorded, indicating that increased data variability alone may not be sufficient to enhance prediction quality. For the *vegetation* class—central to the intended application—the results were mixed. Although the new model reduced the overestimation observed in the previous version, this came at the cost of a more widespread tendency to underestimate, particularly in areas with dense tree coverage. Nevertheless, in the specific context of vegetation near railway tracks, the new model produced values closer to the ground truth, which is a relevant outcome for risk monitoring purposes.
Ultimately, the model architecture showed a certain degree of robustness, as no critical performance drops occurred despite the changes in the training data. While the results are not entirely satisfactory, they provide a foundation from which targeted improvements can be developed, especially by introducing context-aware post-processing or refining the training strategy for critical areas.

5.2.4. "Semantic Masking" experiment: refining vegetation detection through class-based filtering

This experiment aimed to reduce contextual complexity by directly separating pixels classified as *terrains*, *vegetation*, and *buildings* in both the satellite data and the ground truth.
The input to the neural network consists of only six bands instead of ten, and a separate network is trained for each class.
This section presents the results obtained for the *vegetation* class only.

5.2.4.1. Segmentation mask denoising via mode-based filter

As a preliminary step, given the importance of accurately filtering pixels belonging to each class, a cleaning process was applied to the segmentation mask derived from the classified point cloud. As detailed in section 5.2.3, the mask contains errors stemming from the default assignment of "unclassified" pixels to the *vegetation* class. While this approximation was acceptable in that earlier experiment, in the present context, where the primary goal is to reduce problem complexity, it is essential to ensure that the mask is as accurate as possible. To refine the segmentation mask, a mode-based filter with a 25×25 kernel was applied. Specifically, for each group of 625 pixels, the value of the central pixel was reassigned to the most frequent value among its neighbours within the kernel. Figure 5-12 illustrates an example of mask before and after the filtering process.

Figure 5-12: Comparison between a segmentation mask as initially generated from the classified point cloud (left) and the same refined through a mode-based filtering process (right).

The resulting mask is visibly cleaner and more accurate. The satellite images can now be filtered, and the dataset for training the neural network is ready to be constructed.

5.2.4.2. Dataset creation for training and inference

The corrected segmentation mask was used to filter the pixels of both the satellite images and the ground truth CHMs, allowing for the construction of three separate datasets, one for each class. The data and ground truth were then divided into tiles measuring 256 pixels per side, with an overlap of 64 pixels, and subsequently allocated to the training (90%) and validation (10%) sets. A fixed area from the new dataset, identical to the one used in the "Expanded Run" experiment, was set aside for inference, ensuring a consistent basis for comparison. Following data augmentation, a total of 28426 training tiles and 3158 validation tiles were obtained for the *vegetation* class, while 304 tiles were reserved for inference.
An example of a filtered data tile and a corresponding filtered CHM tile is shown in Figure 5-13.

Figure 5-13: Example of filtered multispectral data tile and its corresponding CHM. The terrain and buildings class is filtered out.

5.2.4.3. Neural network training results

The model selected for this experiment is again a U-Net with a ResNet34 as encoder and a linear activation function in the final layer. However, the initial layer has been modified to accept input data with 6 bands instead of 10. The training parameters are summarized in the following Table.

Input Data	Input Label	Training Batch Size	Validation Batch Size	Learning Rate Adam Optim.	Loss Function	Metric
Filtered multispectral satellite orthoimages Shape: (256, 256, 6)	Filtered CHM Shape: (256, 256, 1)	64	32	0.01	MAE	MAE

Table 5-2:Training parameters for "Expanded Run" experiment.

The trend of the Mean Absolute Error during training is shown in Figure 5-14.

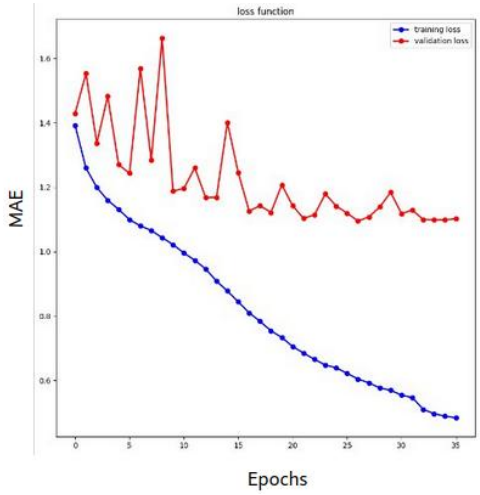

Figure 5-14: Mean Absolute Error monitored during training as loss function for Semantic Masking experiment. Red line: trend of validation loss function. Blue line: trend of training loss function.

The validation loss function curve rapidly diverged from the training one and stabilized on a medium plateau, although several learning spikes were observed. The loss function value corresponding to the best-performing model, which occurred at epoch 27, was 1.095 m.

5.2.4.4. Inference results on selected “new” data

The following results refer to the inference performed by the newly trained model on previously unseen data by the neural network, as shown in Figure 5-15, for the *vegetation* class.

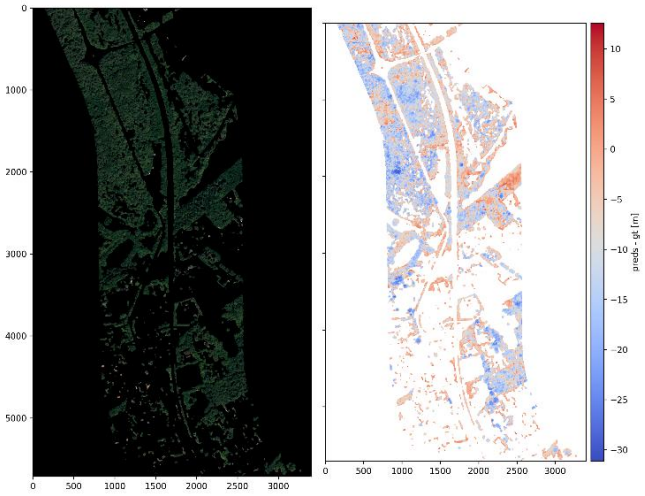

Figure 5-15: Comparison of predicted and ground truth CHM values for the vegetation class.

The results did not improve compared to those obtained in the "Expanded Run" experiment. In fact, the tendency toward underestimation became more pronounced, and the MAE reached a value of 9.12 m.

5.2.4.5. Final considerations on “Semantic Masking” experiment

This experiment showed that filtering the input data pixels does not assist the neural network in estimating object height. It is likely that the colours and textures of other classes contribute useful context for distinguishing what can or cannot reach a certain height. For this reason, this approach is unlikely to be pursued further in future developments.

5.2.5. Potential exploitation of ground data obtained from WP4

In this section we demonstrate the possibility of utilising the ground data obtained from diagnostic data in WP4, to assess vegetation encroachment. The main result of this section paves the way for subsequent works.

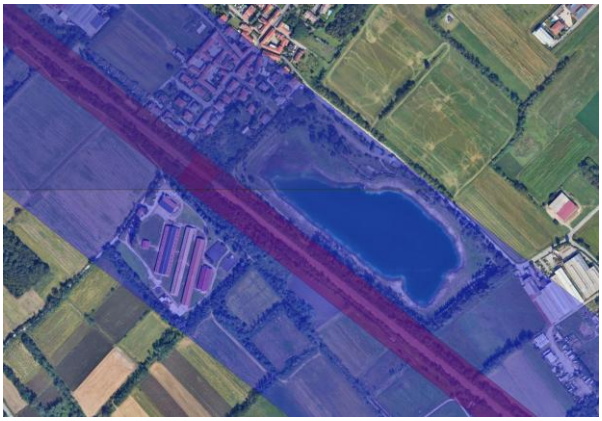

Figure 5-16: Overlay between the airplane's lidar data (highlighted in blue, acquired July 2023) and the ground data obtained by a lidar mounted on a train (highlighted in red, acquired during November 2022).

The lidar mounted on the train is has a rotation frequency of 600Hz, pulse frequency 800kHz and associated absolute precision of 20cm. Although the point clouds available have been acquired every 5 meters only, the specifications pertaining the lidar make this measurement ideal as absolute ground truth. The point cloud obtained from the train is not automatically usable to detect encroachment, so it needs to be handled.

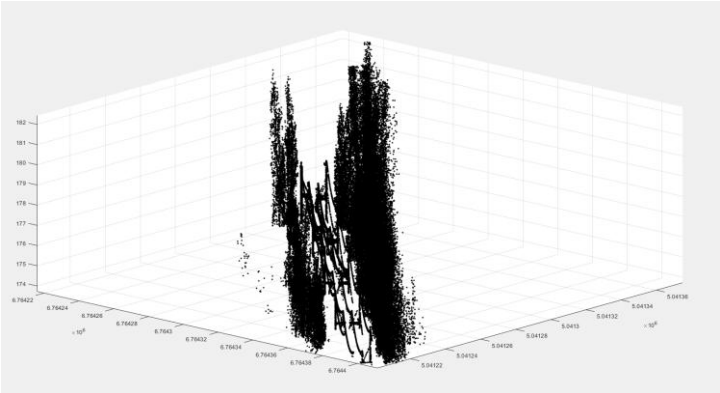

Figure 5-17: Raw point cloud (Matlab).

The point cloud needs to be projected on a plane orthogonal to the track centre line. Manually rotating the point cloud reveals details such as the catenary and the vegetation surrounding the rail (next figure).

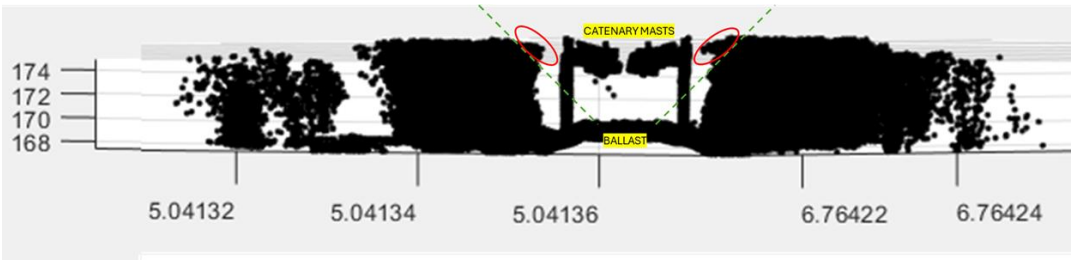

Figure 5-18: Rotated Point cloud (Matlab). The points encircled are threes higher than distant (vs TCL).

In Figure 5-18, resulting from projecting the point cloud along the TCL's transversal plane, two green lines with slope ±45 degrees, departing from the TCL, divide the space underlining the infringement/normal area. For each side, vegetation falling above green line represent plants that are higher than distant (this part of vegetation is in infringement, as representing a thread according to the Italian law).

A way to automate the rotation and automatically spot threes that are higher than distant, as the train travels, would involve the following steps:

- For each train's position, calculate the Frenet–Serret reference system (FSRS) relative to the TCL (one for every snapshot of the lidar).
- From FSRS, calculate two transverse & parallel planes to the TCL (e.g. spaced one meter apart).
- Detect all points within the two mentioned transverse planes (all points within a slice of one meter).
- Filter in only those points that are higher than distant (e.g. above the green line).
- Label via AI by Filtering in only the points pertaining reflections coming from vegetations (no bridges or under pass aliasing, see next image).

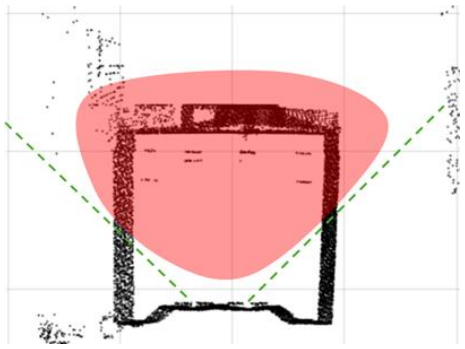

Figure 5-19: Part of the bridge falling above the green lines, currently indistinguishable from vegetation.

The experiment conducted so far proves to be interesting, but it is certainly subject to a series of limitations. First, the points above the green lines could belong to bridges and other infrastructure, so these would easily be mistaken in any automatic algorithm that does not include training. Second, the data of the train does not have the right spatial sampling (one point cloud every 5 meters of travel). Third, the hardware is limited in the colour response (not RGB), so a typical green plant would not be distinct from another artifact reflecting the beam. Finally, the aerial, satellite & train data do not match in time, so a direct overlap would sub-optimal for numerical

comparisons. All drawbacks listed can be addressed by improving the hardware, disposing of data with matching dates, developing orthonormalization and AI algorithms.

5.2.6. Final considerations & new proposals

The innovative technique has proven practical to extract an estimation of height tree next to the railway corridor. The “Expanded Run” experiment produced a model capable of recognizing a broader range of scenarios and performs similarly to the earlier model in terms of absolute prediction. Specifically, the mild discrepancy observed between old a new area could be attributed to the fact that the satellite images had different inclinations. The outcome of this algorithm may serve as a useful starting point for the development of post-processing strategies aimed at defining risk zones based on continuous height ranges (contour). Although this would reduce the granularity of the predictions, it would still provide a practical indicator for identifying potentially hazardous situations, such as overly tall trees that could fall and obstruct railway tracks. Neither increasing the size and variety of the dataset nor filtering by pixel class improves dramatically the performance, so new approaches must be tested. For instance, the reliability of such approach could be further enhanced by incorporating vegetation indices derived from the six available multispectral bands. Indices such as NDVI (for assessing vegetative vigour), GNDVI (for estimating chlorophyll content), and NDRE (for detecting stress in mature plants) can provide valuable insights into plant health. Future developments will continue in this direction, as it appears to offer a promising path forward.

5.3. Classification & Change detection

The objective of this activity is the extraction of specific asset classes, from multispectral satellite imagery, by mean of semantic segmentation neural network. The goal is to enable detection of temporal changes affecting the classes of interest. These changes, such as the emergence of illegal buildings in proximity of the tracks, may represent unauthorised activities, impacting the railway infrastructure. It is also possible to extract geolocation information for specific objects, such as overpasses or rail crossings. This method aims to improve traditional inspection’s technique, both by lowering costs and by enabling coverage of wider or otherwise inaccessible areas. Following an initial phase aimed at assessing the feasibility of the approach by extracting more general classes, the focus will then shift to asset categories directly relevant to the railway domain, such as stations and rail crossings.
During the feasibility phase, the following classes were extracted:

1. *Seas, lakes, rivers*
2. *Groups of trees and fields*
3. *Yards, technical areas and streets*
4. *Buildings*
5. *Railway tracks*
6. *Road–rail intersections*

The first five classes are used to train the neural network, while the sixth was derived through post-processing of the inference results. The sixth class was derived separately because the available training data did not contain enough number of examples for the NN to learn effectively.

5.3.1. EO data acquisition and dataset preparation

Multispectral satellite data with six bands, at a resolution of 30 cm per pixel were acquired, covering six macro-areas. These areas are in the regions of Marche, Lazio, and Campania, and exhibit diverse characteristics: some are sparsely urbanized rural zones, while others are urban environments. The ground truth data, for five out of six areas, consisted of segmentation masks manually created on aerial images of similar resolution, which were adapted for the purposes of this project. Although the correspondence was not perfect, the neural network was expected to compensate for these gaps. For the sixth area, specifically the one depicting the Rome train station and a section of railway tracks extending from it, highly precise and detailed cadastral vector data are used. A segmentation mask was derived from this dataset. Figure 5-20 shows a snippet of the two types of ground truth segmentation mask.

Figure 5-20: Left: manually created ground truth segmentation mask. Right: cadastral ground truth segmentation mask.

The satellite images were cropped according to the extent of the available ground truth data, resulting in a total area of approximately 59 km². Of this, 6 km² were allocated to the inference phase and were excluded from the training phase. To construct the dataset, image tiles of 256 x 256 pixels per side were extracted, with an overlap of 64 pixels on each side to reduce prediction discontinuities at the tile borders. Data augmentation was then performed by mirroring the tiles along both the x-axis and y-axis. This process yielded 61288 tiles for the training phase, with 90% assigned to the training set and 10% to the validation set. For the inference phase, 1858 tiles were generated.

5.3.2. Neural network training results

The neural network selected for this task is a DeepLabv3+ with ResNet34 encoder, a convolutional neural network designed for semantic image segmentation.
The training parameters are summarized in Table 5-3.

Input Data	Input Label	Training Batch Size	Validation Batch Size	Learning Rate Adam Optim.	Loss Function	Metric
Multispectral satellite orthoimages Shape: (256, 256, 6)	Segmentation masks Shape: (256, 256, 1)	64	32	0.0001	Dice Loss	mIoU

Table 5-3:Training parameters for "Expanded Run" experiment.

The monitored metrics included the Dice Loss, used as the loss function to be minimized, and the mean Intersection over Union (mIoU). The trends of the loss function and the mean Intersection over Union on both the training and validation sets are shown in Figure 5-21.

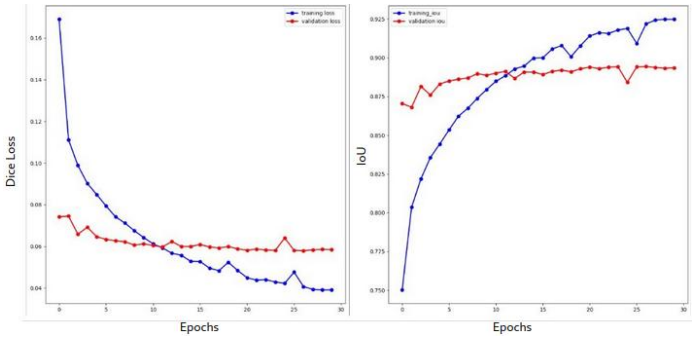

Figure 5-21: Metrics monitored during training. Left: Dice Loss, function to be minimized. Right: mean Intersection over Union.

The validation metrics indicate that the model converged earlier in the training process, with only marginal improvements observed up to the 21st epoch. At that point, the lowest Dice Loss value of 0.058 and the highest mean IoU value of 0.894 were recorded. The results are considered highly satisfactory, given dataset and task complexity, since the model achieved both a very low Dice Loss and a high mean IoU, demonstrating accurate segmentation and strong generalization on validation data. The next step is to evaluate the model's performance on previously unseen data.

5.3.3. Inference results and asset digitization

The results obtained by applying the model to the tiles reserved for inference are shown in Figure 5-22.

Figure 5-22: Segmentation model predictions on inference data. Blue: Seas, lakes, rivers; light brown: Groups of trees and fields; grey: Yards, technical areas and streets; red: Buildings; purple: Railway tracks.

This is a raster image in which each pixel has been assigned the class that was predicted by the model with the highest confidence score, provided that the confidence exceeded an arbitrarily defined threshold of 60%. This threshold was only precautionary and intended to filter out clearly spurious detections. In practice, the confidence associated with the majority classes was generally well above 60%. As shown in Figure 5-23, which displays a particularly significant fragment of the results, all classes were predicted with high accuracy, with only a few misclassification errors.

Figure 5-23: Segmentation results close-up. Blue: Seas, lakes, rivers; light brown: Groups of trees and fields; grey: Yards, technical areas and streets; red: Buildings; purple: Railway tracks.

Few notable exceptions were noticed in the prediction of the *Railway tracks* class (Figure 5-24): the network was not able to recognize a train on the track. This occurred because the neural network had not been exposed to enough examples of this situation during training (train on the track). Probably, not detecting the typical pattern of alternating railway sleepers, the pixels of the train were mistakenly assigned to the *Yards, technical areas and streets* class.

Figure 5-24: Train wagons on railway track.

This limitation could potentially be mitigated through an additional training phase, during which the model would be exposed to more samples containing instances of trains on railway tracks. Such an improvement appears plausible, given that the network was able to learn that roads remain identifiable as such even when partially occluded by vehicles.
The digitization of the recognized assets was subsequently performed by separating pixels based on their values and generating distinct vector layers. Contour simplification was applied to smooth and regularize the resulting geometries. The vector files were georeferenced and exported in formats compatible with standard GIS platforms, enabling efficient visualization and manipulation. The area where railway tracks were misclassified was manually corrected to allow for the extraction of road–railway intersections, considering the expectation that a more accurate model will be available in the near future. The resulting vectors are shown in Figure 5-25.

Figure 5-25: Digitized assets.

5.3.4. Road-railway intersections extraction

With the objective of automatically identifying intersections between roads and railway tracks within satellite imagery, a deterministic procedure was developed to work on a raster segmented semantic map obtained through inference using the previously trained neural network. The process was structured into multiple phases, forming a pipeline that included mask cleaning, skeletonization, segment connection, intersection detection, and a final local geometric evaluation to filter relevant crossings, excluding those resulting from parallel structures. First, the semantic raster map was filtered to retain only roads and railway tracks, and then cleaned of noise consisting of isolated pixels or small pixel clusters using a mode-based filter. This filter assigned to each central pixel the most frequent value within a 21×21 kernel and was applied across the entire raster. Subsequently, morphological operations typical of classical computer vision were applied, particularly to close small gaps and connect fragmented regions. Finally, an additional cleaning of small pixel blobs that had escaped the initial pass was carried out. In Figure 5-26 the comparison between the original and the cleaned mask is shown.

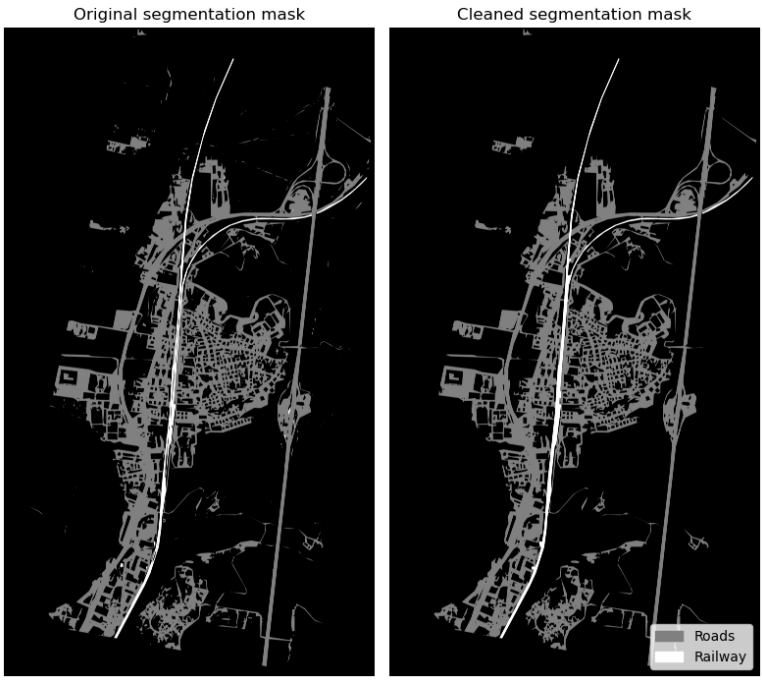

Figure 5-26: Left: Original segmentation masks of roads and railway. Right: cleaned segmentation masks.

At this point, binary skeletonizations of the cleaned masks are generated, followed by pruning of short segments below a certain threshold length to eliminate artifacts and irregular paths. The threshold was set differently for roads and railway tracks, as less irregular and jagged paths are expected for the railway tracks.
To improve the connectivity of the road and railway network, the isolated endpoints of the skeletonized segments are connected using a function that:

- identifies terminal nodes as pixels with only one active neighbour,
- finds nearby endpoints within a certain distance,
- draws connection segments, avoiding loops between elements of the same connected component.

This procedure is not optimal, as some spurious connections are created, but these have been limited by avoiding loops and imposing a smaller maximum threshold distance for roads compared to railway tracks, which have far fewer branches. Subsequently, intersections are identified by calculating a binary intersection mask using a logical AND operation. In this way, the shared pixels between the two connected skeletons are identified. In Figure 5-27 the comparison between the original skeletons and the pruned, connected ones is shown.

Figure 5-27: Left: original roads and railway skeletons. Right: skeletons after pruning and endpoints connecting.

To exclude false positives arising from parallel or overlapping segments, a local geometric analysis is performed around each intersection point:

- active pixels for roads and railway tracks are extracted within a local window,
- the two most distant points within each set are determined, from which the directional vectors of the two segments are derived,
- the angle between the two vectors is calculated using the normalized dot product. If the angle is below a threshold of 30° or close to 180°, the intersection is discarded as it can be interpreted as a parallel or coincident segment rather than a true crossing.

The points are georeferenced, and their coordinates can be exported in CSV format, to then be visualized in a GIS. The intersections filtered by angle are shown in Figure 5-28: Left: Intersection points between roads and railway tracks. Figure 5-28: Left: Intersection points between roads and railway tracks. Figure 5-28: Left: Intersection points between roads and railway tracks.

Figure 5-28: Left: Intersection points between roads and railway tracks.

The identified intersections were correct in 80% of the cases (precision = 0.8), with only one false positive detected. However, several true intersections present in the image were missed, resulting in a recall of 0.5. The quality of this result depends heavily on the accuracy of the neural network predictions. The more accurate these predictions are, the less fragmented the skeleton branches will be. It would be definitively worth, in a future development, to directly assign the recognition of intersections to the neural network as well, perhaps also attempting to distinguish overpasses from level crossings.

5.3.5. Change detection

An ancillary activity related to classification is change detection, which allows for the identification of changes occurring in the same area over time. In this section, the results obtained by performing change detection on the buildings class using the previously trained neural network model are presented.

5.4. Input data description

For this demonstration, two multispectral satellite images were acquired, sharing the same characteristics as those used during the classification training, namely, six spectral bands and a spatial resolution of 30 cm per pixel. The images depict the same geographic area but were captured on different dates: July 17, 2022, and June 2, 2024, with similar cloud coverage and time of acquisition.
This temporal selection was motivated by the known presence of a construction site near the Sesto San Giovanni train station, in the municipality of Milan, where a new building was completed in 2024. This structural change constitutes the target modification to be detected by the neural network. Accordingly, a subset of the area of interest was extracted, corresponding to a surface of 0.024 km². Figure 5-29shows the area of interest on the two different dates.

Figure 5-29: Left: Sesto San Giovanni station during the initial stages of construction. Right: completed Sesto San Giovanni train station.

5.4.1.1. Segmentation of time-separated images with the pretrained neural network

The images were divided into tiles of 256 pixels per side, and the model was applied obtaining the results shown in Figure 5-30.

Figure 5-30: Left: classes predictions for 2022 data. Right: classes predictions for 2024 data.

Differences can also be observed in the *Groups of trees and fields* and *Railway tracks* classes, in addition to the *Buildings* class; however, the focus here will be on the latter. In this case, the change does not involve the emergence of a new building, but rather the variation of a building's dimensions, so the goal is to calculate the percentage area difference. This allows for the identification of significant changes in the extent of objects between two time periods.

5.4.1.2. Extraction of the "Buildings" Class

The two raster images (representing the predicted segmentation masks for the years 2022 and 2024) contain categorical pixel values, where each label represents a different object or building. The pixel values representing the buildings are extracted from both images, creating binary masks one for 2022 data and one for 2024 data. The individual connected components in the binary masks are identified and labelled with unique integer values. These labels allow for the association of each object with a corresponding region in the mask. For each object in 2022 mask, the overlapping object in 2024 mask is identified by checking the intersection of their spatial coordinates. A pair is formed when the overlap between buildings from the two masks is found. Figure 5-31 shows the prediction masks for the *Buildings* class for the years 2022 and 2024. The colours uniquely identify the buildings, enabling the observation of the evolution of the purple and red buildings over time.

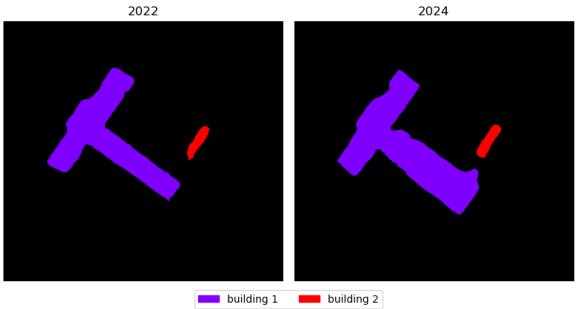

Figure 5-31: Predicted buildings class for 2022 and 2024 data. The buildings are uniquely identified by colors.

5.4.1.3. Raster Subtraction and Identification of Changes

The area of each building in 2024 predicted segmentation mask is compared to the corresponding one in 2022 predicted segmentation mask and the percentage area change, calculated as the relative percentage difference between 2022 and 2024 areas.
A 15% change threshold is applied to filter out insignificant changes. A 15% threshold is applied to exclude minor variations. This value was empirically identified as the best trade-off between suppressing most false positives and retaining meaningful changes. If the area difference exceeds the threshold, the building is marked as significantly changed. A visual representation of the difference between the areas is presented in Figure 5-32.

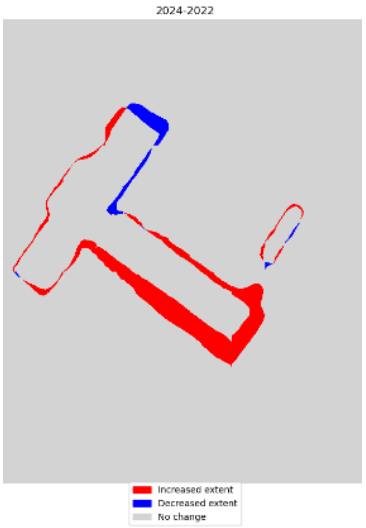

Figure 5-32: Difference between the 2024 predicted buildings areas and the 2022 predicted buildings areas.

It was found that, compared to the 2022 buildings, the area of the larger building increased by 28.27%, while the change in the smaller building did not exceed the 15% threshold. The connected component corresponding to the building with significant variation can be extracted and vectorized, allowing it to be visualized and further analysed in a GIS environment, as it can be seen in Figure 5-33.

Figure 5-33: Vectorized changed building, visualized in a GIS environment.

5.4.2. Conclusions

The results of this work confirm the effectiveness of using a semantic segmentation neural network for the automatic extraction of relevant asset classes from multispectral satellite imagery. The model demonstrated good generalization capabilities across diverse environments and produced accurate predictions for key classes such as buildings, railway tracks, and roads. This enabled the implementation of additional tasks such as change detection and asset vectorization with satisfactory precision.

The feasibility study also highlighted the potential for supporting infrastructure monitoring through automated analysis. In particular, the change detection process proved effective in identifying modifications over time, such as the expansion of existing buildings. Moreover, the method developed for extracting road-railway intersections, while functional, revealed some limitations due to occasional prediction errors and segmentation artifacts. These could be addressed in future work by enriching the training dataset with more representative samples, including edge cases like tracks partially obscured by trains.

To improve the system further, future developments could focus on directly detecting more complex structures such as level crossings or overpasses, reducing reliance on post-processing steps. Overall, the proposed pipeline lays a solid foundation for the automated monitoring of railway infrastructure and surrounding (e.g. change detection on vegetation/deforestation that could pose a risk to the railway corridor).

5.5. Bridge inspection and defects analysis

The Italian railway network is one of the most bridge-intensive in Europe due to the country's complex terrain. The network comprises approximately 17,000 km of railway and about 23,100 civil structures, including bridges, viaducts, underpasses, and overpasses. The distribution of these structures is 37% underpasses, 34% bridges, 22% overpasses, and 7% viaducts.

Inspection and Maintenance Framework

RFI is responsible for monitoring and maintaining the entire railway infrastructure. Inspections are conducted in compliance with national and international regulations, following three main cycles:

- Annual ("routine") inspections
- Triennial ("principal") inspections
- Six-year ("general") inspections

A comprehensive regulatory framework ensures the safety, integrity, and functionality of the railway system. This framework mandates strict adherence to procedures and methods for inspecting bridges and other civil structures.

Two key reference documents guide these processes:

- The procedure for inspecting bridges, tunnels, and other railway structures, which details responsible bodies, inspection frequency, and its record-keeping.
- An operational methodology manual, which outlines the inspection process, documentation, and use of the Bridge Management System (DOMUS).

Inspection Methodology

Inspections include not only the structures themselves but also their surroundings, such as watercourses and slopes, which can impact stability. The six-year general inspection is particularly thorough, requiring close-up examination of all structural components (decks, piles, abutments, etc.), sometimes necessitating specialized equipment like work platforms, scaffolding, or boats to access difficult areas.

The primary goal of inspections is to identify, characterize, and quantify defects using the DOMUS system, which integrates diagnostics and maintenance planning. DOMUS employs models and algorithms to monitor structural health, plan maintenance, and manage assets efficiently.

Technological Advancements in Inspections

Due to the challenging geography, some structures are difficult to access, even with specialized equipment. To address this, RFI has introduced drones (UAVs) to support inspections. Drones enhance coverage and accessibility, allowing inspectors to collect comprehensive photographic data from multiple angles and hard-to-reach locations.

Key Objectives of the ERJU Project

- Automate the identification of structural defects using machine learning (neural networks) to classify defects according to the RFI Defect Catalogue.
- Develop an integrated Asset Management Platform that combines image acquisition and defect detection, supporting maintenance decisions.
- Reduce the costs and time associated with traditional inspections and asset management by leveraging automation and digital data.
- Integrate the bridge inspection platform into a holistic infrastructure monitoring system.

Compared to traditional methods, which rely on manual inspections using cranes and scaffolding, the adoption of drones and machine learning significantly shall reduce the time and effort required for assessments.

Drone-Based Inspection Workflow

- **Pre-inspection:** Preliminary site visits identify potential obstacles, such as vegetation, accessibility issues, regulatory constraints, equipment needs, and environmental conditions.
- **Flight planning:** An inspection plan is created to address identified challenges and ensure complete coverage.
- **Data acquisition:** Multiple drone flights capture images of all structural elements (minimum two flights under each deck/vault, one for each bridge front, and one above the bridge, with adjustments for steel bridges as needed).
- **Post-processing:** Collected images are processed to produce:
  - General and photographic reports
  - Sparse and dense point clouds (3D models)
  - 3D graphic renderings

These digital outputs allow inspectors to identify and classify defects according to the DOMUS system, with calibration procedures ensuring accuracy.

Benefits

Drones provide better physical access, save time, and generate rich digital data, which can be analysed by artificial intelligence or human experts. This approach enables the detection of a wide range of defects across various bridge types and materials (masonry, concrete, steel, etc.), in line with RFI's Bridge Management System requirements.

In summary, the integration of drones, AI, and digital asset management platforms is transforming the inspection and maintenance of Italy's railway civil infrastructure, making the process more efficient, comprehensive, and data driven.

5.5.1. Description of Trial Site in Melfi (Leonessa Bridge) in Basilicata (Italy) and scope of this experimentation

"Leonessa bridge", subject of trial inspection, is situated on the single-track railway line Cervaro - Potenza and is in Italy, near the city of Melfi (PT) on the border between two regions, Puglia and Basilicata.

The civil work consists of 11 round-arched spans in brick masonry with a span of 12.00 m for a total length of approximately 150 meters. The substructures are made of masonry composed of squared stone blocks, as is the tympanum. Both abutments have concrete retaining walls on both sides. The following figures show respectively a satellite view of the area where the civil work is located and its side view.

Figure 5-34: Satellite view of the Viaduct.

Figure 5-35: Side view of the Viaduct (Janurary 2024).

This viaduct has been chosen because it has been subject to recent inspections by RFI personnel, also carried out using special equipment (elevating platforms) and according to IM procedures.
The experimental activity, carried out in January 2024, involved the use of a drone to acquire data aimed at carrying out the photogrammetric survey of civil work. Furthermore, this data will provide a basis for the development of an Artificial Intelligence created through a defect tagging activity carried out via the support of personnel specialized in bridge inspection visits and according to RFI inspection procedures. This experimental activity also aims to evaluate the advantages (economic, temporal, etc.) in the use of innovative technologies in the field of bridge inspections.

For the UAV survey on Leonessa Bridge in Melfi, the DJI MAVIC 3M drone was used. It weighs only 1,050 grams and is foldable for easier storage.

Figure 5-36: DJI Mavic 3M.

Each battery of the drone ensures a high flight autonomy of about 43 minutes that can be recharged very quickly thanks to a high efficiency charging station. It is equipped with an extraordinary imaging system consisting of a 20 MP RGB Camera, 4/3 CMOS and mechanical shutter. In addition, this drone also has 4 5MP multispectral cameras that could be used for environmental monitoring. The drone is equipped with a sunlight sensor that regulates the exposure of the camera, thus equalising the data collected at different times of the day.

The presence of the RTK (Real Time Kinematics) module allows precise and real-time positioning data on images. During the flight, the camera and the RTK Module synchronize instantly to acquire

the position of the imaging centre of each image. The high levels of precision obtained thanks to the RTK module allow to avoid using ground control points, optimizing survey times.
The communication system present in the drone integrates two transmission signals and four reception signals. This allows communication even over long distances. The drone also has vision sensors capable of detecting obstacles in an omnidirectional manner.

DJI MAVIC 3M	
Dimensions	Folded without propellers: 223×96×122 mm (L×W×H) Unfolded without propellers: 348×283×140mm (L×W×H)
Max Take-off Weight	1,050 g
Max Ascent Speed	6 m/s (Normal Mode) 8 m/s (Sport Mode)
Max Descent Speed	6 m/s
Max Wind Speed Resistance	12 m/s
Max Flight Time	43 min
Max Flight Speed	15 m/s (Normal Mode) 21 m/s (Sport Mode)
Max Take-off Altitude	6000 m (above sea level)
Operating Temperature	-10°C to 40°C

Table 5-4: Main specs of the UAV.

5.5.2. Artificial intelligence applied to bridges structural defects detection

This part of the project focuses on artificial intelligence for the automatic classification of structural defects in bridges, based on the image acquisition via drone. This functionality shall facilitate the work of operators who typically inspect the bridges in person and then manually highlight the areas that need attention.

5.5.2.1. Recap of previous data analyses

In the initial phase of the work (as presented in D12.1 of WP12), an analysis was conducted on the available data, which included drone-acquired photographs of viaducts made of concrete, masonry, and steel, as well as the ground truth data and point clouds of the structures. The ground truth data was represented by the coordinates of markers that coincided with the centre of the defects. The defects were categorized based on the material in which they were detected and the specific type. The nomenclature standards used were those established by RFI, which also provided the data. The images of three bridges, each made from a different material, were selected for the preliminary analysis. The analysis of this data revealed significant challenges for AI implementation. A high density of markers was frequently used to indicate problem areas;

however, for AI model training, it was necessary to know the exact extent of the defects, their precise positioning, and their corresponding categories. Additionally, many defect categories were underrepresented, making it extremely difficult for the neural network to learn each category in a comprehensive manner. Given these considerations, a new strategy was developed to optimize the use of the available data for the intended goals. This strategy involves the creation of new ground truth data Processing pipeline overviews. The pipeline developed for this work addresses the problem through a two-step approach: Semantic segmentation for material identifications Defect detection specific to the identified material.

Due to the high variability in optical imagery, such as uncompensated changes in lighting and visual features, and the wide heterogeneity of defect types, even within the same material category, the problem was decomposed to reduce its overall complexity.
The first stage involves training a semantic segmentation model to classify each pixel according to the material it represents (e.g., concrete, masonry, steel). Based on this output, a second model, specialized in detecting defects associated with that material, is applied exclusively to the relevant pixels.
Each material class thus has a corresponding defect segmentation model, activated only when that material is detected in the image. A visual representation of the described pipeline is shown in Figure 5-37: Example of defect recognition pipeline applied to a metal viaduct.

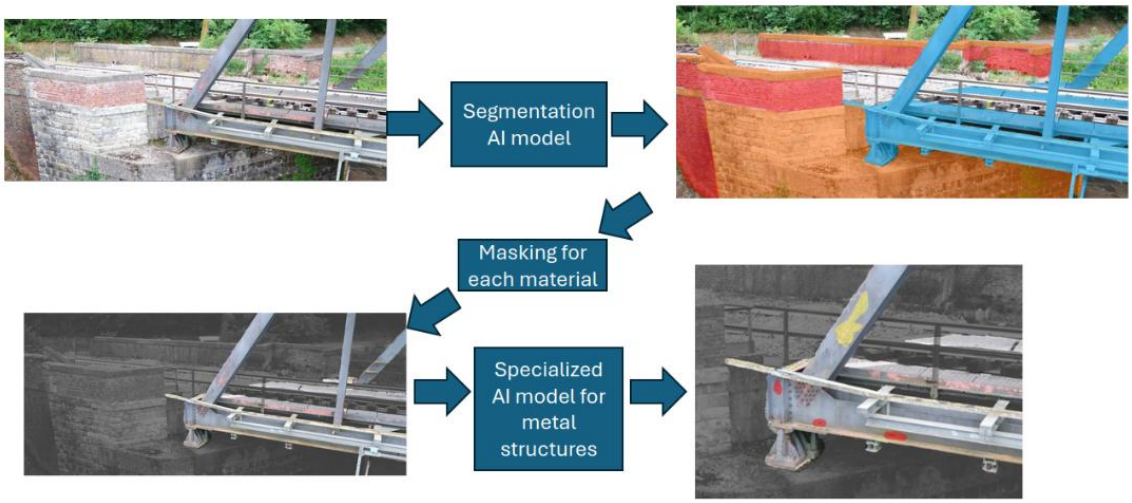

Figure 5-37: Example of defect recognition pipeline applied to a metal viaduct.

By separating material identification from defect recognition, the approach simplifies the learning task for each model and improves robustness in varying image conditions.

5.5.2.2. Stage 1: Bridge's material classification via segmentation

In this section, the results obtained during an initial training phase of a neural network dedicated to recognizing the material composing the various parts of the bridge are presented. This process constitutes the first stage of the processing pipeline for defect detection.

5.5.2.2.1. Ground truth data generation process

As part of the development of a semantic segmentation neural network for material recognition at the pixel level, a dedicated dataset was created using 56 selected images from the available pool. These images were of high resolution and varied in size: for instance, some measured 5280 × 2970 pixels, while others were 5280 × 3956 pixels.
Five target classes were defined, corresponding to the primary materials of interest:

- *Background*
- *Stone blocks and bricks*
- *Concrete*
- *Metal*

Ground truth segmentation masks were manually annotated through a labour-intensive and time-consuming process. Two examples of these annotated masks are shown in Figure XX.

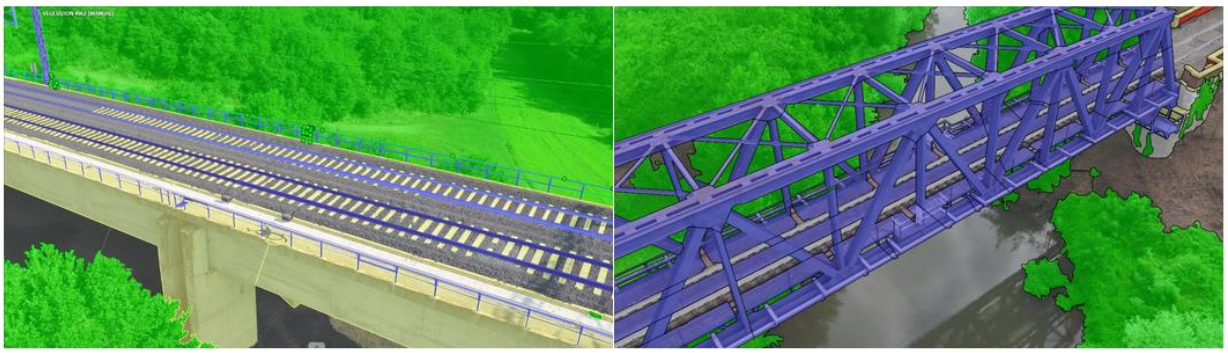

Figure 5-38: Annotated images for material semantic segmentation.

In these initial examples, the class definitions had not yet been finalized, and vegetation was treated as a separate category from the rest of the background. However, subsequent testing showed improved neural network performance when the classes were grouped as previously described. Once the ground truth data had been created in vector format, it was converted into raster format and, together with the corresponding images, cropped into 256×256 pixel tiles. A total of 11627 tiles were allocated to the training set (80%), 2179 to the validation set (15%), and 726 to the test set (5%).

5.5.2.2.2. Neural Network training results

The neural network of choice for this task is a DeepLabv3+ with ResNet34 encoder, pretrained on ImageNet dataset, which contains images of the real world and can help the neural network to start its learning process from a more solid basis.
The training parameters are summarized in Figure 5-39.

Input Data	Input Label	Training Batch Size	Validation Batch Size	Learning Rate Adam Optim.	Loss Function	Metric
Drone-acquired images Shape: (256, 256, 3)	Segmentation masks Shape: (256, 256, 1)	128	128	0.0001	Dice Loss	mIoU

Figure 5-39: Training parameters for material segmentation.

During training, some probability-driven data augmentation was performed on the tiles to increase the model generalization capabilities. They were flipped left to right or upside down with a probability of 0.5, once they were seen by the model.
The monitored metrics were the Dice Loss and the mean Intersection over Union (mIoU). The trends of the loss function and the mean Intersection over Union on both the training and validation sets are shown in Figure 5-40.

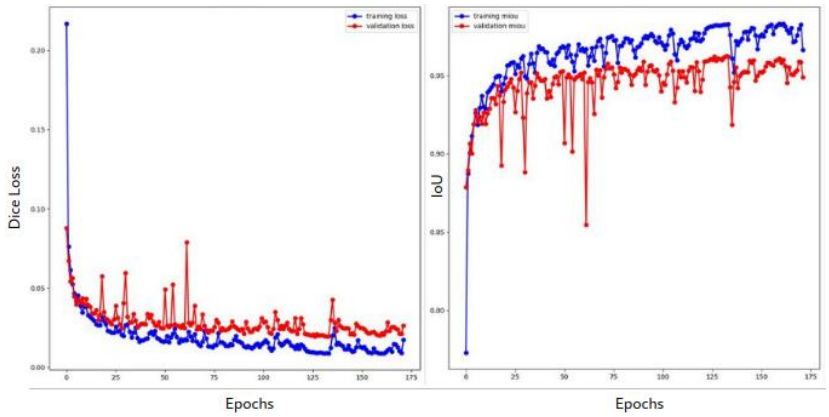

Figure 5-40: Metrics monitored during training. Left: Dice loss (minimized loss function). Right: mean Intersection over Union.

The trend of the validation metrics mirrored that of the training metrics throughout the process, except for adjustment peaks where the neural network fine-tuned its performance as it learned. The best model was achieved at epoch 133, when the Dice loss reached 0.019 and the mean IoU was 0.962. These values indicate that the neural network had learned effectively.

5.5.2.2.3. Inference results

Results on test set
In this section, a selection of representative results was presented, obtained by applying the trained model to test tiles that had not been seen during training. These tiles, however, were still related to the same bridges used in the training phase. This occurred because the images used to construct the dataset, including the test set, had been acquired sequentially and were all associated with the same structures, without any prior randomization. The following paragraph will present results obtained from unrelated, arbitrary images. In the present section, by contrast, since ground truth was available, a comparison was made between the original tile, the ground

truth, and the output produced by the neural network.

The colour scheme used for the different classes was as follows:

- *Background*: grey,
- *Stone Blocks and Bricks*: green,
- *Concrete*: red,
- *Metal*: blue.

The model demonstrated accurate recognition of all classes, with misclassifications occurring only rarely. Its good behaviour can be seen in Figure 5-41. On the left, the original image is displayed, in the centre the ground truth and on the right the model's predictions.

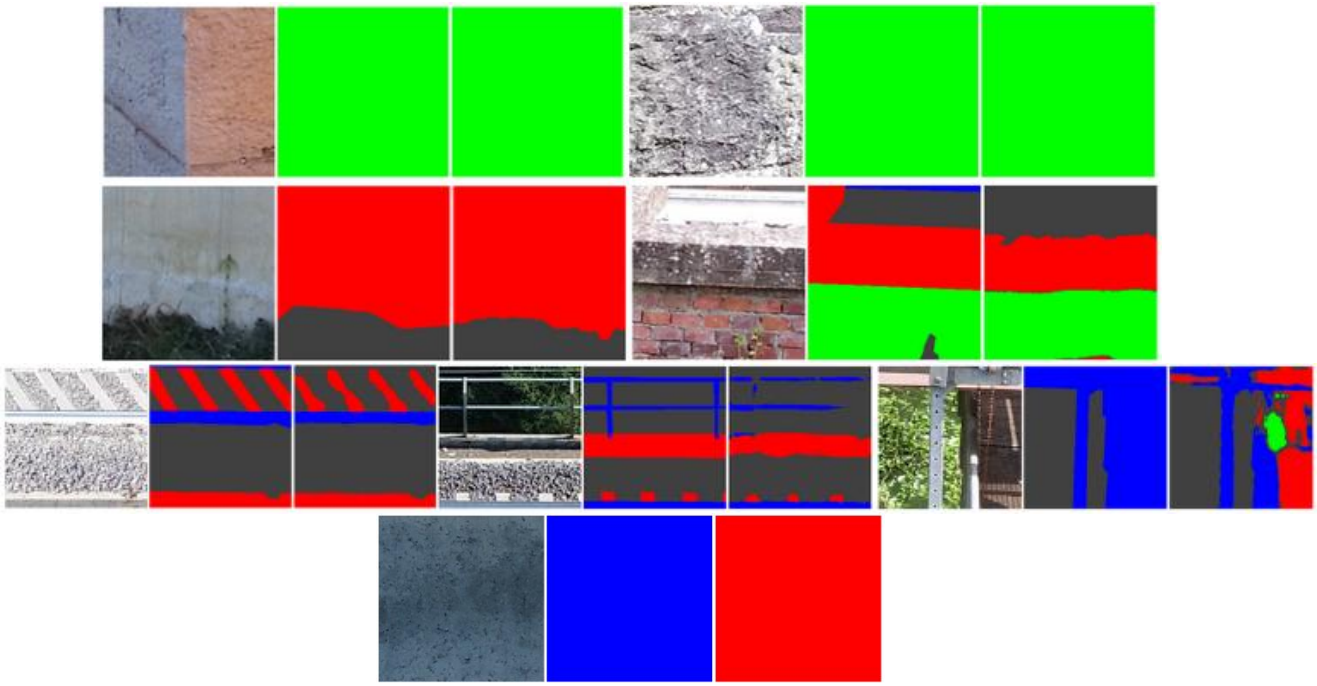

Figure 5-41: Examples of results obtained by the trained model applied in inference on images of the test set.

It can be observed that the network is generally able to distinguish between different materials even in complex scenarios. The last set of images at the bottom shows the neural network correcting an incorrect label during inference: the material was identified as *Concrete*, not *Metal*.

Results on random images

The following results (Figure 5-42) were obtained by applying the network in inference mode to random images, selected from the large pool of data available for this work, but corresponding to bridges that had not been seen during training in any part.

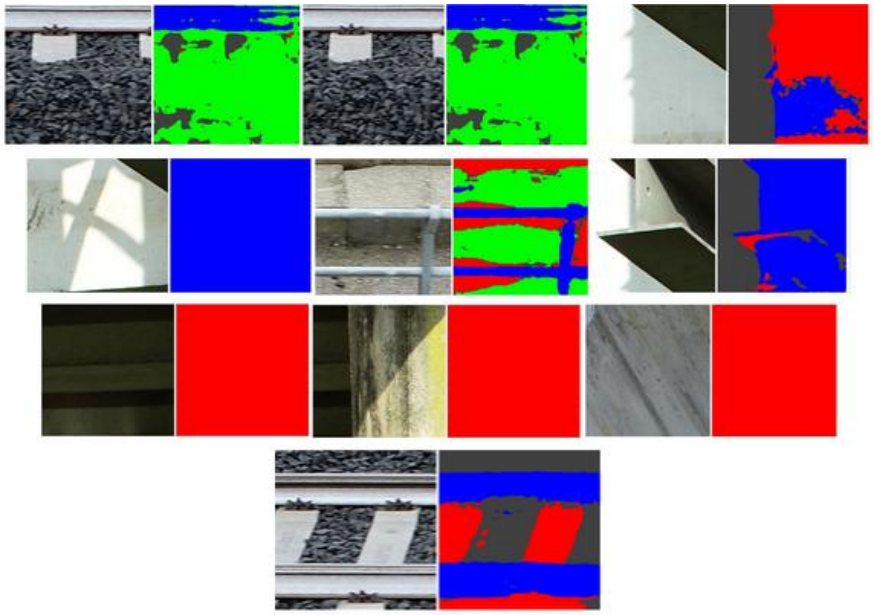

Figure 5-42: Examples of results obtained by the trained model applied in inference on random images.

It becomes evident that the neural network has not yet developed a strong generalization capability. *Concrete* was frequently confused with *Metal*, and *Stone Blocks and Bricks* were rarely identified correctly. Nevertheless, the network appears to be more robust in recognizing *Concrete*, which provides motivation to continue development efforts by initially focusing on this class. At the same time, model performance across all classes is to be further consolidated. This implies the need for a new training phase using a broader and more diverse set of manually annotated ground truth data.

5.5.2.3. Stage 2: Material-specific defect detection via segmentation

Once the neural network dedicated to material recognition has been thoroughly trained, at least on the *Concrete* class, it will be possible to proceed with the training of a semantic segmentation model to identify defects in this type of material. The ultimate goal is to apply the same pipeline to *Stone Blocks and Bricks* as well as to *Metal*.

5.5.2.3.1. Ground truth data generation process

A data labelling phase has been initiated by RFI's inspectors to categorize certain particularly relevant defect classes. It will not be feasible to identify a large number of defect classes, as confirmed during the initial phase of this work, when an analysis of the previously available marker types was conducted. This is due to the risk of having poorly represented categories, which would prevent the network from effectively learning the visual features of such defects. This limitation is further compounded by the inherently heterogeneous appearance of defects, a characteristic that applies to all anomalies targeted for detection through AI-based methods. The current labelling phase mainly concerns bridges made of concrete and masonry, based on images consistently acquired via drone. The images of the Leonessa masonry bridge in Melfi were specifically collected for this purpose. Figure 5-43 presents several examples of RFI inspected and labelled defects intended for the second phase of the pipeline.

Figure 5-43: Examples of labelled defects in the Leonessa masonry bridge.

5.5.3. Final considerations and next steps

The initial phase of this project has demonstrated the feasibility and potential of applying artificial intelligence to the task of structural defect detection in bridges, using drone-acquired imagery from the Italian railway network. The two-stage processing pipeline, consisting of material classification followed by material-specific defect detection, was designed to address the complexity and heterogeneity of the data while enhancing the overall robustness and precision of the models.

The results obtained from the first stage are encouraging. The model achieved high performance on the test data, particularly for the *Concrete* class, validating the segmentation-based approach. However, when applied to images from previously unseen bridges, the model showed limited generalization capabilities, especially in distinguishing between similar materials such as *Concrete* and *Metal*, or in correctly identifying *Stone Blocks and Bricks*. These observations indicate that the current dataset is not sufficiently representative of the variability present in real-world scenarios. In response to this limitation, efforts have already been initiated to expand and diversify the annotated ground truth dataset. A larger and more heterogeneous dataset will be essential to improve model generalization and to ensure reliable performance across a wider range of bridge typologies and conditions.

Regarding the second stage of the pipeline, defect detection conditioned on material type, preliminary labelling work has begun. This stage presents its own challenges, particularly in relation to class imbalance and the inherent visual variability of defects. It is therefore crucial to adopt a selective approach in defining target classes, prioritizing those that are both critical for structural integrity and adequately represented in the data.

5.6. Subsidence & Landslides

Subsidence and Landslides describes two different phenomena:

- The subsidence describes a slow lowering of the ground typically due to natural (e.g. compression of sediments) or anthropic causes (e.g. extraction of water, oil or gas for underground).

- The landslides are quick movements downward of rocks, or other materials on a slope typically due to natural (e.g. rainfall, earthquakes) or anthropic causes (slope destabilization through earthmoving works), once the landslide is active it needs to be secured and monitored.

The main difference between the two phenomena is the temporal evolution (slow the in the first case and rapid in the second). However, once started, monitoring of these phenomena is essential. This presents an opportunity to use InSAR data and integrate these with measurements coming from inclinometers or GPS for landslides and subsidence.

In deliverable D12.1 of WP12, the InSAR processing concept has been presented and applied on only two Single Look Complex (SLC) SAR products on different dates for each site. Using only two products proven the concept, but the results are affected by high atmospheric and decorrelation noise.
In this deliverable, the period analysed spans on 10 years from April 2015 to April 2025 and this is an advantage with respect to what is currently freely available (e.g. European Ground Motion, EGM). Using a decade of Single Look Complex (SLC) SAR products for the processing pipeline allows to filter geometrical decorrelation, temporal decorrelation and atmospheric noise.

The Pipeline for InSAR Processing is structured as follows (see Reference Document SPINUA: A Flexible Processing Chain For ERS / ENVISAT Long Term Interferometry):

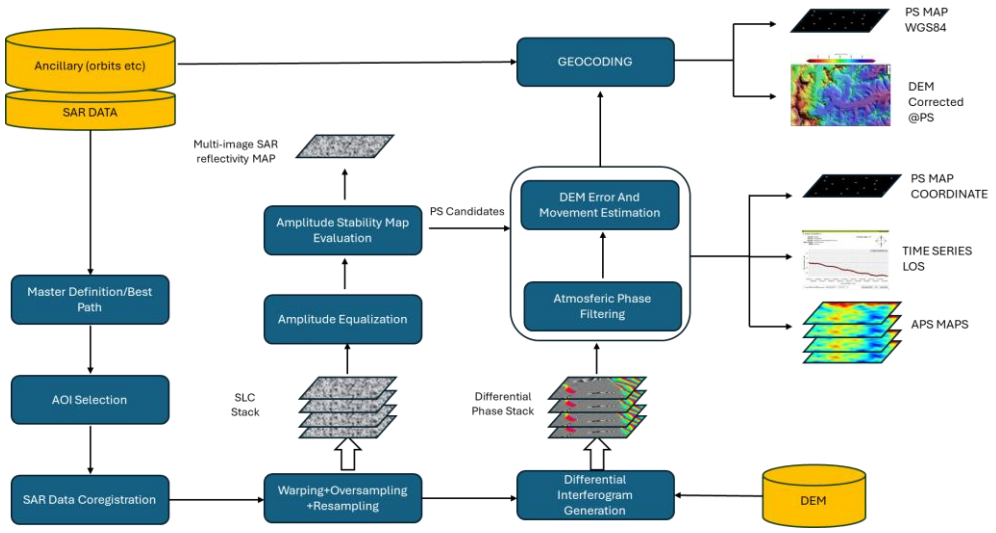

Figure 5-44: Pipeline for InSAR Processing.

The processing is composed by the following steps:

- **SAR Data selection:** Selection of SLC Data on the same site covering the time span under monitoring.
- **Master Definition:** two strategies are possible:
  - **Single Master Approach:** Selection of the master product with respect to which all other products are referred. Typically, the choice for the master is performed collecting information of temporal baseline B_T (time distance) and geometric perpendicular baseline B_{PE} (component

of the distance between satellites perpendicular to the line of sight) and selecting the product corresponding to the barycentre of this 2D space. This improves the temporal and spatial correlation of the interferograms.

- **Best Path Approach**: Alternatively, a "best path" strategy can be adopted, in which all SAR acquisitions are connected through a sequence of step-by-step interferograms following an optimal path in the (BPE–BT) space. This path is typically derived from a minimum spanning tree (MST), minimizing spatial and temporal baselines and improving coherence and phase stability.

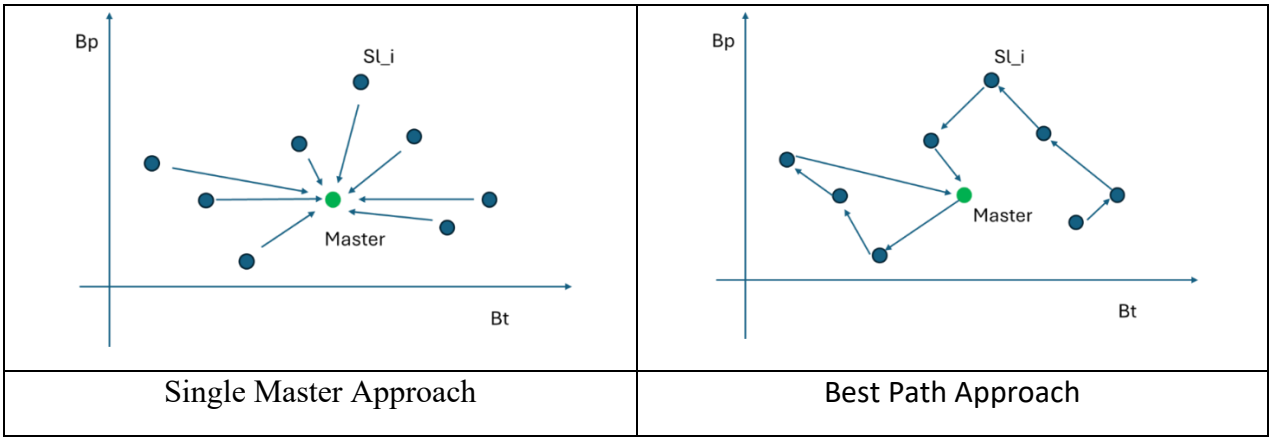

Single Master Approach	Best Path Approach

Figure 5-45: Single vs Best Path Approach.

- **AOI Selection:** The AOI selection (working on a smaller data matrix) allows to considerably speeds the DIINSAR PS processing chain.
- **SAR Data Co-registration:** The Co-registration is a process by which images are aligned pixel by pixel and so each pixel of the image (i) is aligned to that of the image (i+1), and both corresponds to the same feature on ground. The correct co-registration, reducing the geometrical decorrelation, improves the coherence and the phase difference retrieval. The co-registration is performed according to a two steps approach coarse and fine:
  - **Coarse:** this first alignment provides a rigid translation, in range and azimuth, of the slave image on the master one and is performed at pixel-level relying on acquisition geometry information like:
    - Metadata
    - Orbits
    - Acquisition geometry (slant range, look angle)
    - DEM (Optional to estimate the true pixel position due to SAR geometrical distortion)
  - **Fine:** this second alignment is a refinement at sub-pixel level and is performed splitting both matrices (Master and Slave) in smaller portions (patches), these patches are then put in cross-correlation slightly moving one with respect to the other and when a maximum in cross-correlation is obtained, the local translation X and Y is obtained.
- **Warping:** Starting from the local translation X, Y evaluated for each patch at previous step, a polynomial function (warping) of first or second order is defined. This polynomial function

describes how each point of the slave image shall translate to be overlapped on the master image.

The warping can be performed or for each slave image over the master according to the single master approach, or according the "best path" strategy (i.e. Slave 1 resampled on Slave 2 resampled on Master ……resampled on Slave i …… resampled on Master), see Figure 5-45.

- **Oversampling:** typically, the grid is oversampled (e.g. 2x or 4x) to improve the apparent image resolution and the resampling result.
- **Resampling:** After the Warping and the Oversampling, it is possible to perform the resampling, i.e. assign new values in module and phase to warped pixel. The interpolator kernel shall be one specifically designed for SAR Data (e.g. sinc, mod bilinear or cubic spline) in terms of phase preservation without introducing distortions.
- **Amplitude Equalization:** This step is performed prior to the selection of point scatters in order to ensure homogeneous weighting of all the acquisitions. The amplitude for each scatter in general can vary from an acquisition to another due to variations in sensor calibration, acquisition geometry or environmental conditions.

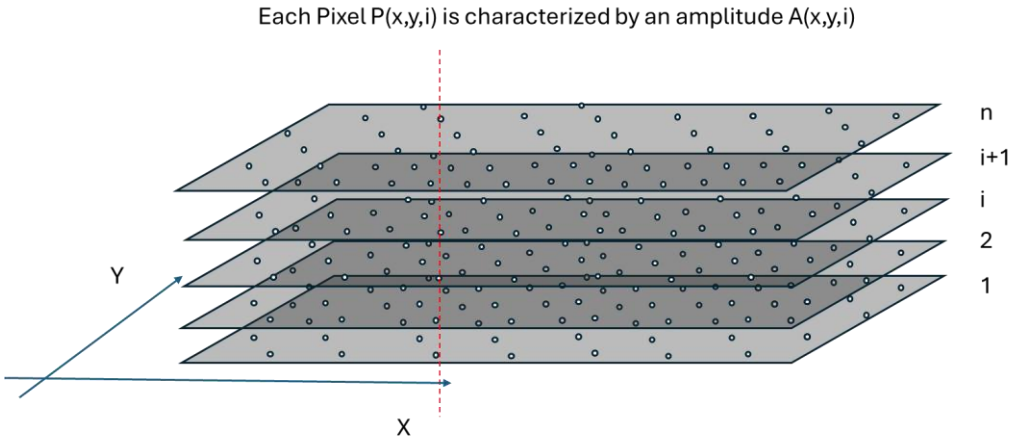

Figure 5-46: Amplitude Equalization.

Only the image Master undergoes to a full absolute radiometric calibration considering SAR antenna parameters and geometric parameters, other slave images in the stack are instead only calibrated in a relative manner (scaled in amplitude with respect to the Master).

This recalibration of the slave images on the master one is performed as follows:

- **ICV (Inverse Coefficient Variation) calculation**:
  Each Pixel P(x,y,i) is characterized by an amplitude A(x,y,i) and so is possible to evaluate its temporal average and its temporal standard deviation (here n is the number of images of the stack):

$$\mu(x,y) = \frac{\sum_{i=1}^{n} A(x,y,i)}{n}$$

$$\sigma(x,y) = \sqrt{\frac{\sum_{i=1}^{n}\left(A(x,y,i) - \mu(x,y)\right)^2}{n}}$$

$$ICV(x,y) = \frac{\mu(x,y)}{\sigma(x,y)}$$

- **Stable Pixel Selection:** The ratio between the average and the standard deviation is a measure of how much that pixel is stable in time, pixels with high ICV are good Permanent Scatters (PS) candidates. Typically, the PS mask is obtained though the selection of a proper threshold (e.g. 0,8 -1.0).
- **Evaluation of correction scaling factor for each image:** Given the N selected PS at the previous point, a correction factor f_i, based on ratio of PS amplitudes A between Master and Slave, is calculated for each image of the stack i. (here N is the number of PS for each image, the same for each image of the stack).

$$f_{slave} = \frac{1}{N}\sum_{(x,y)}^{\in PS}\frac{A_{master}(x,y)}{A_{slave}(x,y)}$$

- **Correction Factor application:** Each image is processed through an amplitude correction according to the formula:

$$A_{slave}^{corrected}(x,y) = A_{slave}^{original}(x,y)\cdot f_{slave}$$

- **Amplitude stability map evaluation:** This step has been described above and corresponds to the PS detection/selection, an operator can increase/decrease the density of PS, moving up and down the ICV threshold, but the choice of this threshold shall be properly evaluated, a too high threshold in a high noise dataset could bring to few PS, on the other hand a too low threshold in a good scene (e.g. urban) can bring to too many PS. Main consideration driving the threshold choice are reported below:
  - The number of images in the stack (More images -> better statistics -> higher ICV)
  - The sensor noise floor (Low Noise floor ->better signal-> higher ICV)
  - The scene characteristics (Urban Scenes ->more stable pixel -> higher ICV)
  - The desired PS density (lower threshold means more candidates)

- **Differential interferogram Generation:** For each pair of acquisitions (Slave- Master or Slave-Slave) the interferometric phase is computed:

$$\Phi_{interf} = \arg\left(S_{master} \cdot S^*_{slave}\right)$$

This phase contains multiple contributors:

- ϕ_{Topo}: Topography
- ϕ_{Def}: Ground deformation
- ϕ_{Atm}: Atmospherics effects or also APS (Atmospheric Phase Screen)
- ϕ_{Orb}: Orbit errors
- ϕ_{Noise}: Noise

$$\Phi_{diff} = \Phi_{Topo} + \Phi_{Def} + \Phi_{Atm} + \Phi_{Orb} + \Phi_{Noise}$$

Where ϕ_{Def} is the desired component.

As seen in previous deliverable:

- The ϕ_{Topo} component (Topography) is simulated and subtracted using a DEM (digital elevation model) and orbit information.
- The ϕ_{Orb} (orbit errors) are due to small inaccuracies in orbit information and are simulated and subtracted as slow deriving phase ramp through first/second degree polynomial estimated on areas particularly stable and free from deformation.
- The ϕ_{Atm} (atmospheric errors) are managed through proper filters, the atmospheric errors are in fact radar signal delays (induced by water vapour content) characterized by spatially low frequency variation but chaotic in time (water vapor content has a spatially homogeneous distribution but changes for each acquisition).

So, summarizing the atmospheric errors have a different behaviour with respect to the deformation: deformation is slow in time with recognizable trends and localized in space, while the APS is spatially continuous but random in time. Typically, a model of the APS is built (e.g. 2D polynomial for each interferogram), to be subsequently subtracted.
The extent of the APS is estimated by comparing the phase variation obtained on known stable zones (without deformation). Atmospheric profiles from GNSS, MODIS or weather models (e.g. ERA5) can also be used as input data to estimate APS.

- The ϕ_{Noise} (Noise error) is due to sensor thermal error, geometrical decorrelation, etc. this kind of error is intrinsically attenuated by PSI technique through the selection of stable scatters and the use of local averaging near the Permanent Scatters. So incoherent noise tends to be cancelled, enhancing the retrieving of the deformation estimates.
- **Phase Unwrapping:** The interferogram obtained at previous step is ambiguous (i.e. limited to the interval $\pm\pi$), so, to obtain the absolute phase induced by deformation, unwrapping techniques are used as the sparse-grid Minimum Cost Flow or others. This allows to pass from a phase displacement always between $\pm\pi$ to a ϕ_{Def} considering also a certain number of whole cycles. The wavelength and is fractional part return the displacement along the line of sight. This

is finally projected in terms of vertical up/down deformation. Sentinel-1 wavelength is 5.6 cm, the displacement in LOS corresponding to a full cycle is the half (2,6 cm) due to double trip of radar signal from the satellite to target and vice versa.

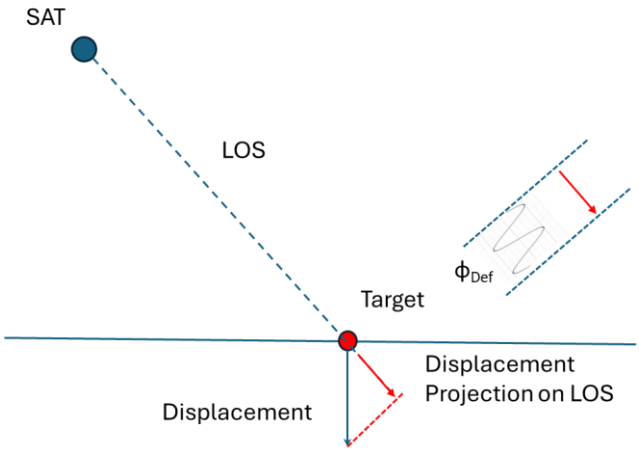

Figure 5-47. Relation between displacement projection on LOS and actual vertical displacement

The output of this processing is a shapefile in geo-package format containing the deformations along the observation period for all the Permanent Scatters (P.S.).

All the described process has been applied to two areas of interest:

- Railway Station of Cerignola Campagna affected by a subsidence phenomenon
- Talud Briones area affected by a landslide phenomenon

5.6.1. Location of Cerignola Campagna

The 4 km long path under analysis lies across Cerignola Campagna and Borgo Incoronata and it is subject to a slow subsidence. Interferometric analysis allowed obtaining a great density of measurement points, providing a detailed overview of surface deformations and instability phenomena. Both distributed (DS) and point (PS) radar targets were analysed.

The period analysed spans on 10 years from April 2015 to April 2025 and this is an advantage with respect to what is currently available on the European Ground Motion (EGM) service since information relevant to deformation are available from 01/2019 up to 12/2023 (see below).

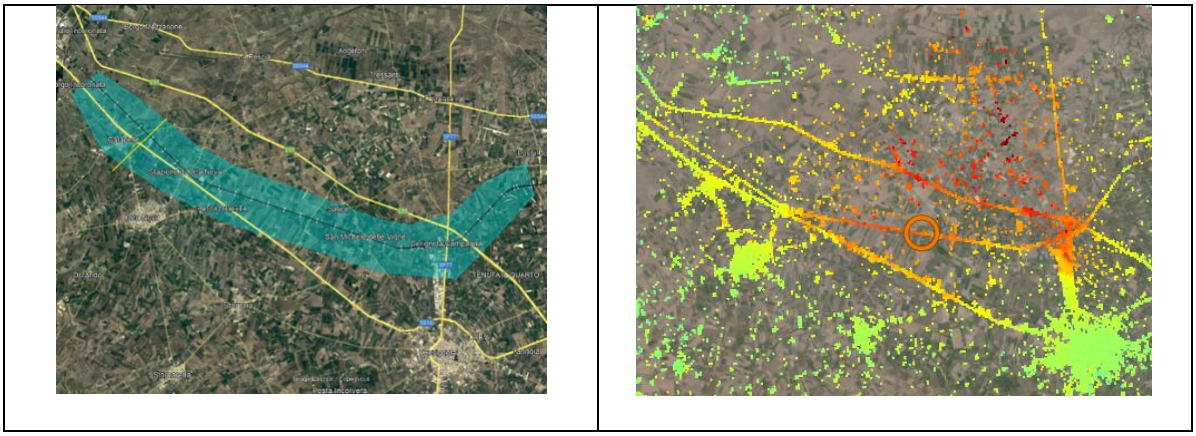

Figure 5-48: Cerignola AOI and Deformation MAP from EGM.

Here below an example of deformation retrieved by the EGM service on the point highlighted with the red circle.

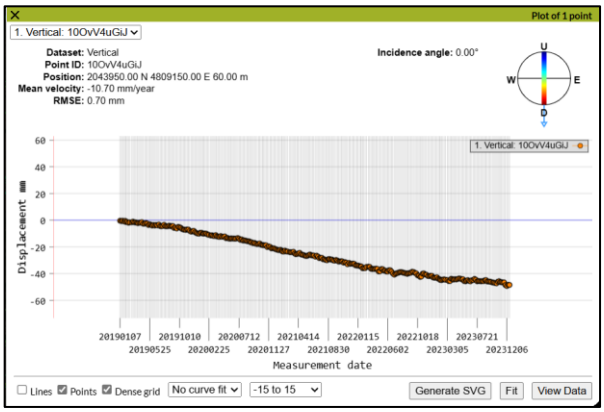

Figure 5-49. Trend Deformation on example point on Cerignola AOI as derived by EGM.

We anticipate that cluster of areas with different subsidence properties have been already spotted, creating discontinuity that can potentially impacting the rail corridor. The physical insight related to the observation period (2015-2025), the potential comparison with ground data and maintenance data will be provided within the deliverable D13.3 to demonstrate the benefits associated to this technique. The FP3-IAM4RAIL web platform developed by MERMEC (specifically reported in section 5.8.2.4 for landslides), allows to analyse the last decade of data related to displacement time series, average velocity, position, and elevation.

5.6.2. Talud Briones

The area under analysis is about 300 m x 150 m near Talud Briones (Coordinates N 42.5542 W 2.8269). This area was suffering for a significative landslide in 2015, so after the event a PSI monitoring has been performed. The period analysed spans on 10 years from April 2015 to April 2025 and also in this case it is an advantage with respect to what is currently available on the European Ground Motion (EGM) service since information relevant to deformation are available from 01/2019 up to 10/2023 (see below).

Figure 5-50: Talud Briones AOI and Deformation MAP from EGM.

Here below an example of deformation retrieved by the EGM service on the point highlighted with the orange circle.

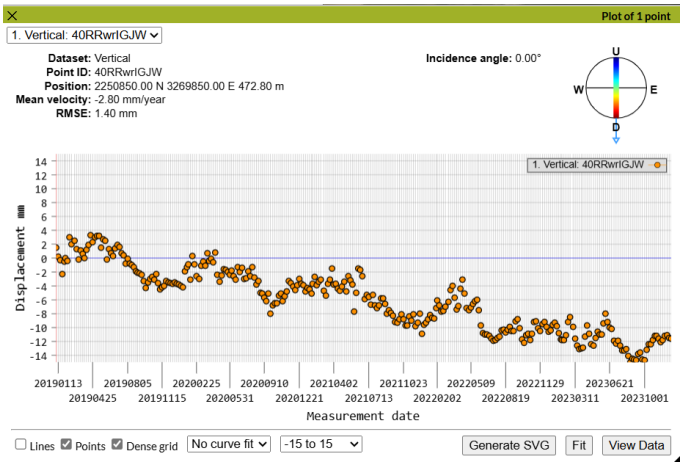

Figure 5-51.Trend Deformation on example point on Talud Briones AOI as derived by EGM

Physical insight pertaining the extended observation period (2015-2025) and connection with the ground sensors position on this area will be provided in D13.3. A preview of the extended data processing for Talaud Briones is shown in this document, in section 6.4.

5.7. Flood risk assessment

In Italy, floods have a significant impact on the population and on the territory as highlighted in the Report on Hydrogeological Instability published by ISPRA in 2018. The railway infrastructure, covering more than 16,000 km of railway lines, is in some cases strongly affected by this problem. To this purpose, we have developed a monitoring and forecasting tool based on the collection and analysis of satellite available data of sensitive "*climate*" variables (with respect to the phenomena that are intended to be monitored).

Precipitation, soil moisture, Land Surface Temperature (LST), and Land Cover (LC) maps are the parameters considered for the flooding risk monitoring. The analysis was executed for the Area Of Interest (AOI) "Milano-Novara". However, an additional AOI, "Tortona-Voghera", was considered as a further case study for the validation of the processing and algorithms.

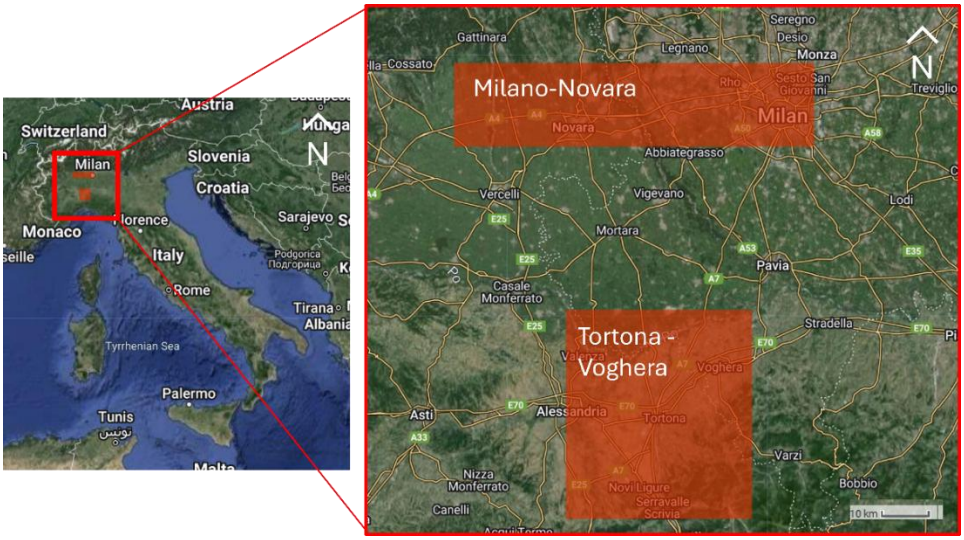

Figure 5-52: Novara and Tortona-Voghera AOI.

The considered analysis time ranges from January 2000 to December 2024, being this year the last one to provide a complete series of data. The 24 years taken into consideration can be referred as climatological period, providing proper detail to define and monitor precipitation intensity and variability. Within the considered climatological period, for each year the main flooding events happened in the test areas were identified and according to the availability of data the information related to the previous 3 days of were also considered. This choice aims to maximize the study years, considering data availability. Data are collected and processed using Google Earth Engine (GEE) platform and Microsoft Visual Studio editing Python. In the Python environment, input data are the outputs from GEE which are additionally processed to obtain one or more products which can consist of CSV files or graphs. For what concern precipitation, soil moisture, and LST, produced outputs can be differentiated based on the time interval considered for the analysis (hourly, daily, or monthly). Additionally, analysis based on extreme values, i.e., values during or near the event and maximum values, were executed. This information was summarized in a final output consisting of statistical analysis and cross plots that compare the different parameters for the different scenarios of event or non-event.
The data used is: GPM IMERG (https://gpm.nasa.gov/missions/GPM): Global Precipitation Measurement (GPM) data provide observations of rain and snow and were used to estimate precipitation.

The following products were considered:

- GPM IMERG Final Precipitation L3 Half Hourly 0.1 degree x 0.1 degree V07: this product reports precipitation data adjusted in accordance with gauge data and climatological.
- GPM IMERG Late Precipitation L3 Half Hourly 0.1 degree x 0.1 degree V07: this product was considered only in case of unavailability of the first one, as it does not have the same corrections as the former.
- GLDAS Soil Moisture Data (https://ldas.gsfc.nasa.gov/gldas): Global Land Data Assimilation System (GLDAS) data provide hydrogeological products, and was used to estimate soil moisture. Two dataset versions exist, the following was considered:
- GLDAS-2.1: this is the more recent version and climatologically more consistent compared to the previous one.

- MODIS Terra Data (https://modis.gsfc.nasa.gov/): Moderate Resolution Imaging Spectroradiometer (MODIS) measures were used to obtain LST. Among the data products available, the following from the current Collection-6 was considered:
- MODIS Land Surface Temperature and Emissivity (MOD11).

For LC, considered data, which are further described later, are:
- CORINE (Coordination of Information on the Environment) Land Cover by Copernicus.
- MODIS Collection 6.1 Land Cover Type provided by NASA.

CORINE (Coordination of Information on the Environment) Land Cover
GEE data collection used is "*Copernicus CORINE Land Cover*". CORINE LC product offers a pan-European LC and land use inventory with 44 thematic classes. Spatial resolution is 100 meters. The product is updated with new status and change layers every six years, with the most recent update made in 2018. The first dataset was produced in 1990. Five assets exist which cover different time periods: 1990 asset (from year 1989 to year 1998), 2000 asset (from year 1999 to year 2001), 2006 asset (from year 2005 to year 2007), 2012 asset (from year 2011 to year 2012), and 2018 asset (from year 2017 to year 2018). The following table summarizes the main characteristics of the CORINE LC products.

Data	COPERNICUS/CORINE/V20/100m
Version	NA
Data availability	1989 – 2018
Frequency	5 different assets within the available dates
Spatial resolution	100 m
Variable	landcover

Table 5-6: Main characteristics of CORINE LC data.

MODIS Collection 6.1 Land Cover Type
The considered data collection in GEE is "*MCD12C1.061 MODIS Land Cover Type Yearly Global 0.05 Deg CMG*". MODIS LC Climate Modeling Grid (CMG) Version 6.1 data product provides a spatially aggregated and reprojected version of the tiled MCD12Q1 Version 6.1 data product. Spatial resolution is 5600 m. Maps from different classification schemes are provided, and the International Geosphere-Biosphere Programme (IGBP) was considered in this case. MODIS LC is available from 2001 to 2023 with a yearly cadence.
The below table summarizes the main characteristics of the MODIS LC products.

Data	MODIS/061/MCD12C1
Version	6.1
Data availability	2001 – 2023
Frequency	Yearly
Spatial resolution	5600 m
Variable	Land_Cover_Type_1_Percent_Class_{class_number}

Table 5-7: Main characteristics of MODIS LC data

5.7.1. Data processing

Considered data for precipitation, soil moisture, LST, and LC parameters were processed at different levels for their analysis.

The processing steps executed in GEE can be summarized as follows:

1. **Input dataset collection:** dataset collection is imported in GEE considering the data available in the GEE Data Catalog;
2. **Dataset processing:** this step includes dataset filtering, i.e., the dataset is filtered based on area, time range and variable of interest. A spatial resampling was executed to upscale resolution of precipitation, soil moisture, LST, and MODIS LC data collections to the finest one, i.e., GPM precipitation products. A downscaling was executed for CORINE LC;
3. **Output:** a CSV file for each considered year is produced for precipitation, soil moisture, LST, and MODIS LC. For CORINE LC, the available years were considered.

The csv file includes a number of rows that correspond to the number of available data within the considered year or time period and a set of columns that include the acquisition date, acquisition time and the variable value for each pixel within the AOI.
The CSV files are used as input for further elaborations, implemented with Python programming language.

5.7.1.1. Generation of the flood probability maps based on climatological period

The most significant output from elaborations previously described was selected in order to train a Neural Network (NN) model. A fully connected NN was developed to correlate the considered parameters, i.e., precipitation, soil moisture, LST, and LC, with the extreme meteorological events. Firstly, the dataset was created and then the model was trained and test.
LST was discarded, since it does not exhibit a strong correlation with the extreme meteorological events. Between the two considered LC data collections instead, CORINE was selected given its finer spatial resolution.
In order to build the dataset, the whole number of flood events registered during the considered time period (2000-2024) was considered, for a total of 22 events. 22 non-event dates were

randomly selected among the available to obtain a balanced dataset. For each event, the considered variable, i.e. soil moisture for the different layers, precipitation, and CORINE LC are used as input for the NN:

- vsm_0_10;
- vsm_10_40;
- vsm_40_100;
- vsm_100_200;
- precipitation;
- landcover.

Here, vsm_0_10, vsm_10_40, vsm_40_100, and vsm_100_200 are the volumetric soil moisture values for the different soil depth, precipitation is the data from GPM, and landcover is the data from CORINE LC.
The value over the AOI in the 3 days before the event was considered for precipitation and soil moisture, while the available value for the year range was considered for CORINE LC.
The whole dataset is composed of 200 × 20 (20 is the number of pixels within the resampled AOIs) samples that were normalized between 0 and 1 and split into training, validation, and test sets with a defined proportion. For each AI model, the initial input dataset was divided with 70% of the available dataset dedicated to the training phase, while the remaining 30% was further divided into testing (20%) and validation (remaining 10%).

In this case, the input of the NN is a vector with 18 entries, that are the value for each pixel over the AOI in the 3 days before the event for each considered variable.
The model was trained in Python with TensorFlow and Keras libraries (TensorFlow, 2024; Keras, 2024). One hidden layer with 2 units was considered with *relu* activation function. *sigmoid* activation function was used for the output layer. Binary crossentropy loss function and Adam optimizer were used. The results are first presented as "on-off" type (binary classification):

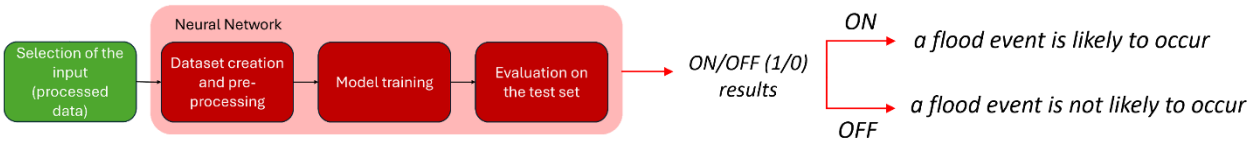

Figure 5-53: Workflows and results.

Then, transition from hard classification (on/off, 1/0) to soft classification has been carried out in order to generate maps of probability of occurrence of a flood event on the territory.
Different attempts were made to define the best NN architecture, which finally consists of 3 hidden layers with 18, 5, and 1 unit, respectively. Different learning rates (5e-2, 1e-2, 5e-3, 1e-3) and batch sizes (8, 16, 32, 64, 128) were tested, and the early stopping algorithm was used to avoid overfitting.

	AOI	
	Milano-Novara	Tortona-Voghera
Learning rate	0.005	0.01
Batch size	16	32
Test accuracy	0.75	0.80

Table 5-5: Training configuration and test results for flooding probability NN.

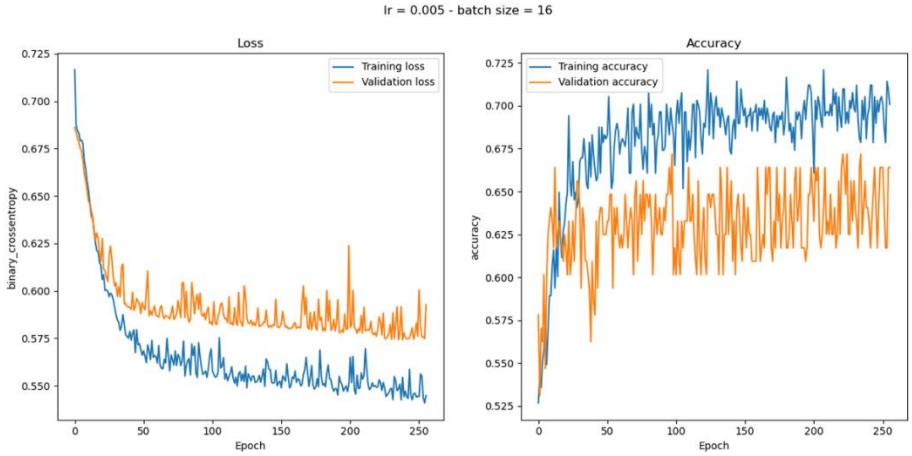

Figure 5-54: Loss function and accuracy for AOI Milano-Novara for training (in blue) and validation set (in orange).

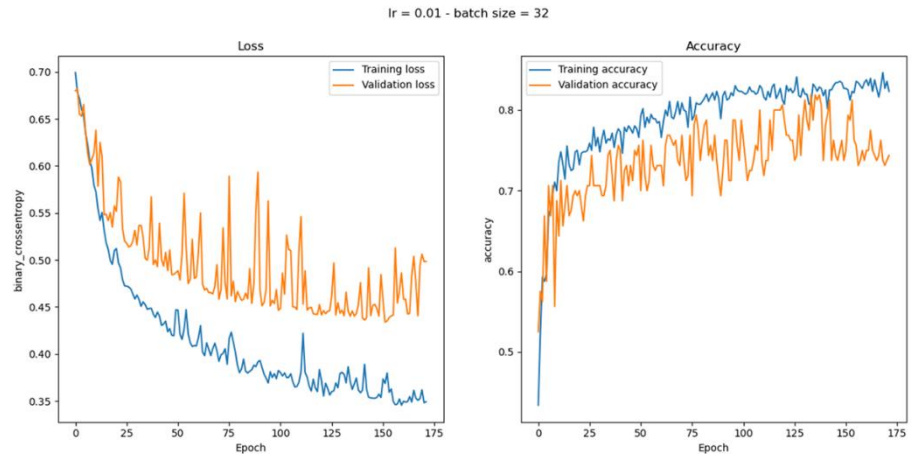

Figure 5-55: Loss function and accuracy for AOI Tortona-Voghera for training (in blue) and validation set (in orange).

Previous figures show the loss function and accuracy during training for Milano-Novara and Tortona-Voghera AOI, respectively, for the best configuration described in the above table. Loss values and accuracy evaluated on both the training and validation sets are reported in the graphs.

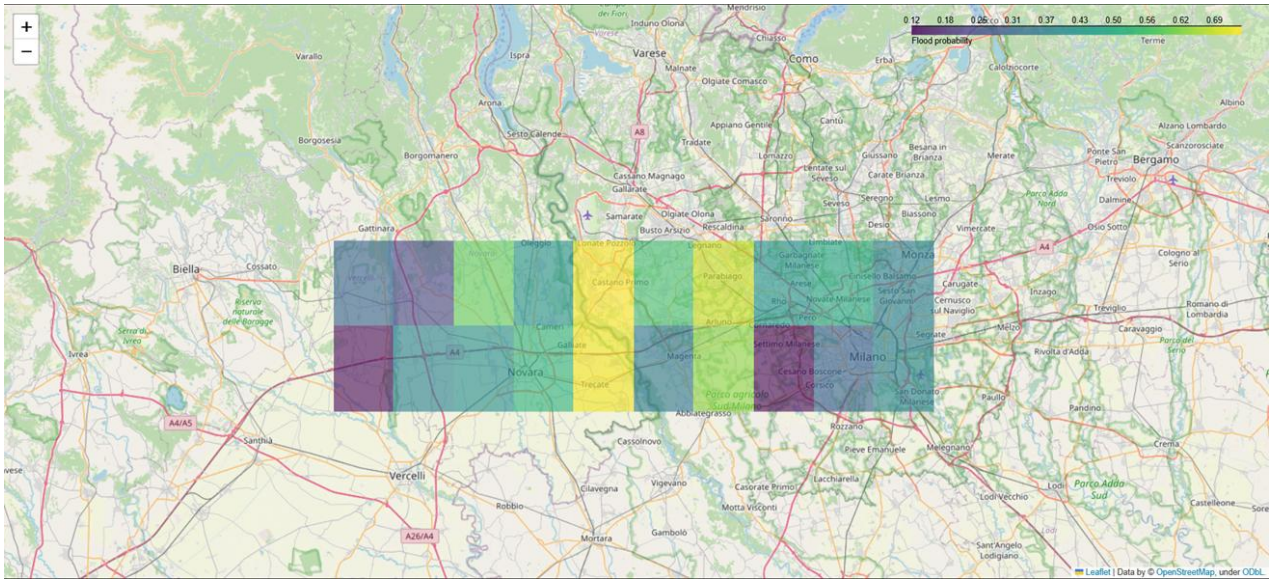

Figure 5-56: Milano-Novara AOI: map of probability of occurrence of a flood event generated with the AI algorithm from the climatological period (2000-2024).

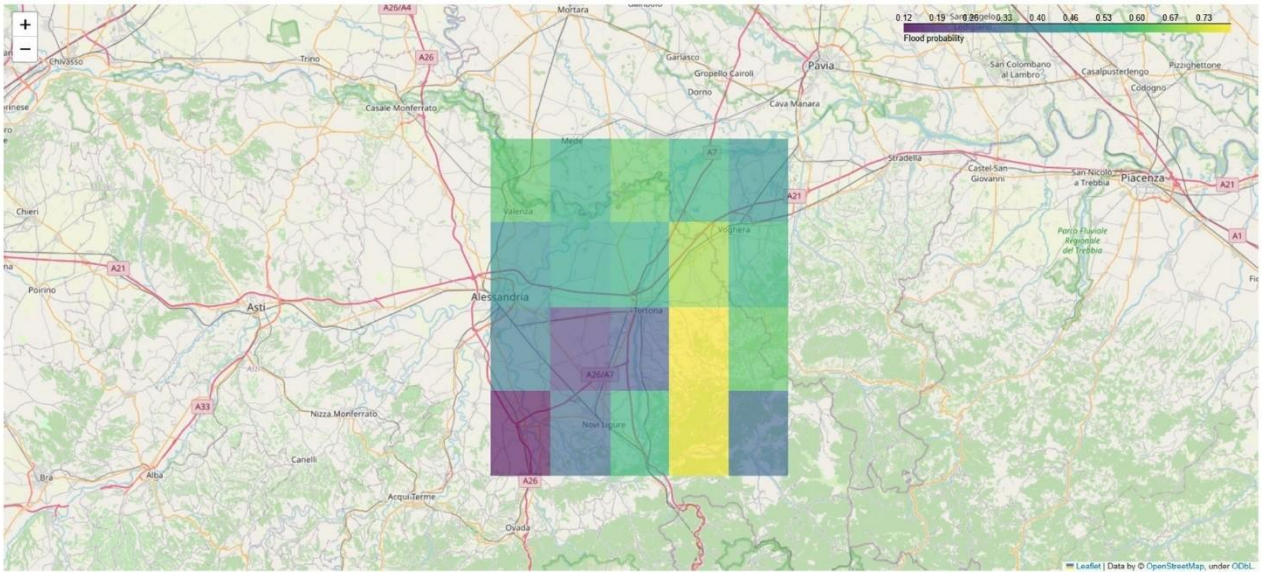

Figure 5-57: Tortona-Voghera AOI: map of probability of occurrence of a flood event generated with the AI algorithm from the climatological period (2000-2024).

The above figures show the probability maps obtained from the dataset dedicated to test for the AOIs of Milano-Novara and Tortona-Voghera, respectively.
The validation of the NN outcomes is carried out evaluating the results obtained by applying the algorithm to flooding events, occurred in the AOIs, during the year 2025, which information is not included in the input training dataset. This strategy is necessary to provide a validation dataset that is consistent in terms of spatial and temporal resolution with the resolutions identified to map the distribution of the flooding probability.

In particular, a strong flood event occurred in April 2025 was considered. It occurred between Tuesday 15th and Thursday 17th April 2025, generated by the depression called “Hans” which deepened over the central-western Mediterranean, causing a highly disturbed phase over north-western Italy. The event mostly affected the western mountainous areas, but total cumulative precipitation was widely above 100 mm across the whole Piemonte region (for more details, please see https://www.regione.piemonte.it/web/media/49088/download).

Similarly, as the previous analysis, the parameters over AOIs during the 3 days before the main flood event were taking as input to the NN model, so days from 15th to the 17th of April 2025.

The following figures show the results of the validation with the event occurred in 2025 for the AOI of Milano-Novara and Tortona-Voghera, respectively, which show high levels of probability according to the intensity of the flooding event occurred in those days.

The collection of data to insert in the input dataset can benefit of additional samples and the implementation by inserting coming years into the training initial dataset can give further examples to the model to train on and can then optimize the performances and the capability of the flooding prediction.

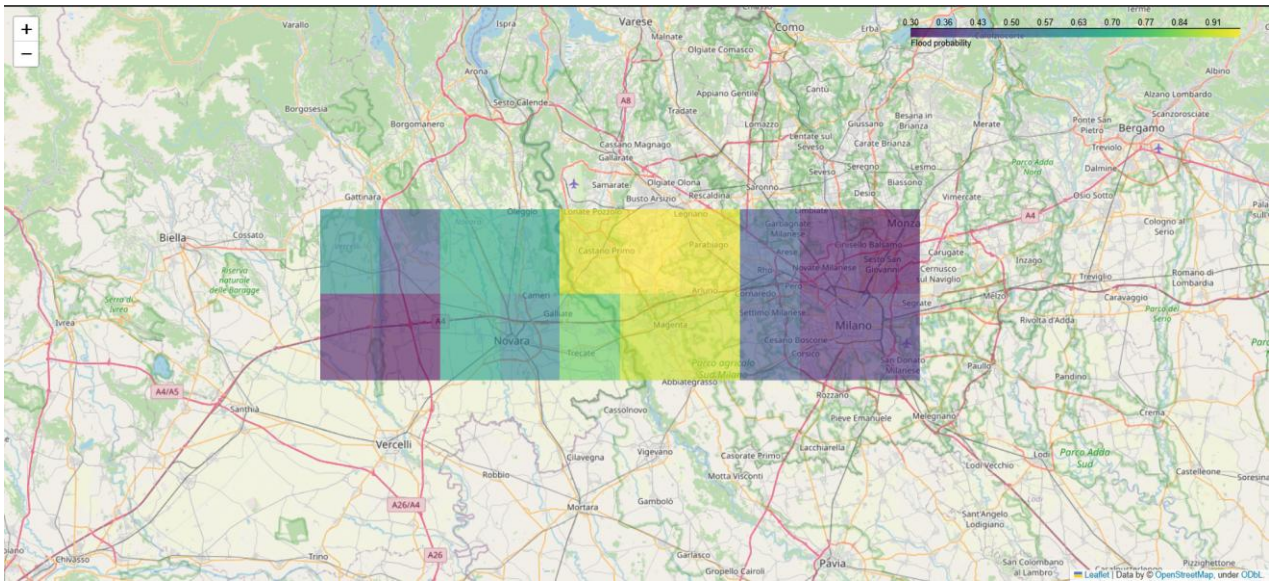

Figure 5-58: Milano-Novara AOI: validation map of probability of occurrence of a flood event generated with the AI algorithm from the climatological period (2000-2024). Validation for event occurred in 2025.

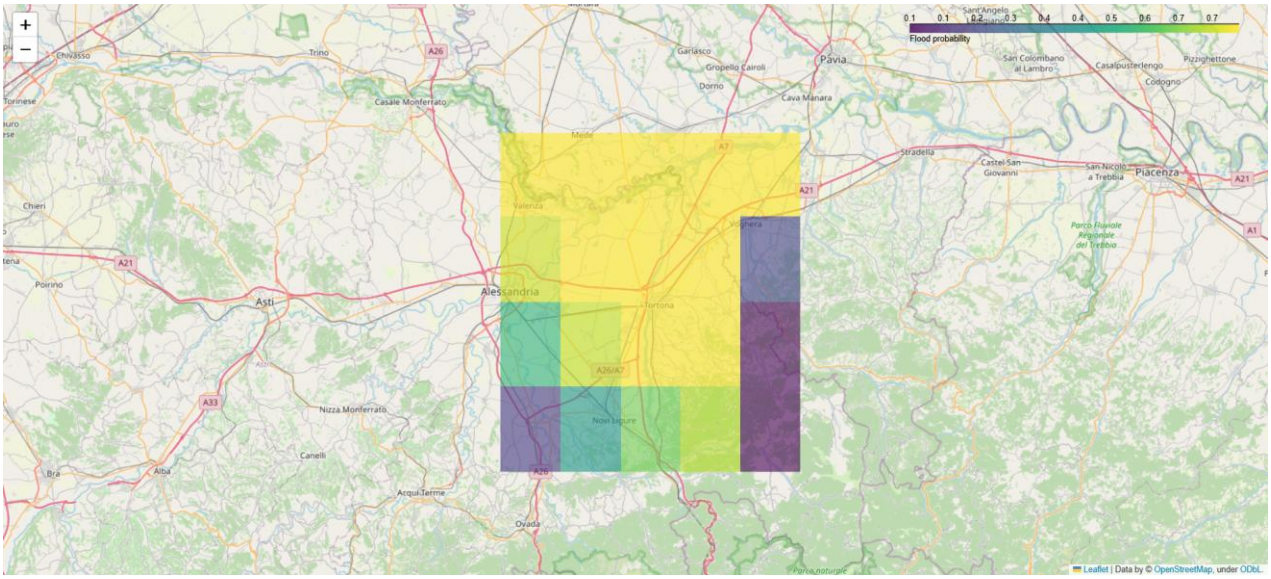

Figure 5-59: Tortona-Voghera AOI: validation map of probability of occurrence of a flood event generated with the AI algorithm from the climatological period (2000-2024). Validation for event occurred in 2025.

The methodology developed, that includes both data collection and NN training, has also the potential to be reproduced and tailored to any specific area of interest. The implementation of the workflow to different geographical and climatological areas can benefit with the customization and the accuracy of the prediction realized.
A railway line, classified according to the relevant assets (e.g. embankment, trench, bridge,...), can be thus superimposed on these maps generated through the methodology above proposed and described for the purpose of assessing the related vulnerability.

5.7.1.2. Generation of the flood probability maps based on future projection

Future projected precipitation, as estimated in next Section, are used to generate flood probability maps for future scenarios.
Two new NN models was trained for the two AOIs following analogous preprocessing steps of data collection and definition of best NN architecture.
The dataset, as described in Section “Data processing”, was built and balanced between flood and non-flood events considering the whole number of flood events registered during the climatological period 2000-2024. The same variables are considered for each event, that are:

- vsm_0_10;
- vsm_10_40;
- vsm_40_100;
- vsm_100_200;
- precipitation;
- landcover.

In this case, the data that will be used for the inference phase refers to a single value of future precipitation. For this reason, in order to construct a NN consistent in terms of input units with the available inference data, the variables used to build the training dataset were processed

differently. In order to have a single value, for precipitation and soil moisture the average value of the parameters over the 3 days before the event was considered, while for CORINE LC the same value available for the year interval was considered.
As previous described, the whole dataset is composed of 200 × 20 (20 is the number of pixels within the resampled AOIs) samples that were normalized between 0 and 1 and split into training, validation, and test sets with a proportion of 70%, 20%, and 10%, respectively.

However, in this case the input of the NN is a vector with 6 entries, that are the value of precipitation, the 4 soil moisture values at different depths, calculated as the average value for the 3 days before the event, and the LC, as summarized in the following Equation 1.

$$NN\ input = average(vsm\_0\_10_3,\ vsm\_0\_10_2,\ vsm\_0\_10_1),\ average(vsm\_10\_40_3,\ vsm\_10\_40_2,\ vsm\_10\_40_1),\ average(vsm\_40\_100_3,\ vsm\_40\_100_2,\ vsm\_40\_100_1),\ average(vsm\_100\_200_3,\ vsm\_100\_200_2,\ vsm\_100\_200_1),\ average(precipitation_3,\ precipitation_2,\ precipitation_1),\ (landcover) \quad (1)$$

The model architecture, as well as activation function, loss function, and optimizer, are similar to the one defined for the climatological period in the previous section.

	AOI	
	Milano-Novara	Tortona-Voghera
Learning rate	0.005	0.01
Batch size	64	32
Test accuracy	0.75	0.76

Table 5-6: Training configuration and test results for flooding probability NN on future projection.

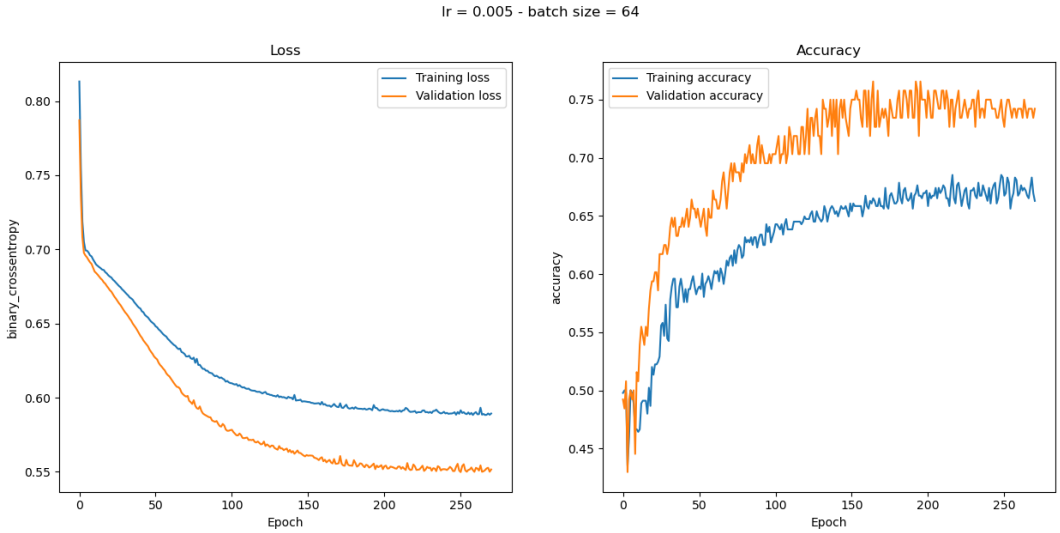

Figure 5-60: Loss function and accuracy for AOI Milano-Novara for training (in blue) and validation set (in orange).

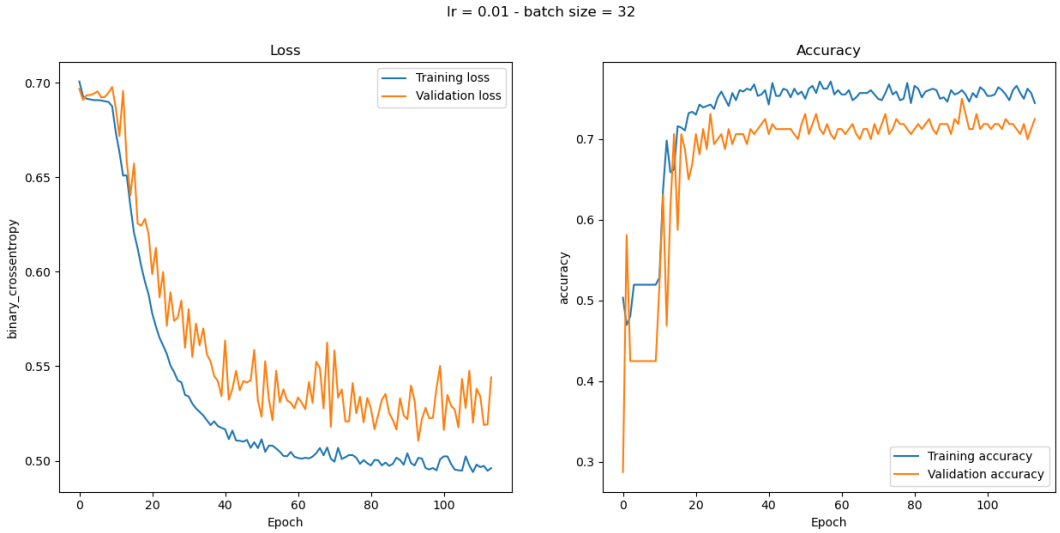

Figure 5-61: Loss function and accuracy for AOI Tortona-Voghera for training (in blue) and validation set (in orange).

Previous figures show the loss function and accuracy during training for Milano-Novara and Tortona-Voghera AOI, respectively, for the best configuration described in the above table. Loss values and accuracy evaluated on both the training and validation sets are reported in the graphs.

During the inference phase, these two models take as input the future projected precipitation as estimated in the next Section, for the two considered datasets, maximum values and return period of 200 years, as well as maximum soil moisture values occurred during the climatological period 2000-2024, in order to provide flood probability maps for future scenarios.

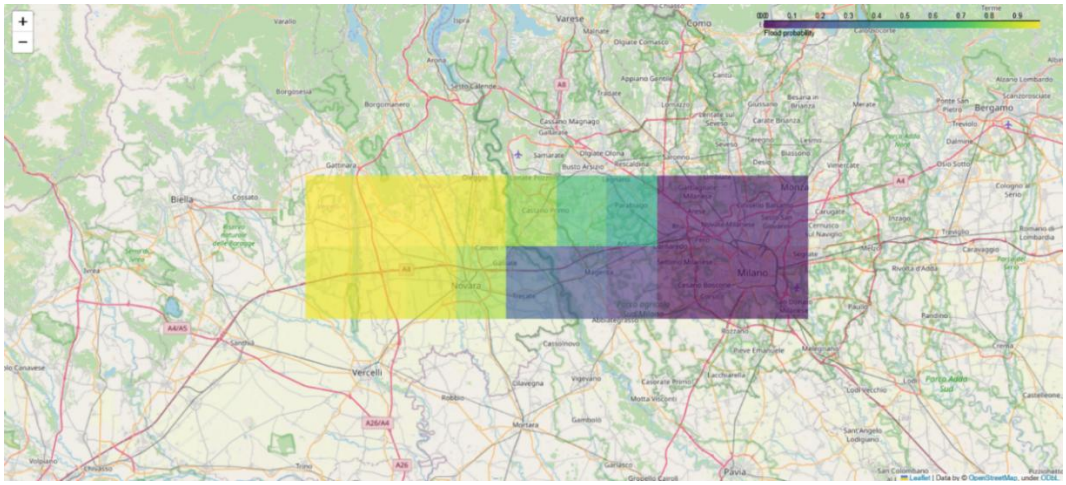

Figure 5-62: Milano-Novara AOI: map of probability of occurrence of a flood event generated with the AI algorithm from the climatological period (2000-2024) adjusted for future projection dataset. Maximum values dataset.

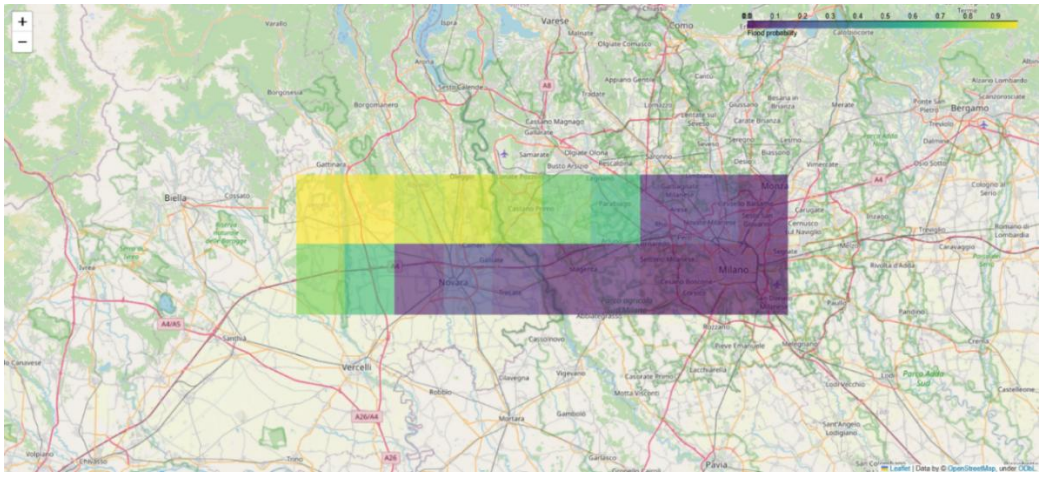

Figure 5-63: Milano-Novara AOI: map of probability of occurrence of a flood event generated with the AI algorithm from the climatological period (2000-2024) adjusted for future projection dataset. Return period of 200 years dataset.

The previous figures show the probability maps for the Milano-Novara AOI obtained from the dataset related to the maximum values and values considering a return period of 200 years, respectively. Probabilities range from 0, represented in purple, to one, represented in yellow.
It is observed that, according to these results, the north – west zone of the Milano-Novara AOI will be subject to more flood events in the future.

The same maps are shown in the following figures for the Tortona-Voghera AOI.
In this case, sensible differences in the analysis carried out for the maximum values and the return period of 200 years can be noticed. Particularly, according to the results based on the maximum values, the south zone of the Tortona-Voghera AOI will be subject to more flood events in the future; while, according to the results based on values considering a return period of 200 years, the north zone of the Tortona-Voghera AOI will be subject to more flood events in the future.
This type of results can be considered to perform a risk analysis of the selected areas.

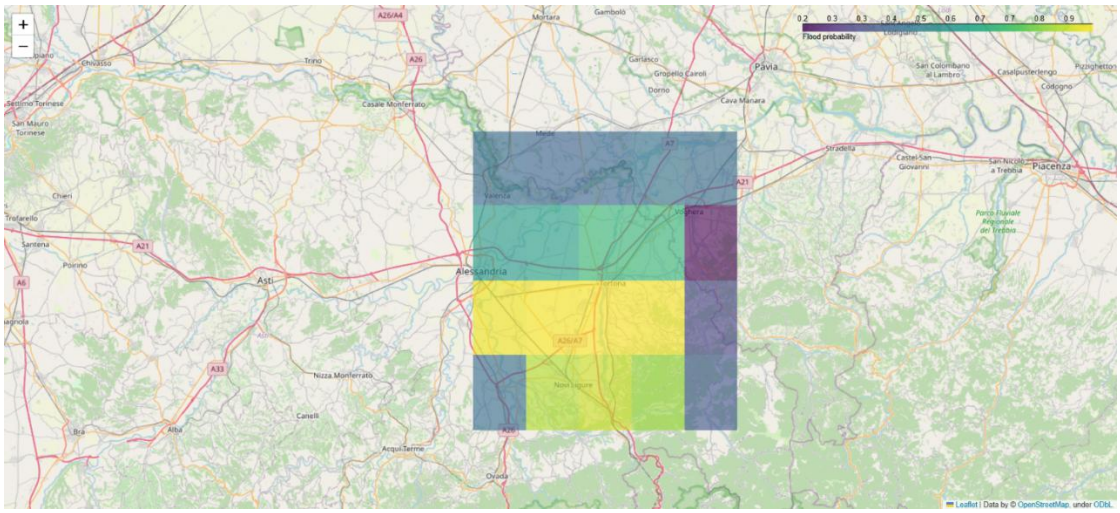

Figure 5-64: Tortona-Voghera AOI: map of probability of occurrence of a flood event generated with the AI algorithm from the climatological period (2000-2024) adjusted for future projection dataset. Maximum values dataset.

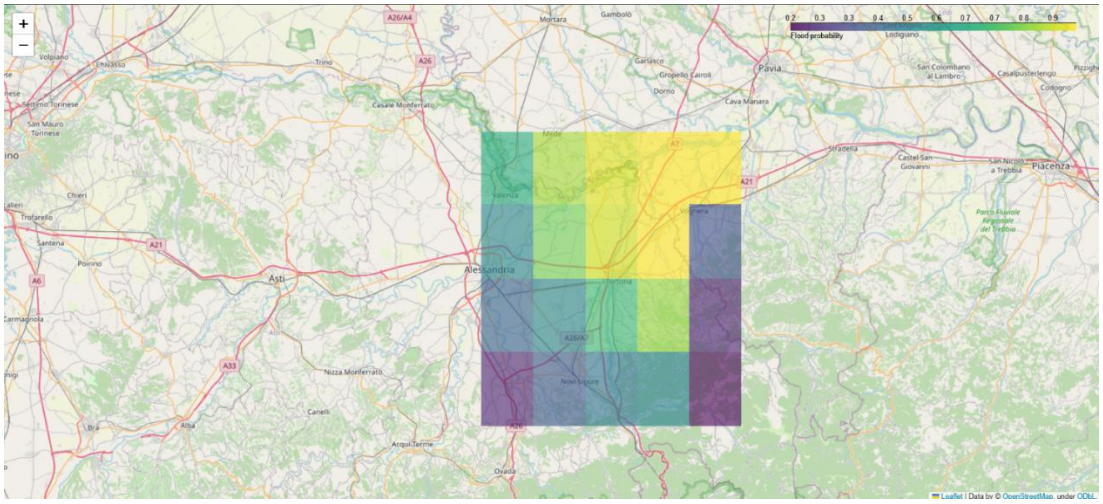

Figure 5-65: Tortona-Voghera AOI: map of probability of occurrence of a flood event generated with the AI algorithm from the climatological period (2000-2024) adjusted for future projection dataset. Return period of 200 years dataset.

5.7.2. Impact of climate change on precipitation

The flood risk assessment is conducted considering the impact of climate change on precipitation. This impact is based on the Representative Concentration Pathways (RCP) defined by the *Intergovernmental Panel on Climate Change* (IPCC). Each RCP is associated with a specific radiative forcing level and a corresponding trajectory of greenhouse gas concentrations. Climate change scenarios include RCP2.6, RCP4.5, RCP6, and RCP8.5, with RCP8.5 being the worst-case scenario. For analysing the impact of climate change on precipitation in the Novara and Tortona regions, the following steps have been carried out:

- First, historical precipitation data from gauging stations is analysed.
- Secondly, models that project[1] precipitation data based on climate change scenarios are compared to identify which provides the information sought.
- Future precipitation projections under different climate change scenarios from these models are evaluated, and a ratio of future to historic precipitation is calculated.
- A weighting score is given to each model's ratio to emphasise how well it represents local precipitation, which allows for calculating future precipitation at local levels.

The projection of precipitations was conducted using two datasets. The first one projected **maximum values** from recordings, while the second projected precipitations associated with a **return period of 200 years**.

[1] Projection refers to the forecast of precipitation based on specific greenhouse gas emission scenarios.

5.7.2.1. Analysis of monitored data (recordings)

Historic data from 12 gauging stations have been used in the analysis of the Novara region and 6 in the analysis of the Tortona region. Figure 5-66, Figure 5-67 illustrates the area of interest (AOI, in orange), the rail track (in green), and the locations of these gauging stations (in blue). Some stations began recording as early as 1988, while others started in 2015. However, all stations have continuously recorded precipitation since their installation. The recorded maximum daily precipitation for each gauging station throughout the observation period is illustrated in Figure 5-68.

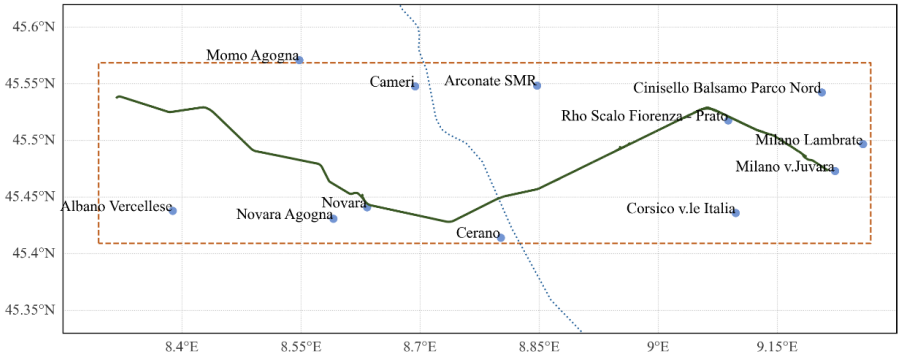

Figure 5-66: Location of gauging stations in Novara.

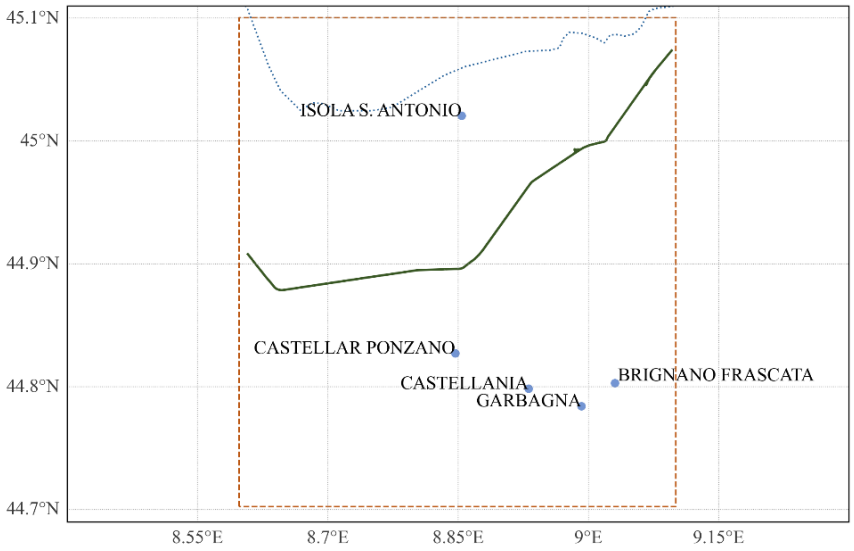

Figure 5-67: Location of gauging stations in Tortona.

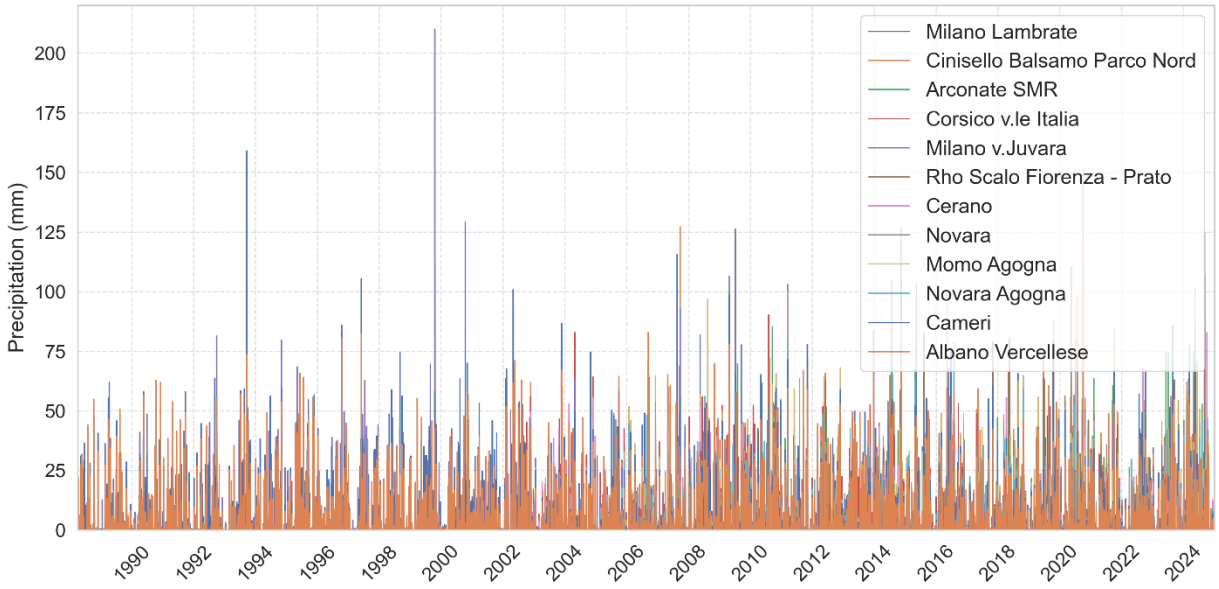

Figure 5-68: Recorded maximum daily precipitation at each gauging station (Novara region).

5.7.2.2. Comparison of models that project precipitation data

The effect of greenhouse gas emissions on climate is projected using Global Circulation Models (GCMs). These models simulate the behaviour of the Earth's climate system on a global scale. However, they operate at coarse spatial resolutions due to computational constraints. To increase the spatial resolution of projections, Regional Climate Models (RCMs) are employed, which operate only on specific regions. These models use GCM data as boundary conditions and downscale global climate information to regional levels. Advanced RCM data is provided by the *Coordinated Regional Downscaling Experiment* (CORDEX), a programme which evaluates and improves downscaling techniques (CORDEX, 2018).

Three models available at the *Climate Data Store*[2] have been examined to define which is most suitable for conducting the flood risk assessment. These include:

- *CMIP6 climate projections* (Copernicus Climate Change Service & Climate Data Store, 2021),
- *CORDEX regional climate model data on single levels* (Copernicus Climate Change Service & Climate Data Store, 2019), and
- *Gridded monthly climate projection dataset underpinning the IPCC AR6 Interactive Atlas* (Copernicus Climate Change Service (C3S), 2023).

The CMIP6 climate projections dataset provides mean daily and monthly precipitation projections, as illustrated in Figure 5-69.
However, since this dataset comes from a GCM, its suitability is questioned due to its coarse spatial resolution.

[2] https://cds.climate.copernicus.eu/

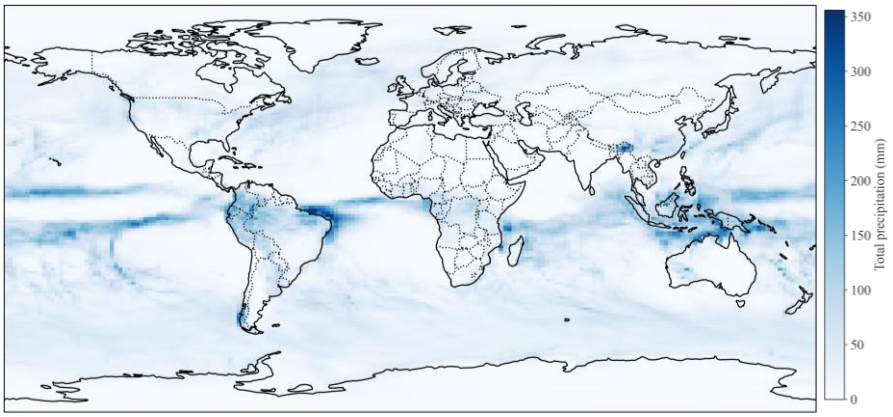

Figure 5-69: Global precipitation illustration for a specific time frame

The *CORDEX regional climate model data on single levels* and the *Gridded monthly climate projection dataset underpinning the IPCC AR6 Interactive Atlas* provide RCM data, both using CORDEX. The first one offers mean precipitation flux with resolutions of 3h, 6h, daily, monthly, and seasonal, while the second provides the monthly maximum of 1-day accumulated precipitation. Projections from the *Gridded* dataset were used for the flood risk assessment, as precipitation is given in millimetres, and the data is more manageable.

5.7.2.3. Analysis of projected precipitation data (numerical)

Numerical models project future precipitation based on the RCP2.6, RCP4.5, and RCP8.5 climate change scenarios. Each of those provide a monthly maximum daily precipitation value from 2006 to 2100. The number of models used within CORDEX vary depending on the climate change scenario: 18 are employed for RCP2.6, 21 for RCP4.5, and 48 for RCP8.5.

Data from models have been used to compute future-to-historic ratios. These ratios provide information about the impact of climate change on precipitation and are used to project precipitation at local levels.

Figure 5-70 illustrates precipitation data for a given model along the area of interest (shown in orange). Based on its spatial resolution, the AOI fell within four sections of the model, named from ID1 to ID4. Therefore, four different ratios were calculated.

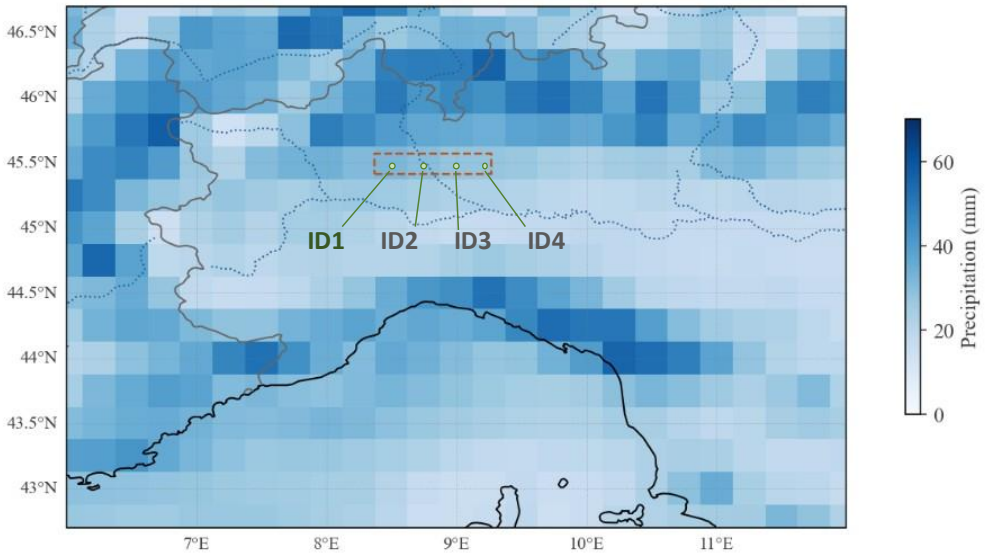

Figure 5-70: Area of Interest coverage on RCM data (Novara region)

Each model provides numerical precipitation data for the RCP2.6, RCP4.5, and RCP8.5 scenarios. Figure 5-71 illustrates the distribution of monthly maximum daily precipitation in section ID1 for the RCP2.6 scenario. As shown in the figure, models estimate distinct magnitudes for the same climate change scenario and location. Consequently, an accuracy analysis of models has been performed to evaluate their precision locally.

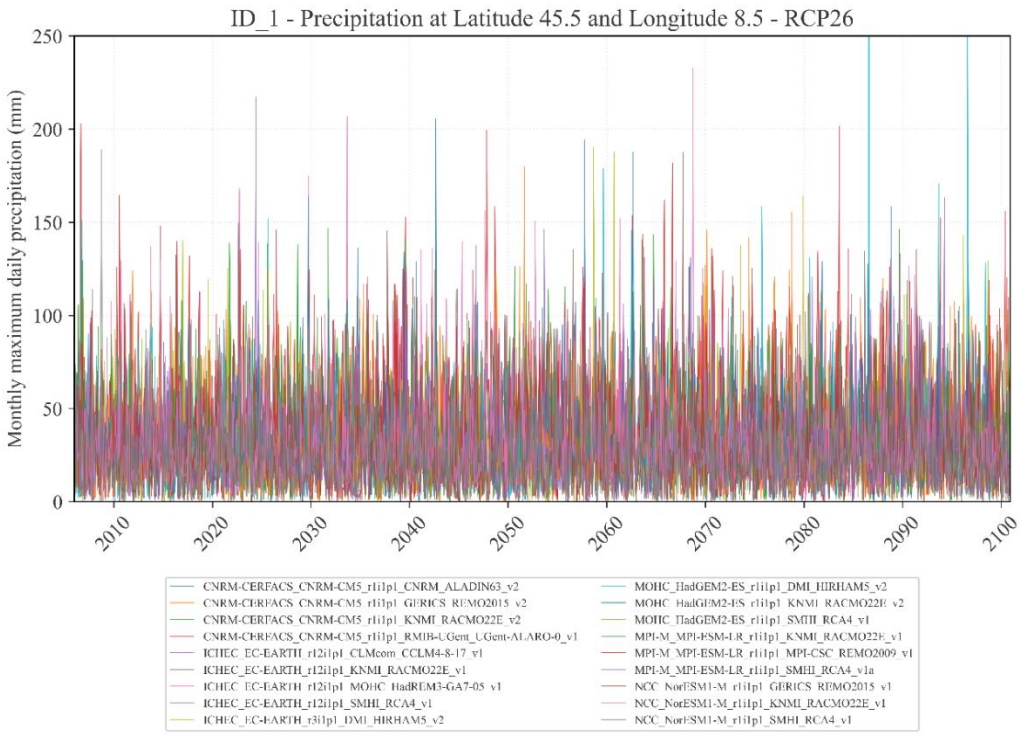

Figure 5-71: Distribution of monthly maximum daily precipitation for the historic scenario (Novara region).

The accuracy analysis compared statistical properties observed in each model with those observed in recordings from gauging stations. The analysis was limited to the period of years when both datasets coincided. Statistical properties, described in detail in *Appendix I*, included standard deviations, trend slopes, Pearson correlations (Schober, Boer, & Schwarte, 2018), and Kolmogorov-Smirnov (KS) statistic values (Lopes, 2011). *Table 5-7* summarises what these metrics measure and their symbology.

Metric	Measures and use	Symbology
Standard deviation	Variability relative to the mean.	SD
Trend slope	Direction of data change over time. Compares increasing/decreasing patterns across models.	T
Pearson correlation	Measures pattern alignment. Similarity in movement between historic & projected data.	P
KS statistic	Difference in distribution shapes. Checks if data distributions match.	KS

Table 5-7: Metrics used for the accuracy analysis.

The accuracy of each model was evaluated through a scoring system based on these metrics.

$$S_i = \alpha_{SD} * SD + \alpha_T * T + \alpha_P * P + \alpha_{KS} * KD \qquad \textit{Equation 1}$$

Where the partial factors α_{SD}, α_T, α_P, and α_{KD} has been considered as 0.2, 0.25, 0.4, and 0.15 respectively. The Pearson correlation (P) receives the highest weight in the scoring system, 40%, as it measures the linear relationship between the model and observations, ensuring that values closely follow trends. The trend slope (T) is the second most important metric, 25%, since it captures the long-term trend, guaranteeing that the rate of change in the model aligns with observations. Standard deviation (SD) (20%) reflects the variability of the data, ensuring the model captures fluctuations and dispersion. Lastly, the Kolmogorov-Smirnov statistic (KS) has the lowest weight, 15%, as it assesses the overall distribution similarity but does not emphasise temporal or trend-based accuracy as strongly as the other metrics.

Models with smaller statistical deviations from the historic data will therefore have values close to 1, while models with larger deviations will have values close to 0. Once the score of each model has been calculated, it is used to assign a corresponding weight to each model, reflecting its relative accuracy. *Table 5-8* summarises the calculated scores and weights of each model used to project precipitation data. Models that represent statistical properties more closely aligned with the historic data are highlighted in green, while those with lesser similarities are shown in purple.

For the analysed region, models based on MPI-M[3] provide better estimates, followed by NCC. The lowest similarities were observed using models based on MOHC, CNRM, and ICHEC.

Model	Score	Weight
CNRM-CERFACS_CNRM-CM5_r1i1p1_CNRM_ALADIN63_v2	0.254	0.052
CNRM-CERFACS_CNRM-CM5_r1i1p1_KNMI_RACMO22E_v2	0.389	0.080
CNRM-CERFACS_CNRM-CM5_r1i1p1_RMIB-UGent_UGent-ALARO-0_v1	0.324	0.066
ICHEC_EC-EARTH_r12i1p1_CLMcom_CCLM4-8-17_v1	0.217	0.045
ICHEC_EC-EARTH_r12i1p1_KNMI_RACMO22E_v1	0.261	0.054
ICHEC_EC-EARTH_r12i1p1_SMHI_RCA4_v1	0.280	0.057
ICHEC_EC-EARTH_r3i1p1_DMI_HIRHAM5_v2	0.332	0.068
MOHC_HadGEM2-ES_r1i1p1_DMI_HIRHAM5_v2	0.365	0.075
MOHC_HadGEM2-ES_r1i1p1_KNMI_RACMO22E_v2	0.341	0.070
MOHC_HadGEM2-ES_r1i1p1_SMHI_RCA4_v1	0.299	0.061
MPI-M_MPI-ESM-LR_r1i1p1_MPI-CSC_REMO2009_v1	0.430	0.088
MPI-M_MPI-ESM-LR_r1i1p1_SMHI_RCA4_v1a	0.528	0.108
NCC_NorESM1-M_r1i1p1_GERICS_REMO2015_v1	0.481	0.099
NCC_NorESM1-M_r1i1p1_SMHI_RCA4_v1	0.367	0.075

Table 5-8: Metric results used in the accuracy analysis (Novara region).

5.7.2.4. Future-to-historic ratios (numerical)

Future-to-historic ratios are used to feature the effects of climate change on precipitation. These ratios are calculated by dividing the future by the historic precipitation simulated by models for each RCP; see *Equation* ***2***. Ratios above 1 indicate an increase in precipitation over time, while ratios below 1 indicate a decrease. These ratios also indicate the magnitude of change; for example, a ratio of 1.4 indicates a 40% increase, while a ratio of 0.8 indicates a 20% reduction.

$$\alpha_i = \frac{Future\ precipitation}{Historical\ precipitation} \qquad \textit{Equation 2}$$

Figure 5-72 shows ratios calculated for section ID1 according to models for the RCP 2.6, 4.5 and 8.5 scenarios. It can be observed that models based on CNRM project an increase in precipitation, as well as those based on MOHC, with the latter's increase being more pronounced. However, models based on ICHEC, MPI-M, and NCC project a reduction in precipitation for the RCP 8.5 scenario. This variability highlights the need for evaluating the accuracy of each model compared to historic data, as performed in *Section 5.7.2.3*, to calculate a resulting ratio.

[3] These terminologies refer to Global Circulation Models (GCM)

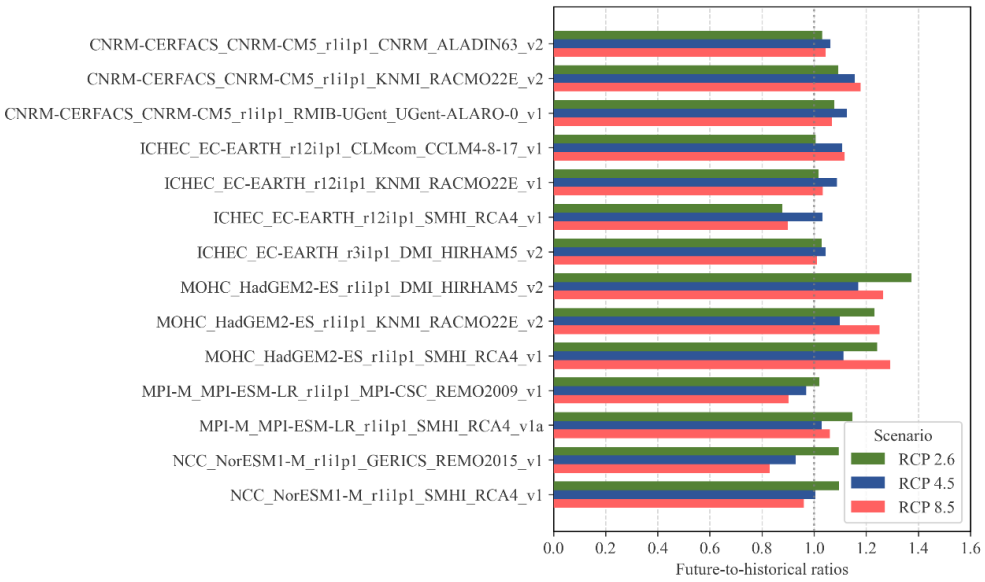

Figure 5-72: Ratios calculated on ID-1 for each model and climate change scenario (Novara region).

A resulting ratio was computed by considering the individual ratios estimated by models and their associated weight score (see *Table 5-8*).

$$Ratio = \sum Ratio_{RCM} * Weight_{RCM} \qquad \textit{Equation 3}$$

Table 5-9 to *Table 5-12* summarise, for each region, the resulting ratios for the RCP 2.6, 4.5 and 8.5 scenarios, after considering and applying the weighting score of models.

Section	RCP 2.6	RCP 4.5	RCP 8.5
ID1	1.10	1.07	1.08
ID2	1.10	1.08	1.10
ID3	1.10	1.07	1.09
ID4	1.10	1.07	1.09

Table 5-9: Resulting ratios by climate change scenario for the Novara region.

Section	RCP 2.6	RCP 4.5	RCP 8.5
ID1	1.20	1.17	1.18
ID2	1.17	1.15	1.17
ID3	1.20	1.18	1.20
ID4	1.20	1.16	1.19

Table 5-10: Resulting ratios by climate change scenario for the Tortona region.

Section	RCP 2.6	RCP 4.5	RCP 8.5
ID1	1.14	1.23	1.24
ID2	1.11	1.19	1.31
ID3	1.08	1.12	1.21
ID4	1.16	1.20	1.32

Table 5-11: Resulting ratios by climate change scenario for the Novara region – 200 years return period.

Section	RCP 2.6	RCP 4.5	RCP 8.5
ID1	1.04	1.16	1.22
ID2	0.99	1.13	1.18
ID3	1.10	1.16	1.28
ID4	0.97	1.08	1.23

Table 5-12: Resulting ratios by climate change scenario for the Tortona region – 200 years return period.

5.7.2.5. Future precipitations for the flood risk assessment

The flood risk assessment uses precipitations accounting for the impact of climate change. Future precipitation is provided based on two different datasets; based on **maximum values** and **a return period of 200 years**. Ratios accounting for the effects of climate change calculated in the previous sections are used to project precipitation data.

Based on maximum values: The worst-case scenario among the analysed is used to embrace all variations in climate data. Therefore, ratios for the long-term time frame and RCP 2.6 scenario were used for the Novara and Tortona regions. *Table 5-13* and *Table 5-14* summarise future precipitation based on historical data considering the effects of climate change for each region.

Section	Precipitation	Section	Precipitation
ID1	141	ID11	132
ID2	134	ID12	133
ID3	128	ID13	134
ID4	121	ID14	128
ID5	110	ID15	112
ID6	99	ID16	109
ID7	96	ID17	106
ID8	91	ID18	99
ID9	93	ID19	102
ID10	96	ID20	106

Table 5-13: Future precipitation (mm) at the Novara region.

Section	Precipitation	Section	Precipitation
ID1	133	ID11	104
ID2	134	ID12	102
ID3	133	ID13	102
ID4	131	ID14	103
ID5	127	ID15	105
ID6	118	ID16	120
ID7	119	ID17	109
ID8	118	ID18	110
ID9	118	ID19	113
ID10	118	ID20	106

Table 5-14: Future precipitation (mm) at the Tortona region.

Based on a return period of 200 years: The same approach has been employed to calculate the future precipitation based on a return period of 200 years. *Table 5-15* and *Table 5-16* summarise the future precipitation based on this approach for each region.

Section	Precipitation	Section	Precipitation
ID1	208	ID11	168
ID2	186	ID12	160
ID3	174	ID13	157
ID4	177	ID14	165
ID5	167	ID15	159
ID6	152	ID16	149
ID7	149	ID17	152
ID8	146	ID18	145
ID9	147	ID19	150
ID10	139	ID20	142

Table 5-15: Future precipitation (mm) at the Novara region – 200 years return period.

Section	Precipitation	Section	Precipitation
ID1	127	ID11	137
ID2	118	ID12	129
ID3	112	ID13	124
ID4	106	ID14	118
ID5	103	ID15	114
ID6	127	ID16	148
ID7	119	ID17	139
ID8	113	ID18	135
ID9	105	ID19	131
ID10	101	ID20	129

Table 5-16: Future precipitation (mm) at the Tortona region – 200 years return period.

5.7.3. Conclusions

A monitoring and forecasting tool based on the collection and analysis of satellite available data of sensitive "*climate*" variables, specifically precipitation, soil moisture, Land Surface Temperature (LST) and Land Cover (LC), is proposed and developed. To this purpose, the analysis time ranged from January 2000 to December 2024 (being this year the last one to provide a complete series of data) was considered. The 24 years taken into consideration can be referred as *climatological period* for the developed analyses, providing proper detail to define and monitor precipitation intensity and variability. Within the considered *climatological period*, for each year the main flooding events happened in the tested areas were identified and according to the availability of data the information related to the previous 3 days of were also considered. On the basis of the collected data, a Neural Network (NN) model was trained. Particularly, a fully connected NN was developed to correlate the considered parameters, i.e., precipitation, soil moisture, LST, and LC, with the extreme meteorological events. Its validation was carried out evaluating the results obtained by applying the algorithm to flooding events, occurred in the AOIs, during the year 2025, which information is not included in the input training dataset. The outputs of the developed NN are maps of probability of occurrence (with a 3-day pre-warning) of a flood event, in a specific area of interest. Then, given a pair of precipitation and soil moisture values, the proposed NN provides the probability that an extreme flood event occurs in the AoI in three days. Through the developed NN, maps of probability of occurrence of a flood event on the basis on the precipitation expected by 2100 were also generated in order to evaluate the impact of climate change.

A railway line, classified according to the relevant assets (e.g. embankment, trench, bridge,...), can be thus superimposed on the maps generated through the methodology above proposed and described in order to identify the most critical and vulnerable sections to an imminent flood event (with a certain probability of occurrence and three days' notice) and then to better manage and prevent any emergencies.

The impact of climate change on precipitation was evaluated using climate models, which project future precipitation based on CO_2 emissions. Outputs from climate models were compared with historical data to perform an accuracy analysis based on standard deviations, trend slopes, Pearson correlations, and Kolmogorov-Smirnov (KS) statistic values to assign an accuracy score. Based on the projection of each model and the accuracy score, a unique future-to-historic ratio was computed in each region. Results showed that the maximum precipitation in one day is expected to increase by 32% in the Novara region and 28% in the Tortona region for a 200-year return period precipitation.

5.8. Web Platform for multiscale monitoring

The Web platform for multiscale monitoring is designed to be a strategic tool for the collection, analysis, and visualization of territorial and environmental data related to railway infrastructures and surrounding areas. The solution is designed to develop an integrated system for managing the flow of information from various sources (e.g. ground & airborne sensors, field surveys, open datasets) and supports complex analyses at multiple spatial scales. Thus, enabling:

- Monitoring of environmental conditions near railway lines.
- Identification of territorial interdependencies and critical events.
- Support for decision-making.
- Data consultation, management, and publication through web interfaces and RESTful APIs.

The platform enables the management of both graphical and alphanumeric territorial databases, accessible via Internet or Intranet. An interactive interface allows users to easily navigate through geographic and thematic data. A key feature is the ability to configure and display multiple thematic layers, integrating various territorial datasets to highlight spatial interdependencies, promote multidisciplinary integration, and enhance decision-making processes.

Through an intuitive interface, FP3-IAM4RAIL project stakeholders (public authorities, railway operators, technicians, citizens) can access thematic information, explore interactive maps, and contribute to collaborative territorial management in line with an intelligent asset management approach.

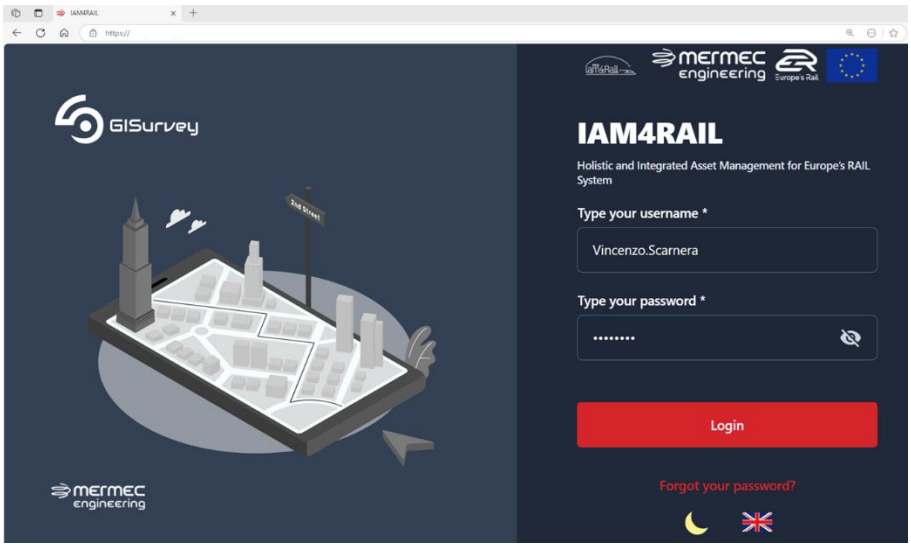

Figure 5-73: Accessing securely the web platform (https login page).

The web application is a complex system of IT components designed to manage a large amount of multidisciplinary data, referenced to geographic coordinates and stored in various formats. Its primary goal is to create a flexible and technologically advanced tool that enables the organization to quickly manage and access available data and strategically plan actions and interventions within its institutional role.

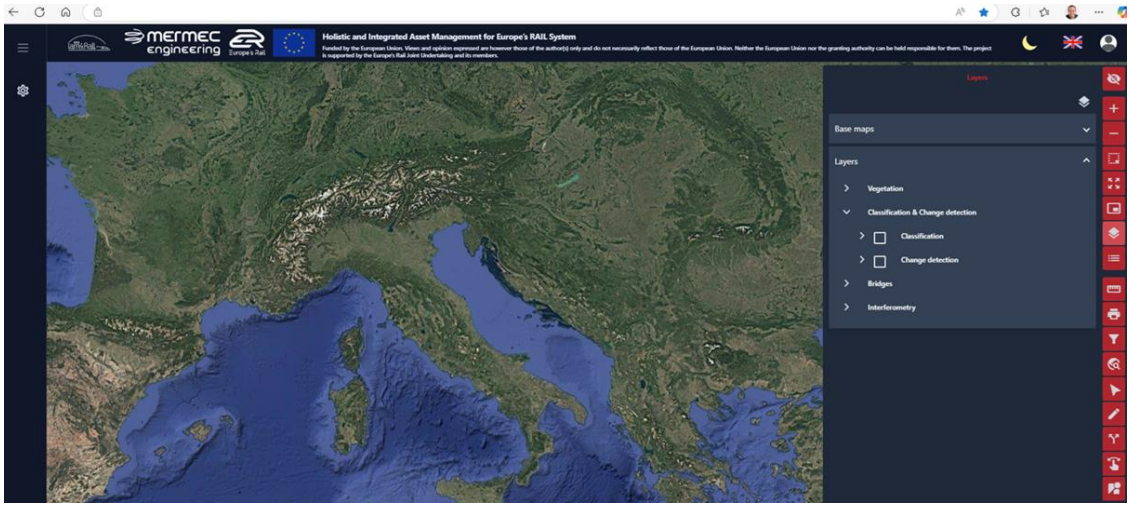

Figure 5-74: Interactive map.

Specifically, the customization of the platform for real-time monitoring allows the collection of different types of information into a single synoptical interface. When projected onto a cartographic solution, this can enable specific territorial analysis, immediate interventions, and strategic decision-making. The solution is designed to provide a centralized view of the database and to ensure maximum robustness, consistency, and availability of information.

The implementation of territorial databases can play a strategic role in decision-making processes related to land management and governance at local, regional, and national levels. To make this infrastructure usable, a web based platform will be provided, offering a centralized map-based view of the information and the ability to overlay multiple data layers.

5.8.1. Functionalities of the platform

User Access & Role Management: Enables role-based access control, allowing administrators to define permissions for different user roles (e.g., administrator, operator, viewer). This ensures secure and controlled handling of data while maintaining operational efficiency.
Custom Data Visualization: Provides tailored data visualization based on users' roles. This feature not only ensures the protection of sensitive information but also delivers relevant insights to aid informed decision-making.
Data Collection: Facilitates the collection of data, which can be visualized and exported in standard formats such as JSON, CSV, and XML. These formats support advanced data analysis and easy integration with external tools.
Advanced Graphical & Statistical Reporting: Includes robust tools for generating detailed reports and interactive dashboards that feature visual representations of data, empowering users to analyze trends and statistics effectively.
Advanced Map Tools includes:

- **Overview Map**: Displays the exact location and geographic extent of the viewed map portion within the overall reference territory.
- **Pan**: Enables interactive map dragging using a left mouse click and hold.

Zoom Functions: Provides tools to dynamically change the viewing scale.
Measure Distances, Perimeters, and Areas: Allows users to perform linear (distance) and polygonal (area) measurements. The system provides the total length or the perimeter and area of the polygon, even if virtually closed. Results can be converted into various units.
Print: Accesses print functionality with customizable parameters such as scale and title; predefined standard print layouts are available within the system.
Search: Facilitates search (with map highlighting) across various thematic layers, including the use of complex search conditions.
Reference System Management: Permits changing the display reference system with the re-projection of all data; also enables coordinate conversion between systems.
Add WMS Services: Supports adding WMS layers from any OGC-compliant map server to enhance the knowledge base with new data.
Scale Bar: Indicates the current map scale.
Coordinate Conversion Tool: Converts coordinates between the application's reference system and other known systems.
Base Layer Manager: Provides options for selecting background base maps and thematic reference layers, as well as reordering and adjusting transparency levels.

To ensure the correct functioning of the described features, the system meets the following technical requirements:

- **Data Hosting**: Secure infrastructure guaranteed throughout the project.
- **GIS Data Support**: Integrates GIS functions for accurate user analysis.
- **Interoperability**: Exports data in line with European Open Data standards.
- **Scalability & Reliability**: The platform is engineered for continuous operation, featuring an infrastructure capable of scaling to accommodate a growing user base and data volume.

The proposed solution is based on a typical multi-tier architecture with the following layers:

- Presentation Layer: This is the user-facing layer, adapted to the device and channel in use, and handles layout structuring for the end user. It is responsible for rendering the view of a specific function for a specific user.
- Service Layer: This layer executes the business logic, implementing function, process, and interaction logic. It includes application components that expose functionalities as services, both for internal architecture levels (data access services and services used by interfaces) and for external systems.
- Data Layer: This layer handles data retrieval and storage, implementing access logic for local or remote data sources.

The front-end application is hosted on an Apache web server. For front-end interface development, JavaScript frameworks such as Angular and OpenLayers (for Web GIS components) have been used. The front end communicates with the back end via HTTP, using JSON/GEOJSON as the data interchange format. The back end contains all business logic components implementing the features of the application solution. Its development is based on the open-

source Node.js framework, which allows JavaScript—typically a client-side language—to also be used server-side. One of the main back-end components is the entity management module, which abstracts the data layer (non-geographic) in the central system architecture, offering an object-oriented representation of domain data and database management system (DBMS) abstraction, ensuring full independence of application functions from the RDBMS.

At the heart of the solution lies the cartographic services module, which provides users with a user-friendly web interface to monitor ongoing activities across the territory. The Map Server used in this project is GeoServer, which allows for the distribution, manipulation, and analysis of data using the most common OGC standards (WMS, WFS, WCS, WPS), while also supporting extensions for transparent interaction with clients such as Google Earth and other commercial software, as well as widely adopted REST and GeoJSON protocols for simplified vector data distribution.

The PostgreSQL open-source DBMS engine is used for database implementation due to its robustness, performance, and scalability. Vector-based cartographic data is also stored in PostgreSQL using the PostGIS spatial extension, which seamlessly integrates with PostgreSQL, introducing geometric data types and spatial functions. PostGIS is considered the most mature open-source spatial extension and adheres to OGC standards, ensuring efficient information exchange between applications and simplified geospatial data

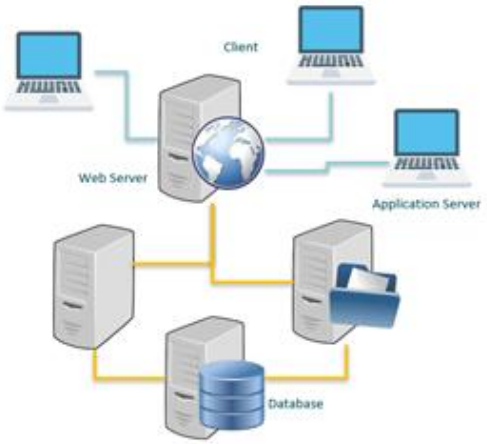

Figure 5-75. Solution Architecture.

5.8.2. Visualisation Layers

The image below shows a view of the user interface. This is designed to provide an intuitive and interactive experience, allowing users to easily activate, configure, and analyse the available information layers. In particular, the layer control panel allows users to manage the visualization of spatial data through selection checkboxes, transparency sliders, and dedicated navigation tools.

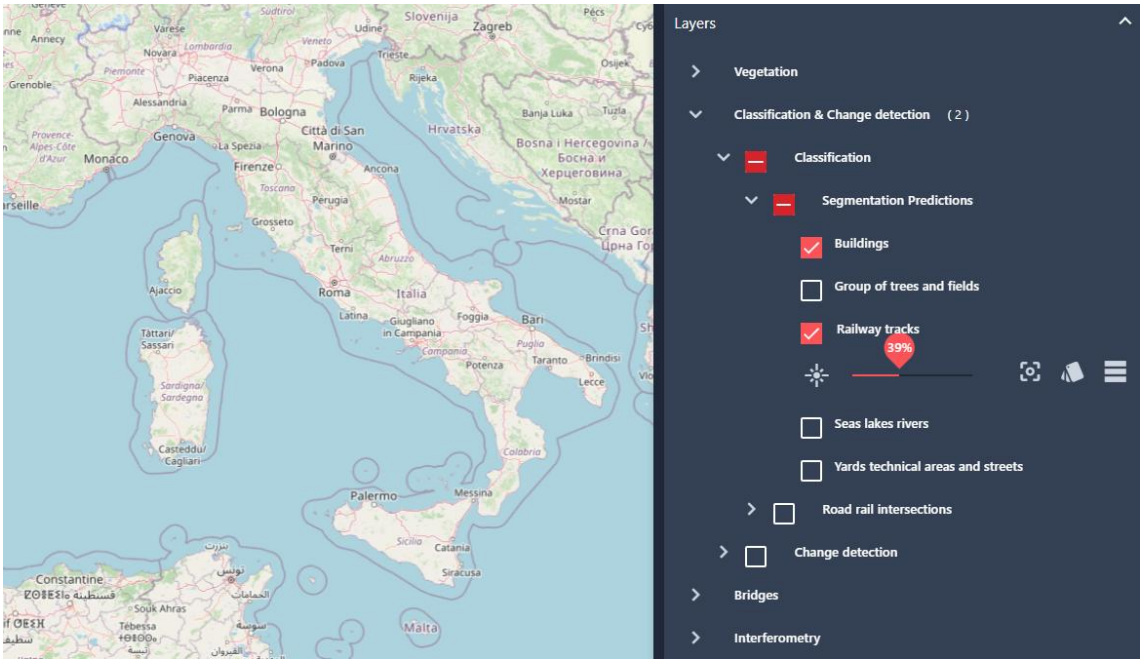

Figure 5-76:FP3- IAM4RAIL Web platform layers.

Operatively, layer visualization is managed through checkboxes (a white square, possibly with a graphic symbol overlaid) next to the layer's descriptive title. A checked checkbox indicates that the layer is visible on the map. For layers with display settings limited to certain scales, this information is shown in parentheses. An empty checkbox (no overlaid graphic symbol) indicates a layer that is not currently displayed on the map but can be made visible.
By clicking on the layer name, a box appears at the bottom of the screen where the user can adjust the transparency of the selected layer using a slider and, if enabled, view the information related to the layer itself. Additionally, the "Center on extent" button shifts the map to the geographical extent of the layer.

5.8.2.1. Vegetation encroachment

In the web platform, it is possible to explore a raster layer of vegetation cover, which quantifies the presence and density of vegetation along and near the railway line.

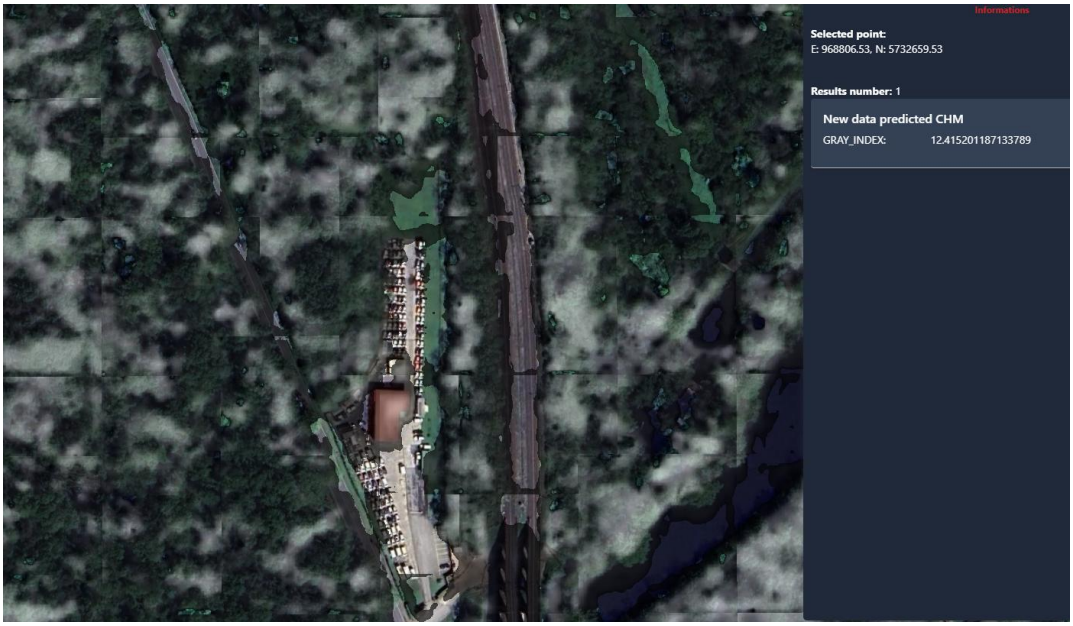

Figure 5-77: The raster layer of vegetation encroachment displayed with a different transparency value.

The image below shows the raster layer displayed with a different transparency value, highlighting how adjusting transparency can facilitate the overlay and combined analysis with other spatial data present on the map. By modifying the transparency, users can achieve better visual perception of the underlying information, thereby enhancing the understanding of the territorial context and the characteristics of the vegetation cover. A three 12.415meter tall is revealed by clicking on the map (calculated via AI in section 5.2)

5.8.2.2. Bridge platform

In the web platform, it is possible to visualize layers related to railway bridge platforms, including georeferenced data on the structures and their maintenance status. These layers enable monitoring of the location, characteristics, and any critical issues of the infrastructure, supporting inspection activities and intervention planning.

The web platform integrates a 3D module enabling rigorous and fast management of digital twins (bridges acquired using UAV technology), addressing the challenges of heritage knowledge, information management, and technologies for the temporal planning of interventions. It ensures and optimizes the exchange of data between the virtual and physical components.

When clicking on a project marker, access will be granted, the view will zoom into the relevant area, all available assets and associated photos will be displayed, and the side menu will offer additional options.

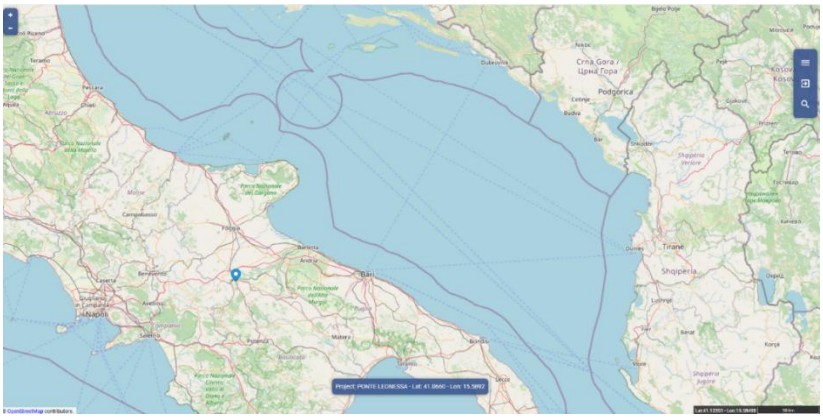

Figure 5-78: 3d module interface

By clicking on the marker, you can access the view of the drone-captured photos (white squares with colored borders represent rectangular photos). By clicking on one of them, you will enter the 3D visualization of the entire infrastructure (railway bridge), with a geolocated view that corresponds to the selected photo.

Figure 5-79: UAV photo viewing interface.

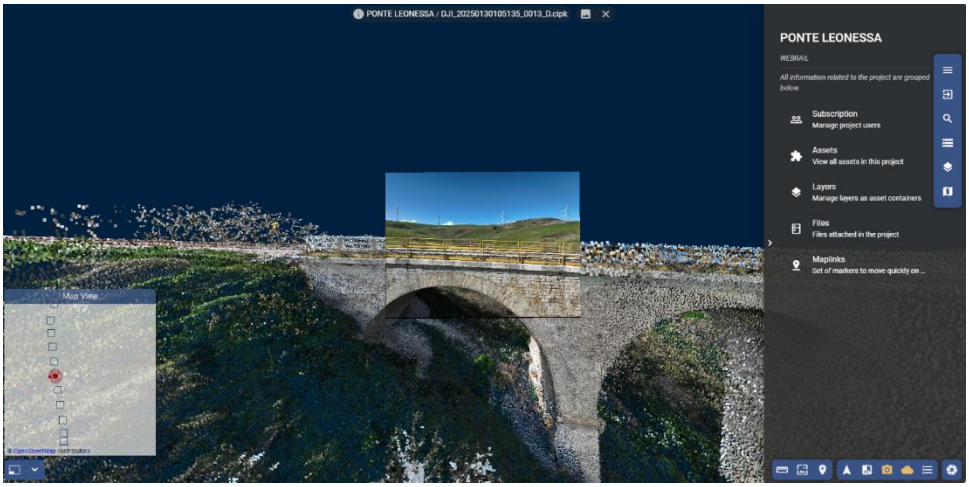

Figure 5-80: Overlay between UAV photos and visualization of the entire bridge in a point cloud.

The 3D environment interface includes:

- **Project Information** (at the top center): displays key details about the current project.
- **Content Menu** (on the right): contains controls for all application functionalities, organized by thematic area.
- **Action Menu** (at the bottom right).
- **2D Map** (at the bottom left).

Below are some of the most significant features:

Coordinates retrieval of a point in 3D space by left-clicking on the point cloud.

Figure 5-81: Measuring a point from the point cloud

Measure of the distance between two or more points.

Figure 5-82: Linear measurement of a part of a bridge reconstructed with the point cloud

Angular measurements.

Figure 5-83: Angular measurement of a bridge part reconstructed with the point cloud.

Area measurements.

Figure 5-84: Area measurement of a part of the bridge reconstructed with the point cloud.

Possibility to highlight a vertical profile on the point cloud and export it.

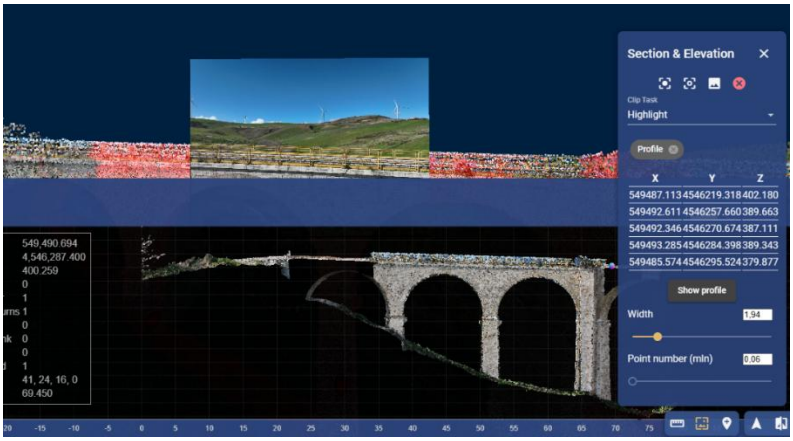

Figure 5-85: Section of part of the bridge reconstructed with point cloud.

5.8.2.3. Classification & Change detection

Land classification and change detection are essential for monitoring transformations in railway areas. The platform provides layers representing different land cover classes (vegetation, buildings, artificial surfaces, water bodies) and temporal changes obtained through analysis of multispectral satellite images and machine learning techniques.

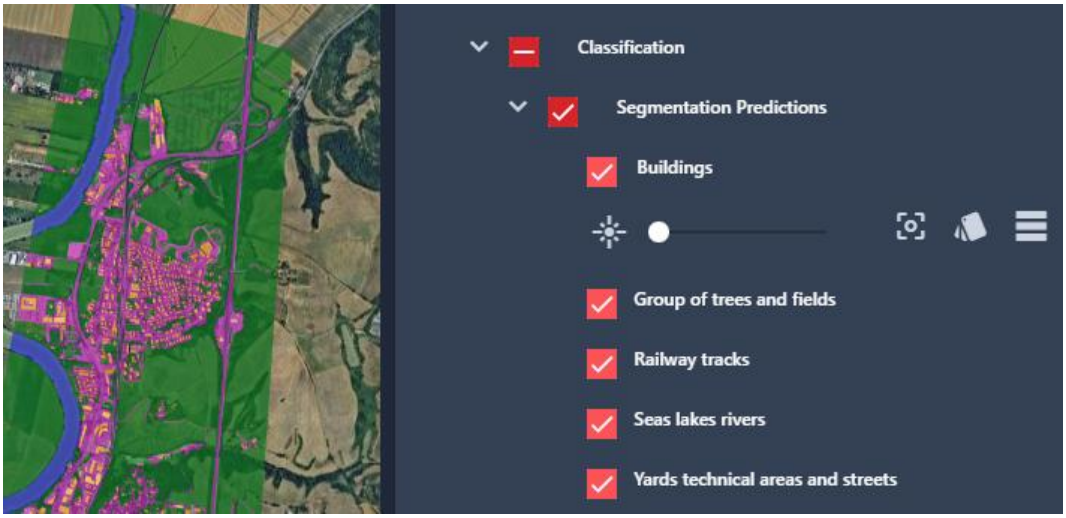

Figure 5-86: View of layers representing the different land cover classes.

Users can activate these layers, adjust their transparency, and focus on areas of interest using the navigation tools.

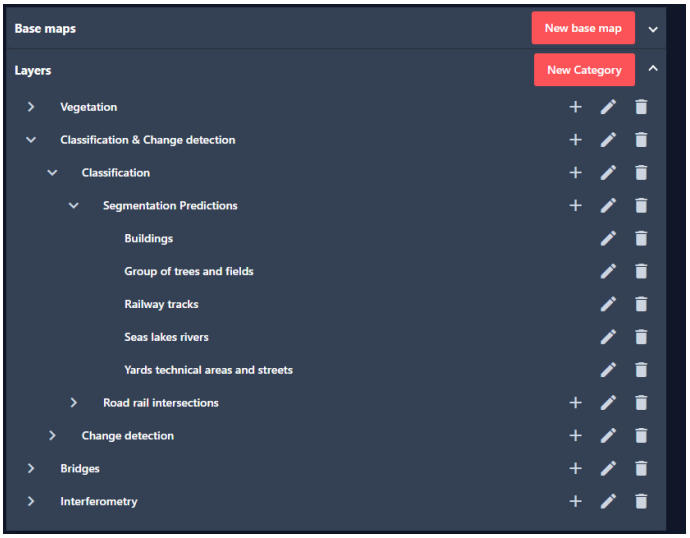

Figure 5-87: Layer style customization panel

For each of the different land cover classes included in the classification and change detection layer, users have the option to customize the layer's style by changing the colors according to their preferences or visualization needs. Additionally, it is possible to view the attribute table associated with the layer by clicking the corresponding buttons, allowing for a more detailed analysis of the

data and the characteristics of each class.

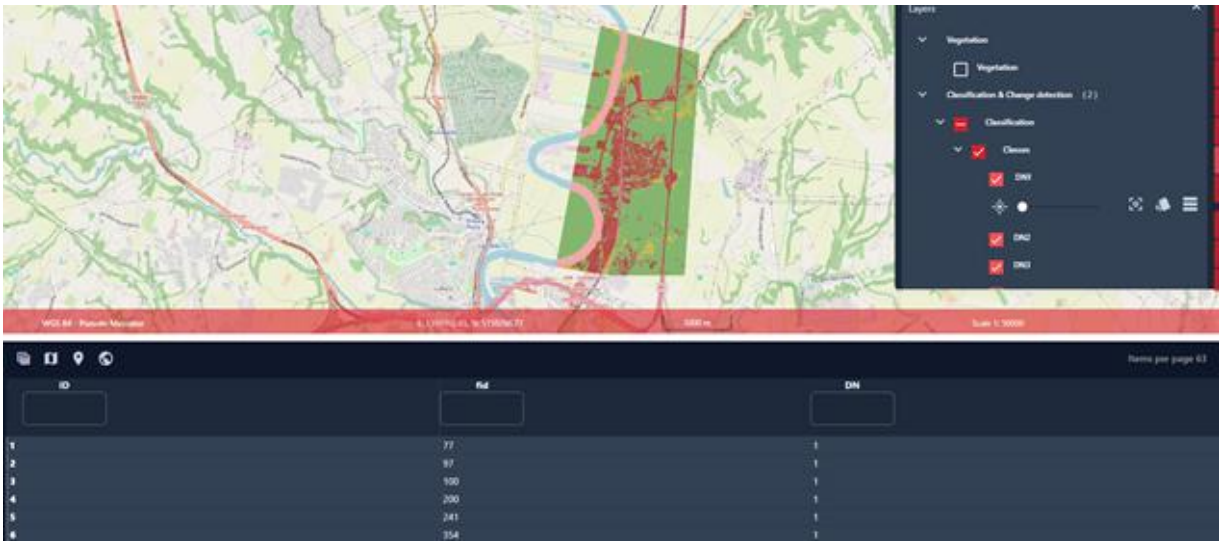

Figure 5-88: The attribute table of layer.

Within the classification and change detection layer, specific intersection points between roads and the railway network have been identified and mapped. These points represent critical areas for safety and traffic management and are highlighted in the WebGIS to facilitate monitoring and analysis. The ability to view and query these points enables the assessment of potential risks, planning of maintenance interventions, and improvement of connected infrastructure management.

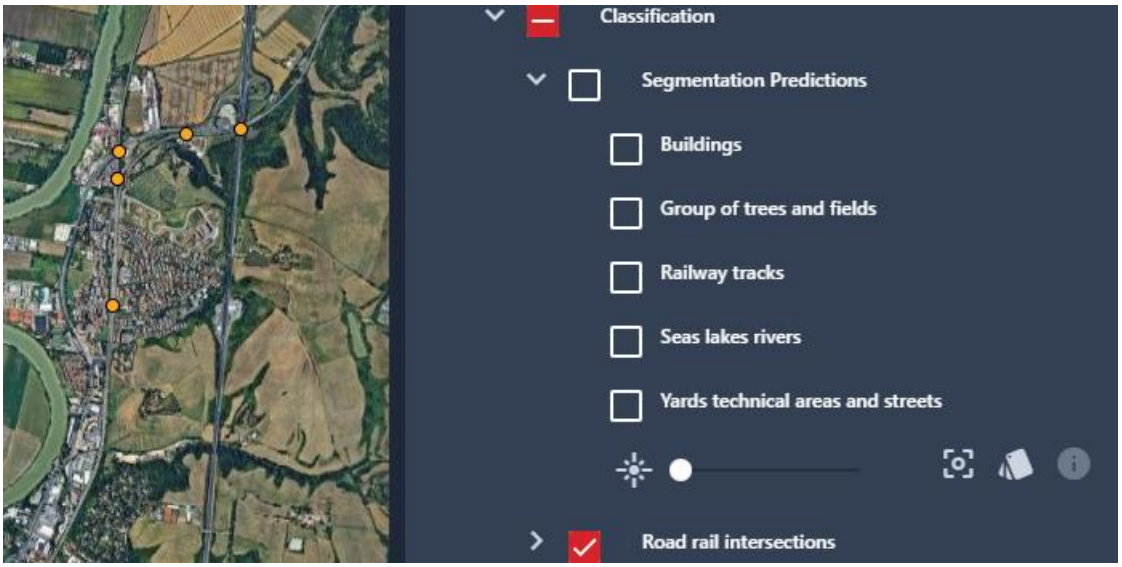

Figure 5-89: Road-rail intersection layer visualization.

5.8.2.4. Interferometry

Interferometric SAR (InSAR) data enables the detection of millimeter-scale ground displacements by comparing the phase information of radar images acquired over the same area at different times. By analysing the differences in the returned radar signals, it is possible to detect subtle surface deformations caused by natural or anthropogenic processes such as earthquakes, volcanic activity, landslides, or subsidence. The web platform integrates data related to landslides and ground subsidence along railway routes. These layers contain information on risk areas, ground movements detected by satellite data. Users can visualize the extent of unstable zones, analyse their temporal evolution, and overlay these with railway infrastructure. Again, layer visualization is managed through checkboxes, transparency sliders, and navigation tools.

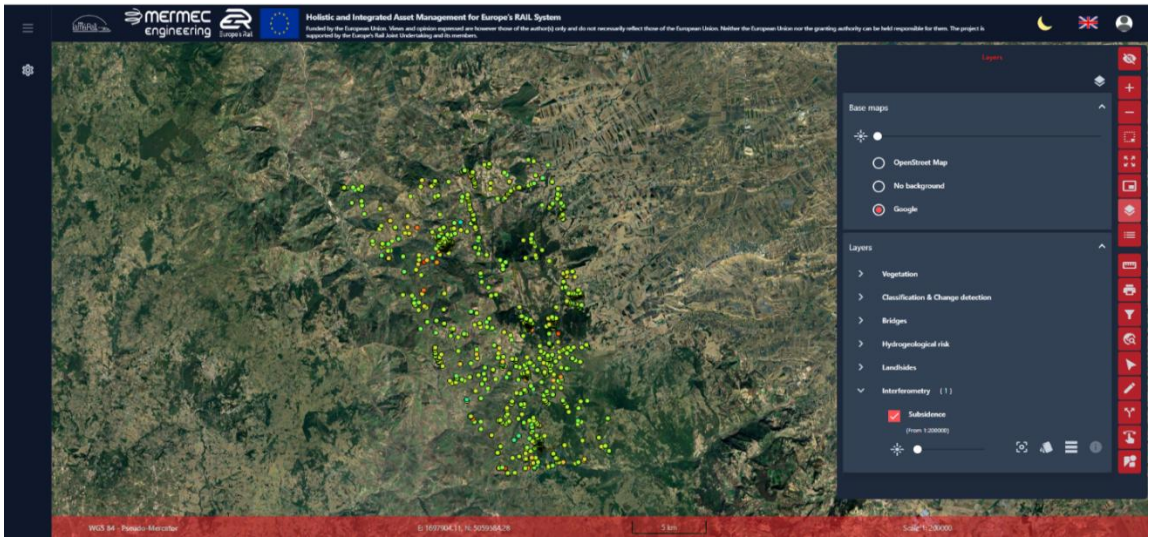

Figure 5-90: Interferometric SAR (InSAR) data layer.

Figure 5-91: Interferometric data legend.

Figure 5-92: InSar dat on Cerignola campagna. Millimetre-scale ground displacement chart.

5.8.3. Conclusion

The web platform developed in FP3-IAM4RAIL represents a significant step forward in the monitoring and management of railway infrastructure and the surrounding territory. One of its most successful features is the integration of heterogeneous environmental data from various sources (sensors, field surveys, aerial and satellite data), which are harmonized and made available in a single digital environment. This ability to aggregate, analyze, and visualize multidisciplinary information provides an unprecedented overview of the conditions of the territory and infrastructure, facilitating complex analyses and timely, informed decision-making.

The platform stands out as a multi-scale monitoring solution, as there are currently few or no systems with a comparable level of integration, interoperability, and flexibility. The ability to overlay multiple thematic layers, perform advanced analyses, and customize data visualization is a fundamental added value for all stakeholders involved, from public authorities to technical operators.

The FP3-IAM4RAIL platform establishes itself as an innovative and cutting-edge reference in the European landscape for multi-scale monitoring, laying a solid foundation for further technological developments to benefit the safety, sustainability, and resilience of railway infrastructures. As a key exploitable result of this work-package, this platform can be further developed by hosting data from other sensors (e.g. land sensors or data from diagnostic vehicles) and spanning across various regions of Europe.

6. Bridges and earthworks assets management aided by geotechnics (Use Case 13.2, Spain)

6.1. Introduction

This use case, “bridges and earthworks assets management aided by geotechnics”, brings together three critical demonstrators aimed at enhancing the management and safety of railway infrastructure in the face of structural and geotechnical challenges.

The first demonstrator focuses on the premature degradation of pot bearings in long-span railway bridges, particularly those exceeding 1000 meters. The study is focused on Huertas de Mateo viaduct (Bif. Torrejón de Velasco – Valencia Joaquín Sorolla at PK 285+486). This type of structures, often located in regions with high thermal gradients and subjected to high-speed rail traffic, experience complex dynamic interactions and significant relative displacements. These factors accelerate the deterioration of essential components like pot bearings, threatening the structural integrity and operational reliability of the bridges. The bridge is thereby analysed using operational modal analysis techniques (section 6.2.2) and with a degradation analysis focused on the pot bearings (section 6.2.3).

The second and third demonstrators address geotechnical instabilities that compromise railway safety and performance. At Tunnel No. 40 – Vilar de Silva, a historically unstable slope continues to pose risks due to persistent landslides driven by hydrological and geological conditions, affecting both the tunnel and track alignment. Similarly, the Briones slope along the Castejón–Bilbao line presents a high-risk scenario where saturated clay-rich soils trigger mass movements, undermining existing retaining structures. Together, these demonstrators provide a comprehensive framework for studying and mitigating the multifaceted risks facing critical railway assets, with the ultimate goal of informing more robust design, monitoring, and maintenance strategies.

6.2. Structural health monitoring and degradation models in bridges

6.2.1. Bridge Background Information

This study aims to analyse the behaviour of the bridge spanning the Barranco del Arroyo de las Huertas de Mateo (referred to in this work as the Huerta de Mateo bridge) through a monitoring system composed of triaxial accelerometers, displacement sensors, inclinometers, and temperature sensors. The bridge is located on the Madrid–Valencia high-speed rail line. UTM coordinates: X = 621,133; Y = 4,375,077. The structure under study is part of the construction works of the Minglanilla–Embalse de Contreras subsection, which belongs to the Gabaldón–Siete Aguas section of the Madrid–Castilla-La Mancha–Comunidad Valenciana–Región de Murcia High-Speed Line, as shown in Figure 6-1 (a).

The bridge structure is essentially a continuous prestressed reinforced concrete box girder with

23 spans, for a total length of 995 m, as shown in Figure 6-1 (b). It has no expansion joint, since regulations require such joints only for bridges longer than 1,000 m, which means this bridge undergoes significant axial movements due to temperature changes. The bridge bearings are of the Pot type, consisting of an elastomer (rubber) disc fully encapsulated within a steel "pot," as shown in Figure 6-1 (c). Due to the curvature of the bridge and trains passing at speeds exceeding 300 km/h, the bridge is subjected to high torsional stresses that can damage support elements such as the Pot bearings. To address this issue, it is necessary to design an inspection system that provides relevant, real-time information on the bridge's condition. In addition, this bridge typology is representative of the Spanish high-speed rail network system, so its developments can be extrapolated to other structures.

Figure 6-1: (a) Location; (b) View of the Huerta de Mateo Bridge; (c) Pot bearings (photograph taken on September 23rd, 2024).

6.2.2. Structural health monitoring using operational modal analysis in bridges

6.2.2.1. Bridge Geometry & Monitoring System

On the Huerta de Mateo Bridge there are two railway tracks with a center-to-center spacing of approximately 4.70 m and a total structural width of 14 m, as shown in Figure 6-2(b). The outer spans have a clear span of 36 m, while the inner spans have working spans of 45 m and 43 m. The box girder has a depth of 3.04 m, crowned with a 2 % camber on each side of the axis. The bottom width of the box is 5.50 m. The piers feature box sections with a constant longitudinal width of 2.30 m and a variable transverse width, with heights ranging from 7.82 m to 21.54 m. The abutments are cast integrally around the deck to create a keying effect between the two elements, and the bearings are Pot-type, longitudinally guided on the left side and free on the right.

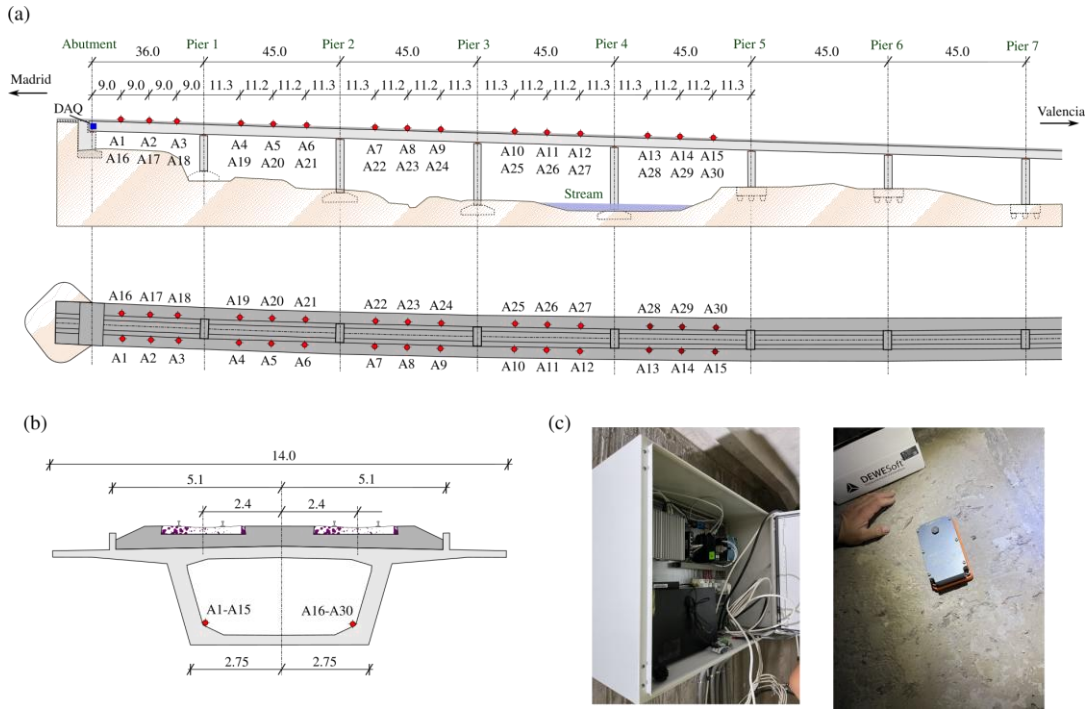

Figure 6-2: (a) Plan and elevation views of the Huerta de Mateo Bridge with sensor layout; (b) cross-section typology; (c) acquisition system (DAQ) and triaxial accelerometer positions. Dimensions in meters.

To study and assess the bridge's condition, an Ambient Vibration Test (AVT), LVDTs on the pot bearings, clinometers on the piers, and temperature sensors have been installed. Data acquisition was continuous, but for this study the AVT was limited to the period from March 3rd, 2025, to April 17th, 2025. The monitoring system comprises 30 triaxial accelerometers, labeled A1 to A30 (model IOLITE 3xMEMS-ACC (Figure 6-2: (a) Plan and elevation views of the Huerta de Mateo Bridge with sensor layout; (b) cross-section typology; (c) acquisition system (DAQ) and triaxial accelerometer positions. Dimensions in meters.(c)); dynamic range: ±2 g; noise power spectral density: 25 µg/√Hz; sampling frequency: 100 Hz, downsampled from 4 kHz; bandwidth: 1 kHz). Three types of LVDTs differ only in displacement range 25 mm, 250 mm, and 300 mm (output current: 4–20 mA; ripple: 50 µA; bandwidth: 250 Hz). The accelerometers monitored accelerations at fifteen cross-sections of the bridge (see Figure 6-2(a)). Acceleration records are triggered by train passages based on a predefined threshold, yielding 40-second train-passage records and 10-minute AVT records. LVDT and clinometer data are likewise triggered but recorded for only 30 seconds, while static measurements run for 5 minutes. Each temperature sensor produces one value per record, averaged over the entire monitoring period.

Two identical PCs (Intel® Core™ i7-9700T CPU at 2.00 GHz, 32 GB RAM) collect sensor data (see Figure 6-2 (c). The accelerometer sensor-node network on PC 1 directly converts analog signals into digital form for recording. The remaining sensors feed PC 2 via a SIRIUS® Modular data acquisition system, which offers a 160 dB dynamic range and galvanic isolation, using the EtherCAT protocol for data transfer. Both systems run DewesoftX software to acquire and locally compress data into .dxd files; these files are then forwarded to CEMOSA's broker for processing and identification. For further details, see Section 6.2.2.3.

6.2.2.2. Deck dynamics monitoring

The dynamic behavior of the deck is monitored using records from the 30 accelerometers distributed across the first five spans of the bridge. The sensor configuration (name, serial number, and location) is shown in the following table:

Channel	Sensor	Location (side)	Situation in the span
AI A-1	IOLITE-3xMEMS-ACC [X] (MEMS ACC; 2 g .. AAF (distorsión de fase-cero) (BE);) SN: DA22341187	Right	
AI A-2	IOLITE-3xMEMS-ACC [Y] (MEMS ACC; 2 g .. AAF (distorsión de fase-cero) (BE);) SN: DA22341187	Right	L/4
AI A-3	IOLITE-3xMEMS-ACC [Z] (MEMS ACC; 2 g .. AAF (distorsión de fase-cero) (BE);) SN: DA22341187	Right	
AI B-1	IOLITE-3xMEMS-ACC [X] (MEMS ACC; 2 g .. AAF (distorsión de fase-cero) (BE);) SN: DA22341188	Right	
AI B-2	IOLITE-3xMEMS-ACC [Y] (MEMS ACC; 2 g .. AAF (distorsión de fase-cero) (BE);) SN: DA22341188	Right	L/2
AI B-3	IOLITE-3xMEMS-ACC [Z] (MEMS ACC; 2 g .. AAF (distorsión de fase-cero) (BE);) SN: DA22341188	Right	
AI C-1	IOLITE-3xMEMS-ACC [X] (MEMS ACC; 2 g .. AAF (distorsión de fase-cero) (BE);) SN: DA22341189	Right	
AI C-2	IOLITE-3xMEMS-ACC [Y] (MEMS ACC; 2 g .. AAF (distorsión de fase-cero) (BE);) SN: DA22341189	Right	3L/4
AI C-3	IOLITE-3xMEMS-ACC [Z] (MEMS ACC; 2 g .. AAF (distorsión de fase-cero) (BE);) SN: DA22341189	Right	
AI D-1	IOLITE-3xMEMS-ACC [X] (MEMS ACC; 2 g .. AAF (distorsión de fase-cero) (BE);) SN: DA22341191	Right	
AI D-2	IOLITE-3xMEMS-ACC [Y] (MEMS ACC; 2 g .. AAF (distorsión de fase-cero) (BE);) SN: DA22341191	Right	L/4
AI D-3	IOLITE-3xMEMS-ACC [Z] (MEMS ACC; 2 g .. AAF (distorsión de fase-cero) (BE);) SN: DA22341191	Right	
AI E-1	IOLITE-3xMEMS-ACC [X] (MEMS ACC; 2 g .. AAF (distorsión de fase-cero) (BE);) SN: DA22341192	Right	
AI E-2	IOLITE-3xMEMS-ACC [Y] (MEMS ACC; 2 g .. AAF (distorsión de fase-cero) (BE);) SN: DA22341192	Right	L/2
AI E-3	IOLITE-3xMEMS-ACC [Z] (MEMS ACC; 2 g .. AAF (distorsión de fase-cero) (BE);) SN: DA22341192	Right	
AI F-1	IOLITE-3xMEMS-ACC [X] (MEMS ACC; 2 g .. AAF (distorsión de fase-cero) (BE);) SN: DA22341193	Right	
AI F-2	IOLITE-3xMEMS-ACC [Y] (MEMS ACC; 2 g .. AAF (distorsión de fase-cero) (BE);) SN: DA22341193	Right	3L/4
AI F-3	IOLITE-3xMEMS-ACC [Z] (MEMS ACC; 2 g .. AAF (distorsión de fase-cero) (BE);) SN: DA22341193	Right	
AI G-1	IOLITE-3xMEMS-ACC [X] (MEMS ACC; 2 g .. AAF (distorsión de fase-cero) (BE);) SN: DA22341194	Right	
AI G-2	IOLITE-3xMEMS-ACC [Y] (MEMS ACC; 2 g .. AAF (distorsión de fase-cero) (BE);) SN: DA22341194	Right	L/4
AI G-3	IOLITE-3xMEMS-ACC [Z] (MEMS ACC; 2 g .. AAF (distorsión de fase-cero) (BE);) SN: DA22341194	Right	
AI H-1	IOLITE-3xMEMS-ACC [X] (MEMS ACC; 2 g .. AAF (distorsión de fase-cero) (BE);) SN: DA22341195	Right	
AI H-2	IOLITE-3xMEMS-ACC [Y] (MEMS ACC; 2 g .. AAF (distorsión de fase-cero) (BE);) SN: DA22341195	Right	L/2
AI H-3	IOLITE-3xMEMS-ACC [Z] (MEMS ACC; 2 g .. AAF (distorsión de fase-cero) (BE);) SN: DA22341195	Right	
AI I-1	IOLITE-3xMEMS-ACC [X] (MEMS ACC; 2 g .. AAF (distorsión de fase-cero) (BE);) SN: DA22341196	Right	
AI I-2	IOLITE-3xMEMS-ACC [Y] (MEMS ACC; 2 g .. AAF (distorsión de fase-cero) (BE);) SN: DA22341196	Right	3L/4
AI I-3	IOLITE-3xMEMS-ACC [Z] (MEMS ACC; 2 g .. AAF (distorsión de fase-cero) (BE);) SN: DA22341196	Right	
AI J-1	IOLITE-3xMEMS-ACC [X] (MEMS ACC; 2 g .. AAF (distorsión de fase-cero) (BE);) SN: DA22341197	Right	
AI J-2	IOLITE-3xMEMS-ACC [Y] (MEMS ACC; 2 g .. AAF (distorsión de fase-cero) (BE);) SN: DA22341197	Right	L/4
AI J-3	IOLITE-3xMEMS-ACC [Z] (MEMS ACC; 2 g .. AAF (distorsión de fase-cero) (BE);) SN: DA22341197	Right	
AI K-1	IOLITE-3xMEMS-ACC [X] (MEMS ACC; 2 g .. AAF (distorsión de fase-cero) (BE);) SN: DA22341198	Right	
AI K-2	IOLITE-3xMEMS-ACC [Y] (MEMS ACC; 2 g .. AAF (distorsión de fase-cero) (BE);) SN: DA22341198	Right	L/2
AI K-3	IOLITE-3xMEMS-ACC [Z] (MEMS ACC; 2 g .. AAF (distorsión de fase-cero) (BE);) SN: DA22341198	Right	
AI L-1	IOLITE-3xMEMS-ACC [X] (MEMS ACC; 2 g .. AAF (distorsión de fase-cero) (BE);) SN: DA22341199	Right	
AI L-2	IOLITE-3xMEMS-ACC [Y] (MEMS ACC; 2 g .. AAF (distorsión de fase-cero) (BE);) SN: DA22341199	Right	3L/4
AI L-3	IOLITE-3xMEMS-ACC [Z] (MEMS ACC; 2 g .. AAF (distorsión de fase-cero) (BE);) SN: DA22341199	Right	
AI M-1	IOLITE-3xMEMS-ACC [X] (MEMS ACC; 2 g .. AAF (distorsión de fase-cero) (BE);) SN: DA22341200	Right	
AI M-2	IOLITE-3xMEMS-ACC [Y] (MEMS ACC; 2 g .. AAF (distorsión de fase-cero) (BE);) SN: DA22341200	Right	L/4
AI M-3	IOLITE-3xMEMS-ACC [Z] (MEMS ACC; 2 g .. AAF (distorsión de fase-cero) (BE);) SN: DA22341200	Right	
AI N-1	IOLITE-3xMEMS-ACC [X] (MEMS ACC; 2 g .. AAF (distorsión de fase-cero) (BE);) SN: DA22341201	Right	
AI N-2	IOLITE-3xMEMS-ACC [Y] (MEMS ACC; 2 g .. AAF (distorsión de fase-cero) (BE);) SN: DA22341201	Right	L/2
AI N-3	IOLITE-3xMEMS-ACC [Z] (MEMS ACC; 2 g .. AAF (distorsión de fase-cero) (BE);) SN: DA22341201	Right	
AI O-1	IOLITE-3xMEMS-ACC [X] (MEMS ACC; 2 g .. AAF (distorsión de fase-cero) (BE);) SN: DA22341202	Right	
AI O-2	IOLITE-3xMEMS-ACC [Y] (MEMS ACC; 2 g .. AAF (distorsión de fase-cero) (BE);) SN: DA22341202	Right	3L/4
AI O-3	IOLITE-3xMEMS-ACC [Z] (MEMS ACC; 2 g .. AAF (distorsión de fase-cero) (BE);) SN: DA22341202	Right	

Channel	Sensor	Location (side)	Situation in the span
AI P-1	IOLITE-3xMEMS-ACC [X] (MEMS ACC; 2 g .. AAF (distorsión de fase-cero) (BE);) SN: DA22341172	Left	
AI P-2	IOLITE-3xMEMS-ACC [Y] (MEMS ACC; 2 g .. AAF (distorsión de fase-cero) (BE);) SN: DA22341172	Left	L/4
AI P-3	IOLITE-3xMEMS-ACC [Z] (MEMS ACC; 2 g .. AAF (distorsión de fase-cero) (BE);) SN: DA22341172	Left	
AI Q-1	IOLITE-3xMEMS-ACC [X] (MEMS ACC; 2 g .. AAF (distorsión de fase-cero) (BE);) SN: DA22341173	Left	
AI Q-2	IOLITE-3xMEMS-ACC [Y] (MEMS ACC; 2 g .. AAF (distorsión de fase-cero) (BE);) SN: DA22341173	Left	L/2
AI Q-3	IOLITE-3xMEMS-ACC [Z] (MEMS ACC; 2 g .. AAF (distorsión de fase-cero) (BE);) SN: DA22341173	Left	
AI R-1	IOLITE-3xMEMS-ACC [X] (MEMS ACC; 2 g .. AAF (distorsión de fase-cero) (BE);) SN: DA22341174	Left	
AI R-2	IOLITE-3xMEMS-ACC [Y] (MEMS ACC; 2 g .. AAF (distorsión de fase-cero) (BE);) SN: DA22341174	Left	3L/4
AI R-3	IOLITE-3xMEMS-ACC [Z] (MEMS ACC; 2 g .. AAF (distorsión de fase-cero) (BE);) SN: DA22341174	Left	
AI S-1	IOLITE-3xMEMS-ACC [X] (MEMS ACC; 2 g .. AAF (distorsión de fase-cero) (BE);) SN: DA22341175	Left	
AI S-2	IOLITE-3xMEMS-ACC [Y] (MEMS ACC; 2 g .. AAF (distorsión de fase-cero) (BE);) SN: DA22341175	Left	L/4
AI S-3	IOLITE-3xMEMS-ACC [Z] (MEMS ACC; 2 g .. AAF (distorsión de fase-cero) (BE);) SN: DA22341175	Left	
AI T-1	IOLITE-3xMEMS-ACC [X] (MEMS ACC; 2 g .. AAF (distorsión de fase-cero) (BE);) SN: DA22341176	Left	
AI T-2	IOLITE-3xMEMS-ACC [Y] (MEMS ACC; 2 g .. AAF (distorsión de fase-cero) (BE);) SN: DA22341176	Left	L/2
AI T-3	IOLITE-3xMEMS-ACC [Z] (MEMS ACC; 2 g .. AAF (distorsión de fase-cero) (BE);) SN: DA22341176	Left	
AI U-1	IOLITE-3xMEMS-ACC [X] (MEMS ACC; 2 g .. AAF (distorsión de fase-cero) (BE);) SN: DA22341177	Left	
AI U-2	IOLITE-3xMEMS-ACC [Y] (MEMS ACC; 2 g .. AAF (distorsión de fase-cero) (BE);) SN: DA22341177	Left	3L/4
AI U-3	IOLITE-3xMEMS-ACC [Z] (MEMS ACC; 2 g .. AAF (distorsión de fase-cero) (BE);) SN: DA22341177	Left	
AI V-1	IOLITE-3xMEMS-ACC [X] (MEMS ACC; 2 g .. AAF (distorsión de fase-cero) (BE);) SN: DA22341178	Left	
AI V-2	IOLITE-3xMEMS-ACC [Y] (MEMS ACC; 2 g .. AAF (distorsión de fase-cero) (BE);) SN: DA22341178	Left	L/4
AI V-3	IOLITE-3xMEMS-ACC [Z] (MEMS ACC; 2 g .. AAF (distorsión de fase-cero) (BE);) SN: DA22341178	Left	
AI W-1	IOLITE-3xMEMS-ACC [X] (MEMS ACC; 2 g .. AAF (distorsión de fase-cero) (BE);) SN: DA22341179	Left	
AI W-2	IOLITE-3xMEMS-ACC [Y] (MEMS ACC; 2 g .. AAF (distorsión de fase-cero) (BE);) SN: DA22341179	Left	L/2
AI W-3	IOLITE-3xMEMS-ACC [Z] (MEMS ACC; 2 g .. AAF (distorsión de fase-cero) (BE);) SN: DA22341179	Left	
AI X-1	IOLITE-3xMEMS-ACC [X] (MEMS ACC; 2 g .. AAF (distorsión de fase-cero) (BE);) SN: DA22341180	Left	
AI X-2	IOLITE-3xMEMS-ACC [Y] (MEMS ACC; 2 g .. AAF (distorsión de fase-cero) (BE);) SN: DA22341180	Left	3L/4
AI X-3	IOLITE-3xMEMS-ACC [Z] (MEMS ACC; 2 g .. AAF (distorsión de fase-cero) (BE);) SN: DA22341180	Left	
AI Y-1	IOLITE-3xMEMS-ACC [X] (MEMS ACC; 2 g .. AAF (distorsión de fase-cero) (BE);) SN: DA22341181	Left	
AI Y-2	IOLITE-3xMEMS-ACC [Y] (MEMS ACC; 2 g .. AAF (distorsión de fase-cero) (BE);) SN: DA22341181	Left	L/4
AI Y-3	IOLITE-3xMEMS-ACC [Z] (MEMS ACC; 2 g .. AAF (distorsión de fase-cero) (BE);) SN: DA22341181	Left	
AI Z-1	IOLITE-3xMEMS-ACC [X] (MEMS ACC; 2 g .. AAF (distorsión de fase-cero) (BE);) SN: DA22341182	Left	
AI Z-2	IOLITE-3xMEMS-ACC [Y] (MEMS ACC; 2 g .. AAF (distorsión de fase-cero) (BE);) SN: DA22341182	Left	L/2
AI Z-3	IOLITE-3xMEMS-ACC [Z] (MEMS ACC; 2 g .. AAF (distorsión de fase-cero) (BE);) SN: DA22341182	Left	
AI AA-1	IOLITE-3xMEMS-ACC [X] (MEMS ACC; 2 g .. AAF (distorsión de fase-cero) (BE);) SN: DA22341183	Left	
AI AA-2	IOLITE-3xMEMS-ACC [Y] (MEMS ACC; 2 g .. AAF (distorsión de fase-cero) (BE);) SN: DA22341183	Left	3L/4
AI AA-3	IOLITE-3xMEMS-ACC [Z] (MEMS ACC; 2 g .. AAF (distorsión de fase-cero) (BE);) SN: DA22341183	Left	
AI AB-1	IOLITE-3xMEMS-ACC [X] (MEMS ACC; 2 g .. AAF (distorsión de fase-cero) (BE);) SN: DA22341184	Left	
AI AB-2	IOLITE-3xMEMS-ACC [Y] (MEMS ACC; 2 g .. AAF (distorsión de fase-cero) (BE);) SN: DA22341184	Left	L/4
AI AB-3	IOLITE-3xMEMS-ACC [Z] (MEMS ACC; 2 g .. AAF (distorsión de fase-cero) (BE);) SN: DA22341184	Left	
AI AC-1	IOLITE-3xMEMS-ACC [X] (MEMS ACC; 2 g .. AAF (distorsión de fase-cero) (BE);) SN: DA22341185	Left	
AI AC-2	IOLITE-3xMEMS-ACC [Y] (MEMS ACC; 2 g .. AAF (distorsión de fase-cero) (BE);) SN: DA22341185	Left	L/2
AI AC-3	IOLITE-3xMEMS-ACC [Z] (MEMS ACC; 2 g .. AAF (distorsión de fase-cero) (BE);) SN: DA22341185	Left	
AI AD-1	IOLITE-3xMEMS-ACC [X] (MEMS ACC; 2 g .. AAF (distorsión de fase-cero) (BE);) SN: DA22341186	Left	
AI AD-2	IOLITE-3xMEMS-ACC [Y] (MEMS ACC; 2 g .. AAF (distorsión de fase-cero) (BE);) SN: DA22341186	Left	3L/4
AI AD-3	IOLITE-3xMEMS-ACC [Z] (MEMS ACC; 2 g .. AAF (distorsión de fase-cero) (BE);) SN: DA22341186	Left	

Figure 6-3: Channel configuration.

Figure 6-4: Accelerometer.

Figure 6-5: Wiring of the accelerometers.

The monitoring system was brought online in December 2024. Since then, extensive system performance testing has been conducted to ensure its robustness. During one of these tests, with the system acquiring data from the 30 triaxial accelerometers, representing 90 channels, at a readout rate of 4000 Hz, the first problems with data loss and sudden acquisition stops were detected. The failure was duly documented and reported to the supplier for correction.

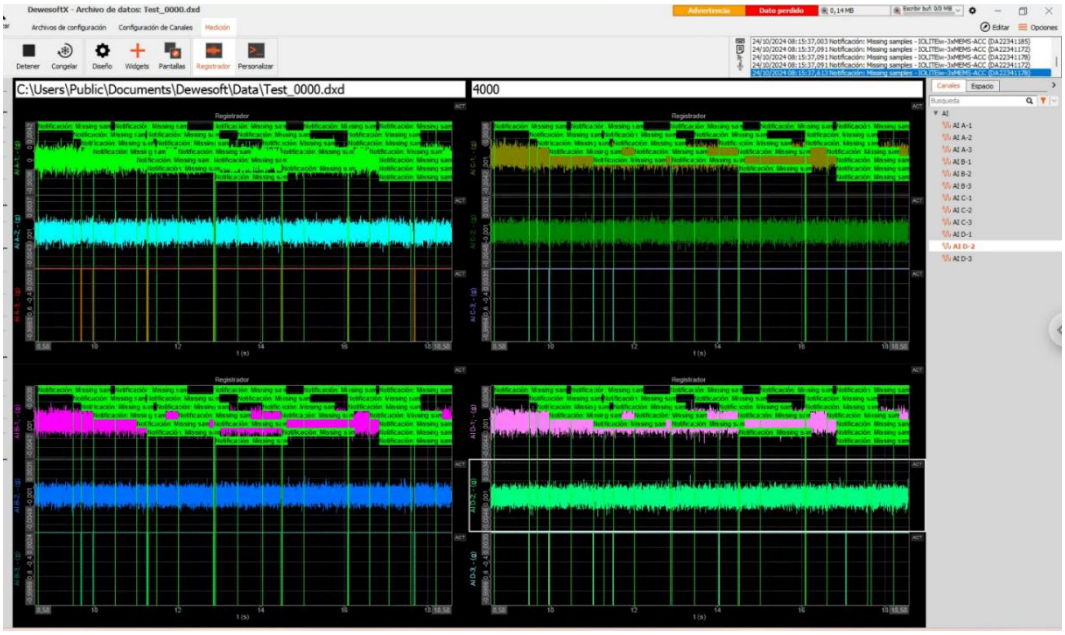

Figure 6-6: Loss of data from the monitoring system.

Among the corrective measures adopted, the main one was the replacement of the industrial PC, which, after analysis, showed defects in its power management, resulting in very poor performance. Additionally, the lengths of the first cable sections of the two accelerometer lines were shortened, as they had excess cable to accommodate different PC locations relative to the accelerometers.

Reliability tests were repeated at maximum performance without apparent problems until the first system shutdowns began in May 2025. The PC's operating conditions were monitored, and temperatures were detected on the solid-state drive that were outside the operating range for this element. Finally, it was decided to replace the solid-state drive with one capable of withstanding higher operating temperatures. In this case, the high-performance reliability tests yielded satisfactory results, and to date, the system has been operating without apparent problems. In parallel with the tasks described above, work was carried out on transferring the records from the PC installed on the bridge to the servers of the collaborating companies. The records are sent via an MQTT server, through which they are published. We have two types of records: ambient vibration records, to which OMA algorithms are applied to obtain estimates of the modal parameters, and train-passing records, which provide actual values of the main frequencies and their associated damping.

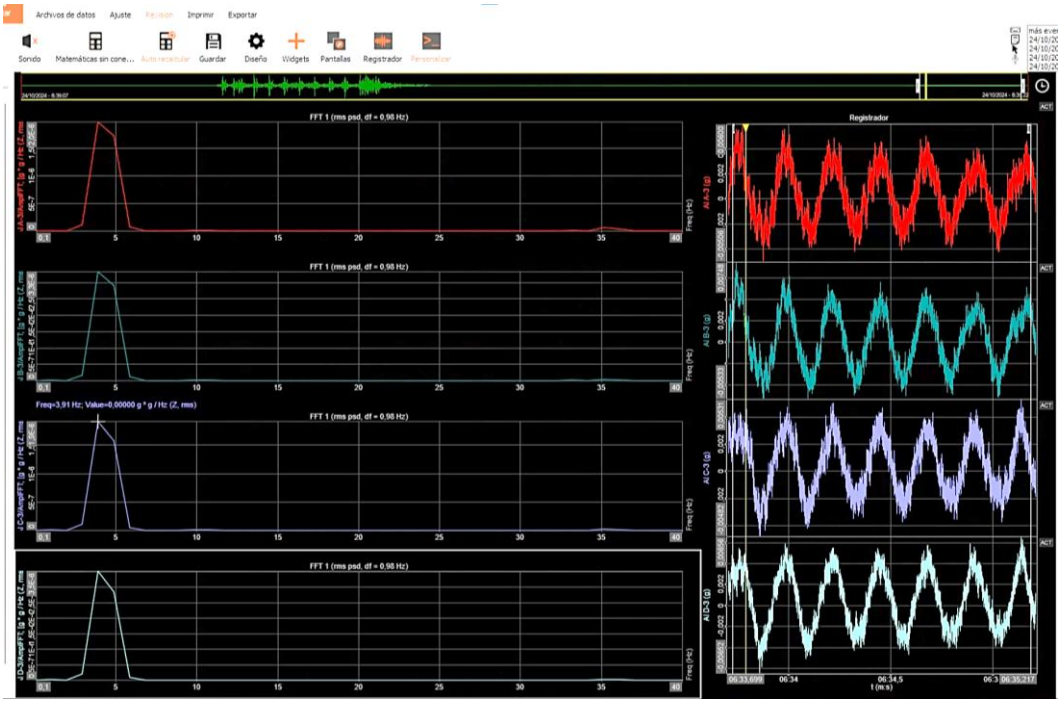

Figure 6-7: FFT analysis of free vibration registers.

Signal processing is performed using proven algorithms in a free programming language (Python). However, verifications have been performed by comparing results with commercial software. An example of these comparisons would be the operational modal analysis. Artemis Modal Pro software from SVS was used for this purpose.

ARTEMIS Modal Pro is advanced software specialized in vibration analysis, primarily focused on Operational Modal Analysis (OMA). This means that it allows the dynamic characteristics of a structure (natural frequencies, damping, and mode shapes) to be identified using only measurements of its response to environmental or operational excitations, without the need to know or control the input forces. The Pro version is the most comprehensive, offering multiple analysis methods in both the time and frequency domains, and tools for validation, data management, and process automation. It is used in civil and mechanical engineering for large structures and machinery.

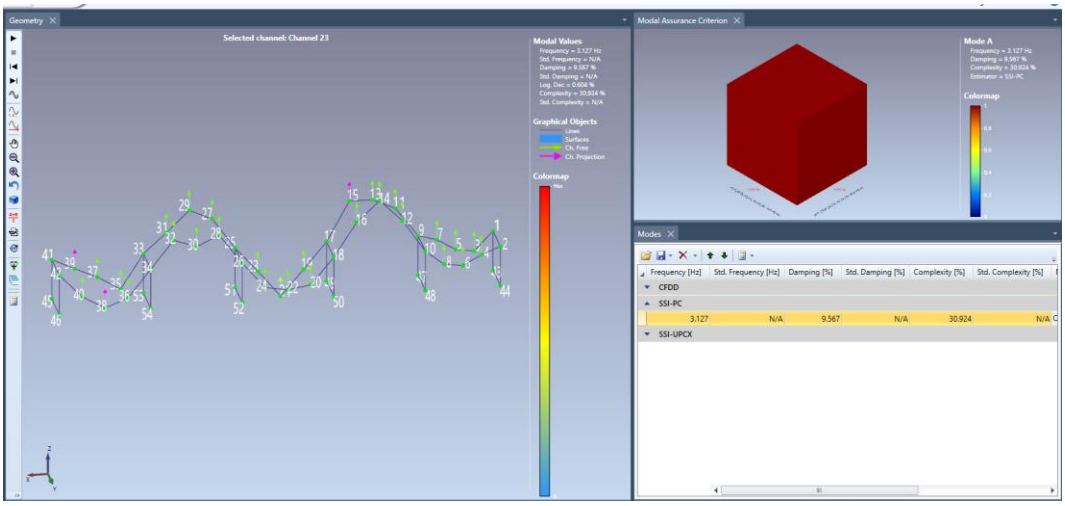

Figure 6-8: SSI-PC analysis of ambient vibration test through Artemis.

Based on the results presented in section 6.2, "Structural health monitoring in bridges and degradation models for pot bearings," the only mode detected by Artemis using the 3.127 Hz SSI-PC algorithm (time domain) corresponds to the first mode identified. However, it is striking that, using the same environmental record, at least in the automatic detection of commercial software, the number of modes identified is much lower than those obtained with the SHM strategy adopted in this project.

It is worth noting that, although most of the tests were performed remotely, from the offices, much of the work is related to the logistics required to access the structure.

6.2.2.3. Sensor Data Acquisition and Publishing Pipeline

CEMOSA has implemented a comprehensive system for receiving data via MQTT. Within this framework, the entire workflow for collecting, processing, and publishing sensor data is organized into six key stages, as shown in Figure 6-9. At each stage, raw field signals are transformed into structured JSON messages delivered over MQTT, ensuring that every piece of information—from high-frequency vibrations to slow-moving displacement readings—is accurately captured, classified, and transmitted in real time.

(A) Dewesoft – Data Acquisition and. dxd File Generation: At this step, all physical sensors (accelerometers, LVDTs, clinometers, etc.) feed their analog and digital outputs into the Dewesoft data acquisition system. Here, channel parameters such as sampling rate, input range, and measurement units are defined. Dewesoft performs on-the-fly compression and wraps both raw measurements and metadata (timestamps, channel names, units) into a proprietary .dxd file, providing a self-contained record of the entire recording session.

(B) Event Separation: A Python-based processing script parses each .dxd file to detect and segment individual events. It distinguishes dynamic events—such as passing trains and ambient vibration tests—from static events, which consist of regular, low-frequency readings taken every five minutes. Events are defined by an acceleration threshold of 10 m/s², with an automated

trigger. When the trigger detects an acceleration exceeding this threshold, it begins a 20-minute recording at 100 Hz; within this window, 40-second train-passage events and 10-minute ambient-vibration intervals are captured. For the other sensors, the same trigger initiates a 200 Hz dynamic measurement lasting 30 seconds, while between triggered periods static readings are recorded every five minutes.

(C) Event Classification: Once segmented, each event is labelled according to its signal characteristics. Dynamic events are those containing rapid vibrations and displacements, recorded at high sampling rates (e.g., 1 kHz), while static events cover slow-varying measurements like temperature or inclinometer readings at low sampling rates (e.g., 1 Hz or one sample per five minutes). This classification guides downstream processing and storage policies.

(D) Each extracted event is first serialized into a compact binary form using Python's pickle module (e.g. pickle.dumps(signal_event)). The resulting byte stream is then encoded in Base64 so it can be safely transmitted as text. This workflow minimizes bandwidth usage while preserving the full fidelity of the original data.

(E) JSON Message Construction: A structured JSON object is assembled for each event, typically following this template:

```
event = {
  "date": "2025-03-17T20:34:39.000Z",
  "name": "AI A-3",
  "value": base64.b64encode(values).decode('utf-8'),
  "signal_type": "train_pass",
  "fs": 100,
}
```

(F) Each JSON message is published to a corporate MQTT broker under a topic. Quality of Service (QoS) level is set 1 to ensure delivery without duplication, and retained flags are disabled so that only new events propagate. Subscribed clients—whether real-time dashboards or cloud ingestion services—receive and process these messages immediately, completing the real-time data pipeline.

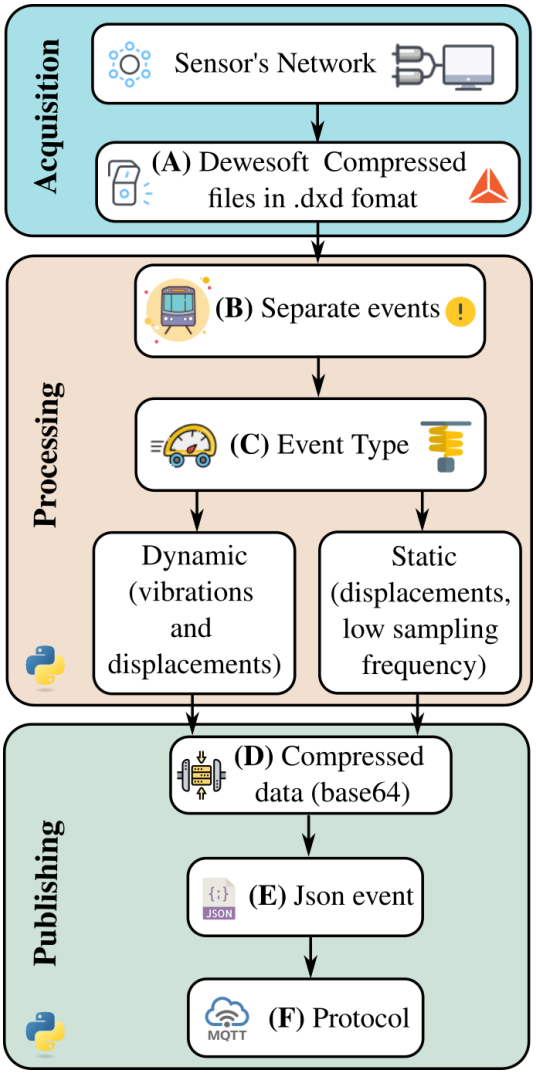

Figure 6-9: Flowchart of the Dewesoft data acquisition process, dynamic and static event separation, Base64 compression, and JSON publication over MQTT.

6.2.2.4. Methodology for Continuous Structural health monitoring (SHM)

The proposed methodology for studying the bridge's condition using time-history accelerometer readings is based on constructing a Digital Twin (DT) for online damage identification. The workflow of the implemented DT-based continuous structural identification (St-Id) approach is illustrated in Figure 6-10. The process iteratively acquires experimental data from the physical asset, performs structural identification by inverse calibration of the DT, and detects potential damage. To achieve quasi-real-time damage identification, it is crucial to ensure that the total computational time required for signal processing and inverse calibration of the DT remains within acceptable limits. In this context, the procedure comprises four consecutive steps:

(A) Automated Operational Modal Analysis (OMA) – Ambient vibrations are periodically recorded and sent via MQTT and stored in separate data files containing a certain time duration. Then, a set of modal signatures (resonant frequencies, mode shapes, and damping ratios) is extracted through automated OMA.

(B) Structural DT based St-Id – This step relates the St-Id of the asset through the model updating of the DT. This is accomplished by solving a certain optimization problem with an objective function $J(x)$ accounting for the mismatch between the theoretical predictions of the model and the previously identified experimental modal signatures. As a result, certain damage-sensitive model parameters $\boldsymbol{x}$ are calibrated ($\hat{\boldsymbol{x}}$) and collected in an observation matrix $\mathbf{X}$.

(C) Damage Detection – The presence of benign Environmental and Operation Conditions (EOC)-driven fluctuations in the previously identified modal parameters is minimized through statistical pattern recognition. The trend of the residual values, after removing environmental effects, is analyzed using a control chart; this ensures that any change in the structure's properties is detected following the training period.

(D) Damage Identification – Finally, the appearance of structural damage can be appraised by novelty analysis of the time series of modal signatures and model parameters contained in $\hat{\mathbf{X}}$. Since the latter are defined according to certain structural elements or damage mechanisms, the identification of permanent variations in their time series provides direct assessment of the location and severity of the damage.

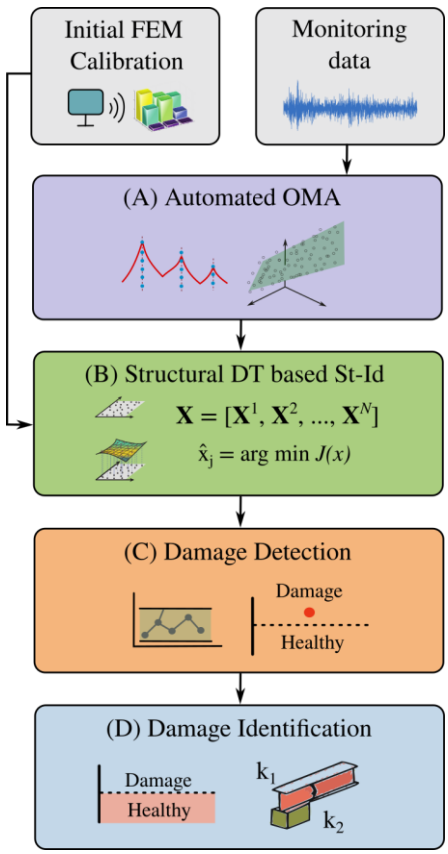

Figure 6-10: Flowchart of the implemented DT-based continuous St-Id of bridges.

For the identification of dynamic parameters, stabilization diagrams combined with hierarchical clustering are commonly used. In this sense, once the identification parameters are selected (time lag j_b and maximum model order), the poles of the identified linear system are computed for model orders ranging from n_{min} to n_{max}. Then, the poles are filtered by the application of a set of hard criteria (HC) and soft criteria (SC) to remove the mathematical or spurious poles. The HC

criteria concern the elimination of complex conjugate poles, damping ratios above physically feasible values (in this work $\xi \leq 10\%$), and high Mode Phase Collinearity (MPC) values ($\mathrm{MPC} \geq 70\%$). After applying HC, a list of stable poles is obtained by finding those poles abiding certain tolerances between consecutive model orders, including relative variations of resonant frequencies and damping ratios ($\Delta f \leq 1\%, \Delta\xi \leq 3\%$), MAC values ($\mathrm{MAC} \geq 0.95$), and Modal Transfer Norms (MTF) ($\mathrm{MTN} \leq 0.1$). Once a list of stable poles are selected and represented in a stabilization chart, the identification of physical modes (columns of stable poles) needs to be automatically performed for continuous SHM. In this work, a hierarchical clustering approach is applied in three sequential steps:

- From the highest model order (step $k = 1$), each identified pole λ_i is considered as a single element cluster. Let us note where f_λ and $\boldsymbol{\phi}_\lambda$ the frequency and mode shaped computed from a pole λ, respectively. At the k-th step, the distance d_{ij}^k is computed between each analyzed stable-pole of the model order n_k and each identified stable-poles λ_j in the lower model order n_{k-1} as:

$$d_{ij}^k = (1-\eta)\frac{\left|f_{\lambda_i^{(k)}} - f_{\lambda_j^{(k-1)}}\right|}{f_{\lambda_j^{(k-1)}}} + \eta\left[1 - \mathrm{MAC}\left(\boldsymbol{\phi}_{\lambda_i^{(k)}}, \boldsymbol{\phi}_{\lambda_j^{(k-1)}}\right)\right] \qquad (4)$$

with η being a weighting factor between the contributions of Δf and MAC.

- Once all the distances are calculated, the minimum distance d_i^k in Eq. (4) is retained. The minimum distances are collected in a vector $\mathbf{d}^k = \left(d_1^k \; d_2^k \; \ldots \; d_n^k\right)$ containing the minimum distances of the poles between two-consecutive model orders (n_k and n_{k-1}).
- The cut-off threshold is estimated as the 80th percentile of the distribution of the distances $\mathbf{d}^k$.
- The hierarchical tree (dendrogram) is constructed based on d_i^k, and an optimal cut-off threshold is applied to divide the tree, grouping the stable poles into clusters. Clusters with low dimensions are removed by setting a minimum number of poles necessary to constitute a valid physical cluster.
- The physical modes are ultimately determined as the centroids of the previously selected clusters.

This approach allows for the automatic extraction of the modal properties of the monitored structure from periodic ambient vibration data. However, in practical applications, some of the identified clusters may not correspond to actual physical modes. These inaccuracies may stem from errors in the identification process or the influence of non-Gaussian excitations. Furthermore, the identification may miss certain modes during times when they are weakly excited, such as during nighttime when ambient excitations are generally lower.

6.2.2.5. Continuous modal identification of the Huerta de Mateo Bridge.

Initially, the records obtained from the bridge's accelerometers require preprocessing before dynamic identification. The first step is to detrend each channel, ensuring that all accelerometer signals have a zero mean. This standardization guarantees that every channel shares a common magnitude baseline. The second step involves identifying the frequencies of interest. In this case, we used the finite-element model defined in Section 3, which revealed eight modes in the 3 Hz–5 Hz range, since the power spectral density (PSD) of each channel did not show clear resonant peaks. Once the target peaks are determined, the signals are decimated to retain only the relevant frequencies. For this case study—with an original sampling rate of 100 Hz—the data were decimated to 10 Hz, preserving frequencies from 0 to 10 Hz in accordance with the Nyquist theorem.

Following preprocessing, we extracted the bridge's modal signatures using the automated covariance-driven stochastic subspace identification (CoV-SSI) procedure. The time-lag parameter j_b was set to 150, and system matrices along with their modal features were estimated for model orders ranging from 20 to 200 in increments of two. We observed eight columns of stable poles up to 4.6 Hz, including five distinct columns within the 3 Hz–4 Hz band, as shown the Figure 6-11. This clustering of modes arises primarily because all modes exhibit very similar stiffness-to-mass ratios, and because the bridge is a continuous structure with uniform material properties along its entire length. As a result, the low-frequency region shows a high modal density dominated by numerous flexural modes, as demonstrated in this case study.

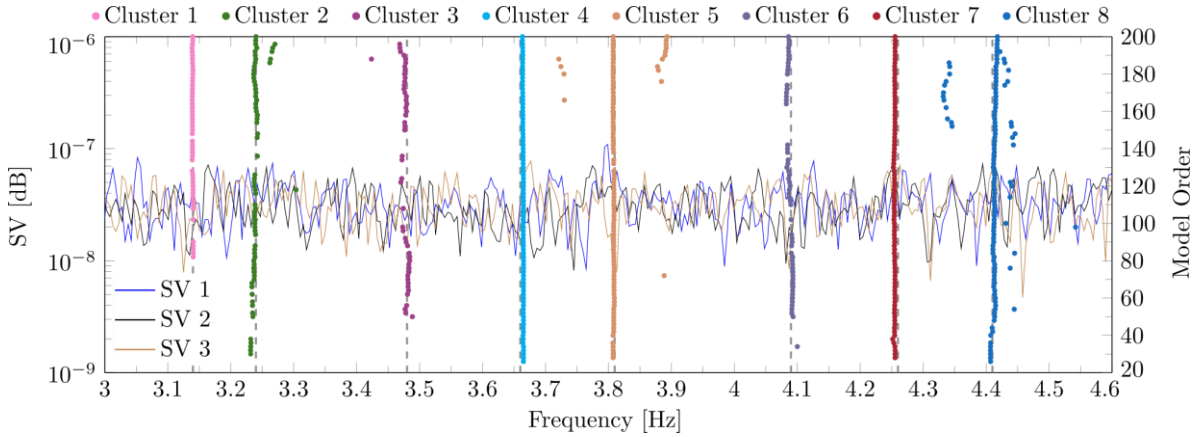

Figure 6-11: Stabilization diagram obtained by CoV-SSI of the Huerta de Mateo Bridge (March 12th, 2025, 08:40 pm).

¡Error! No se encuentra el origen de la referencia. that the damping ratios for each identified mode are exceptionally low for a structure of this stiffness. This is largely due to the high sensitivity of the sensors used for OMA, which exceeds what is required for such a rigid bridge. As a result, the measurements contain residual noise that degrades the quality of the modal estimates. To address this, Section 6.2.2.7 presents a method for estimating the bridge's damping using vibration data recorded during train passages. It is also noteworthy that no torsional modes were identified among the first eight modes—an omission caused by the poor quality of the vibration spectra and the minimal spacing between sensors in each bridge section, which prevents capturing the opposite-sign displacement pairs needed to resolve torsional behaviour. Figure 6-12 presents four

representative mode shapes and the Modal Assurance Criterion (MAC) matrix for each mode. The Modal Phase Collinearity (MPC) is notably low for the fundamental mode. High MAC values are observed between modes 1–2 (0.8), 3–4 (0.6), 4–5 (0.9), 6–7 (0.8), and 7–8 (0.8). This MAC clustering results from the poor quality of the acquired signals, which complicates frequency tracking throughout the monitoring period and requires stringent criteria to extract reliable frequency time series while avoiding modal coupling. Each of the modes has been validated against the finite-element model, allowing us to confirm with confidence that all identified modes are indeed physical. Such validation is common practice when the quality of the acceleration records is poor.

Mode	Label	March 12th 2025 8:40 pm		Continuous Monitoring		
		Frequency [Hz]	Damping [%]	Mean Freq. [Hz]	Mean Damp. [%]	SR [%]
1	F_1	3.14	0.29	3.14 ± 0.04	0.29 ± 0.23	41.7%
2	F_2	3.24	0.80	3.24 ± 0.04	0.80 ± -.43	52.2%
3	F_3	3.48	1.15	3.45 ± 0.03	1.15 ± 0.35	8.2%
4	F_4	3.66	0.37	3.67 ± 0.06	0.37 ± 0.12	31.7%
5	F_5	3.81	0.34	3.80 ± 0.04	0.34 ± 0.23	18.6%
6	F_6	4.09	0.43	4.09 ± 0.05	0.43 ± 0.29	16.8%
7	F_7	4.26	0.52	4.25 ± 0.05	0.52 ± 0.15	13.2%
8	F_8	4.41	0.58	4.40 ± 0.03	0.58 ± 0.33	11.2%

Table 6-1: Experimentally identified modal signatures of the Huerta de Mateo Bridge on March 12th, 2025, 08:40 pm and all throughout the monitoring period.

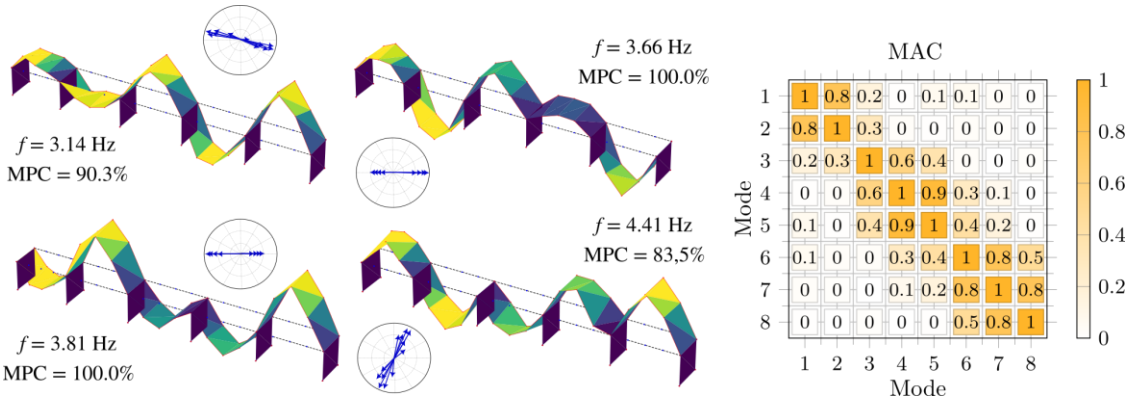

Figure 6-12: Mode shapes F1, F4, F5, and F7 of the Huerta de Mateo Bridge and MAC matrix identified on March 12th, 2025, at 8:40 pm.

The identification results obtained March 12th acceleration record in **¡Error! No se encuentra el origen de la referencia.** was used to define the baseline modal features of the bridge to be tracked throughout the monitoring period from March 3rd, 2025, until April 17th, 2025 (785 acceleration records). To prevent misclassification, modal tracking is only applied to sets of poles that meet specific user-defined tolerances relative to the reference modes. Specifically, each time a new identification is performed, only the modal clusters that are sufficiently close to the reference modes in terms of both frequency and mode shape are retained for tracking. In this case, the maximum allowable relative difference in frequencies is set to $\Delta f \leq 3\%$, and $MAC \leq 0.95$ for Modes 1 to 5, while frequency differences of $\Delta f \leq 5\%$, and $MAC \leq 0.90$ are applied to the remaining modes.

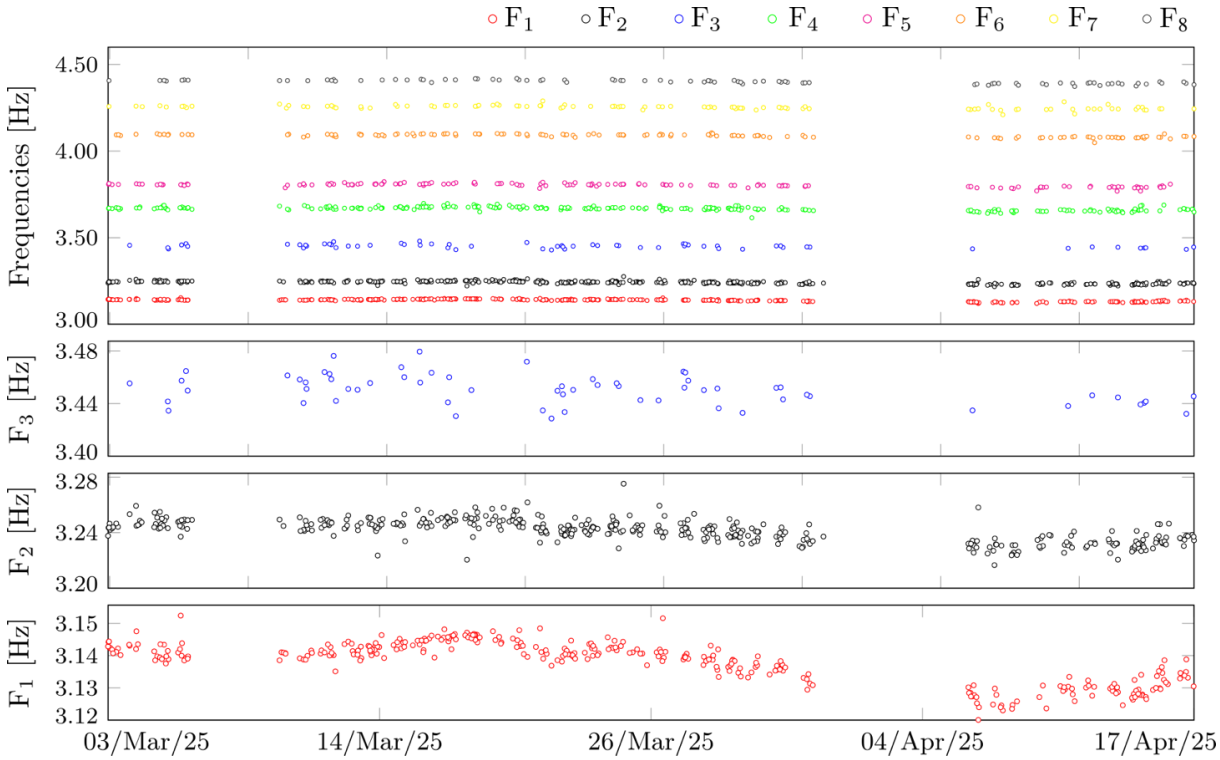

Figure 6-13: Tracking of the resonant frequencies of the Huerta de Mateo Bridge from March 3rd until April 17th, 2025.

During each step of the tracking process, all poles that meet these tolerances are assigned to the reference mode that has the smallest distance metric as defined by Eq. (4), with $\eta = 0.5$. Based on this, the time series of identified resonant frequencies are presented in Figure 6-13, accompanied by several statistical descriptors in **¡Error! No se encuentra el origen de la referencia.**. For each mode, the average values as well as their deviation in terms of frequencies and damping ratios are shown. The deviation in both cases tends to increase, which is due to the fact that the amplitude of the time series tends to grow as the resonant frequency increases. Additionally, for Modes 5 to 8, clusters with a higher amplitude than the remaining modes have been used to capture the entire time series and avoid eliminating relevant data.

It is worth noting that the success ratio for the eight identified modes is very low (see **¡Error! No se encuentra el origen de la referencia.**). This low ratio arises because dynamic identification must

be stringent—avoiding mode coupling and relying on the baselines defined in **¡Error! No se encuentra el origen de la referencia.** to correctly distinguish each mode. As a result, substantial interpolation is required to reconstruct the modes that were not identified. In the case of frequency time series, interpolation is performed by fitting a spline (degree-2 polynomial) to the time instants where the frequency values are known. Since there are many long gaps without data, in some cases the interpolated values oscillate above the calculated values, which must be considered during processing. For modal shapes, point-by-point interpolation (spatial splines) is used: for each coordinate of each mode node, a tensor spline is applied as a function of time. Both interpolation methods make it possible to produce Figure 6-14 with the time series filled in blue (Experimental Data).

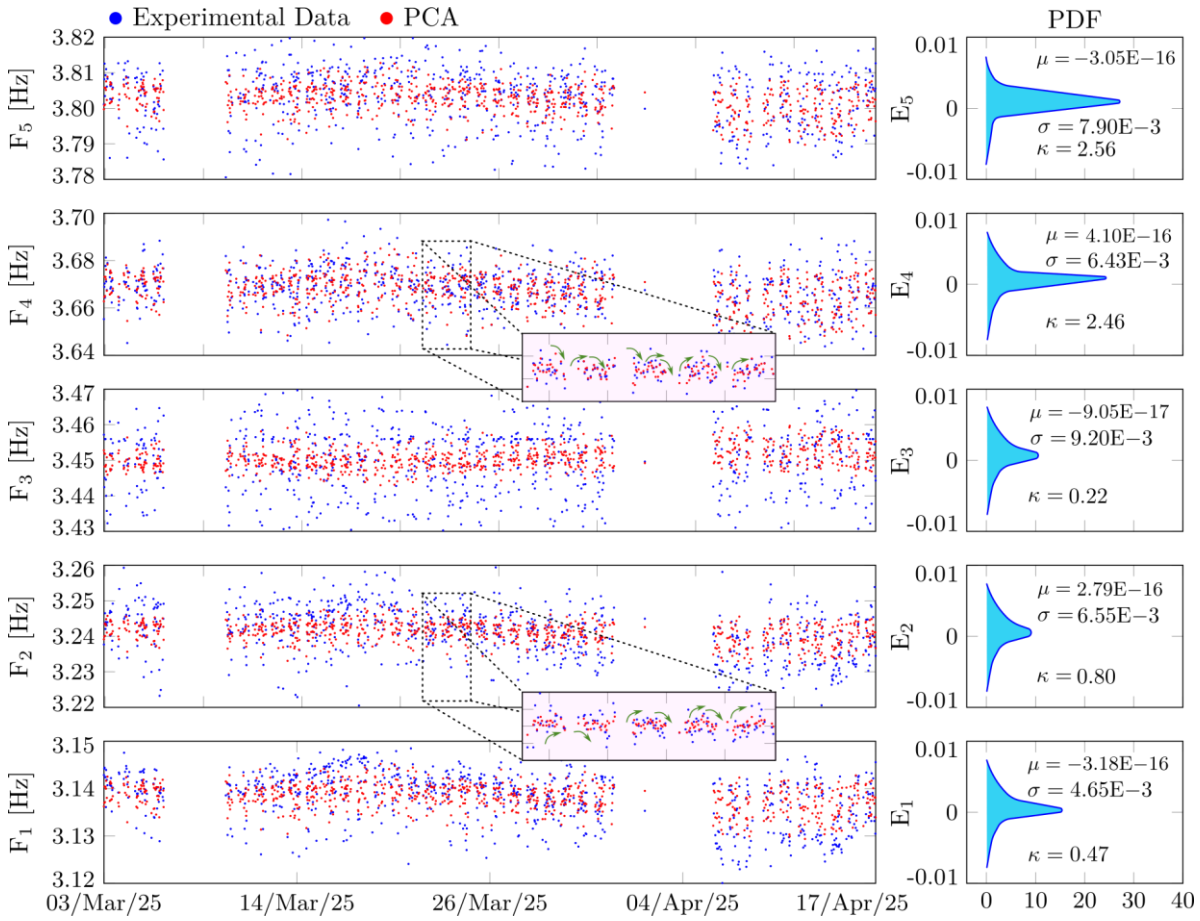

Figure 6-14: Elimination of EOC from the time series of the first three resonant frequencies of the Huerta de Mateo Bridge by PCA, and probability distribution functions (PDFs) of the resulting residuals.

It is evident that time series, in the frequency domain, exhibit fluctuations due to environmental and operational conditions (EOC). It is common to use multiple linear regression (MLR) models to extract residuals by removing these fluctuations from the time series; this approach requires measured independent variables such as temperature, humidity, etc. In the absence of such environmental data, Principal Component Analysis (PCA) can be applied: PCA identifies the directions (components) that explain the greatest proportion of total variance, since the environmental effects are captured across the time series. Figure 6-14 shows the results of removing these environmental effects, with the adjusted time series trace highlighted in red.

The effectiveness of the pattern recognition can be evaluated by examining the probability density functions (PDFs) of the residuals shown in Figure 6-14. Ideally, during normalization, the residuals from the training period should only reflect normally distributed errors due to limitations in defining the healthy baseline and minor environmental and operational condition (EOC) effects. In this context, it is noteworthy that the residuals have means (μ) very close to zero, with a maximum of 4.10×10^{-16} for Mode 4 (F_4)—an excellent result, since the goal is to get as close to zero as possible. In terms of standard deviation (σ), the greatest dispersion is 9.20×10^{-3}, which is also very good for this kind of analysis, as values closer to zero are ideal. Additionally, kurtosis values (κ) of 0.47, 0.80, 0.22, 2.46, and 2.56 were obtained for Modes 1–5, respectively. Given that $\kappa = 3$ is the theoretical value for a perfect Gaussian distribution, these results indicate that Modes 4 and 5 yield the best residual distributions, while Modes 1–3 perform considerably worse.

For Modes 4 and 5, the residuals meet quality expectations; this is not the case for Modes 1–3, largely because those time series require extensive interpolation and sometimes fail to capture true fluctuations. Moreover, only a month and a half of data are available (an admittedly small sample) so future analyses should improve as more data become available, since model training generally benefits from larger datasets.

6.2.2.6. Estimation of structural damping from vibrations induced by train traffic

In Section 6.2.2.5, using OMA, the dynamic properties of the bridge were determined over the entire monitoring period. As noted earlier, the estimated damping ratios were remarkably low an artifact of ambient background noise and the limited sensitivity of OMA under those conditions. Accordingly, the monitoring scheme, in addition to AVT, is designed to capture vibrations induced by train passages at a sampling frequency of 100 Hz, yielding the signal shown in Figure 6-15. Each signal spans 50 seconds—10 seconds before and 40 seconds after the train passage—triggered by sensor A7 (see Figure 6-1 (a) for its location) at a threshold of 1 g (≈ 10 m/s²). The use of these signals, together with the generated impulses, allows the extraction of damping ratios that accurately reflect the dynamic behaviour. However, this represents an inherent limitation of OMA, due to the low level of excitation the bridge receives during AVT. To address this, we have developed a methodology to correlate the frequencies and mode shapes obtained in Section 6.2.2.5 with the damping ratios determined from signals generated by train passages.

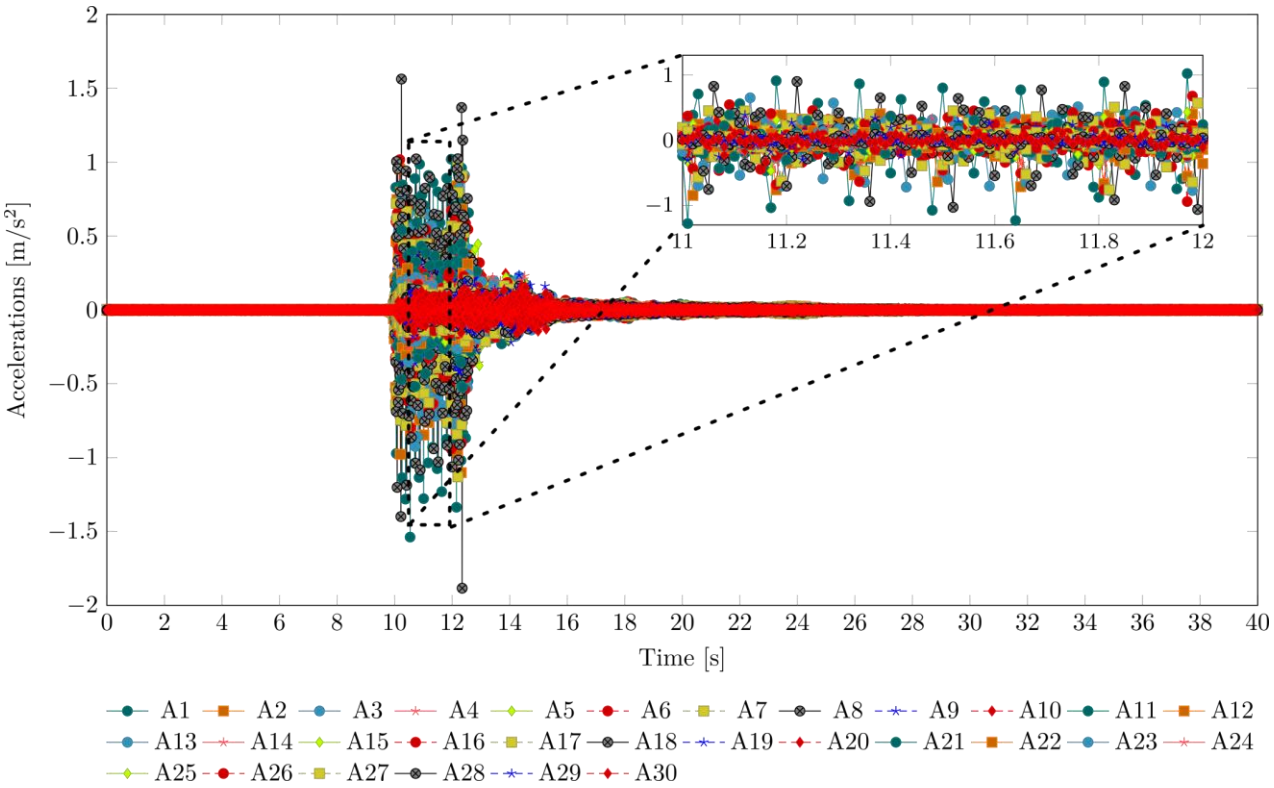

Figure 6-15: Acceleration signal generated by passing trains, recorded on March 3rd, 2025, at 12:40 p.m.

Figure 6-16 displays a flowchart outlining the methodology used for damping determination. The process begins with applying a Butterworth filter to each channel with a 3–5 Hz bandwidth, in accordance with the baseline identification defined in **¡Error! No se encuentra el origen de la referencia.**. Next, the number of components is reduced using Blind Source Separation (BSS); the extracted components correspond directly to the previously identified modes. Of the 30 initial components, 8 are retained, matching the baseline identification in **¡Error! No se encuentra el origen de la referencia.**. This component exhibits single-degree-of-freedom (SDOF) behaviour. Once the components of interest have been extracted, the free-decay response of one mode is determined using the Natural Excitation Technique (NExT). From that response, the dynamic parameters—namely natural frequency and damping ratio—are identified. To consolidate the results for each mode defined earlier (see Table 5), all estimates whose frequencies differ by no more than 3 % are grouped together. Finally, by repeating this procedure for each acceleration record corresponding to a train passage, time series of damping ratios are obtained using Ibrahim Time Domain (ITD).

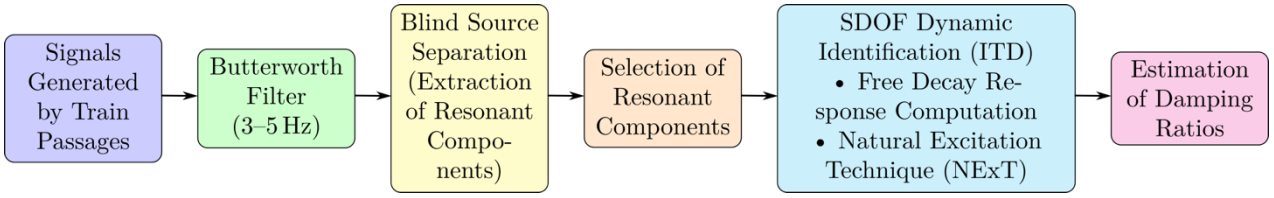

Figure 6-16: Flowchart for damping determination from train-induced signals.

Using the methodology outlined above as a reference, damping ratios are extracted for the entire monitoring period. The signal recorded on March 12th, 2025, at 12:40 p.m. (previously plotted in Figure 6-15) serves as the benchmark. From this dataset, the next step is to identify the resonant components via BSS. In this respect, Figure 6-17 Figure (a) shows the 30 channels in the frequency domain, where the resonant peaks appear across the 0–50 Hz range. Two prominent peaks are visible in the 0–10 Hz band, and around ten resonant peaks are observed in the 15–50 Hz band. Meanwhile, in Figure 6-17 (b) the eight resonant components are obtained, which correspond to the identification carried out by CoV-SSI in Section 6.2.2.5.

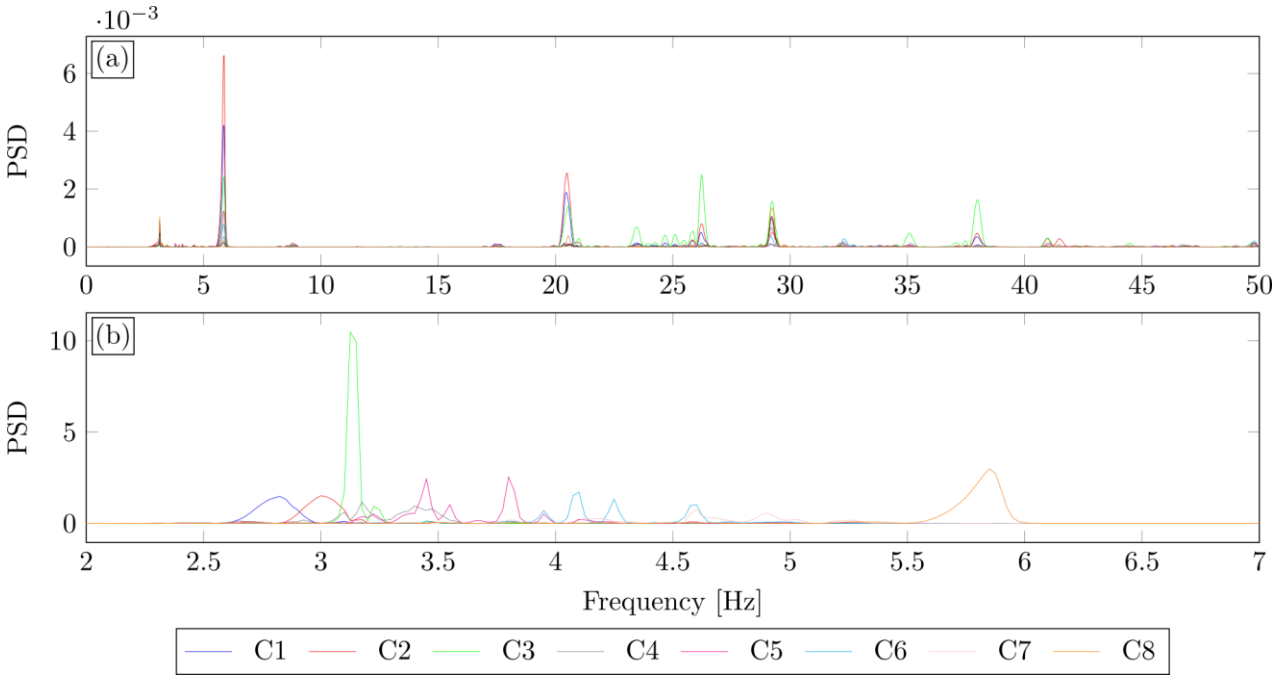

Figure 6-17: (a) Frequency-domain spectrum of the original signal and (b) blind source separation to obtain the eight resonant components.

To obtain the frequencies and damping rates for each of the eight resonant components using BSS, it is necessary to extract the free-decay response via the NExt method. Figure 6-18 shows the response for the resonant components corresponding to modes F_1 (a) and F_2 (b), respectively. Once these responses are available, the dynamic parameters governing their behaviour—in terms of frequency and damping rate are identified using the ITD method. The results for the reference signal are presented in **¡Error! No se encuentra el origen de la referencia.**.

For this case study, the Huerta de Mateo Bridge, it is very useful to obtain time series of damping over the entire monitoring period. In this context, the values previously obtained from the generated signal are used as a baseline to form clusters for each of the modes. Thus, the time series of damping rates are shown in Figure 6-19, and their statistical characteristics are summarized in **¡Error! No se encuentra el origen de la referencia.**.

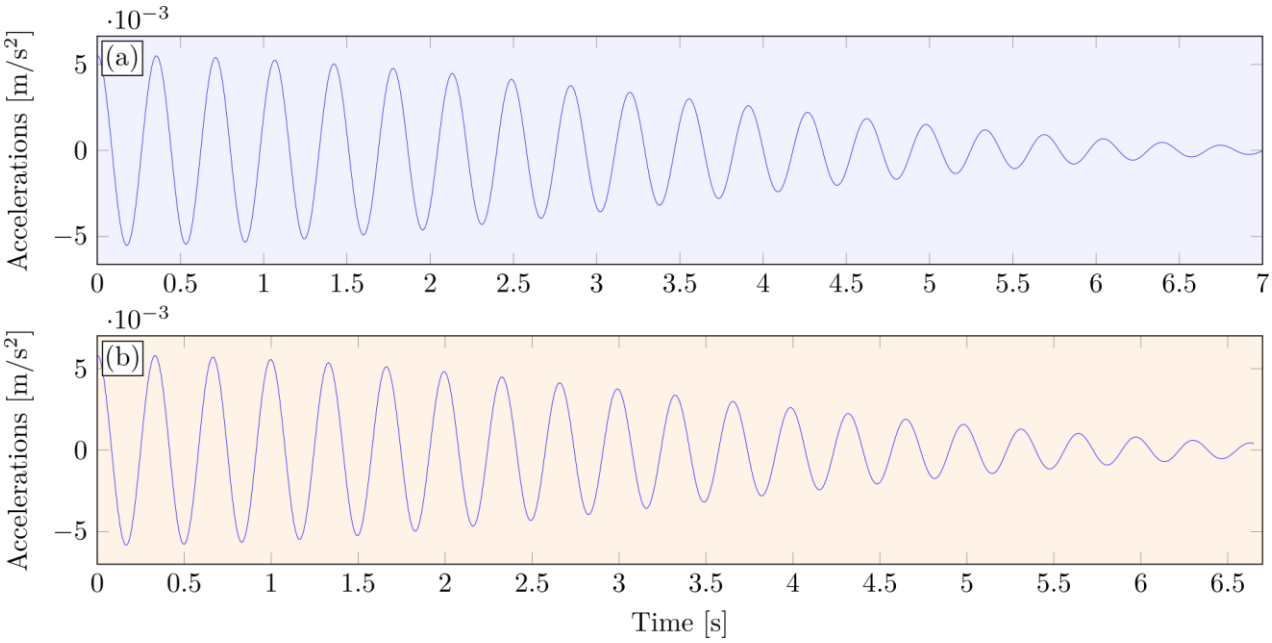

Figure 6-18: Free-decay response obtained using the NExt method for the components corresponding to (a) 3.14 Hz (F_1) and (b) 3.24 Hz (F_2).

As shown in **¡Error! No se encuentra el origen de la referencia.**, the frequency error—relative to the OMA results previously reported in **¡Error! No se encuentra el origen de la referencia.**—is very small; from a practical standpoint, these values are only needed to obtain the damping ratio for each mode. By contrast, the error in the damping-ratio estimates is quite large, owing to the low damping ratios determined by OMA as a result of the sensors' limited sensitivity. Although these values differ from those obtained via OMA, they are nonetheless appropriate for this type of structure. In some cases, the SR is low—as with modes 3 and 7—because their frequencies are so close that the tracking algorithm had to be adjusted.

Mode	Label	March 3rd, 2025, 12:40 pm				Continuous monitoring	
		Frequency [Hz]	Error [%]	Damping [%]	Error [%]	Mean Damp. [%]	SR [%}
1	F_1	3.16	0.01	2.12	6.32	2.12 ± 0.07	63.7
2	F_2	3.26	0.62%	2.03	154%	2.02 ± 0.12	87.7
3	F_3	3.42	-0.02	0.95	-0.17	0.99 ± 0.02	48.8
4	F_4	3.66	0.00%	1.60	333%	1.64 ± 0.04	77.6
5	F_5	3.89	0.02	1.37	3.02	1.33 ± 0.04	86.9
6	F_6	4.10	0.24%	1.96	356%	1.98 ± 0.06	93.5
7	F_7	4.21	-0.01	1.00	0.91	0.98 ± 0.01	54.2
8	F_8	4.45	0.91%	1.82	214%	1.84 ± 0.08	81.4

Table 6-2: Experimentally determined damping ratios of the Huerta de Mateo Bridge measured at 12:40 PM on March 3rd, 2025, and throughout the monitoring period.

The temporal variation of mode-specific damping ratios does not arise solely from structural behaviour but also reflects changing environmental conditions. For instance, gradual shifts in

ambient temperature and humidity tend to modulate material damping, producing slow drifts in the measured values, while sporadic wind gusts or rain events can trigger short-term spikes or drops. In Figure 6-19: Evolution of the Huerta de Mateo Bridge's damping ratios under train-pass vibrations, March 3rd to April 17th, 2025., you can see how, for Mode 1, damping gradually increases on warmer afternoons—likely due to temperature-dependent changes in joint friction—whereas Mode 3 shows sharp fluctuations coincident with high-wind periods. Accounting for these environmental effects is essential to distinguish true structural changes from natural variability and to set reliable alert thresholds for maintenance.

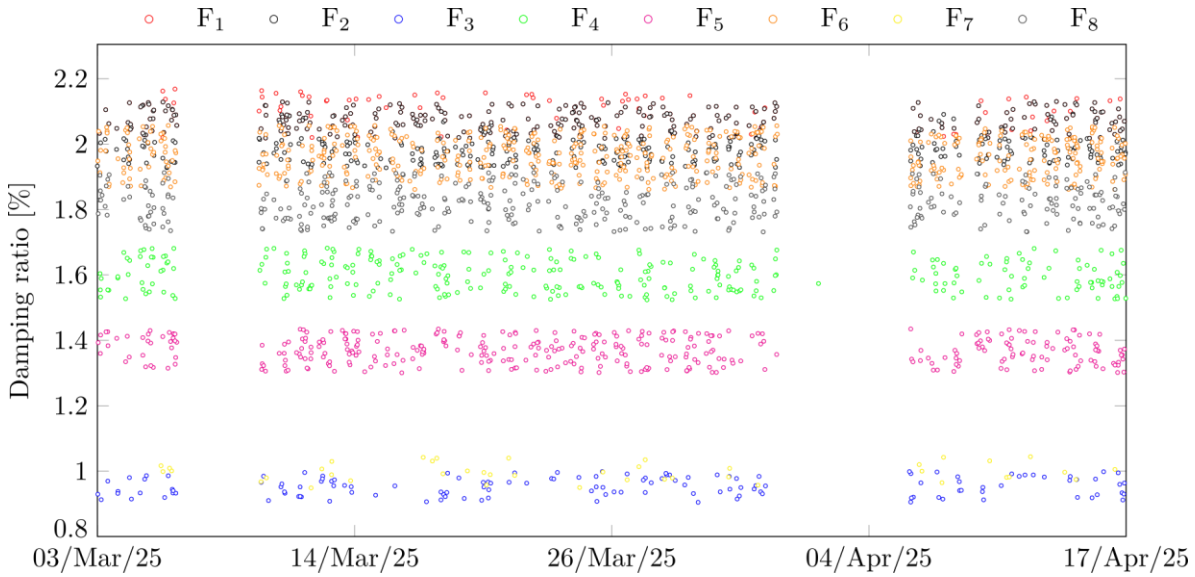

Figure 6-19: Evolution of the Huerta de Mateo Bridge's damping ratios under train-pass vibrations, March 3rd to April 17th, 2025.

The study of these structural properties is of vital importance, since any defect in the structure is reflected in them, which is why their monitoring is maintained in real time. Moreover, their use is crucial as a complement to the results obtained by OMA.

6.2.2.7. Finite element modelling and model calibration

To train the digital twin using a realistic, physics-based numerical model, we built a 3D finite-element model of the Huerta de Mateo Bridge in the SAP2000 environment (Figure 6-20). The geometry was derived from structural drawings and in situ inspections. Because of the structure's massive nature, only the portions of the columns embedded in the surrounding solidified areas were included; the columns' supports were represented by springs, and the pot bearings by Link elements. Modelling the pot bearings as Link elements in SAP2000 enables direction-specific stiffnesses and custom force-displacement curves that capture nonlinearity, gap opening, and hysteresis; incorporates sliding/friction behaviour via yield points or Coulomb-friction laws; and allows each support to be assigned directly between nodes with unique properties. This approach avoids artificial rigidities and faithfully simulates the elastomeric and PTFE sliding characteristics of the bearings, yielding more accurate seismic and structural responses.

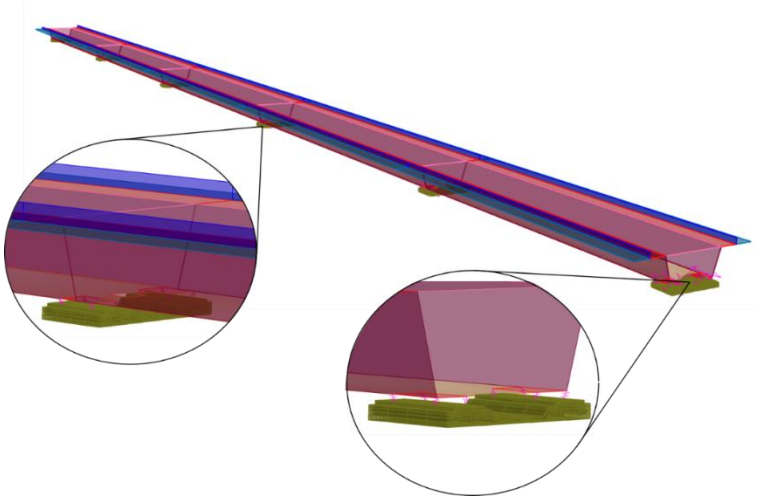

Figure 6-20: FEM of the Huerta de Mateo Bridge.

The FEM is built with shell elements for the deck and bridge ribs, link elements to simulate the pot supports (deck–column interaction), and solid elements for the top of the columns. The shell elements are meshed with square faces of 0.50 m side length, while the solid elements use cubes of 0.40 m side length. In total, the model comprises 13 620 nodes, 63 shell elements, 48 link elements, and 9 120 solid elements. A modal analysis takes approximately 35 seconds on a PC equipped with an Intel(R) Xeon(R) Gold 6136 CPU @ 3.00 GHz (6 cores) and 8 GB of RAM.

A single homogenized material is considered for the entire model. The initial constitutive properties were selected from the values corresponding to an elastic modulus of 34 GPa ±5% and a density of 2350 kg/m^3 ±5%, both parameters extracted from the structural drawings. This variation in both parameters has been considered because the properties of concrete may increase in the short term but decrease in the long term due to creep or degradation effects.

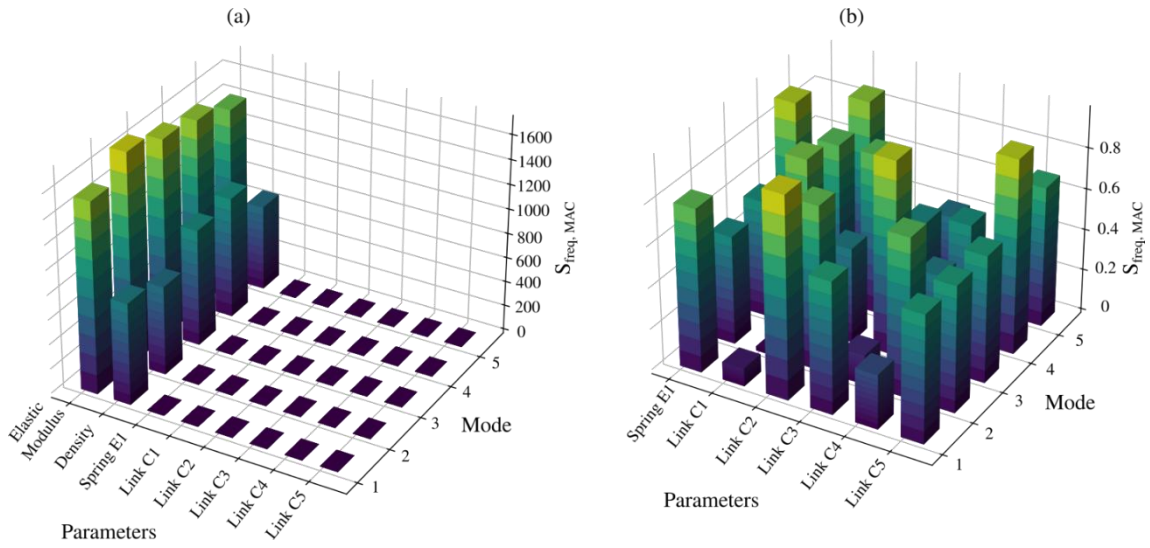

Figure 6-21: Model sensitivities for the most critical regions based on frequencies and mode shapes ($S_{freq, MAC}$), using a 5 % sensitivity threshold.

In Figure 6-21(a), density and the modulus of elasticity exhibit very high sensitivity values (density roughly 500–1 000 and modulus of elasticity between 1 000–2 000) compared to the other parameters, whose values—shown in Figure 6-21(b)—all lie within a narrow range (0–1) with none standing out, indicating similar importance; this analysis shows that, for model updating, validation and refinement should be prioritized for density and modulus of elasticity due to their strong influence on the modal response, while joint calibration of the remaining parameters can be treated as a secondary step.

6.2.3. Structural health monitoring for pot bearings

Following the analysis on Huertas de Mateo viaduct in section 6.2, as part of the project aimed at modernizing and improving the predictive maintenance of critical railway infrastructure, a comprehensive sensor-based monitoring system for pot bearings has also been implemented on the Viaduct Arroyo de las Huertas de Mateo. As stated before, this viaduct, known for its considerable length and curved design, is subject to significant dynamic and torsional loads due to high-speed rail traffic. These operational conditions generate substantial relative displacements and stresses between the deck and its supports, leading to premature deterioration of structural support elements, particularly the pot bearings.
To analyse this structural behaviour and anticipate potential failures, an advanced sensor network has been designed and deployed (system described in section 6.2.3.1), providing real-time data on the condition of critical structural elements and their surroundings. Structural Health Monitoring techniques are applied on the data which is continuously retrieved through this monitoring system as explained on section 6.2.4.1.

6.2.3.1. Pot bearing monitoring system

The monitoring system for pot bearing is composed by the following sensors:

- A total of **14 Linear Variable Differential Transformers** (LVDTs) were installed on four piers (P1, P5, P9, P15) and at Abutment 1 of the viaduct. These sensors are responsible for measuring linear displacements between the bridge deck and its supports, providing essential information to assess potential unwanted movements or excessive shifts that could compromise the structural integrity or functionality of the pot bearings.
- In addition, **8 inclinometers** were installed across the supports and adjacent slopes to monitor rotational movements of the supports and surrounding ground. This is crucial to detect abnormal tilting or rotations that, combined with the linear displacement measurements, allow for a precise diagnosis of the support behaviour.

- To complement the structural monitoring, **8 resistance thermometers** were positioned at strategic points to measure the thermal behaviour of the structure. Given that temperature gradients significantly affect material expansion, contraction, and internal stress distribution, tracking temperature variations is essential for understanding and contextualizing displacement data.

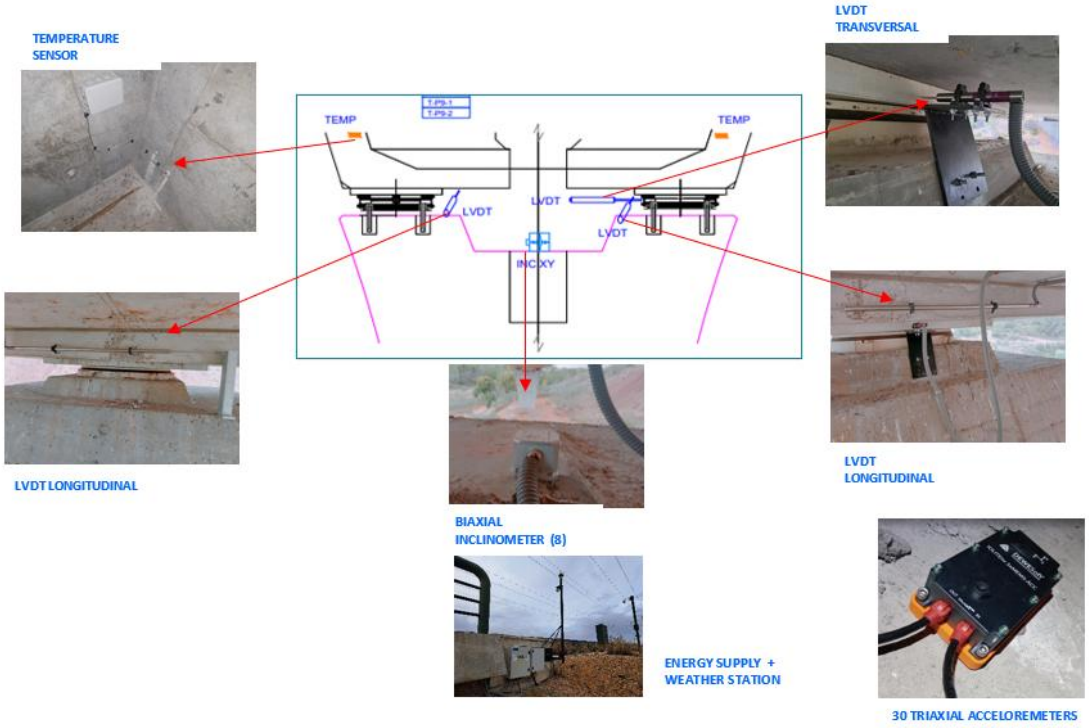

Figure 6-22: Location of the sensors.

- To complement the monitoring, a **series triaxial accelerometers** have been installed, for detecting and analyzing dynamic responses and vibrations, which will allow to gather more information about the dynamic behavior of the viaduct, enabling us to compare the theoretical acceleration with the values recorded in the central spans.

Figure 6-23: Tiltmeter installed on P11 and outside at the beginning of the bridge.

Figure 6-24: Gateway installed between spans 11 and 12, on p11

The integrated sensor systems on the viaduct and surrounding infrastructure enable real-time structural assessment under static and dynamic conditions. The monitoring system aims to:

- Diagnose the condition of pot bearings by detecting displacements, rotations, and thermal effects.
- Predict structural damage early to enable preventive maintenance and avoid costly repairs.
- Optimize maintenance planning with continuous performance data.
- Analyze interactions between the bridge deck, supports, and adjacent railway infrastructure for a comprehensive structural understanding.
- Enhance safety, reliability, and extend the lifespan of critical railway components.

This solution advances predictive maintenance by combining advanced sensors, dynamic modelling, and continuous analysis for safe and efficient high-speed rail operations
The monitoring of the behaviour of the pot bearings has focused on instrumentation installed at abutment E1 and piers P1, P5, P9, and P15. As previously indicated, each monitored pier is equipped with three LVDT displacement sensors, two internal concrete temperature sensors, and biaxial inclinometers to measure tilt along the X and Y axes.
This instrumentation system comprises a total of 35 data acquisition channels (including environmental channels and the aforementioned measurement devices).
Since the completion of the installation in December 2024, various calibration and adjustment operations have been carried out. During this testing and adjustment period, data from the sensors have been collected almost daily at different sampling frequencies to determine the optimal configuration for data logging.

The table below summarizes all measurement points:

	ID	Name	Location	MEDIDA	TYPE	N/S SENSOR	N/S Adq. IOLITE	Measuring ranee	Sensitivity	Unit	
Estribo E-1	A-1	E TEMP EXT	Estribo	Temperatura	RTD	-	DB23031538	-200 -850 ºc ?	1	ºC	Temperatura
	A-2	NA	Estribo			SN	DB23031538				
	A-3	E LVDT FIJO	Estribo	Desplazamiento Long.	DCC760C/1870	248343	DB23031538	±300 mm	0.027 mA/mm	mm	Desplazamiento
	A-4	E LVDT LIBRE	Estribo	Desplazamiento Long.	DCC760C/1870	248345	DB23031538	±300 mm	0.027 mA/mm	mm	Desplazamiento
	A-5	E TEMP CAJON	Estribo	Temperatura			DB23031538	ºC		ºC	Temperatura
	A-6	E HUM CAJON	Estribo	Humedad			DB23031538	%		%	Humedad
	B-1	VANO 1 ACC X	Estribo	Aceleración Longitudin	IOLITEiw-3xMEMS-ACC-8g	DA22341190	DA22341190	±2 g	1	g	Aceleración
	B-2	VANO 1 ACC Y	Estribo	Aceleración Transversa	IOLITEiw-3xMEMS-ACC-8g	DA22341190	DA22341190	±2 g	1	g	Aceleración
	B-3	VANO 1 ACC Z	Estribo	Aceleración Vertical	IOLITEiw-3xMEMS-ACC-8g	DA22341190	DA22341190	±2 g	1	g	Aceleración
Pila 1	C-1	P1 TEMP NORTE	P1	Temperatura Horm.	RTD	-	DB23031540		1	ºC	Temperatura
	C-2	P1 TEMP SUR	P1	Temperatura Horm.	RTD	-	DB23031540		1	ºC	Temperatura
	C-3	P1 INC AXIS X	P1	Inclinación eje Long.	SST420	P12005D0005	DB23031540	±5 º	1,60 mA/deg	deg	Angulo
	C-4	P1 INC AXIS Y	P1	Inclinación eje Trans.	SST420	P12005D0005	DB23031540	±5 º	1,60 mA/deg	deg	Angulo
	C-5	P1 LVDT TRANSVERSAL	P1	Desplazamiento Trans.	DCC025A/256	245642	DB23031540	±12.5 mm	0.641 mA/mm	mm	Desplazamiento
	C-6	P1 LVDT LIBRE	P1	Desplazamiento Long.	DCC760C/1870	248341	DB23031540	±300 mm	0.027 mA/mm	mm	Desplazamiento
	D-1	P1 LVDT FIJO	P1	Desplazamiento Long.	DCC760C/1870	248342	DA22342273	±300 mm	0.027 mA/mm	mm	Desplazamiento
Pila 5	I-1	P5 LVDT FIJO	P5	Desplazamiento Long.	DCC760C/1870	248340	DA22342274	±300 mm	0.027 mA/mm	mm	Desplazamiento
	J-1	P5 TEMP NORTE	P5	Temperatura Horm.	RTD	-	DB23029001		1	ºC	Temperatura
	J-2	P5 TEMP SUR	P5	Temperatura Horm.	RTD	-	DB23029001		1	ºC	Temperatura
	J-3	P5 INC AXIS X	P5	Inclinación eje Long.	SST420	P12004D0005	DB23029001	±5 º	1,60 mA/deg	deg	Angulo
	J-4	P5 INC AXIS Y	P5	Inclinación eje Trans.	SST420	P12004D0005	DB23029001	±5 º	1,60 mA/deg	deg	Angulo
	J-5	P5 LVDT TRANSVERSAL	P5	Desplazamiento Trans.	DCC025A/256	245640	DB23029001	±12.5 mm	0.640 mA/mm	mm	Desplazamiento
	J-6	P5 LVDT LIBRE	P5	Desplazamiento Long.	DCC760C/1870	248344	DB23029001	±300 mm	0.027 mA/mm	mm	Desplazamiento
Pila 9	G-1	P9 LVDT FIJO	P9	Desplazamiento Long.	DCC500C/256	248336	DA22342277	±250 mm	0.032 mA/mm	mm	Desplazamiento
	H-1	P9 TEMP NORTE	P9	Temperatura Horm.	RTD	-	DB23029186		1	ºC	Temperatura
	H-2	P9 TEMP SUR	P9	Temperatura Horm.	RTD	-	DB23029186		1	ºC	Temperatura
	H-3	P9 INC AXIS X	P9	Inclinación eje Long.	SST420	P12001D0005	DB23029186	±5 º	1,60 mA/deg	deg	Angulo
	H-4	P9 INC AXIS Y	P9	Inclinación eje Trans.	SST420	P12001D0005	DB23029186	±5 º	1,60 mA/deg	deg	Angulo
	H-5	P9 LVDT TRANSVERSAL	P9	Desplazamiento Trans.	DCC025A/256	245638	DB23029186	±12.5 mm	0.639 mA/mm	mm	Desplazamiento
	H-6	P9 LVDT LIBRE	P9	Desplazamiento Long.	DCC500C/256	248338	DB23029186	±250 mm	0.032 mA/mm	mm	Desplazamiento
Pila 15	E-1	P15 TEMP NORTE	P15	Temperatura Horm.	RTD	-	DB23031539		1	ºC	Temperatura
	E-2	P15 TEMP SUR	P15	Temperatura Horm.	RTD	-	DB23031539		1	ºC	Temperatura
	E-3	P15 INC AXIS X	P15	Inclinación eje Long.	SST420	P12003D0005	DB23031539	±5 º	1,60 mA/deg	deg	Angulo
	E-4	P15 INC AXIS Y	P15	Inclinación eje Trans.	SST420	P12003D0005	DB23031539	±5 º	1,60 mA/deg	deg	Angulo
	E-5	P15 LVDT TRANSVERSAL	P15	Desplazamiento Trans.	DCC025A/256	245641	DB23031539	±12.5 mm	0.641 mA/mm	mm	Desplazamiento
	E-6	P15 LVDT LIBRE	P15	Desplazamiento Long.	DCC500C/256	248334	DB23031539	±250 mm	0.032 mA/mm	mm	Desplazamiento
	F-1	P15 LVDT FIJO	P15	Desplazamiento Long.	DCC500C/256	248337	DA22342275	±250 mm	0.032 mA/mm	mm	Desplazamiento

Figure 6-25: Sensor Configuration Table.

As a sample of the data collection process, the following figures show temperature sensor readings along with longitudinal displacement measurements at the piers for the past four months. For long-term analysis, it is necessary to record data over a full year in order to draw meaningful conclusions about the structural behavior.

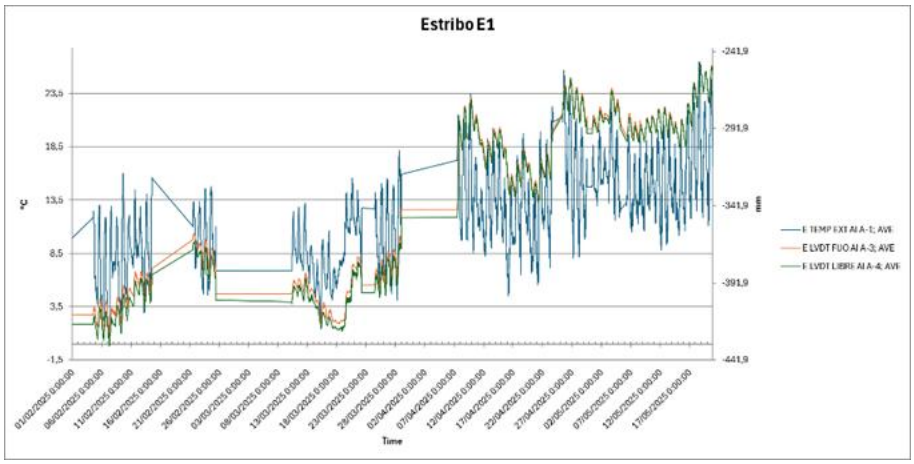

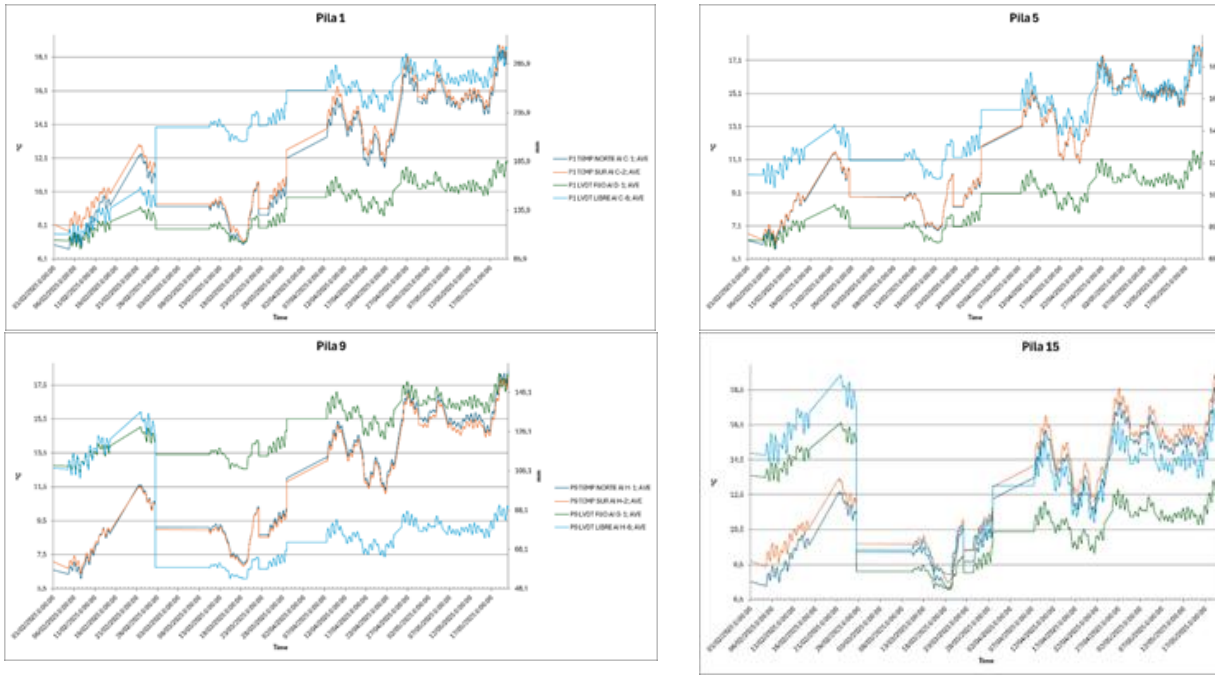

Figure 6-26: Recorded temperature and displacement data. February-May 2025.

6.2.3.2. POT inspection

On May 28 and 29, 2025, an initial visual inspection of all the structure's supports was carried out with the three-fold purpose of characterizing them, establishing their state of conservation, and taking a series of measures to allow for objective monitoring over time.

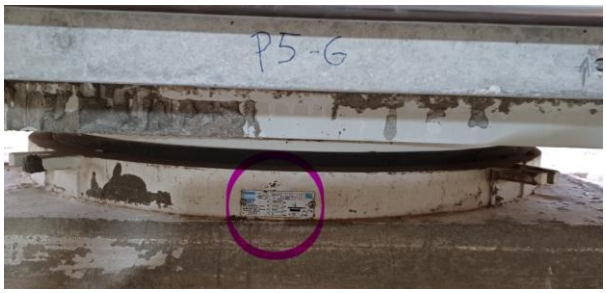

Figure 6-27: Pot bearing ID.

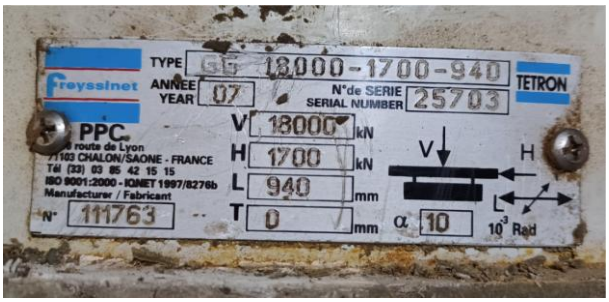

Figure 6-28: Pot bearing ID detail.

All supports include, at a minimum, side, front, and back photos, as well as those that help describe any unique features or defects in the support apparatus. General photos were also taken to provide a comprehensive overview of the element.

- Special care was taken to detect and measure support displacement and possible rotation.

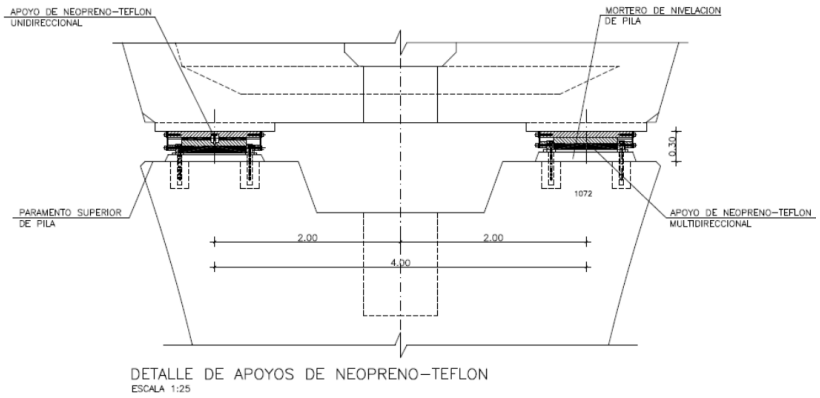

Figure 6-29: Pot bearing cross section.

- Dimension measurements: These were measured at three points on each support (marked in yellow below) in addition to the two dimensions near the Teflon disc (marked in pink below). Sets of gauges were used to take measurements.

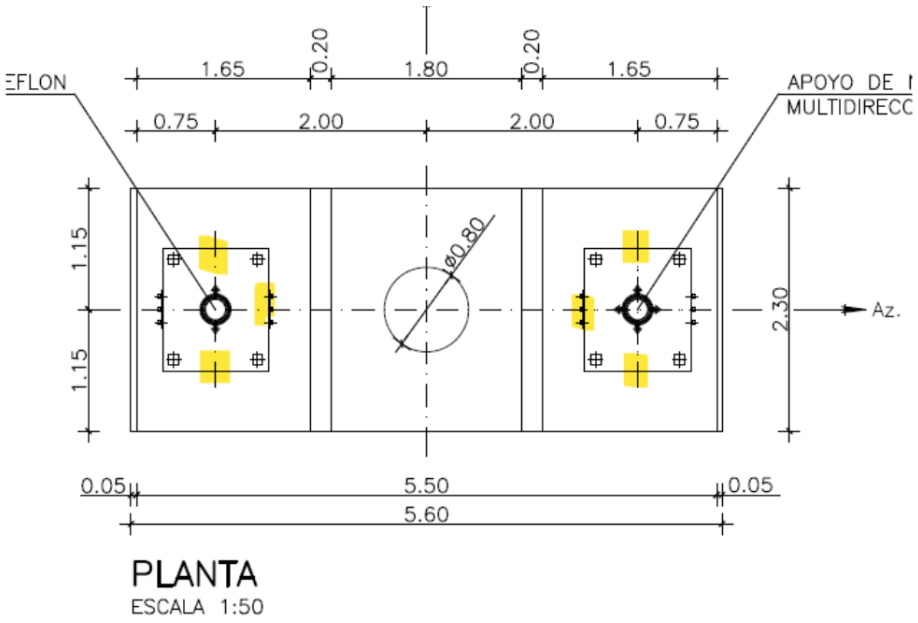

Figure 6-30: Pot bearing measurement points.

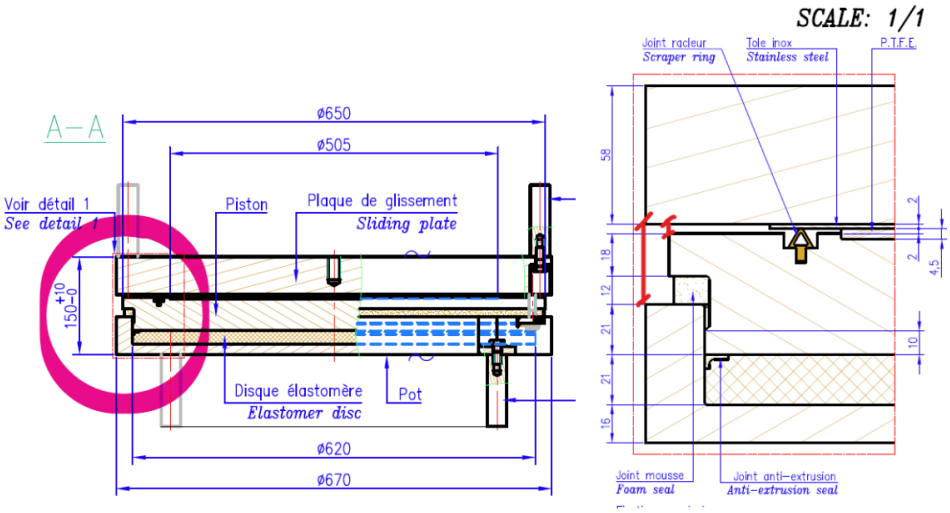

Figure 6-31: Pot bearing measurement points detail.

6.2.4. Bridge platform monitoring

To extend the scope of structural monitoring, additional instrumentation has also been deployed in adjacent railway infrastructure: three manholes equipped with embedded accelerometers and inclinometers have been installed in the trenches of the catenary post foundations near the viaduct. These manholes are specifically designed to monitor displacement and rotational behaviour of nearby infrastructure components, capturing potential stress transfers or ground movements that may affect structural stability. In addition to these instruments, a dedicated gateway has been installed to enable the collection, preprocessing, and transmission of data from all sensors, ensuring reliable communication with the central monitoring platform and supporting continuous data analysis in real time.

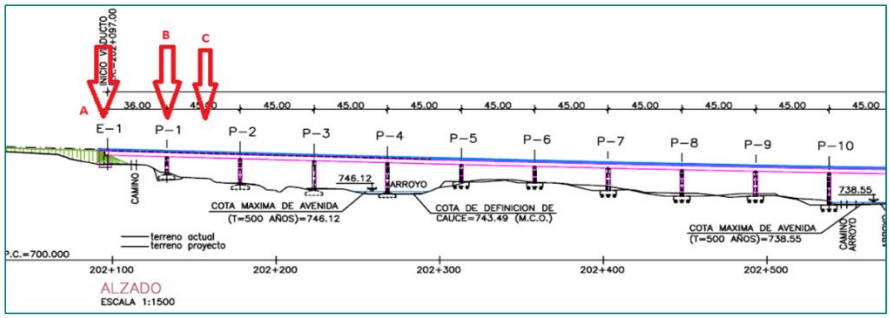

Manhole A

Manhole B

Manhole C

Figure 6-32: Location of the manholes with the sensors and gateway.

To ensure measurement accuracy and prevent unwanted sensor displacement, these manholes were securely anchored using mortar. This installation method guarantees reliable, high-quality data collection over extended periods, minimizing risks of external interference.

As part of the structural monitoring project for the Huertas Mateo Viaduct, two accelerometers and two inclinometers have been installed to assess the dynamic response of the structure during the passage of high-speed trains. This system is part of an Infrastructure Health Monitoring (IHM) strategy that enables real-time evaluation of the viaduct's structural condition through data analysis, processed using the Fast Fourier Transform (FFT).

The accelerometers installed on the viaduct record vertical structural acceleration over time, allowing engineers to observe the structure's dynamic response, particularly during the passage of high-speed trains. By applying Fast Fourier Transform (FFT) to the time-domain data, the signals are translated into the frequency domain, enabling the identification of dominant vibration frequencies associated with both the viaduct's natural modes and excitations caused by train movement. Additionally, the FFT reveals the energy distribution across frequency bands, which helps distinguish structural responses—typically found at lower frequencies (<10 Hz)—from external sources of interference such as mechanical noise or catenary system effects. By monitoring temporal changes in the frequency spectrum, it is also possible to detect variations in stiffness in the deck or supports, which may indicate early signs of deterioration or changes in structural performance.

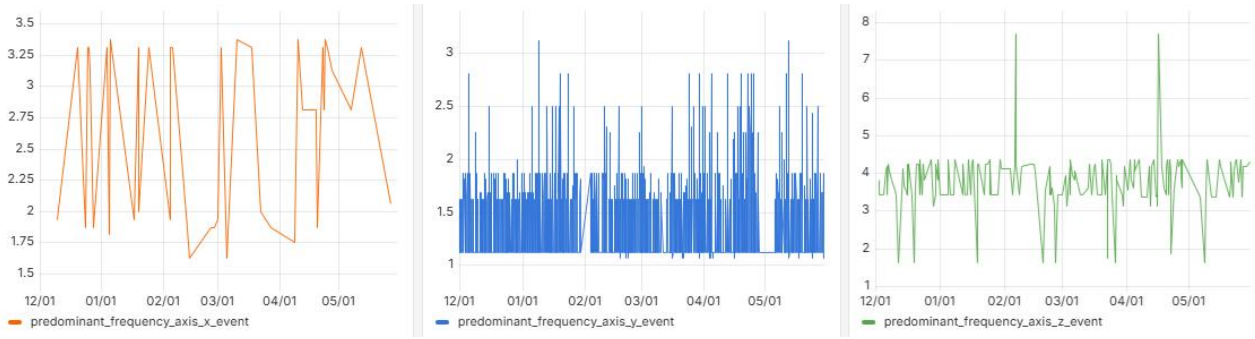

Figure 6-33: Accelerometer measurements.

Inclinometers complement the dynamic analysis by measuring angular displacements of the deck at key cross-sections, providing valuable insights into how the structure deforms under load. When combined with FFT results from the accelerometers, inclination data allows for a correlation between vibration peaks and actual physical movements of the deck or supports, validating the observed dynamic behaviour. This integration also facilitates the detection of structural imbalances or asymmetries, especially when inclination readings differ significantly across the span. Furthermore, it supports the assessment of excessive deflections under dynamic loading conditions, which may indicate accumulated deformation over time or the early onset of mechanical issues in elements such as bearings or expansion joints.

Figure 6-34: Inclinometer readings.

Beyond ensuring operational safety and comfort, this monitoring approach provides the foundation for predictive maintenance, allowing for the early detection of structural issues before they become critical. This strategy helps ensure the durability, resilience, and efficiency of the infrastructure, while also optimizing resource use and reducing operational costs—fully aligned with innovation and sustainability goals in modern railway asset management.

6.2.4.1. Pot bearing Structural Health Monitoring

This section describes how monitoring information is used to assess and predict the pot bearing condition and degradation using the bridge monitoring through the LVDT sensors.

Following the installation of the sensors and the data acquisition and publishing system, ongoing work is focused on properly structuring the received measurements to support various analyses of the LVDTs.

The original system captures 55-second signal segments at a frequency of 200 Hz, triggered by the accelerometers upon detecting a passing train. In parallel, a new system is being developed to enable continuous monitoring at a lower frequency, tailored to the pot beating degradation model.

The available data is analysed in order to get a first glance of the system behaviour until a proper set of the data with the adequate monitoring is obtained. This preliminary data analysis analyses a batch of data from 10-03-2025 until 23-04-2025, which includes 1252 signals of 55 seconds.

Figure 6-35 to Figure 6-38 show the signals measured during the entire time period for the longitudinal displacement of the guided pots, the free pots and the transversal displacement of the free pots correspondingly. The longitudinal measurements for E1 showed abnormal behaviour with noisy signal and unreasonable measurements, and adjustments were performed, therefore these signals can only be studied from 08-04-2025 on. Figure 6-36 the same measurement without E1. These plots illustrate the pot displacements during train passages, highlighting their trends and displacement ranges.

The longitudinal displacement ranges ordered from higher to lower is E1, P1, P5 and P15. The ranges between longitudinal measurements in guided and free are similar (but in the E1 cases due to the noise in the original measurements). Transversal movements show shorter displacements with a range lower than 0.8 mm in all cases.

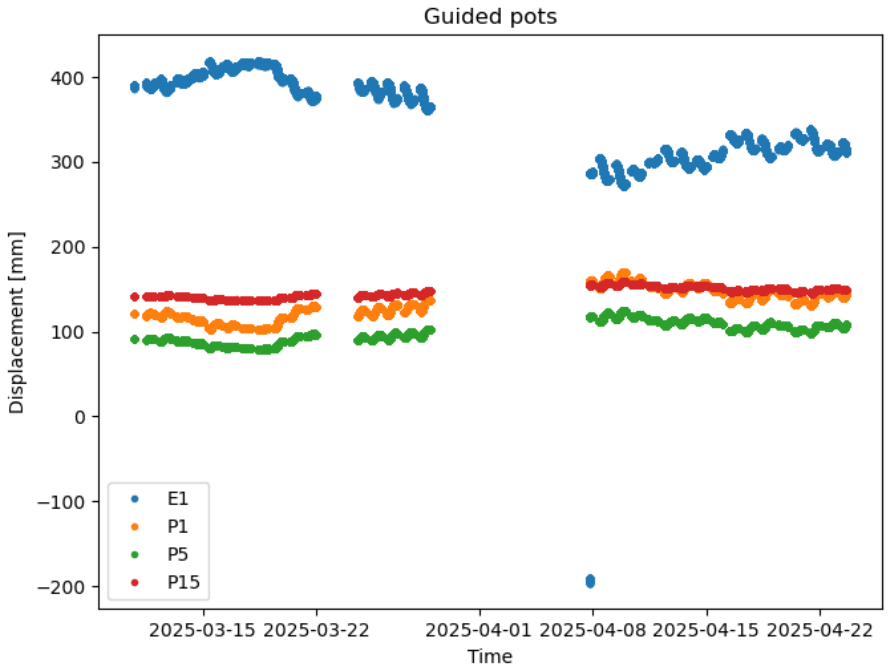

Figure 6-35: Guided pots longitudinal displacement.

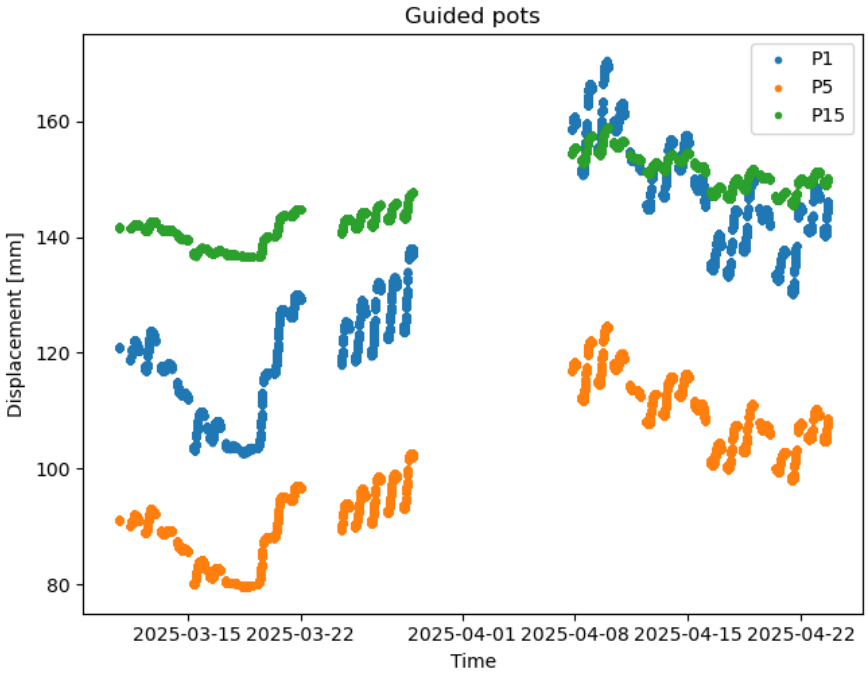

Figure 6-36: Guided pots longitudinal displacement without embankment.

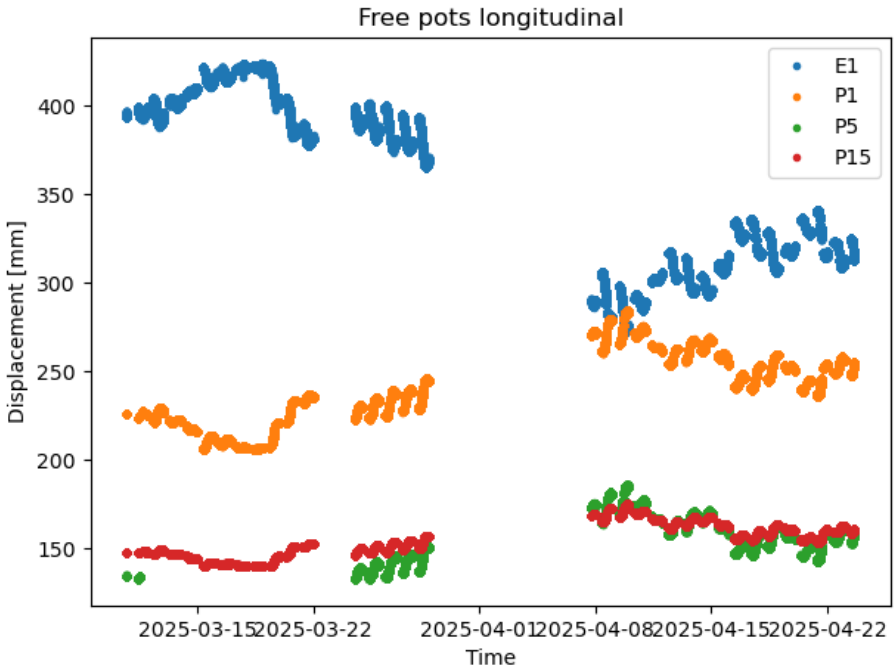

Figure 6-37: Free pots longitudinal displacement.

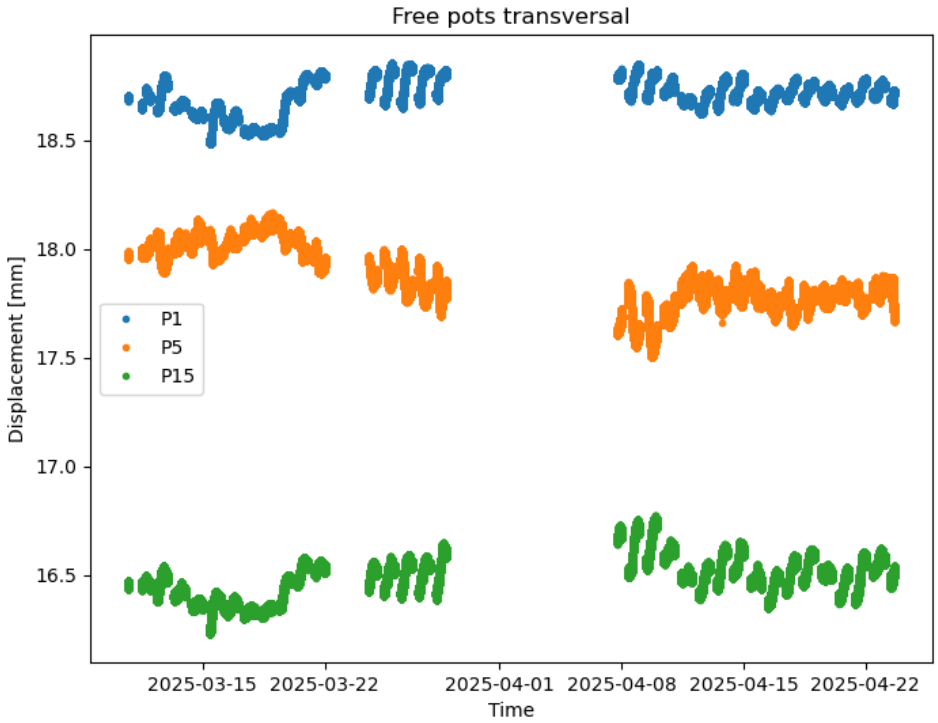

Figure 6-38: Free pots transversal displacement.

Displacements [mm]	E1	P1	P5	P15
Guided min	-196.053574	102.661514	79.538658	136.527756
Guided max	418.92218	170.530746	124.807701	158.929901
Free Longitudinal min	273.139801	206.036072	132.484436	140.21846
Free Longitudinal max	424.150238	284.743439	186.005951	175.138596
Free transversal min	-	18.482803	17.501303	16.228268
Free transversal max	-	18.853912	18.163565	16.769976

Table 6-3: Maximum and minimum displacements.

To get a better insight in the measurements, Figure 6-39 shows the whole signal with different black rectangles showcasing the next figure zoom. (a) Shows the whole measurement, (b) the zoom of signal on rectangle of graph (a) and (c) the zoom of signal on rectangle of graph (b).

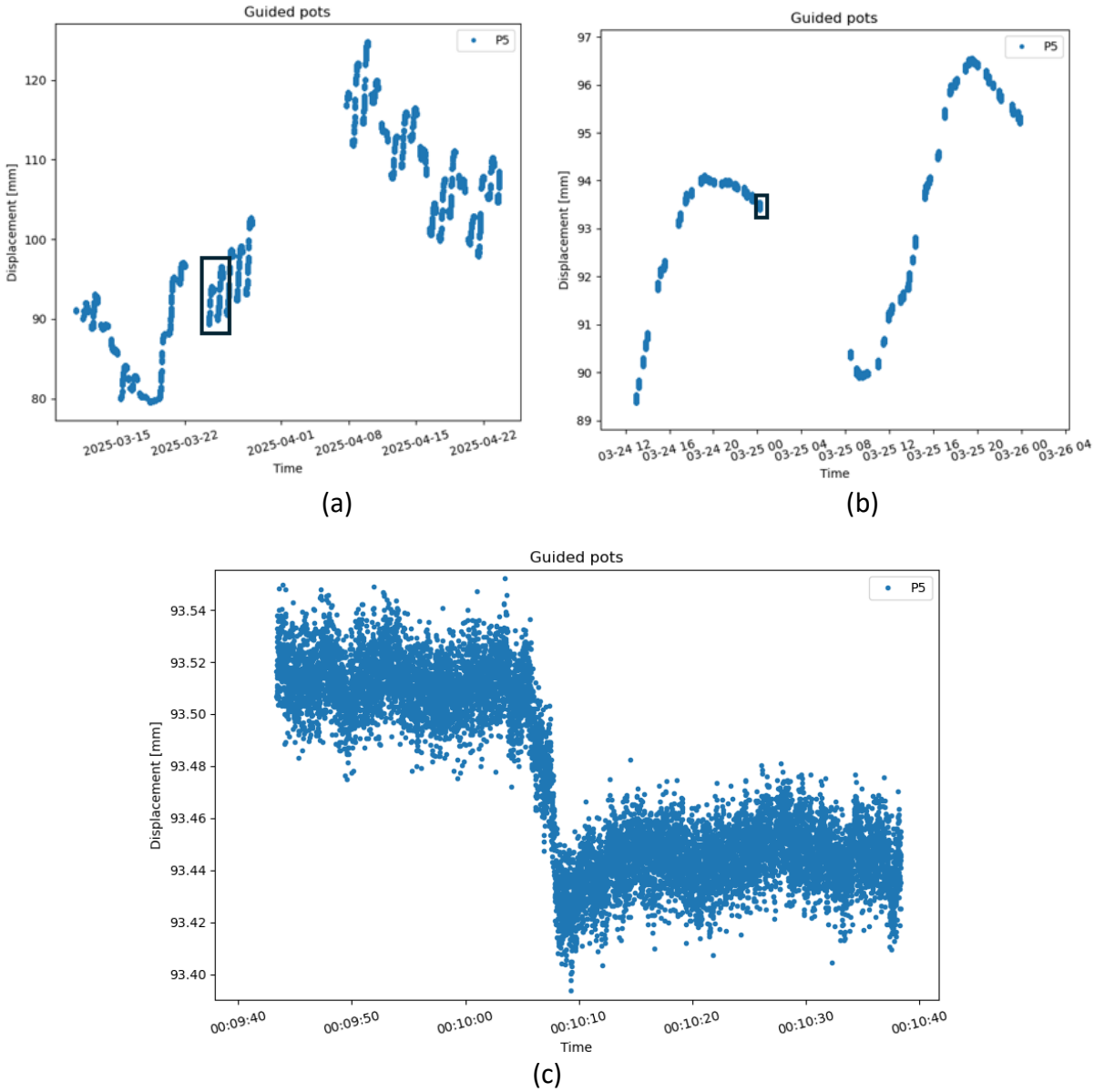

Figure 6-39: P5 guided pot LVDT zooms from signal. (a) Whole measurement. (b) Zoom of signal on rectangle of graph (a). (c) Zoom of signal on rectangle of graph (b).

Figure 6-39 presents the correlation matrix between the different LVDT sensors and temperature. The LVDT measurements exhibit strong mutual correlations, with sensor E1 showing a notably strong negative correlation with most of the others. Transversal sensors tend to display lower correlation levels. Notably, temperature shows a strong correlation with the LVDT readings, indicating that a temperature correction may be necessary depending on the specific analysis methodology applied.

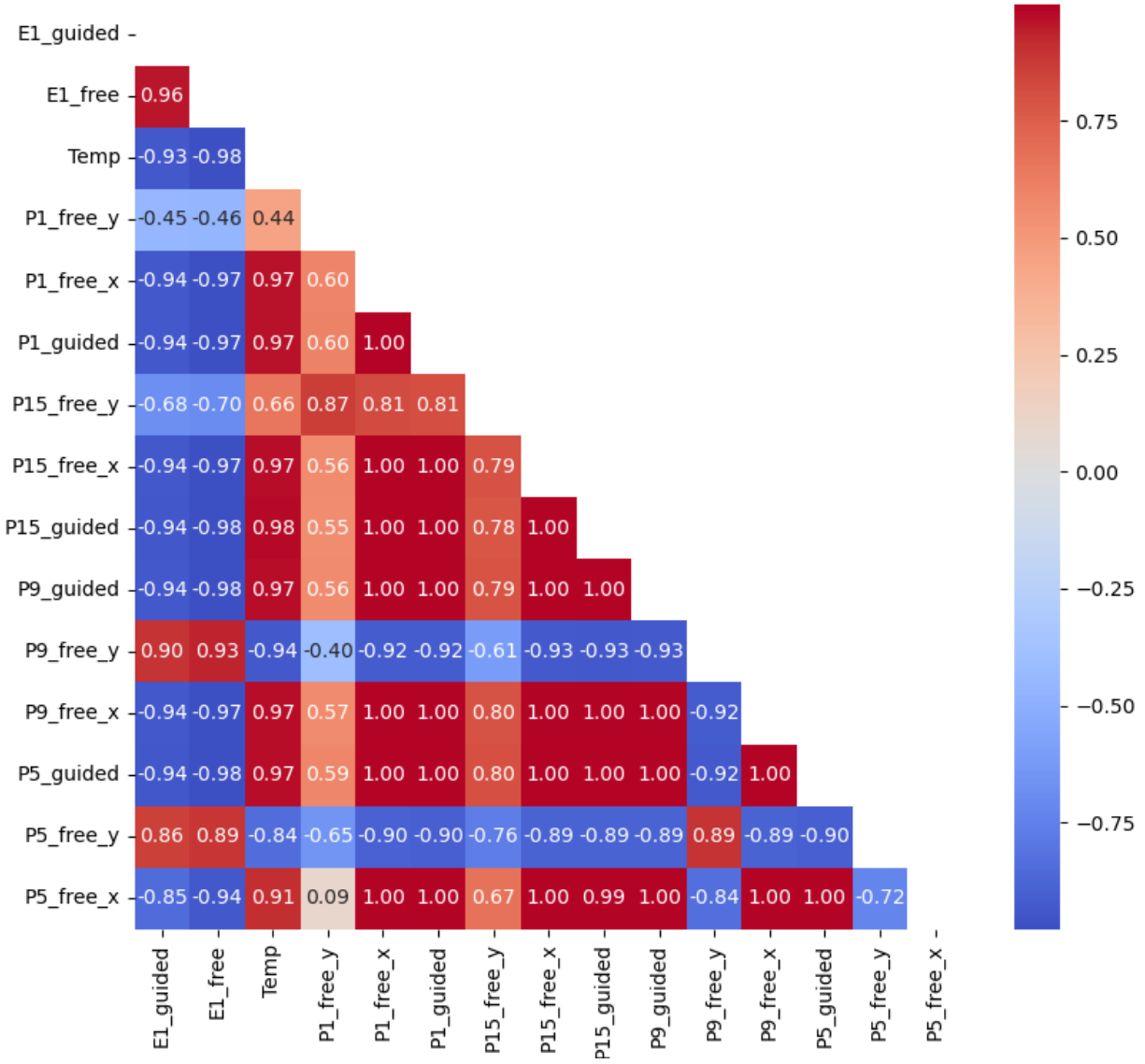

Figure 6-40: Correlation Matrix heatmap.

A deeper analysis will be performed when the continuous data with the lower frequency is available with a reasonable volume of data.

Two different analysis will be performed with the LVDT continuous data: (1) LVDT condition based on regulation and (2) Anomaly detection based on LVDT measurements, as it is simplified on the scheme of Figure 6-40 First, the available LVDT information will be analysed through an Exploratory Data Analysis to get better insights and reveal critical information. Second, the data coming from the LVDT must me pre-processed and structures in the adequate format for its handling. In the third step, the signals must be treated using the adequate filters. The filtered

signals will be used in the Anomaly detection algorithms. For their usage on the analysis of condition based on regulations, the signals will also be analyzed with outlier techniques.

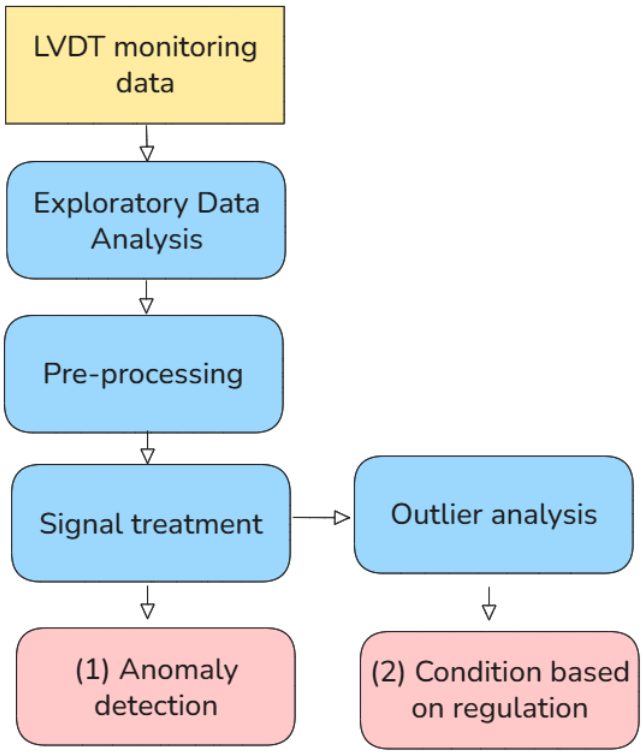

Figure 6-41. LVDT workflow scheme

6.2.4.2. LVDT condition based on regulation

First, different normative relative to pot bearings has been analysed to find the standards to ensure the asset good condition. The regulations analyzed are:

- UNE-EN 1337-5 Apoyos estructurales. Parte 5: Apoyos “pot”.
- UNE-EN 1337-1 Apoyos estructurales. Parte 1: Reglas generales de diseño.
- UNE-EN 1993-1-9 Eurocódigo 3: Proyectos de estructuras de acero. Parte 1-9: Fatiga.
- UNE-EN 1337-2. Apoyos estructurales. Parte 2: Elementos de deslizamiento.

The presented regulations gather, among others, the requirements to be reached regarding materials, dimensions, design, maximum and minimum displacements, strains, loads and others. After the analysis, the key parameters that can be monitored using the LVDT sensors is the accumulated sliding distance. Following UNE-EN 1337-5, the internal seal has a normalized accumulated sliding distance (s_T), which due to the specifications of the Use Case: Pot for railway is of type “c” which corresponds to 2000 metres of accumulated sliding distance, as used in (Khbeis & Huth, 2007) or (FREYSSINET). This norm also shows how to calculate the real accumulated sliding distance ($S_{A,d}$) following equations [5] and [6].

$$S_{A,d} = n_v \cdot \Delta\alpha_2 \cdot \frac{D}{2} \quad [5]$$

$$S_{A,d} \leq c \cdot s_T \quad [6]$$

Where n_v is the number of vehicles considered within the useful life of the bearing, c is a correction coefficient applied, in this case its value is 5, $\Delta\alpha_2$ is the Pot rotation angle interval due to extreme position of variable loads and D is the Pot diameter. This provides a real accumulated sliding distance of 10000 metres.

This analysis allows an accurate analysis of the pot life through the LVDT by summing up the measured values of the guided pots (equation [7]) and summing up the module of the measured values on the free pots which can move in any direction of the horizontal plane (equation [8]).

$$s_T = s_0 + \sum |\Delta x| \quad [7]$$

$$s_T = s_0 \sum \sqrt{\Delta x^2 + \Delta y^2} \quad [8]$$

Where Δx is the displacement in the longitudinal direction, Δy the displacement in the transversal direction and s_0 the displacement occurred before the monitoring.

6.2.4.3. Anomaly detection based on LVDT measurement

Anomaly detection has been used for decades to identify and extract anomalous components from data. Many techniques have been used to detect anomalies. One of the increasingly significant techniques is Machine Learning (ML), which plays an important role in this area. Examples of these include cyber intrusion detection, fraud detection, medical anomaly detection, industrial damage detection, image processing detection, textual anomaly detection, and sensor networks (Nassif, Talib, Nasir, & Dakalbab, 2021)
Preventive maintenance applied on bridges using these machine learning algorithms has been previously applied in research activities. An anomaly alarm approach was established using the extracted sliding friction indicator from the temperature-displacement hysteresis model proposed by considering the friction of bridge bearings (Wu, Yi, Yang, Li, & Liu, 2023). A condition assessment approach was developed using the girder end displacement measurements to calculate cumulative displacement parameter into isolation forest algorithm for anomaly detection to detect damper malfunction in bridges (Sun, Siringoringo, Chen, & Lu, 2023). Support vector regression was applied on bridge response for anomaly detection (Kromanis & Kripakaran, 2013). A hybrid model based on an ANN with BO was utilized to determine the relationship between the critical influencing factors and long-term horizontal displacement of an overpass bridge (Asad, Kim, Cho, & Sim , 2023).

There are three types of anomaly detection techniques:

- Supervised anomaly detection. In this case the anomalous cases are known, these methodologies require a labeled dataset with both normal and anomalous instances.
- Semi-supervised anomaly detection. In this methodology data in unlabeled, but it is assumed that if the anomalies are present they are rare, and therefore you have a training dataset with mostly normal data.
- Unsupervised anomaly detection: no labels are provided at all.

Following this classification, and based on the assumption that the bridge of study has been adequately maintained and the inspections performed do not show problems on the Pot bearings, we can assume that the LVDT data will show the undamaged condition of the bridge. Therefore, Unsupervised and semi-supervised methodologies can be applied, for example:

- Neural Network-based models:
  - Autoencoders for time series
  - LSTM/GRU Forecasting models
  - Variational Autoencoder
- Isolation Forest
- Support Vector Machine
- Hybrid/specialized tools:
  - Facebook prophet
  - Twitter AnomalyDetection
  - DeepAR

6.2.5. Bridge platform for asset management

Within the scope of the FP3-IAM4RAIL European initiative, the WebGIS platform has been developed as a strategic solution for the integrated monitoring and management of railway infrastructure and its surrounding environment. This tool supports the real-time acquisition, processing, and visualization of data collected from installed sensors, facilitating informed decision-making and collaborative governance. Designed to integrate data from diverse sources, the platform enables comprehensive, multiscale spatial analysis. Its key functionalities include:

- Continuous monitoring of parameters such as accelerations, inclinations, and environmental measurements collected from sensors installed on the bridge, aimed at assessing its structural condition;
- Anomaly detection based on local and global structural analyses, supported by an information system that classifies damage severity into three distinct levels;
- Decision-making based on the analysis results, aimed at safeguarding the structural health of the case study;
- User-friendly access to data through interactive web interfaces, complemented by seamless connectivity between the BIM-GIS model and the data and results presented on the platform.

The system manages both spatial and alphanumeric datasets, available via Internet or Intranet, and presents them through an intuitive graphical interface. Users can explore and interact with geographic and thematic layers, enabling deeper understanding and targeted analysis. A central feature of the platform is its ability to integrate and display multiple thematic data layers. This fosters cross-disciplinary collaboration, highlights spatial relationships, and strengthens data-driven decision-making.

By providing accessible and interactive tools, the platform empowers stakeholders — including

public authorities, railway operators, and engineers — to engage with territorial information and actively contribute to intelligent asset management. In this regard, Figure 6-42 a screenshot of the platform used to display the results and analyses related to the case study. The platform is divided into two main sections: on the left, the WebGIS interface with the integrated BIM model of the case study; on the right, the monitoring data and analysis results. This layout ensures a highly user-friendly experience.

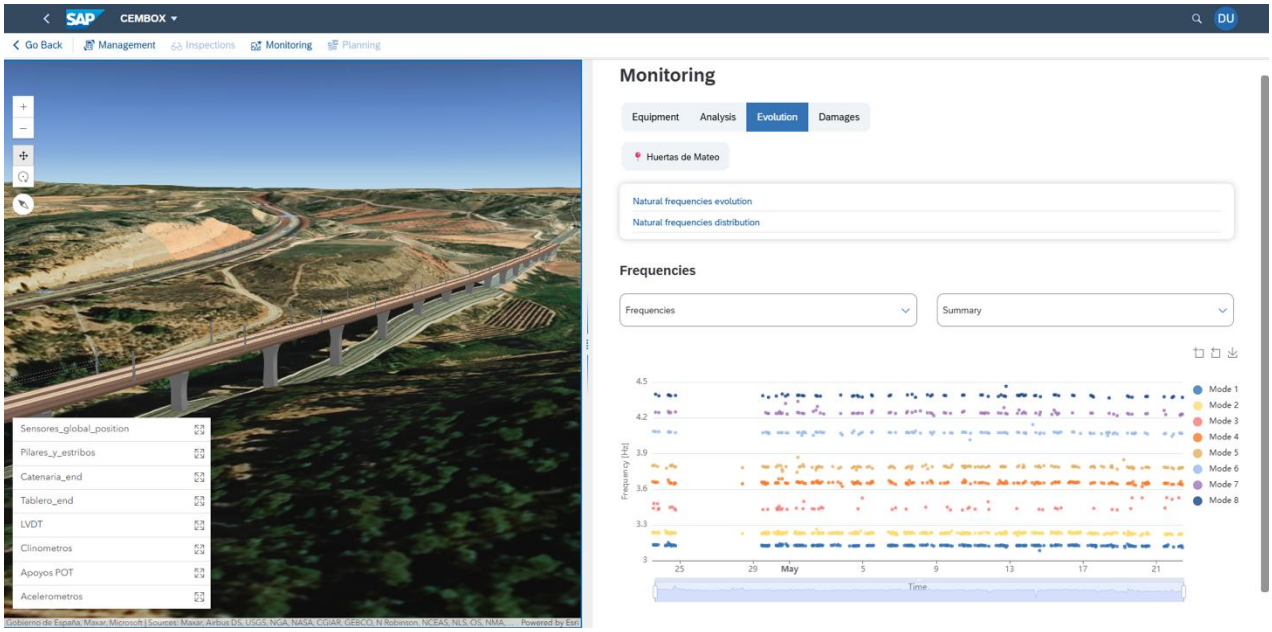

Figure 6-42: Integrated WebGIS platform displaying the case study's BIM model alongside real-time monitoring data and analysis results.

6.3. Large scale multi-soil earthworks monitoring

Large-scale monitoring of earthworks with multiple soils is to be carried out at the Vilar de Silva location.

To carry out this monitoring, a study of the location will be established where, using different sensors and satellite mapping technology (DInSAR), with the corresponding correction of the data and information received, different alarms will be created to monitor this site and its study areas. The application and creation of the alarms will be carried out according to the data and information obtained, in which they will be studied to carry out an accurate study of each of the data to be monitored.

6.3.1. Earth observation data collection and processing

As part of the large-scale multi-soil earthworks monitoring, a study was conducted using **DInSAR satellite technology** (Differential Interferometric Synthetic Aperture Radar). This technique allows for the detection of millimetric ground displacements by comparing radar images captured at different times.

The analysis focused on four designated areas within the study site: **Polygon 1, Polygon 2, Polygon 3, and Polygon 4**. These polygons were strategically selected based on their geotechnical significance and proximity to critical infrastructure. The data obtained revealed varying densities of measurement points (targets), represented on the map using a color-coded scale indicating the number of points per square kilometer.

Figure 6-43: Study Area Polygons and DInSAR Measurement Density Map.

Each polygon exhibits distinct characteristics regarding vegetation cover, structural presence, and satellite visibility, all of which directly impact the quality and quantity of the DInSAR data retrieved.

This satellite-based study plays a key role in remote terrain monitoring, enabling the identification of potentially unstable zones without direct ground intervention, and serves as a foundation for integration with in-situ ground data collection.

6.3.2. Ground data collection and processing

The data collection and processing at the Vilar de Silva slope have been carried out through a combination of advanced technologies and traditional geotechnical monitoring methods.

For field data acquisition, an IoT sensor network has been deployed, consisting primarily of 16 wireless tiltmeters installed at various locations on the unstable slope—including sleepers, rock, tunnel gable, and soil. These sensors are supported by a weather station equipped with temperature, humidity, and rainfall sensors. All devices are connected via a low-power LoRa wireless network, enabling real-time data transmission to a central Gateway. This Gateway manages communication and stores data, which are subsequently integrated into a digital analysis

platform.

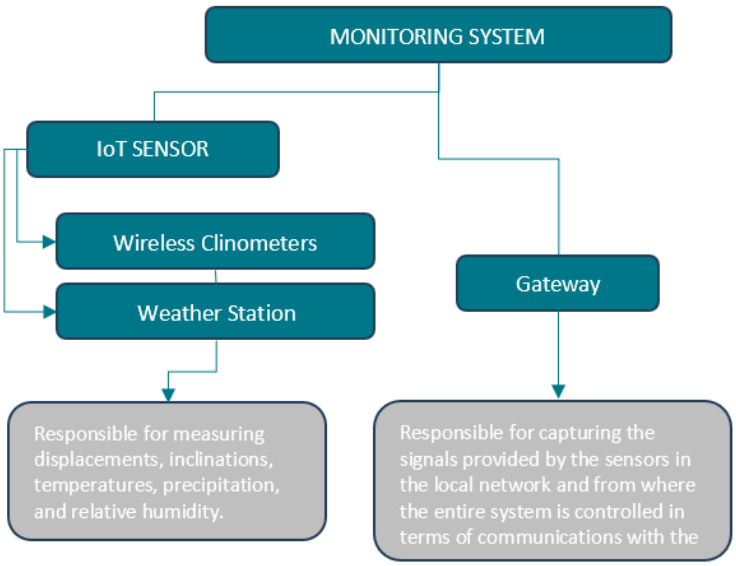

Figure 6-44: Monitoring System Diagram.

The installation of the tiltmeters (16), weather station (1), and Gateway (1) was carried out on a slope that has suffered numerous and severe stability issues, affecting not only the tunnel entrance portal but also the railway track leading up to it. These movements have caused damage to the tunnel lining and levelling defects on the track.

Figure 6-45: Location of the sensors in Vilar de Silva

To complement the field data, DInSAR (Differential Synthetic Aperture Radar Interferometry) satellite technology has been employed. This method has enabled the detection and quantification of deformations in various areas of the slope, with average displacement rates of up to 12 mm/year, depending on the area analyzed. The DInSAR data has been critical in calibrating the geotechnical model and optimizing the instrumentation system design.

Data processing includes the development of anomaly detection algorithms based on time series analysis. Several alarm mechanisms have been implemented to identify:

- Deviations in group sensor values;
- Individual sensor anomalies;
- Prediction-based anomalies using an LSTM neural network (enabling 48-hour forecasts with variables such as extreme rainfall).

Finally, the system supports the integration of data from traditional monitoring methods, including leveling benchmarks, crack meters, piezometers, and others. These are digitally recorded and visualized via a real-time dashboard interface, providing a comprehensive and robust tool for slope stability assessment and maintenance decision-making

6.3.3. Earthworks alarm system

Previously said, we are working in this section with the earthworks located in Vilar de Silva. Like we just see in the previous section, there are multiple sensors along the terrain monitoring all the movements and displacements that occur hourly.

Thanks to all the information that we are receiving from these sensors and after processing, we have just decided first to analyze all the transformed data and how the displacements are related with other information.

The process iteratively acquires real-time data from the inclinometers, which is then analyzed to facilitate real-time anomaly detection. In this light, the procedure consists of five main tasks.

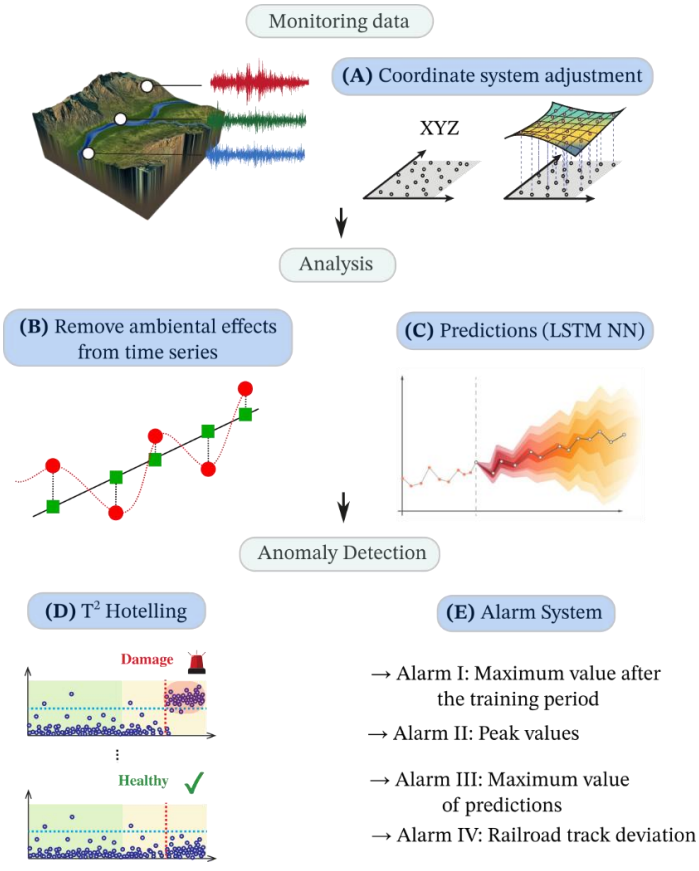

Figure 6-46: Flowchart for the analysis and detection of anomalies in tiltmeter time series.

- **Coordinate system adjustment**. The Figure 6-47 shows the layout of the different tiltmeter across the study area and their corresponding local coordinate system. Therefore, a global coordinate system (the yellow axis) needs to be established by transforming the local coordinate axes. To achieve this, each sensor is treated individually, with its local coordinate system rotated using its respective rotation matrix to align with the global system. The rotation angles were calculated based on the orientation information provided by the installers, measured with a compass.
- **Removal of environmental effects from the time series**. Benign fluctuations caused by varying environmental conditions are minimized using statistical pattern recognition. In this case, the method employed is Linear Regression. Let us denote the time series from the tiltmeters in the observation matrix $Y = [y_1, \ldots\ldots, y_f] \in \mathbb{R}^{N\times 2}$ containing the *N* observations. In this context, data normalization involves subtracting the reversible variability in the selected features of Y induced by benign environmental and operational conditions (EOC). This can be achieved by training a certain statistical model over a set of training period samples from Y defining a baseline in-control population. This baseline dataset must represent the healthy condition of the structure under all possible EOC being a one-year period often adopted. Among the wide variety of data normalization techniques available in the literature, Multiple Linear Regression (MLR) models represent a simple bur powerful approach. MLR models exploit linear correlations between the selected features in Y (estimators) and a set of p independent exploratory variables (predictors or independent variables), which are typically taken from monitoring data of EOC (e.g. temperature, humidity).

The predictions by MLR ($\hat{Y}$) of the observation matrix Y are obtained as:

$$\hat{Y} = \bar{P}\bar{\beta} = [1_{N\times 1}, P]\begin{bmatrix}\beta_0^T \\ \beta\end{bmatrix}$$

Where $1_{N\times 1}$ is a column vector of ones and $P = [p_1, \ldots, p_p] \in \mathbb{R}^{N\times p}$ an observation matrix with columns containing the time series of the p selected predictors. Term $\beta_0 \in \mathbb{R}$ is a vector of intercept terms and $\beta \in \mathbb{R}$ is a matrix of linear regression coefficients. Assuming normally distributed errors between the estimators and the predictions by the MLR model over the training period, the least squares estimate of the coefficient's matrix reads:

$$\bar{\beta} = \left(\bar{P}_{tp}^T \bar{P}_{tp}\right)^{-1} \bar{P}_{tp}^T Y_{tp}$$

Where subscript "tp" has been included to explicitly state that the MLR model is trained considering the set of predictors and estimators within the training period. Once constructed, the predictions of the MLR model $\hat{Y}$ from (insertar número de ecuación) can be used to remove the variance caused by EOC from Y through the so-called residual error matrix $E \in \mathbb{R}^{N\times 2}$, that is:

$$E = Y - \hat{Y}$$

When the system remains healthy, matrix $\hat{Y}$ reproduces the part of the variance driven by EOC, while E only contains the residual variance stemming from modelling errors. Conversely, if a certain damage develops, matrix $\hat{Y}$ remains unaltered while matrix E concentrates the damage-induced variance, being thus apt for damage identification.

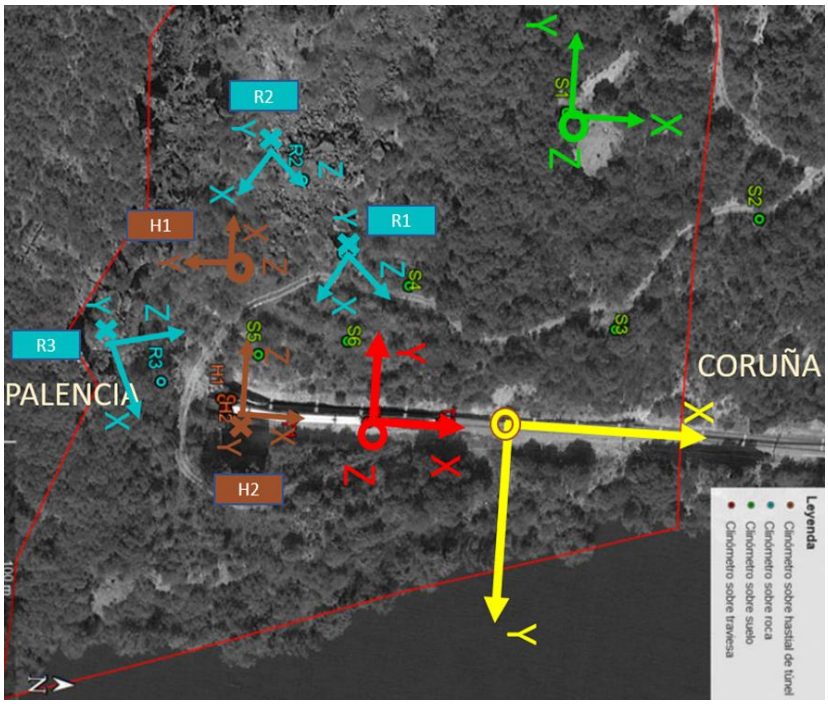

Figure 6-47: Tiltmeters installation with local coordinates systems.

- **Predictions (LSTM Neural Network)**. Long Short-Term Memory (LSTM) neural networks are a specialized type of recurrent neural network (RNN) designed to effectively capture long-term dependencies and temporal patterns in time series data. Unlike standard RNNs, LSTMs address the issue of vanishing and exploding gradients, which can occur during training when dealing with long sequences. In this case, the designed network maintains a cell state that acts as a memory, allowing them to retain information over long periods. This memory helps the network remember important information and forget irrelevant data. Besides the network use three types of gates—input, forget, and output gates—to regulate the flow of information into, out of, and within the cell state: the "Input Gate" that controls how much new information is added to the cell state. The "Forget Gate" that decides which information from the cell state should be discarded and the "Output Gate" Determines the output based on the cell state. The compact forms of the equations for the forward pass of an LSTM cell with a forget gate are:

$$f_t = \sigma(W_f\, x_t + U_f\, h_{t-1} + b_f) \quad (9)$$

$$i_t = \sigma(W_i\, x_t + U_i\, h_{t-1} + b_i) \quad (10)$$

$$o_t = \sigma(W_o\, x_t + U_o\, h_{t-1} + b_o) \quad (11)$$

$$\tilde{c}_t = \sigma(W_c\, x_t + U_c\, h_{t-1} + b_o) \quad (12)$$

$$c_t = f_t \therefore c_{t-1} + i_t \therefore \tilde{c}_t \quad (13)$$

$$h_t = o_t \therefore \sigma_h(c_t) \quad (14)$$

where the initial values are $c_0 = 0$ and $h_0 = 0$ and the operator $\therefore$ denotes the Hadamard product (element-wise product), σ and $tanh$ correspond to the sigmoid and hyperbolic tangent activation functions, respectively. The subscript t indexes the time step. Letting the superscripts h and d refer to the number of input features and number of hidden units, respectively. $x_t \in \mathbb{R}^d$ corresponds to input vector to the LSTM unit, $f_t \in (0,1)^h$ is the activation vector of the forget gate, $i_t \in (0,1)^h$ is the activation vector of the input (update) gate, $o_t \in (0,1)^h$ is the activation vector of the output gate, $h_t \in (-1,1)^h$ is the hidden state vector also known as output vector of the LSTM unit, $\tilde{c}_t \in (-1,1)^h$ is the cell input activation vector, $c_t \in \mathbb{R}^h$ is the cell state vector, finally $W \in \mathbb{R}^{h\times d}$, $U \in \mathbb{R}^{h\times h}$ and $b \in \mathbb{R}^h$ are the weight matrices and bias vector that need to be learned during training.

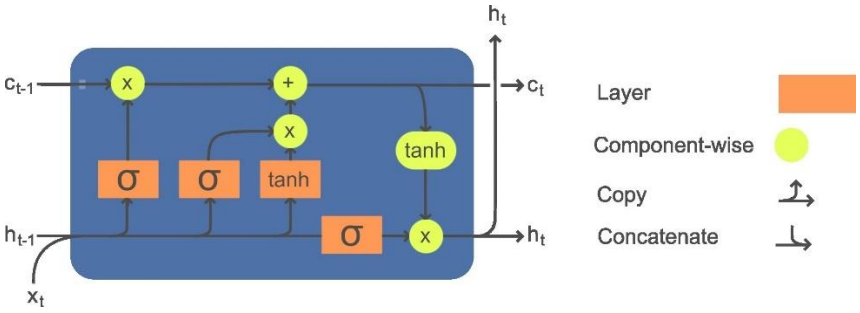

Figure 6-48: LSTM network architecture.

- **T^2 Hotelling**: is a multivariate statistical test used to assess whether the mean vector of a multivariate sample differs significantly from a hypothesized mean vector. It extends the concept of the Student's t-test to multiple dimensions, making it useful for analysing multivariate data. The statistic is calculated using the formula:

$$T^2 = n(\bar{x} - \mu)^T S^{-1}(\bar{x} - \mu) \quad (15)$$

where $\bar{x}$ is the sample mean vector, μ is the hypothesized mean vector, S is the sample covariance matrix, and n is the sample size. For this case study, this statistical method is used to determine if significant differences exist between two sets of data by delimiting the time series for each sensor using a training period defined as “healthy”. Thus, the differences are assessed relative to the healthy case study.

- **Alarm System:** Based on the behaviour of the time series data collected from each tiltmeter, several types of alarms have been defined, corresponding to various potential damage mechanisms that the object under study might experience. The process begins with the acquisition

of real-time data, which is expected to have an average value of approximately zero. Fixed averages are determined for the training period to establish baseline conditions. Each sensor records two components of rotation: the first corresponds to the rotation around the x-axis, and the second corresponds to the rotation around the y-axis. It is important to note that the direction of the steepest slope aligns with the direction of rotation around the x-axis. Once the initial conditions are established, the types of alarms are defined as follows:

Alarm I: Maximum value after the training period. Figure 6-49 shows the main characteristics that trigger the alarm mechanism in question. The process begins by establishing a training period, with the primary assumption that the structure is considered healthy throughout this period. Defining this period allows for the establishment of upper and lower limits for each sensor. Once these values are set, the behaviour of the data post-training period is analysed. If the predefined thresholds are exceeded, it is considered that there is damage to that sensor, as shown in Figure 6-49(a). This failure mechanism has the limitation that under environmental conditions not previously experienced at the study location, these thresholds can be exceeded with relative ease. Therefore, the activation of the alarm depends on detecting anomalous values in three sensors in proximity, as shown in Figure 6-49(b).

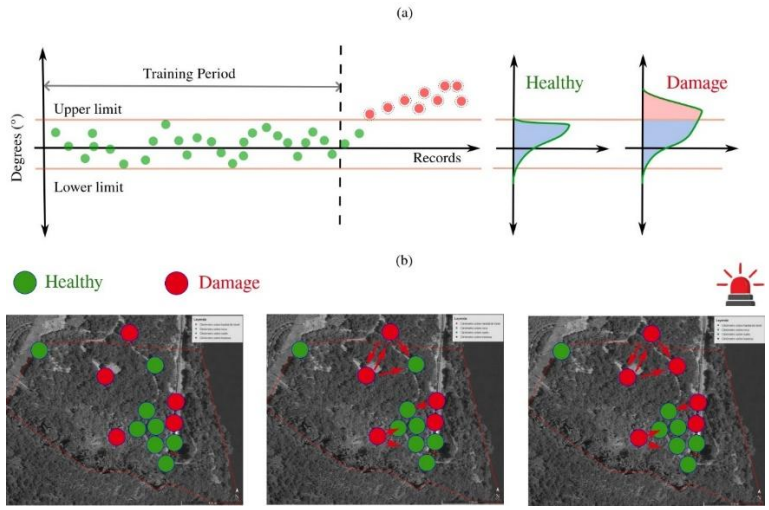

Figure 6-49: (a) Definition of limits based on the training period. (b) Alarm activation mechanism.

Alarm II: Peak values. This alarm is triggered by storing the differences between records during the training period so that peak values can be determined in the post-training period. If the data shows peaks that surpass this amplified threshold during analysis, it indicates potential damage or anomalies in the sensor readings. This mechanism is designed to detect significant deviations that may signal critical issues, as illustrated in Figure 6-50.

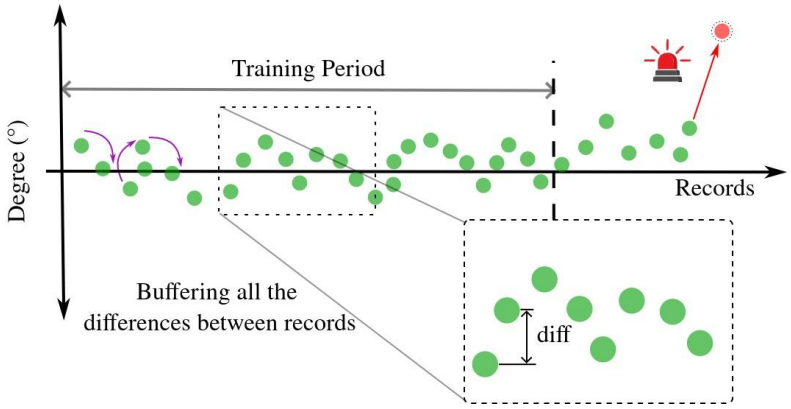

Figure 6-50: Recording Differences to Identify Peak Values.

Alarm III: Maximum value of predictions. Once the differences corresponding to the degree records for each sensor are stored, the next step is to determine if the predictions (48-hour period – LSTM Neural Network) indicate any anomalous values. This neural network has been constructed based on the behaviour of each time series (degrees), with extreme precipitation defined as a variable. The damage mechanism scheme is shown in the following figure:

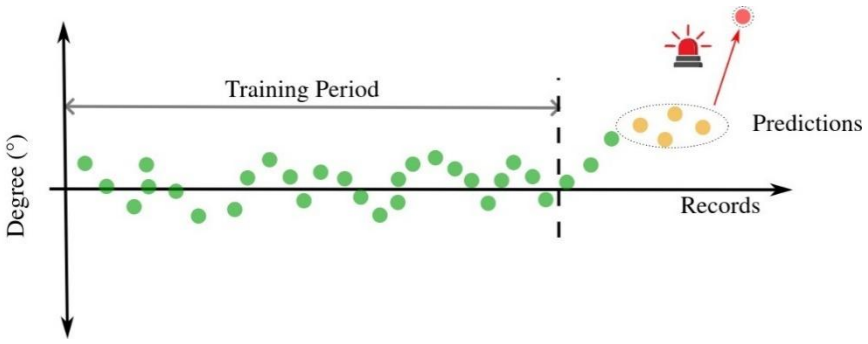

Figure 6-51: Alarm mechanism based on value predictions.

Alarm IV: Railroad track deviation. This alarm is only applied to sensors located on the railroad ties of the train line. By knowing the dimensions of the support element for the sensors, it is possible to determine the rotation (in the longitudinal direction) of four railroad ties on the train line. Figure 6-52(a) illustrates the procedure for calculating the deviation of the tie based on its rotation. In our opinion, this rotation is attributed to changes in the water levels of the nearby lake. According to NAV 3-0-5.2 'Track Geometry Parameters' regulations, the deviation must not exceed 25 mm. Therefore, using this value as a reference, Figure 6-52 (b) outlines the conditions for activating this failure mechanism.

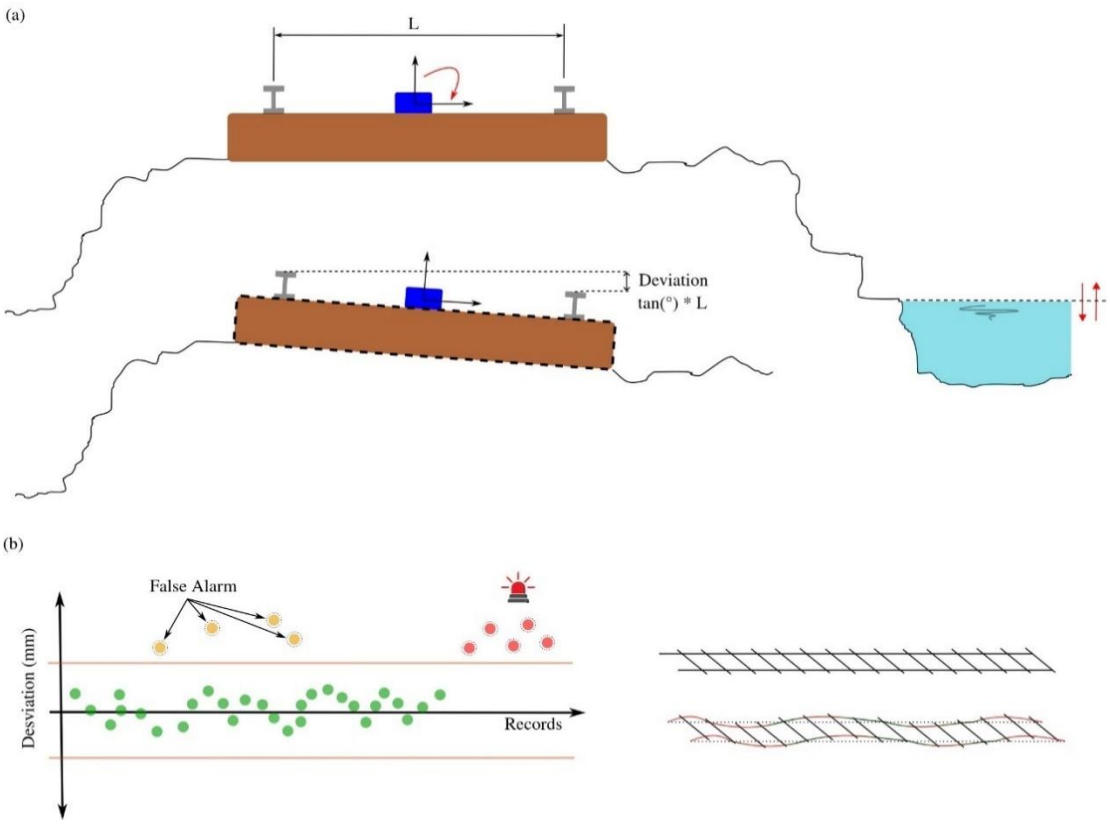

Figure 6-52: (a) Deviation in railway sleepers and (b) damage mechanism based on deviation limit values.

6.3.4. Earthworks asset management platform

In this section the Platform for Vilar de Silva pilot is described. The general platform layout is the same for all the interfaces: on the left the BIM-GIS visor of the slope displaying the different sensors included in the platform, which allows the navigation and the selection of elements and on the right the information which corresponds to the different interfaces like it is showcased in the examples of Figure 6-53 and Figure 6-54.

Different elements are included in the platform both with dynamic and static data. Dynamic elements are connected to IoT sensors which provide real-time monitoring, these include tiltmeters and a weather station. The static data is information coming from a database which is updated punctually with information coming from inspections. This data corresponding with inclinometers, piezometers, levelling and others is included in the platform for its consultation, and the structure is prepared to update the information whenever new inspections are performed. Besides the visualization on the monitoring and inspection data, the platform will integrate a series of interfaces relative to the previously defined UC developments: trends, alarms, predictions, etc. displayed in a user-friendly way for the end-users.

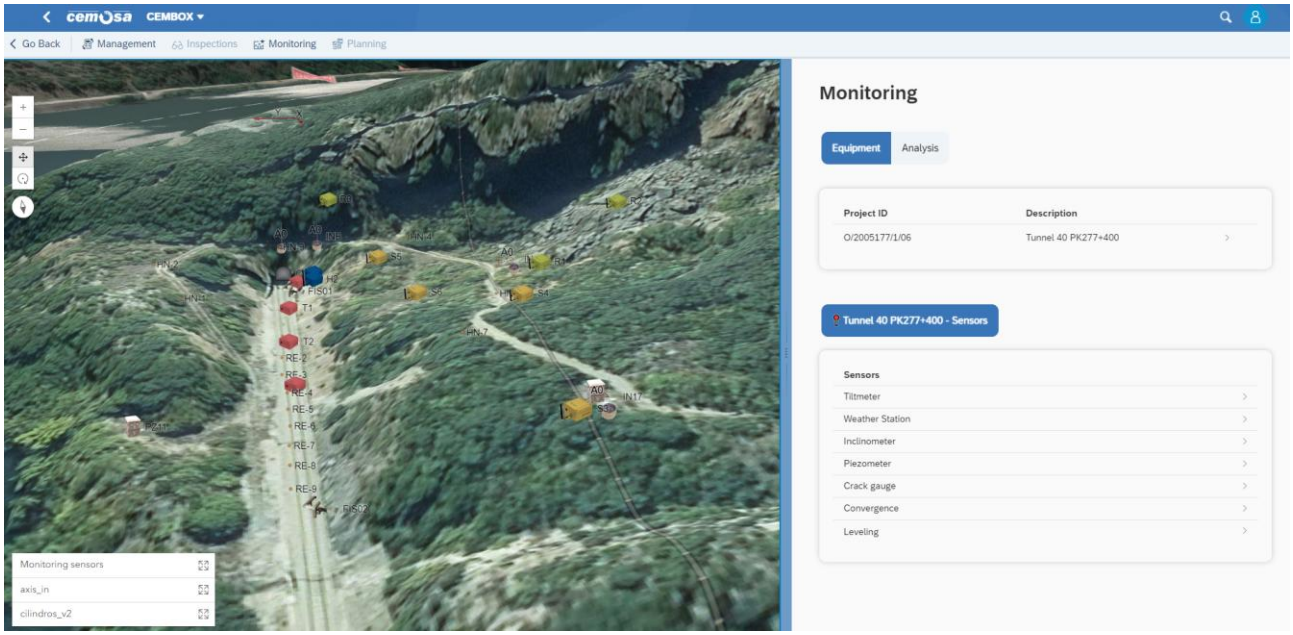

Figure 6-53: Platform interface. Example 1.

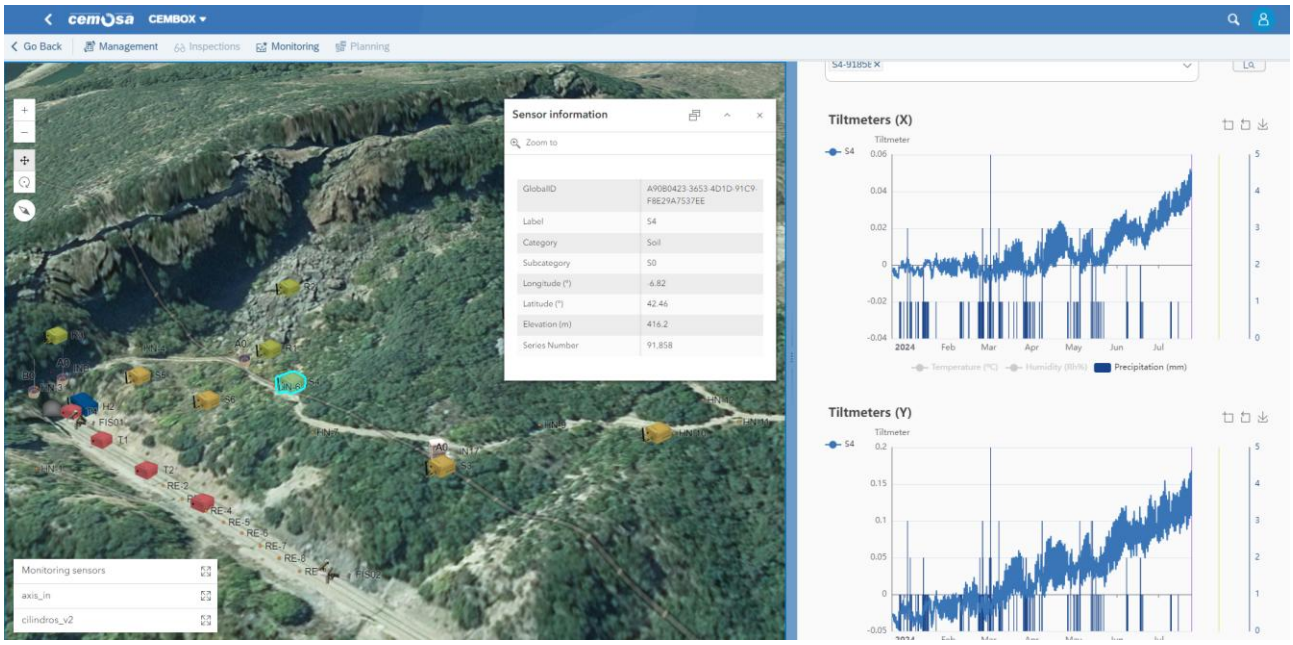

Figure 6-54: Platform interface. Example 2.

6.4. Small scale clay soil earthworks monitoring

Small-scale monitoring of earth movements in clay soils will be conducted, with focus on the Briones hillside in Spain. Various studies will be carried out to establish alarm thresholds for slope safety. Depending on the data obtained, different danger levels can be defined to prevent landslides and ensure the effectiveness of preventive maintenance. To enable slope monitoring, multiple sensors have been installed throughout the terrain; these will be processed and analysed for incorporation into the alarm system.

6.4.1. Earth observation data collection and processing

The InSAR pertaining the Briones hillside in Spain has been acquired and processed by MERMEC (Sitael) with the InSAR techniques described in section 5.6.

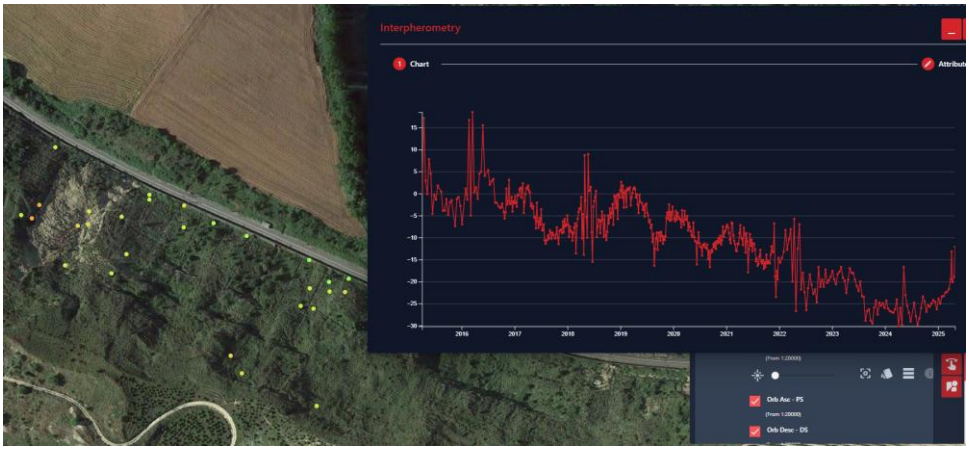

Figure 6-55: MERMEC web platform, InSAR data on Briones hillside in Spain.

The decade of data spans from the beginning of 2015 till May 2025, capturing the landslide occurred around 2015, as explained later on in this chapter. We anticipate how this Interferometric analysis made it possible to obtain a discrete density of measurement points across the entire monitored area, providing a picture of surface deformations and instability phenomena characterizing the territory. Both distributed (DS) and point (PS) radar targets were analysed, delivering accurate information on soil behaviour and the evolution of movements. Different behaviours have been spotted in different areas. In deliverable D13.3, we will try to cross correlate the EO data analysed by MERMEC (Sitael) with the ground data collected on the field by ADIF, highlighting the features of both techniques.

6.4.2. Ground data collection and processing

The Briones slope incorporates a comprehensive system for ground data collection and processing, primarily focused on monitoring slope stability through a network of geotechnical sensors.

A wireless sensor network has been installed, composed of 14 tiltmeters distributed across the slope. These sensors are mounted on corrugated steel rods (25–30 mm diameter, 2 meters long), embedded 1 meter into the ground, with the remaining 1 meter exposed above the vegetation.

The sensors are connected individually or in close clusters to local reading nodes, which function as dataloggers—capturing, recording, and transmitting data.

The installation of tiltmeters (14), a weather station (1), a Gateway (1), and the geotechnical drilling were all carried out directly on the slope. This mass, composed of clayey soil mixed with siltstone and sandstone fragments, becomes unstable due to clay saturation, which causes it to behave plastically and lose resistance to slippage—particularly in the fractured sections of the slope.

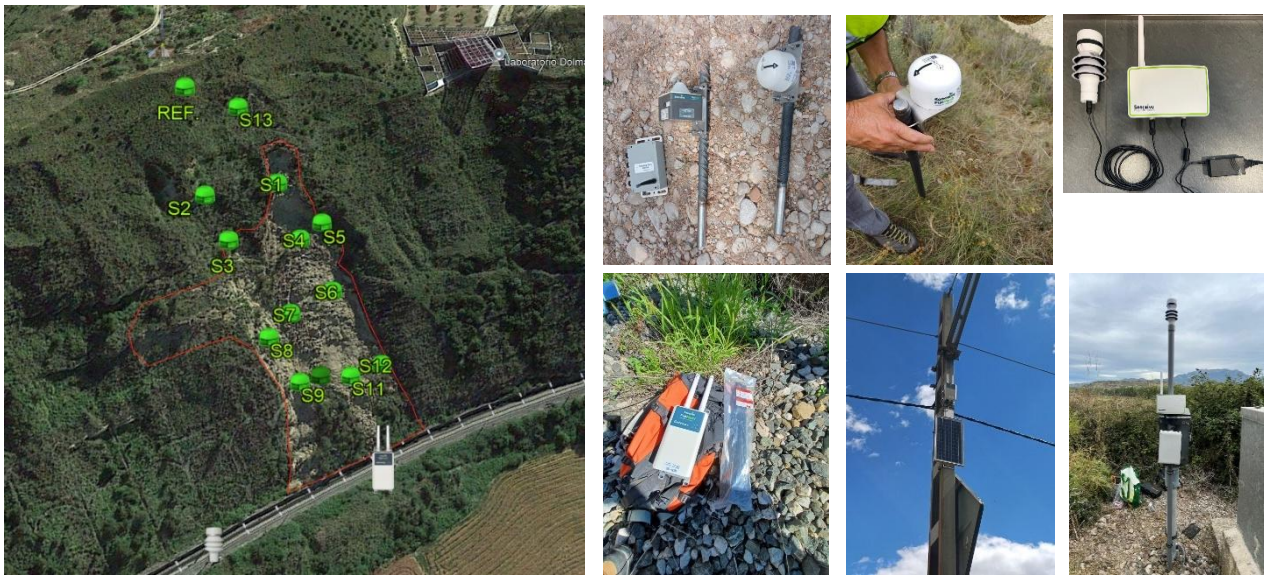

Figure 6-56: Location of the sensors in Briones.

In October, geotechnical drilling began on the Briones slope, advancing at a rate of approximately 15 meters per day and reaching a final depth of 60 meters by October 30. Core samples longer than 30 cm are being paraffined every 3–4 meters. Additionally, four Lefranc permeability tests were carried out between 25 and 50 meters in depth. Lugeon tests are scheduled between 50 and 100 meters once drilling is complete.

Figure 6-57: Geotechnical drilling.

Data transmission is handled via the FlatMesh radio protocol, which allows robust wireless communication between the sensors and a FlatMesh 4G Gateway. This gateway is mounted on a mast anchored into the ground and powered by a solar panel with battery backup, ensuring autonomous operation.

All sensor data are transmitted in real time (1 data point per hour per sensor) and integrated into a digital infrastructure management platform. This system enables data storage, visualization, and analysis. A Human-Machine Interface (HMI) is also planned to enhance supervision and facilitate alarm monitoring.

Although data analysis is still pending due to the short monitoring period, the platform is already equipped to generate anomaly alarms based on real-time sensor readings. These mechanisms will be refined and optimized as more data become available.

6.4.3. Earthworks alarm system

The working system used to create the alarms in this case for the Briones project will be the same as the one used in Vilar de Silva. In that project, 4 different alarms were created (Maximum value after the training period, peak values, Maximum value of predictions, Deviation from the rail), of which the first 3 alarms can be applied, as the working system used is applicable to the Briones site. In the case of the fourth alarm, it cannot be applied because the rail monitoring has not been carried out and therefore this alarm cannot be established in this project.

After an exhaustive analysis of the data received by the sensors, a first alarm can be established to review the data received by the sensors, and if manually established thresholds are exceeded, an alarm is sent to review the area in case a landslide has occurred.

The thresholds that can be established are based on the displacements obtained from the sensors, but a clustering of the sensors has also been carried out, since depending on the area where they are located, the soil has certain properties that will affect the evolution of the displacements in different ways. The clustering to be followed for the sensors is shown below:

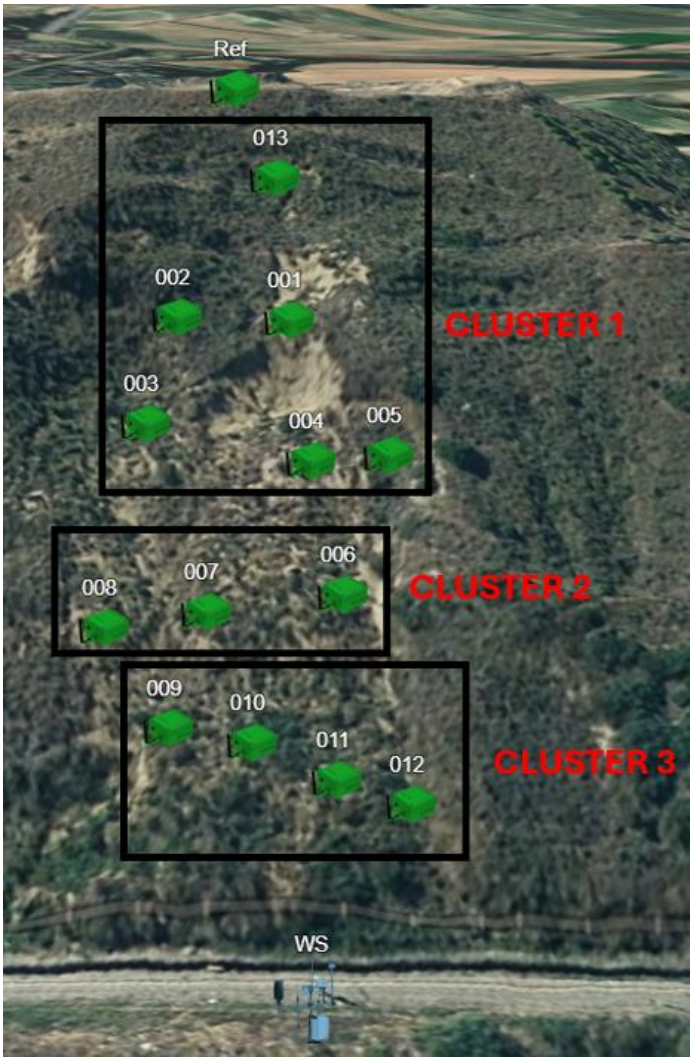

Figure 6-58: Distribution of sensors on the Briones slope.

In this way, different ranges of thresholds can be set depending on the cluster to which they belong.

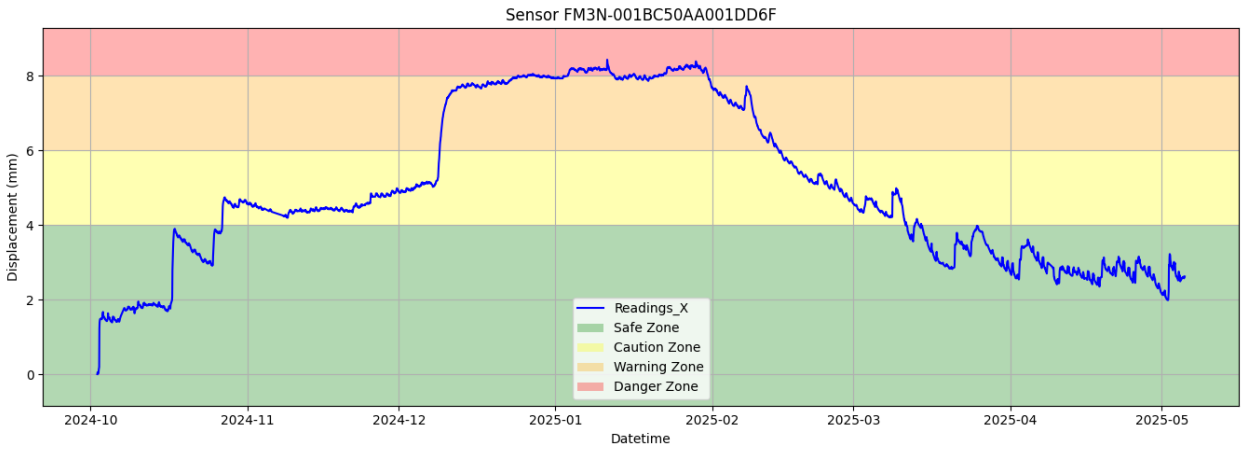

Figure 6-59: Monitoring of sensor FM3N-001BC50AA001DD6F and display of alarm ranges.

Comparing the displacement data with rainfall, it has been observed that rainfall has a great influence on the displacements detected by the sensors, which is why a new alarm will be created, focused on the study of displacements due to rainfall over time.

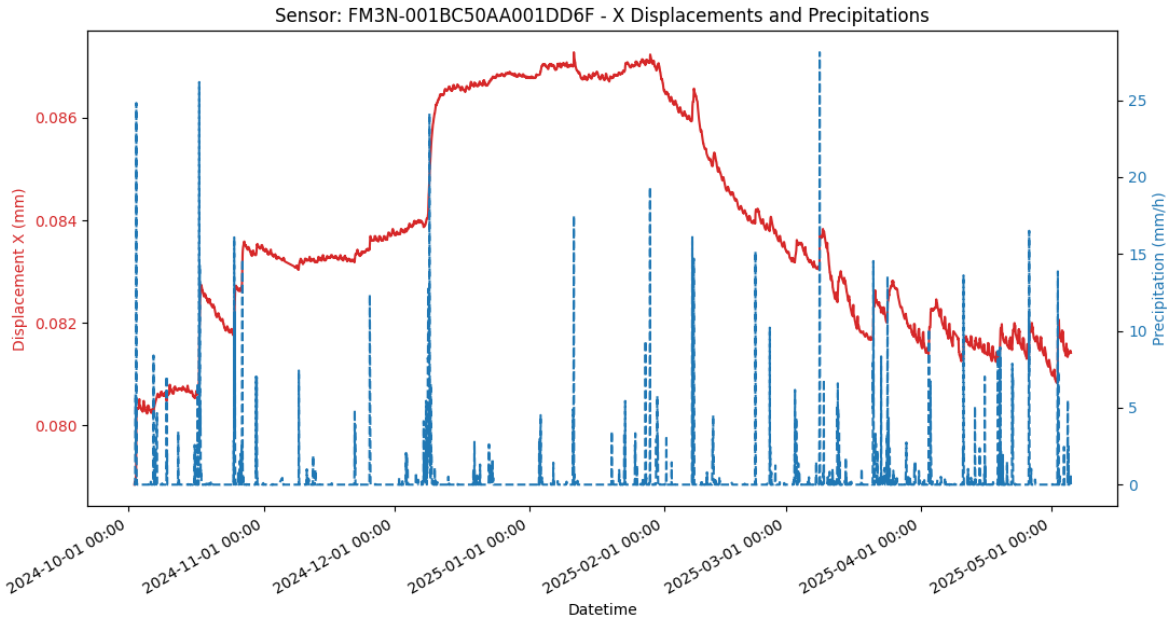

Figure 6-60: Monitoring of the displacements of the FM3N-001BC50AA001DD6F sensor and rainfall.

It is important to state that of all the times when there is a large variation in displacements, they occur in two types of rainfall events, when there is heavy rainfall in a short period of time or when there is prolonged, but low intensity rainfall.

Because the events that can directly affect the displacements are similar, but at the same time different, one of the methods that can mathematically cover this process is by means of the rainfall integral:

$$P_{accumulated} = \int_{t_0}^{t_1} p(t)\, dt$$

Using the rainfall integral, it is possible to know exactly how much precipitation has accumulated in each period. An important factor to consider is the time to be used for the calculation of the precipitation window. To calculate these events, it has been decided to establish a model based on the estimation of the dispersion of the data, i.e. Median Absolute Deviation (MAD).

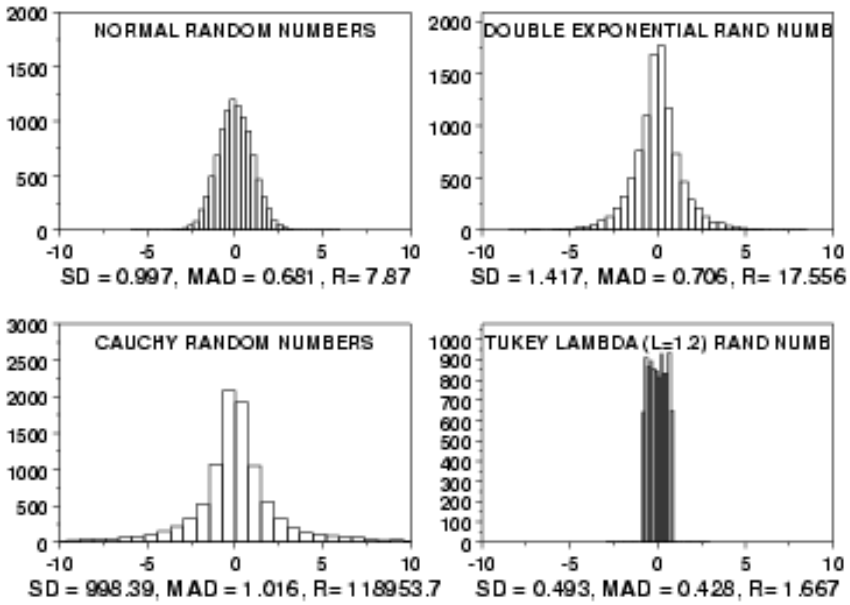

Figure 6-61: MAD prediction model.

This model is one of the most robust methods for estimating dispersion in manufacturing and quality processes. Unlike the sample standard deviation, which is highly sensitive to extreme values and can trigger false alarms, MAD remains reliable even if up to half of the data are contaminated. For a subgroup of size n with observations $x1, \ldots, xn$, the method proceeds as follows:

First, compute the subgroup median:

$$m = med\{xj : j = 1, \ldots, n\},$$

which minimizes the sum of absolute deviations and is unaffected by extremely large or small outliers. Next, calculate the absolute deviations from this median:

$$dj = |xj - m|, \qquad j = 1, \ldots, n,$$

and take the median of these distances:

$$M = med\{dj : j = 1, \ldots, n\}.$$

To ensure the estimator is unbiased under normality, introduce the scaling factor:

$$\kappa = \frac{1}{\Phi^{-1}(3/4)} \approx 1.4826,$$

and define the robust dispersion statistics:

$$MAD = \kappa M.$$

This correction ensures that E[MAD] = σ when data follows a normal distribution, while preserving the robustness of the media.

In Phase II monitoring, calculate MAD_i for each of m independent subgroups, then compute their average:

$$\overline{MAD} = \frac{1}{m}\sum_{i=1}^{m} MAD_i,$$

which replaces the traditional S. Control limits are established using constants B_5^* and B_6^* that depend only on n:

$$CL = \overline{MAD}, \qquad LCL = B_5^*\overline{MAD}, \qquad UCL = B_6^*\overline{MAD}.$$

These constants are defined by:

$$b_n = E[med(|Z_1|, \dots, |Z_n|)], \qquad Z_j \sim N(0,1),$$

The expected median of n draws from a standard normal, and

$$c_4 = \sqrt{\frac{2}{n-1}}\frac{\Gamma(n/2)}{\Gamma((n-1)/2)},$$

which corrects bias in the sample standard deviation. Then:

$$B_5^* = b_n\left(3 - \frac{1}{c_4}\right), \qquad B_6^* = b_n\left(3 + \frac{1}{c_4}\right).$$

These values are tabulated in the literature and can be interpolated for intermediate sample sizes.

The key properties explaining the superiority of the MAD chart in the presence of outliers are:

- 50% breakdown point: the estimator remains stable even if up to half the data are arbitrarily contaminated.
- Bounded influence function: each observation has a limited impact on the statistics.
- Reasonable efficiency: although its asymptotic efficiency relative to the sample standard deviation is about 37% under normality, it remains effective for detecting moderate shifts in dispersion.

Operationally, the MAD chart maintains an in-control average run length (ARL_0) close to the nominal value (around 370 samples) for both normal and heavy-tailed distributions, whereas the traditional S chart may exhibit inflated ARL_0 or inconsistent limits.

Furthermore, upon a sudden increase in dispersion, the MAD chart typically signals faster (lower ARL) than the S chart, enabling quicker intervention.

Computationally, calculating MAD involves sorting n values (practically $O(n\ log\ n)$) and selecting a median, making it suitable for real-time monitoring systems without specialized libraries. Using medians instead of means also enhances numerical stability when outliers or measurement errors occur.

Implementation steps are:

1. Collect m subgroups of size n
2. Compute MAD_i for each subgroup.
3. Estimate $\overline{MAD}$
4. Determine LCL and UCL
5. Continuously monitor by comparing each MAD_i to the limits; any point outside the limits indicates a significant change in process dispersion requiring investigation.

In multivariate settings, MAD concepts extend via robust covariance estimators such as the Minimum Covariance Determinant (MCD) and robust Mahalanobis distances, replacing sensitive covariance matrices with resistant estimates and comparing squared distances to robust chi-square-based thresholds.

In summary, the MAD-based control chart offers statistical robustness, computational simplicity, and clear interpretability, making it especially suitable when outliers or nonnormality are expected in the quality characteristic under observation.

6.4.4. Earthworks asset management platform

The platform to be used for monitoring this slope is the same as the one used for previous monitoring.
As can be seen in Figure 6-62 left side there is a visualization of a navigable BIM-GIS model, by means of this model the position of each of the sensors can be determined by means of a graphic tool.
On the right side is represented the management and monitoring of all the information that we receive from the sensors that are currently installed. In addition, the different alarms that have been decided to implement in this slope and some interfaces with which to see all the evolution of the UC as the most relevant possible events along the monitoring of the sensors will be shown. Knowing the distribution that is followed in the platform, different interfaces have also been implemented so that the accessibility of the data to the sensors is done in the simplest way. For this purpose, thanks to the BIM-GIS model, it will be possible to interact with it so that it is not always necessary to navigate through the right panel, but only with the help of the model will it be possible to navigate directly to the desired sensor.

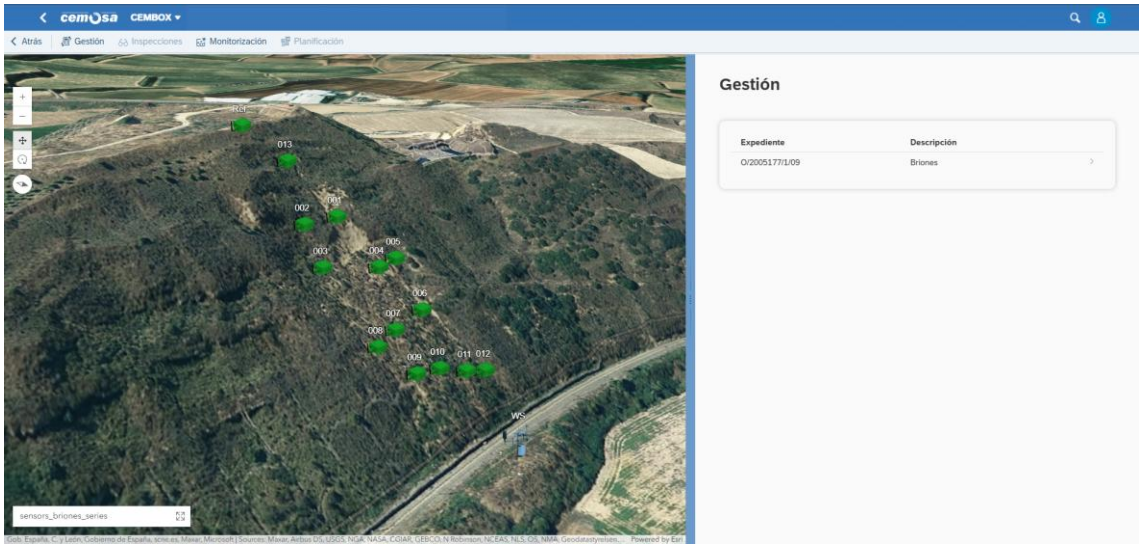

Figure 6-62: Platform to monitor the Briones slope.

7. Demonstration Plan.

The first part of the chapter affirms the assets for KPIs evaluation in the deliverable D13.3. In the second part, the performance indicators of the demonstration are discussed in detail.
To start with, we report a table highlighting the influence of UC1 (Italian Use case) and UC2 (Spanish Use case) to the MAWP KPIs.

	Asset Management & Infrastructure		Asset Management & Digital Twins	Design & Manufacturing			Robotics & Interventions		
	Asset Management of Infrastructure Operation		Asset Management, addressing both Rolling Stock &	Advanced and Holistic Design			Remotely controlled and unmanned interventions		
IAM4RAIL Technical KPIs/ Impacts/ Enablers / Use Cases	3.4.1 Infrastructure Operation: Reduction of maintenance costs *(Targeting 10% in specific use case)*	3.4.2 Infrastructure Operation: Reduction of service failures *(25% reduction)*	3.5 Number of assets managed and monitored by Digital Twin *(Increase by 25 %)*	3.6.1 For repair: Extension of remaining life *(25%)*	3.6.2 Time reduction (from design to manufacturing) *(20%)*	3.6.3 Design and Manufacturing: Cost reduction *(20%)*	3.7.1 Increased accuracy of inspections with respect to conventional interventions *(25%)*	3.7.2 Reproducibility of inspections with respect to conventional interventions *(25%)*	3.7.3 Cost reductions of the interventions *(by at least 10%)*
	Enabler 1, 2, 4, 5	Enabler 1, 2, 4, 5	Enabler 5	Enabler 6, 7	Enabler 6, 7	Enabler 6, 7	Enabler 2, 7	Enabler 2, 7	Enabler 2, 7
UC 12.1 - Multiscale monitoring of civil assets									
UC 12.2 - Bridges and earthworks assets management aided by geotechnics									

Table 7-1: Use Case MAWP-KPI.

Furthermore, in the next table, the Use Case KPIs are explicitly related to the various prototypes set as benchmarks for the demonstration.

PROT ID	PROTOTYPE NAME	TARGETRED MAWP KPI	Use case KPI	Baseline
12.1.1	VEG. ENCHROACHEMENT	3.4.1 + 3.7.3	KPI1+KPI3	Survey on the field
12.1.2	CLASSIFICATION & TRACK CHANGE	3.4.1+ 3.7.3	KPI1+KPI3	Survey on the field
12.1.3	LANDSLIDE & SUBSIDENCE	3.4.1+ 3.7.3	KPI1+KPI3	Survey on the field & other instruments
12.1.4	BRIDGE INSPECTION VIA DRONE	3.4.1 + 3.4.2+ 3.7.3	KPI1+KPI2+KPI3	Survey on the field (e.g. scaffolding /cranes) & manual post-processing (inspector)
12.1.5	HYDROGEOLOGICAL RISK	3.4.1+ 3.7.3	KPI1+KPI3	Consulation of Precipitation historical data (often not updated & with no AI support)
12.**2**.1	BRIDGE ASSET MANAGEMENT	3.4.1+ 3.4.2 + 3.5	KPI 1+KPI 2+KPI4	Regular Visual Inspections
12.**2**.2	EARTHWORKS ASSET MANAGEMENT (VILAR DE SILVA)	3.4.1+ 3.4.2	KPI 1+KPI 2+KPI3+KPI 5	Reading of measuring instruments every 4 months
12.**2**.3	EARTHWORKS ASSET MANAGEMENT (BRIONES)	3.4.1+ 3.4.2	KPI 1+KPI 2+KPI3	Survey on the field

Table 7-2: Prototype-MAW-KPI.

Where:

UC		Description
UC12.1	KPI1	Vegetation/Classification/Subsidence/Hydrological Risk/Bridge inspection - reduction of maintenance costs
	KPI2	Bridge inspection - reduction of traffic disruption caused by traditional bridge inspection in the railway infrastructure
	KPI3	Vegetation/Classification/Subsidence/Hydrological Risk/Bridge inspection - Reduction of on-track data collection time
UC 12.2	KPI1	Failure mode predictability
	KPI2	Reduction of theoretical time per circulation by failures in the railway infrastructure
	KPI3	Cost reduction of instrumentation equipment for earthworks
	KPI4	Reduction of costs in the pot bearings replacement
	KPI5	Effectiveness of slope stabilisation measures

Table 7-3: UC12.1 and UC12.2 PIs.

7.1. Demonstration in Multiscale Monitoring of civil assets

The purpose of this use case is to design, develop and implement a system managing the entire life cycle of civil, railway and surrounding territory infrastructures. Maintenance activities are often managed separately and not integrated, requiring a more holistic approach. Information from different data sources must be jointly exploited both to support the decision-making process of maintenance operators and to minimize response times during emergency phases.

7.1.1. Vegetation encroachment

Vegetation near railway infrastructure can pose safety risks such as threes falling onto trains, blocking signals, and reducing visibility at crossings; leading to accidents and service interruptions. Regular inspections—through field visits and video surveillance—are essential to identify vegetation that needs pruning and to monitor the overall condition of the infrastructure. Since traditional inspection methods are time-consuming and costly, a new prototype is being tested to extract canopy height models (CHM) from satellite images; to improve hazard detection. Thus, potential problems arising from vegetation invasion and human activities can be promptly and cheaply reported, producing quantifiable KPIs. The prototype is to be tested in the Milano -Novara area, where data has been procured, both for AI training and validation.

7.1.2. Classification and change detection

The prototype uses semantic segmentation NN to automatically identify and monitor key railway assets using satellite images. The model effectively detected important features such as buildings, railway tracks, and roads, supporting change detection and asset mapping. This approach is particularly useful for monitoring infrastructure and identifying unauthorized changes, like new constructions. The prototype can be tested in the Marche, Lazio, and Campania regions, which included both rural and urban environments for the training of the AI. Replacing in-situ inspection

techniques, when these are used as background, gives rise to quantifiable KPI.

7.1.3. Civil infrastructure monitoring (railway bridges)

To ease and improve the final quality of bridge inspections, drones (UAVs) have been introduced to capture detailed data; especially in hard-to-reach areas. Experimental Campaigns of measurement from different inspection via drone on the Italian territory, apart from demonstrating the effectiveness of aerial technology, offer rich digital data, suitable for artificial intelligence (AI) training. The “Leonessa bridge,” a brick masonry viaduct near Melfi on the Cervaro-Potenza line, was selected for an experimental drone survey in January. This survey supports AI development through defect tagging by RFI inspectors and permits to evaluate the economic and time benefits associated to the usage of innovative technologies in bridge inspections.

7.1.4. Flood Risk Assessment

Hydrogeological instability, primarily due to rainfall, significantly impacts Italy's railway network (over 16,700 km). Effective risk mitigation requires understanding both hazards (mapped by FSI using local authority plans and GIS) and asset vulnerabilities, though infrequent plan updates limit awareness. To improve inspection efficiency, satellite-based methodologies like SANF (rainfall analysis), Ramses (radar/climate models), PSF (landslide detection), M.O.M.I.T., and EO4I are being explored. In this prototype, a new Neural Network (NN) tool, trained on 2000-2024 data and validated in April 2025, forecasts flood probabilities with a three-day warning using precipitation, soil moisture, temperature, and land cover data. Tested on the Novara-Milan and Tortona-Voghera lines, this prototype aims to identify vulnerable sections and aid emergency management.

7.1.5. Subsidence and Landslide

This prototype monitors ground deformation (subsidence and landslides) by satellite DInSAR (using Sentinel-1 data). Its processing pipeline ensures high accuracy by minimizing noise. Applied to Italy's Cerignola Campagna (subsidence along a railway line) and Spain's Talud Briones (landslide monitoring), it provides long-term, high-resolution deformation. Replacing in-situ human and automatic inspection techniques to measure land deformation (such as ground sensors, incluging diagnostic vehicles), with the InSAR technique, gives rise to quantifiable KPI as satellite inspection allows vast area to be inspected with reasonable costs.

7.1.6. Web Platform

The current railway asset maintenance relies on periodic visual inspections that detect issues only after they occur, leading to urgent interventions impacting safety and service. The proposed web platform collects and integrates data from multiple sources (mostly from the prototypes above mentioned) to monitor civil works and the surrounding environment. This strategic tool supports multiscale analysis of environmental and territorial data, helping identify critical events and promoting sustainable decision-making. Through interactive web interfaces, users can easily access and manage both graphical and alphanumeric data.

7.2. Demonstration in Bridges and earthworks assets management aided by geotechnics

7.2.1. Viaducto Huertas de Mateo, Spain

The scope of this demonstrator focuses on studying the premature degradation of Pot bearings in long-span railway bridges, especially those exceeding 1000 meters in length. These structures are particularly affected in areas with high thermal gradients, where combined effects of curved alignments and train speeds over 300 km/h generate significant dynamic and structural demands that accelerate bearing deterioration.

Such viaducts experience substantial relative displacements between deck and supports, along with high torsional and axial forces, causing essential elements like Pot bearings to lose functionality before their intended service life. This poses risks to infrastructure safety and operational continuity.

For this project, the Viaduct of las Huertas de Mateo, a 999-meter-long bridge on Line 040 (Bif. Torrejón de Velasco – Valencia Joaquín Sorolla at PK 285+486), has been selected. It is considered one of the structures with the greatest axial displacements in the network, making it an ideal case study for testing predictive maintenance strategies.

Currently, maintenance is based on periodic visual inspections, which can only detect damage after it has occurred, leading to urgent corrective actions that impact service and safety. The objective of this demonstrator is to acquire technical knowledge and develop an initial tool to shift from corrective and preventive maintenance to predictive maintenance. Through continuous monitoring of key structural parameters, this approach aims to anticipate deterioration and schedule interventions before functional loss occurs.

This change in asset management is essential for enhancing the availability, safety, and cost-efficiency of the high-speed rail network.

7.2.2. Vilar de Silva, Spain

The slope located at the entrance to Tunnel No. 40 - Vilar de Silva, between kilometre points 277+100 and 277+457 on the Palencia – La Coruña line, exhibits active geotechnical instability with a long-documented history dating back to the 19th century, even before the railway line was constructed in 1880. A combination of high rainfall, the presence of a reservoir with constant water level oscillation, and local geological conditions has led to recurring landslides that affect both the tunnel entrance and the approach track, resulting in damage to the tunnel lining and track geometry deformations.

These phenomena have caused alignment shifts, platform instability, and operational restrictions that compromise both safety and service efficiency.

To transition from a corrective maintenance model to a predictive strategy, the following monitoring system was implemented:

- IoT network of wireless sensors (clinometers on soil, rock, sleepers, and tunnel vault).
- Weather station with temperature, humidity, and rainfall sensors.
- Solar-powered gateway for local and remote communication.

These data streams are collected in real time and fed into a digital infrastructure management platform, which enables statistical analysis, alarm generation, and predictive maintenance decision-making.

This use case marks a significant step toward the digital transformation of geotechnical asset management. The integration of IoT sensors, satellite imagery, and predictive modelling allows for early failure detection, cost optimization, and minimized operational impact. The approach also serves as a reference model for other critical points in the national railway network.

7.2.3. Briones, Spain

Briones slope is located along the Castejón–Bilbao line (Conventional Network), between the towns of Briones and Haro, specifically from P.K. 124+050 to 124+100. This section is geotechnically sensitive, composed of clay soils and detrital fragments (siltstone and sandstone), which become plastic when saturated and lead to mass landslides.

Past incidents show that movements are concentrated in the lower section of the slope, where retaining walls and reinforced concrete buttresses are in place—many of which have suffered damage due to slope failures.

The monitoring system for Briones includes:

- 14 wireless inclinometers installed on corrugated rods embedded in the ground.
- Solar-powered gateway, mounted on a steel mast.
- Weather station (rain, temperature, humidity sensors).

The continuous monitoring system, operational since July 2024, has captured relevant data in real time without incident. The technical feasibility has been proven, and the algorithm training phase is currently in progress. The experience gained in Briones will be instrumental in validating the effectiveness of future slope stabilization measures and demonstrates the value of innovation in railway infrastructure asset management under complex geotechnical conditions.

7.3. Evaluation: Key Performance Indicators

UC12.1: demonstrator's KPI

The key performance indicators (KPIs) indicated by UC12.1 are conceived to measure costs and times. These are optimised through the development of prototypes that, with the help of neural networks and artificial intelligence analysis, allow the monitoring, control and inspection of the railway infrastructure and its civil works, even in extreme weather conditions, with the aim of minimising traffic disruption, in favour of the reliability and availability of the infrastructure and improved safety.

The objectives of this use case are in line with the description of the FP3-IAM4Rail demonstrator #4: "Asset Management & Infrastructure" and the related KPIs. Specifically, the FP3-IAM4Rail Grant Agreement connects the DO4 with the following Key Performance Indicators:

KPI (GA)	Description	Impact
VI	**Infrastructure Operation: reduction of maintenance costs (targeting 10% in specific use case)**	**High/direct**
VII	**Infrastructure Operation: reduction of service failures (25% reduction)**	**High/direct**
VIII	Number of assets managed and monitored by Digital Twin (increase by 25 %)	Little/indirect
IX	For repair: extension of remaining life (25%)	Little/indirect
XIII	Reproducibility of inspections with respect to conventional interventions (25%)	Little/indirect
XIV	**Cost reductions of the interventions (by at least 10%)**	**High/direct**

Table 7-4: UC12.1 KPIs on a FP level from the Grant Agreement.

To contribute to those high-level KPIs, the following specific PIs are proposed for this use case (with Table 7-3: UC12.1 and UC12.2 PIs details):

PI	Description	Target value
12.1-1	Reduction of maintenance costs	10 %
12.1-2	Reduction of traffic disruption caused by traditional bridge inspection in the railway infrastructure	25 %
12.1-3	Reduction of on-track data collection time	10 %

Table 7-5: UC12.1 KPIs.

Relation to FP3-IAM4RAIL's project KPIs

Considering the project pathways called the MAWP KPI, the concrete impacts for the described KPIs are the following:

KPI ID	IMPACT IN WP12	WHY
VI	Infrastructure Operation: reduction of maintenance costs (targeting 10% in specific use case)	Technologies developed in this FA introduce drones and digital/IA solutions to reduce maintenance time and human intervention.
VII	Infrastructure Operation: reduction of service failures (25% reduction)	This KPI relates to the time of traffic disruption/speed reduction, impacting the operability of the line directly referring to the number of trains in service. Studying this KPI, the time the section is in temporary speed limitation will be reduced so that the train service will improve.
XIV	Cost reductions of the interventions (by at least 10%)	This KPI relates to time/cost reduction for track data collection with a new monitoring system using remotely acquired data. Global technological leadership is supported by a combination of innovation and technical standards, defining innovative maintenance decision-making concepts. The harmonisation and simplification of maintenance can be achieved by applying and integrating advanced monitoring approaches, data analytics methodologies, and decision support solutions.

Table 7-6: UC12.1 direct KPI impact.

Finally, regarding the Web Platform, the following is clarified: this prototype contributes to KP3 by reducing track-data collection time, acting as a support for MAWP KPIs 3.4.1 and 3.7.3. The benchmark is trivial, as it is not possible to make a comparison with holistic platforms for the integration of maintenance information and data that are currently acquired from field visits according to IM procedures. So, to calculate the KP3 it is best to consider it as a linear combination of the KP3s of the individual prototypes that are integrated into the platform.

UC12.2: demonstrator's KPI

The KPIs indicated UC12.2 are aimed at measuring the cost and time that is optimised with the development of a predictive maintenance tool, both for the replacement of POT bearings in bridges and the monitoring of slopes with active movements in earthworks with low-cost sensor networks.

The objectives that this use case aims to achieve are in line with the description of the FP3-IAM4Rail demonstrator #4: "Asset Management & Infrastructure" and the related KPIs.

Specifically, the FP3-IAM4Rail Grant Agreement connects the DO4 with the following Key Performance Indicators:

KPI (GA)	Description	Impact
VI	**Infrastructure Operation: reduction of maintenance costs (targeting 10% in specific use case)**	**High/direct**
VII	**Infrastructure Operation: reduction of service failures (25% reduction)**	**High/direct**
VIII	**Number of assets managed and monitored by Digital Twin (increase by 25 %)**	**High/direct**
IX	For repair: extension of remaining life (25%)	Little/indirect
XIV	Cost reductions of the interventions (by at least 10%)	Little/indirect

Table 7-7: UC12.2 KPIs on a FP level from the Grant Agreement.

To contribute to those high-level KPIs, the following specific PIs are proposed for this use case:

PI	Description	Target value
12.2-1	Failure mode predictability	25 %
12.2-2	Reduction of theoretical time per circulation by failures in the railway infrastructure	25 %
12.2-3	Cost reduction of instrumentation equipment for earthworks	10 %
12.2-4	Reduction of costs in the pot bearings replacement	10 %
12.2-5	Effectiveness of slope stabilisation measures	10 %

Table 7-8: UC12.2 PIs.

Relation to FP3-IAM4RAIL's project KPIs

Considering the project pathways called the MAWP KPI, the concrete impacts for the described KPIs are the following:

PI	IMPACT KPI (GA)	DESCRIPTION
12.2-1	Number of assets managed and monitored by Digital Twin (increase by 25 %)	Predictive models will be developed through a digital twin. Currently, there are no predictive models in production for Earthworks and Bridges in ADIF, so we cannot make a comparison with existing data.
12.2-2	25% reduction of in-service failures.	This KPI is directly related to the temporary speed restrictions and time lost per each circulation, parameters that influence the operability of the line by delaying and reducing the number of trains in service. Studying this KPI, the time that the section is in temporary speed limitation will be reduced.
12.2-3	Reduction of maintenance costs up to 10%.	Exact knowledge of the costs of the instrumentation equipment and its effectiveness would reduce some maintenance costs, decreasing the unnecessary ones.
12.2-4	Reduction of maintenance costs up to 10%.	The works processed by emergency represent approximately an extra cost for the administrator of between 45% and 65% compared to a work processed by ordinary procedure. So, with proper planning, it would avoid resorting to emergency works.
12.2-5	Reduction of maintenance costs up to 10%. 25% reduction of in-service failures.	If the stabilising measures were fully effective, the maintenance work of the line would be significantly reduced since the instabilities caused losses of levelling and geometry of the track. On the other hand, since there are no more problems in that section, there would be no temporary speed limits on the track that would cause delays in the train service.

Table 7-9: UC12.2 direct KPI impact.

8. Conclusions

This work covers two main use cases: the Italian case (including multiscale monitoring of various assets using satellite, UAV, and ground data) and the Spanish case (which focuses on asset management for bridges and earthworks supported by geotechnical data). The report details the data collection, the analysis methods and the development of user platforms, providing a comprehensive overview of the innovative solutions. The conclusions for the individual prototypes are as such:

Multiscale Monitoring of Civil Assets (Italian UC)

Vegetation encroachment: The study tested automatic extraction of Canopy Height Models from satellite images to improve hazard detection. Increasing further the dataset size or filtering by class did not significantly enhance further the model performance but generalised the network capability. Although zones with big clusters of three had heights often underestimated, the areas surrounding the railway corridor were sufficiently accurate. Incorporating vegetation indices like NDVI, GNDVI, and NDRE may further improve reliability. Future work will focus on integrating these indices and contour areas, as this direction appears promising.

Classification and change detection: The results of this job confirmed the effectiveness in accurately identifying important features such as buildings, railway tracks, and roads, enabling reliable change detection and asset mapping via AI. The approach proved valuable for infrastructure monitoring, particularly in detecting unauthorized changes like new buildings. Detection of Road-rail intersections are likely to improve by expanding the training dataset. Future work will focus on directly detecting more complex structures to further enhance automation, establishing a strong basis for automated railway asset monitoring.

Bridge inspection and defects analysis: The integration of drone technology and AI into the inspection of railway bridges has proven both feasible and promising, offering significant improvements in efficiency and data quality compared to traditional methods. The two-stage AI pipeline—first classifying materials and then detecting defects—has shown strong initial results, particularly in identifying concrete structures. The current model's limited ability to generalize to new bridge types highlights the need for a more diverse and representative dataset. Ongoing efforts to expand and refine the training data are expected to enhance the system's robustness and accuracy. This innovative approach marks a significant step forward in the digital transformation of infrastructure maintenance, paving the way for safer and more cost-effective asset management.

Subsidence & Landslides: Subsidence and landslides phenomena have been separately threated on two areas (Italy and Spain). For both sites, a ten-year observation period (2015-2025) was analysed, providing a longer and more detailed dataset than currently available public services. The document outlines a refined InSAR processing methodology that utilizes a vast stack of SAR images over time. The INSAR processing pipeline allows for more accurate and reliable monitoring of ground deformation caused by subsidence and landslides. Further insight & possible comparison with ground probes will be threated separately in deliverable D13.3.

Flood risk assessment: A monitoring and forecasting tool was developed using satellite data on

precipitation, soil moisture, land surface temperature, and land cover to assess flood risk along Italian railway lines. On the Novara - Milan railway line, after training with data spanning from 2000 to 2024, the tool can provide probability maps for flood events with a three-day warning. Validation in 2025 confirmed its effectiveness. The tool helps identify vulnerable railway sections and supports emergency management. Climate model projections indicate that, by 2100, maximum daily precipitation could increase by 32% in the Novara region and 28% in Tortona, highlighting a significant rise in flood risk due to climate change.

Web Platform for multiscale monitoring: this platform used for multi-scale monitoring of railway infrastructure and the surrounding environment, represents an advanced tool that integrates data from different sources, such as environmental sensors, field surveys and open datasets, in a centralized system that supports complex spatial analysis and real-time monitoring. The platform hosts the various prototypes of the deliverables, representing a unique multi-scale monitoring solution with unparalleled integration, interoperability and customization capabilities. Future developments aim to integrate 3D visualization, digital twins and UAV data to improve predictive maintenance and infrastructure management.

Bridges and Earthworks Asset Management aided by Geotechnics (Spanish UC)

Earthworks. Wireless sensor networks were installed to monitor two unstable railway slopes (Briones and Vilar de Silva) in real time. Both sites faced recurring slope movements, requiring more reliable, continuous monitoring beyond traditional methods. The objective was to deploy IoT-based systems for early detection of ground movements, integrating data into online platforms with automatic alarms. The methodology combined wireless inclinometers, weather stations, and, at Tunnel 40, satellite-based DInSAR analysis and conventional geotechnical monitoring. Both systems have performed reliably, transmitting hourly data and supporting initial alarm development. Dashboards were created for real-time data visualization and anomaly detection. Although the short monitoring period limits full validation, results confirm system stability and effective data acquisition. The main limitation is the need for a full year of continuous data to train and validate predictive algorithms. Some alarms may react to rare environmental conditions, and geotechnical interpretation remains complex. The most effective solution has been the integration of IoT networks with customized data platforms and alarm systems. The deliverables have met their objectives and offer a scalable monitoring model for other railway slopes and infrastructure assets. Future work will focus on completing the one-year data period, refining algorithms, adding geotechnical sensors, and exploring AI-based data analysis**.**

Bridges. In Huertas de Mateo Bridge, a comprehensive structural health monitoring system has been deployed, with accelerometers, inclinometers, LVDTs and temperature sensors installed on the bridge to capture a wide range of physical parameters. The objective is to characterize the structural behaviour under real-world operating conditions and environmental influences.
Two complementary analysis approaches were developed. The first is grounded in OMA, which allows for the identification of modal parameters such as natural frequencies, damping ratios, and mode shapes using only ambient vibration data. This enables non-intrusive monitoring of dynamic

properties that are sensitive to structural changes. The second focuses on anomaly detection, specifically targeting the time series of displacement measurements recorded at the POT-type bridge bearings. This method seeks to identify deviations from expected behaviour indicating potential damage or degradation. The results, in Section 6, offer a detailed understanding of the structural performance and temporal evolution of the monitored parameters. From these results, threshold values have been established to define acceptable tolerance ranges. These thresholds facilitate the implementation of continuous monitoring frameworks, whereby real-time data can be automatically assessed to detect abnormal patterns. To enhance interpretability and decision-making, the outcomes of these analyses are categorized into three severity levels, representing low, medium, and high concern. This classification framework is currently being integrated into the FP3-IAM4RAIL project's digital platform, enabling visualization, tracking, and timely interventions.

The deliverable's key contribution is a suite of tools that serve as building blocks for a integrated support system for railway operations and maintenance. These tools, developed in Work Packages 12 and 13, are designed to work together to improve the efficiency of maintenance activities, reduce resource use, and minimize service disruptions by enabling better coordination.
A central challenge addressed by all the use cases is the real-time monitoring of railway infrastructure to gain updated knowledge. Each tool focuses on a specific type of infrastructure—such as bridges, tunnels, railway and surrounding—because these assets are subject to different degradation processes and local conditions. Although a one-size-fits-all solution is not possible, the successful, site-specific approaches detailed in the use cases provide a framework for creating generalizable methodologies for future railway infrastructure management.
Another shared challenge is integrating diverse data sources. The tools in this deliverable combine various data signals, which differ in scale and relevance, to produce valuable insights for decision-making. Ultimately, the information from this infrastructure monitoring can be used for both immediate decisions and long-term. This work is critical because a failure in these civil structures and track components can have significant financial and operational consequences.

9. References

Bovenga, Nutricato, Refice, Guerriero, Chiaradia - SPINUA: A Flexible Processing Chain For ERS / ENVISAT Long Term Interferometry – April 2005

Appendix I - Accuracy analysis of models

This appendix describes in detail the statistical metrics used in the accuracy analysis conducted in *Section 5.7.2.*

Standard deviation

The standard deviation (ST) measures how much data varies from the mean. Performance has been evaluated by subtracting the standard deviation from historic data and then taking the inverse of the result.

$$Standard\ deviation = \sqrt{\frac{1}{N} \cdot \sum (x_i - \bar{x})^2}$$

Trend slope

Trend slope measures how data changes over time. A positive trend means an increasing pattern, while a negative trend means a decreasing one. Performance has been evaluated by subtracting the trend slope from historic data and then taking the inverse of the result.

$$Trend\ slope = mx + b$$

Pearson correlation coefficient

Pearson correlation measures how two datasets (historic vs. numerical) move together over time. This correlation measures how well the model follows the historic trend by analysing pattern similarities.

$$r = \frac{\sum (X_i - \bar{X})(Y_i - \bar{Y})}{\sqrt{\sum (X_i - \bar{X})^2} \cdot \sqrt{\sum (Y_i - \bar{Y})^2}}$$

where:

X	*Historic data*
Y	*Projected data*
$\bar{X}, \bar{Y}$	*Means of the datasets*

Pearson correlation coefficients range from -1 to 1:

- 1 indicates perfect positive correlation (both increase/decrease together).
- 0 indicates no correlation.
- -1 indicates perfect negative correlation (one increases while the other decreases).

Kolmogorov-Smirnov statistic (KS)

The KS statistic measures the difference between two probability distributions. It checks whether the historic and projected datasets come from the same distribution shapes by comparing the cumulative distribution functions (CDFs). A low KS value indicates that the distributions are similar, while a high KS value indicates that they are different. Performance has been evaluated by doing the inverse of the result.

$$D = sup_x|F_1(x) - F_2(x)|$$

where:

$F_1(x)$ *Cumulative distribution function (CDF) of historic data.*

$F_2(x)$ *Cumulative distribution function (CDF) of projected data.*

D *Maximum difference between CDFs.*

All metrics have been normalised considering the maximum value within each metric.